Institut für Konstruktion und Entwurf
Stahl- Holz- und Verbundbau
Universität Stuttgart

Buckling Behaviour of Unstiffened and Stiffened Steel Plates Under Multiaxial Stress States

Antonio Zizza

Mitteilungen

Dezember 2016 Nr. 2016-1

Buckling Behaviour of Unstiffened and Stiffened Steel Plates Under Multiaxial Stress States

Von der Fakultät Bau- und Umweltingenieurwissenschaften
der Universität Stuttgart zur Erlangung der Würde eines Doktors der
Ingenieurwissenschaften (Dr.-Ing.) genehmigte Abhandlung

Vorgelegt von

Antonio Zizza

aus Foggia (Italien)

Hauptberichterin: Prof. Dr.-Ing. Ulrike Kuhlmann
Mitberichter: Univ. Prof. Dipl.-Ing. Dr. techn. Gerhard Lener

Tag der mündlichen Prüfung: 14.11.2016

Institut für Konstruktion und Entwurf der Universität Stuttgart

2016

Mitteilungen des Instituts für Konstruktion und Entwurf; Nr. 2016-1

Antonio Zizza — Buckling Behaviour of Unstiffened and Stiffened Steel Plates Under Multiaxial Stress States

Herausgeber — Prof. Dr.-Ing. Ulrike Kuhlmann
Pfaffenwaldring 7
70569 Stuttgart
Germany
Telefon: +49 (0)711 - 685 66245
Telefax: +49 (0)711 - 685 66236

Redaktion — Dipl.-Ing. (FH) Florian Eggert M.Eng.

D 93

ISSN 1439-3751

Vorwort

Die vorliegende Arbeit entstand während meiner Tätigkeit als wissenschaftlicher Mitarbeiter am Institut für Konstruktion und Entwurf der Universität Stuttgart. Mein ganz besonderer Dank gilt Frau Professorin Ulrike Kuhlmann, Leiterin des Instituts, für die Ermöglichung und Förderung meiner Arbeit, das entgegengebrachte Vertrauen während meiner Zeit am Institut sowie die Übernahme des Hauptberichts.

Mein aufrichtiger Dank gilt auch Herrn Professor Gerhard Lener, Leopold Franzens Universität Innsbruck, Österreich, für das Interesse an der Arbeit, die kritische Durchsicht und die Übernahme des Mitberichts.

Ein weiterer Dank gilt der Arbeitsgemeinschaft industrieller Forschungsvereinigungen (AiF) „Otto von Guericke“e.V., dem Research Fund for Coal and Steel (RFCS) sowie der Deutschen Forschungsgemeinschaft (DFG) für die finanzielle Unterstützung der experimentellen und theoretischen Untersuchungen. Allen beteiligten Partnern danke ich für die gute Zusammenarbeit.

Ein besonderer Dank gilt Herrn Oliver Schneider und den Mitarbeitern der Materialprüfanstalt für die konstruktive und tatkräftige Unterstützung bei der Vorbereitung und Durchführung der Versuche.

Weiterhin möchte ich mich an dieser Stelle herzlich bei Dr. Franc Sinur für seine Anregungen und Denkanstöße bedanken.

Den Herren Alessandro Cefalu und Patrick Tutzauer vom Institut für Photogrammetrie danke ich für die Durchführung der photogrammetrischen Messungen im Rahmen der experimentellen Untersuchungen.

Herrn Vahid Pourostad danke ich für die angenehme Zusammenarbeit und die Untersuchungen im Rahmen seiner Masterarbeit und wünsche ihm nun am Institut alles Gute und viel Erfolg bei der Erstellung seiner Dissertation.

Meinen ehemaligen Kollegeinnen und Kollegen möchte ich herzlich für die gute Zusammenarbeit, die angenehme Arbeitsatmosphäre und die schöne Zeit am Institut danken.

Ein ganz besonderer und aufrichtiger Dank gilt meiner Frau und meiner Familie für die stetige Motivation und uneingeschränkte Unterstützung.

Stuttgart, im November 2016 Antonio Zizza

Abstract

Modern steel constructions such as long span bridges are characterised by slender plated structures with low material consumption and the optimisation of their fabrication, leading to low dead loads and a high utilisation. Since often several internal forces act at the same time on the cross-section, very complex multiaxial stress states may develop. The aim of this work is to analyse the buckling behaviour of multiaxially loaded plates in order to increase the insight and to allow the enhancement of the current design rules of unstiffened and stiffened plates under several load combinations focusing on the reduced stress method according to Chapter 10, EN 1993-1-5 [36] and especially to analyse the influence of tensile stresses. As in EN 1993-1-5 [36] according to the reduced stress method multiaxial stress states are already considered in the determination of the single plate slenderness, this theoretically allows for taking into account the positive effect of tensile stress on the buckling behaviour. However, only few studies have looked on this effect until now and systematic investigations are missing, so that this work clarifies this open issue.

In a first step the elastic buckling of flat plates and the effect of multiaxial stress states are described. The buckling coefficient for unstiffened panels is given as a function of the panel aspect ratio and the stress state resulting in significantly elevated values if tensile stresses are acting. However, the evaluation of the buckling coefficient shows pronounced peaks for certain cases, where it is questionable if they should be taken into account for the design. Therefore, a formulation is presented for ignoring these peaks. For the assessment of the buckling coefficient in case of stiffened plates several possibilities are explained. The complexity in the determination of the buckling coefficient, which involves a variety of parameters, leads to the conclusion that nowadays numerical techniques are the most appropriate approaches. Furthermore, the current rules according to EN 1993-1-5 [36] are explained in detail with a particular look on multiaxially loaded plates showing the impact of the stress state on the plate slenderness and therefore on the interaction curves. The interaction curves according to EN 1993-1-5 [36] allow a systematic utilisation of the favourable effect of tensile stresses on the buckling behaviour, especially compared to the rules according to DIN 18800-3 [22]. However, studies to justify this beneficial effect are missing. Therefore, experimental and numerical investigations are conducted to give an insight in the buckling behaviour of multiaxially loaded plates.

Experimental investigations on stiffened and unstiffened steel plates are conducted showing the buckling behaviour under several multiaxial stress states. Therefore, six tests on isolated steel plates have been conducted and presented giving an insight into the buckling behaviour of multiaxially loaded panels. While for the uniaxially loaded reference tests one half-wave failure modes were observed, mode transitions occurred when additional tensile stresses were applied in transverse direction. This behaviour fits well with the behaviour for linear elastic buckling analyses (LBA), where tensile stresses also lead to multi-wave buckling shapes. Furthermore, six full scale plate girders stiffened with transverse and longitudinal stiffeners were tested for the interaction of high bending moment and shear force. The positive effect of tension stresses on the buckling behaviour of slender plates can clearly be seen, as subpanels subjected to compression and shear were the decisive ones and subpanels subjected to tension and shear showed only very slight out-of-plane deformations due to shear.

In order to investigate a wide parametric range for analysing the buckling behaviour of multiaxially stressed plates the Finite Element Method is adopted within this work. After an overview on the method and the assumptions in accordance to Annex C, EN 1993-1-5 [36] the recalculations of the above mentioned experimental investigations are conducted, showing an appropriate agreement between the experimental and the numerical investigations, so that numerical recalculations of the tests confirmed the experimental observations and the applied procedure for conducting the numerical investigations can be regarded as verified. However, for the realisation of the parametric studies, simplified models are generated considering several kinds of boundary conditions. For investigating the buckling behaviour of longitudinally stiffened plates, a numerical model is developed based on the outcomes from the numerical investigations on unstiffened plates. The longitudinal stiffeners are applied as open sections and the dimensions are chosen to avoid torsional buckling of the stiffeners. In order to cover a wide parametric range, three different relative stiffness are applied to the plate as well as different panel aspect ratios and numbers of the stiffeners.

For the numerical parametric studies on plates under multiaxial stress states the stress ratio has a decisive impact on the failure mode, as also observed during the experimental investigations, so that several initial imperfection shapes are applied in order to aim at a lower safe-sided bound for the results and to avoid suppressed failure mode transitions. The parametric study itself is conducted using the ABAQUS-intern Python interpreter and a parametrised model where the respective parameters and imperfections are applied using Matlab subroutines considering the interaction cases tension–compression, tension–shear, compression–shear and bending–shear on unstiffened plates as well as biaxial compression on stiffened plates. In case of plates subjected to tension–compression the boundary conditions show to have mainly an influence on the resistance for predominant uniaxial compression. With increasing tension the differences vanish, so that a simplified expression is presented to estimate if an unstiffened multiaxially loaded panel is subjected to plate buckling independently from the boundary conditions. For plates subjected to shear and predominantly tension a pronounced beneficial effect from ten-

sile stresses is observed, especially for $\psi \geq 0$. Further numerical investigations focus on the buckling behaviour of stiffened plates subjected to biaxial compression. Several combinations of imperfections are therefore applied to the numerical model according to Annex C, EN 1993-1-5 [36]. The results highlight the sensitivity of stiffened plates subjected to biaxial compression in case of weak stiffeners, where pronounced reductions occur. Similar findings are also found for long plates, where global buckling might become decisive for transverse stress, while for smaller aspect ratios usually local buckling occurs even for weak stiffeners. For certain cases local buckling is found for uniaxial compression in both directions, while global buckling occurs in the interaction domain concluding that a general separation of the load cases for stiffened plates does not seem to be reasonable, as deviating forces may lead to a global failure.

Based on the presented parametric study a new design proposal is developed and compared to the numerical results showing good agreements for the investigated load cases justifying the utilisation of positive effects from tensile stresses and an improvement of the interaction considering bending–shear. Furthermore, for the boundary condition with edges free to move in–plane the resistance is found to be overestimated when column–like behaviour plays a role. This was already observed by Seitz [101], who proposed a modified formulation for the interpolation between plate–like and column–like behaviour in case of transverse stresses. The approach is adopted within this work for transverse stresses resulting in an appropriate agreement between the interaction curves and the numerical simulations. In order to give a useful ready to hand tool to the practical engineer for conducting buckling analyses according to the proposal within this work, interaction charts are given in the Annex for a simplified procedure.

The outcomes of this work allow the consideration of tensile stresses for the design of plated structures and is in full accordance with the principles of the reduced stress method for the current design procedure in EN 1993-1-5 [36]. Furthermore, the numerical analyses highlight issues regarding the modelling and the realisation of buckling analyses using the Finite Element Method, especially in terms of initial imperfections.

Keywords:
plate buckling, steel structures, unstiffened plates, stiffened plates, interaction, reduced stress method, tensile stresses

Zusammenfassung

Aus Blechen zusammengesetzte Bauteile sind ein fester Bestandteil des modernen Brücken- und Hochbaus, wenn es darum geht einen Querschnitt bereitzustellen, der durch ein Minimum an Materialeinsatz und ein Maximum an Materialausnutzung gekennzeichnet ist. Da in der Regel am Querschnitt mehrere Schnittgrößen wirken, herrschen in den jeweiligen Bauteilen mehraxiale Spannungszustände, denen Rechnung getragen werden muss. Ziel dieser Arbeit ist es, das Beulverhalten mehrachsig beanspruchter Platten zu untersuchen und daraus Erkenntnisse zu gewinnen, um die derzeit geltenden Bemessungsregeln nach der Methode der reduzierten Spannugen gemäß Abschnitt 10, EN 1993-1-5 [36] für unausgesteifte und ausgesteifte Platten unter verschiedenen Lastkombinationen zu verbessern und dabei insbesondere den Einfluss gleichzeitig wirkender Zugspannungen zu analysieren. Mit Einführung von EN 1993-1-5 [36] ist es nun möglich, unter Anwendung der Methode der reduzierten Spannungen, den gesamten Spannungszustand zur Berechnung eines einzigen Plattenschlankheitsgrades heranzuziehen, was es theoretisch auch erlauben würde den Einfluss gleichzeitig wirkender Zugspannungen zu berücksichtigen. Jedoch existieren hierzu kaum Untersuchungen, so dass die Fragestellung nach dem Einfluss der Zugspannungen im Rahmen dieser Arbeit geklärt werden soll.

In einem ersten Schritt wird das elastische Verzweigungsproblem schlanker Platten und der Einfluss mehrachsiger Spannungszustände beschrieben. Der Beulwert unversteifter Platten wird als Funktion der Seitenverhältnisse und der Spannungszustäde angegeben und resultiert in deutlich erhöhten Werten, wenn gleichzeitig Zugspannungen wirken. Allerdings zeigt die Auswertung der Beulwerte ausgeprägte Spitzen für bestimmte Fälle, bei denen es fraglich ist, ob sie für die Bemessung berücksichtigt werden sollten. Daher wird eine Formulierung hergeleitet, um diese Spitzen zu vernachlässigen. Für die Bestimmung der Beulwerte versteifter Platten werden verschiedene Möglichkeiten erläutert. Die Komplexität bei der Bestimmung des Beulwerts, die eine Vielzahl von Parametern umfasst, lässt die Schlussfolgerung zu, dass heutzutage numerische Verfahren die geeignetsten Verfahren hierfür darstellen. Die derzeitig gültigen Bemessungsregeln nach EN 1993-1-5 [36] werden detailliert dargestellt mit besonderem Blick auf mehrachsig beanspruchte Platten, bei denen der Spannungszustand einen direkten Einfluss auf die Schlankheit und somit auch auf die Interaktionkurven hat. Die Interaktionskurven nach EN 1993-1-5 [36] ermöglichen eine systematische Ausnutzung der günstigen Wirkung von Zugspannungen auf das Beulverhalten, vor allem im Vergle-

ich zu den Regeln nach der zuvor gültigen DIN 18800-3 [22]. Allerdings fehlen bislang Studien, die diese positive Wirkung rechtfertigen. Daher werden im Rahmen der vorliegenden Arbeit experimentelle und numerische Untersuchungen vorgestellt, die einen Einblick in das Beulverhalten mehrachsig beanspruchter Platten zu geben.

Die experimentellen Untersuchungen an ausgesteiften und nicht ausgesteiften Platten zeigen das Beulverhalten unter verschiedenen mehrachsigen Spannungszuständen. Dafür wurden sechs Versuche an mehrachsig beanspruchten schlanken Stahlplatten durchgeführt und vorgestellt, um einen Einblick in das Beulverhalten zu geben. Während für die einachsig belasteten Referenzversuche stets einwellige Versagensformen beobachtet werden konnten, traten mehrwellige Versagensformen ein, wenn zusätzlich Zugspannungen in Querrichtung aufgebracht wurden. Das entspricht dem Verhalten des Verzweigungsproblems nach der linear elastischen Beultheorie (LBA), wo Zugspannungen auch zu mehrwelligen Eigenformen führen. Des Weiteren wurden sechs Versuche an längs- und querausgesteiften Trägern unter Wirkung hoher Biegemomente und Querkraft durchgeführt. Die günstige Wirkung von Zugspannungen auf das Beulverhalten schlanker Platten konnte dabei deutlich beobachtet werden, da die Teilfelder unter Wirkung von Druck- und Schubspannungen maßgebend wurden, während Teilfelder unter Wirkung von Zug- und Schubspannungen nur sehr geringe Verformungen aus der Ebene heraus aufwiesen.

Um einen weiten Parameterbereich für das Beulverhalten mehrachsig beanspruchter Platten zu untersuchen, wird im Rahmen dieser Arbeit die Methode der finiten Elemente (FEM) angewandt. Nach einem Überblick über die Methode und die Annahmen gemäß Anhang C, EN 1993-1-5 [36] werden Simulationen der oben genannten Versuche durchgeführt. Das gleiche Beulverhalten wurde dabei auch bei der numerischen Nachrechnung der Versuche beobachtet. Das validierte numerische Modell wird für die mit ABAQUS durchgeführten Parameterstudien herangezogen, um die Auswirkung verschiedener Einflussgrößen zu beurteilen. Für die Durchführung der Parameterstudien werden vereinfachte Modelle mit verschiedenen Ansätzen für die Randbedingungen erzeugt. Um das Beulverhalten längsversteifter Platten zu untersuchen, wird ein numerisches Modell entwickelt, das auf den Ergebnissen der numerischen Untersuchungen für unausgesteifte Platten beruht. Als Längssteifen werden offene Querschnitte gewählt und die Abmessungen sind so bestimmt worden, dass ein Biegedrillknicken der Steifen nicht maßgebend wird. Um einen weiten Parameterbereich abzudecken, werden drei unterschiedliche relative Steifigkeiten der Längssteifen verwendet, sowie verschiedene Seitenverhältnisse der Beulfelder und Anzahl der Steifen.

Wie auch bei den experimentellen Untersuchungen bereits festgestellt wurde, hat das Spannungsverhältnis bei Platten unter mehrachsigen Spannungszuständen einen entscheidenden Einfluss auf den Versagensmodus, so dass für die numerischen Untersuchungen mehrere Anfangsimperfektionen angesetzt werden, um ein Unterdrücken von Übergängen der Versagensmodi zu vermeiden. Die Parameterstudie selbst wird mit Hilfe des ABAQUS-internen Python-Interpreters und parametrisierten Modellen durchgeführt, bei denen die jeweiligen Parameter und Imperfektionen über Matlab-

Subroutinen hizugefügt werden. Es werden dabei die Interaktionsfälle Zug–Druck, Zug–Schub, Druck–Schub und Biegung–Schub für unausgesteifte Platten sowie biaxialer Druck für ausgesteifte Platten betrachtet. Im Fall von auf Zug–Druck beanspruchten Platten haben die Randbedingungen in erster Linie einen Einfluss auf das Tragverhalten bei vorherrschend einachsigem Druck. Mit zunehmenden Zugspannungen verschwinden diese Unterschiede, so dass ein vereinfachter Ausdruck hergeleitet wird, um zu beurteilen, ob für unausgesteifte Fälle Plattenbeulen maßgebend wird. Für den Fall Zug–Schub wird eine günstige Wirkung der Zugspannungen beobachtet, vor allem für $\psi \geq 0$. Weitere numerische Untersuchungen konzentrieren sich auf das Beulverhalten ausgesteifter Platten unter biaxialem Druck. Verschiedene Kombinationen von Anfangsimperfektionen nach Anhang C, EN 1993-1-5 [36] werden dabei auf das numerische Modell angesetzt. Die Ergebnisse zeigen die Empfindlichkeit ausgesteifter Platten unter biaxialem Druck auf, bei denen ausgeprägte Abminderungen bei Verwendung schwacher Steifen auftreten. Ähnliche Ergebnisse wurden auch für lange ausgesteifte Platten beobachtet, bei denen globales Versagen unter Querbelastung maßgebend wurde, während für kleinere Seitenverhältnisse in der Regel ein lokales Versagen auch unter Verwendung schwacher Steifen beobachtet werden konnte. Für bestimmte Fälle wurde ein lokales Beulen der Teilfelder für einachsigen Druck in beiden Richtungen beobachtet, während unter kombinierter Beanspruchung globales Versagen maßgebend wurde, so dass eine "allgemeine Trennung der Lastfälle" für ausgesteifte Platten nicht sinnvoll zu sein scheint, da abtreibende Kräfte auf die Steifen zu globalem Versagen führen können.

Auf der Grundlage der durchgeführten Parameterstudien wird ein neuer Bemessungsvorschlag entwickelt. Der Vergleich mit den numerischen Ergebnissen zeigt dabei gute Übereinstimmungen für die untersuchten Lastfälle und rechtfertigt den Ansatz der positiven Effekte aus Zugspannungen sowie eine Verbesserung der Interaktion Biegung–Schub. Zudem wurde für Platten mit frei verschieblichen Rändern der Widerstand teilweise überschätzt, wenn knickstabähnliches Verhalten vorliegt. Dies wurde bereits von Seitz [101] beobachtet, der eine Modifikation für die Interpolation zwischen plattenartigem und knickstabähnlichem Verhalten bei Querspannungen vorgeschlagen hat. Der Ansatz wird im Rahmen dieser Arbeit für Querspannungen aufgegriffen und führt zu guten Übereinstimmungen mit den numerische Simulationen. Um den bemessenden Ingenieurinnen und Ingenieuren ein nützliches Werkzeug zur Durchführung von Beulnachweisen nach dem vorgestellten Bemessungsvorschlag bereitzustellen, werden im Anhang Interaktionsdiagramme für eine praktische Anwendung angegeben.

Die Ergebnisse dieser Arbeit erlauben eine Berücksichtigung von Zugspannungen für den Beulnachweis in Übereinstimmung mit den Prinzipien der Methode der reduzierten Spannungen nach EN 1993-1-5 [36]. Des Weiteren wird das Thema der Modellierung und Durchführung von numerisch gestützten Berechnungen behandelt, insbesondere der Ansatz von Anfangsimperfektionen.

Schlagwörter:
Plattenbeulen, Stahlbau, unausgesteifte Platten, ausgesteifte Platten,
Interaktion, Methode der reduzierten Spannungen, Zugspannungen

Contents

1 Introduction

1.1 Motivation

Modern steel constructions such as long span bridges are characterised by slender plated structures and the optimisation of their fabrication. Steel plates then tend to buckle due to high slenderness. Since often several internal forces act at the same time on the cross-section, e.g. during the launching of a bridge, very complex multiaxial stress states develop for these structures as illustrated in Fig.1.1.

Current design codes such as EN 1993-1-5 [36] give, apart from the possibility of using the Finite Element Method, generally two different methods for the design of slender plates. The first method, called "effective width method", is based on the reduction of the cross-section area taking into account the local buckling of the subpanels between the stiffeners and the global buckling of the whole stiffened plate. This verification is done for each individual action separately, while for the interaction of different forces interaction formulas are used. The second method, which may be used for the design of plated structures, is the so called "reduced stress method". It is a classic concept

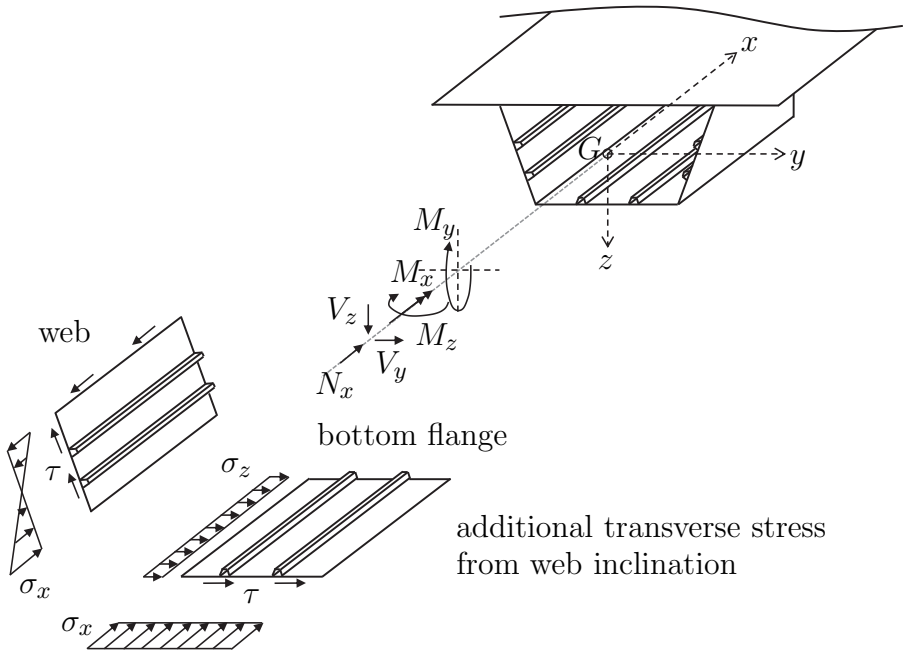

Figure 1.1: Loading of plates on a box-girder cross-section, based on [46].

that limits the allowable stresses in the plate and uses a kind of von-Mises criterion to check the combination of different stresses. This criterion was at first presented in [96] and [95]. The reduction of the allowable stresses in comparison with the full strength is a function of the slenderness of the regarded plate. For the reduced stress method according to EN 1993-1-5 [36] the determination of the plate slenderness is based on the complete stress field, resulting in a unique plate slenderness without the differentiation for the single acting forces. [82] introduces "generalised buckling curves" with the aim of an harmonisation and reduction of the overall number. These are included in Annex B, EN 1993-1-5 [36].

Fig.1.2 shows exemplarily on the cross-section of a box-girder bridge how the inclination of the web may cause transverse tension stress in the bottom flange, which can act stabilising on the buckling behaviour. Another example for the occurrence of multiaxially loaded plates are cable-stayed bridges, see Fig.1.3, where (a) shows the configuration for two outer hangers leading to transverse compression in the upper flange and transverse tension in the bottom flange, while (b) shows the opposite case for a single hanger in the middle of the cross-section. For the consideration of multiaxial stress states such as biaxial compression or tension-compression, as well as for tension-shear with the effective width method there is no option provided for the verification, since the individual loads are in a first step considered separately, so that the design may only be conducted with the reduced stress method.

The verification according to the reduced stress method as mentioned before is derived from the von-Mises criterion with reduced allowable stresses due to buckling, see Eq.(1.1). As here the reduction factors can be determined with a unique plate slenderness taking into account the complete stress field, the consideration of tension stresses leads to positive effects. This gives theoretically the possibility of considering tension stresses for a multiaxially loaded plate subjected to buckling, as there is a direct influence when determining the plate slenderness. Whether the influence of tensile stresses is covered correctly by the design rules given in the code has not yet been investigated, so that this work will clarify this issue.

$$\left(\frac{\sigma_{x,Ed}}{\rho_x f_y/\gamma_{M1}}\right)^2+\left(\frac{\sigma_{z,Ed}}{\rho_z f_y/\gamma_{M1}}\right)^2-\left(\frac{\sigma_{x,Ed}}{\rho_x f_y/\gamma_{M1}}\right)\left(\frac{\sigma_{z,Ed}}{\rho_z f_y/\gamma_{M1}}\right)+3\left(\frac{\tau_{Ed}}{\chi_w f_y/\gamma_{M1}}\right)^2\leq 1 \tag{1.1}$$

Furthermore, recent investigations conducted by Braun [11] on unstiffened plates under biaxial compression showed that the current rules in EN 1993-1-5 [36] may give unsafe results, so that a correction is proposed by introduction of a so-called "V-factor" in the design formula similar to DIN 18800-3 [22]. However, meanwhile questions have raised on the behaviour of stiffened plates and if the proposed factor should be applied also in this case in the formula or if this would lead to uneconomic results.

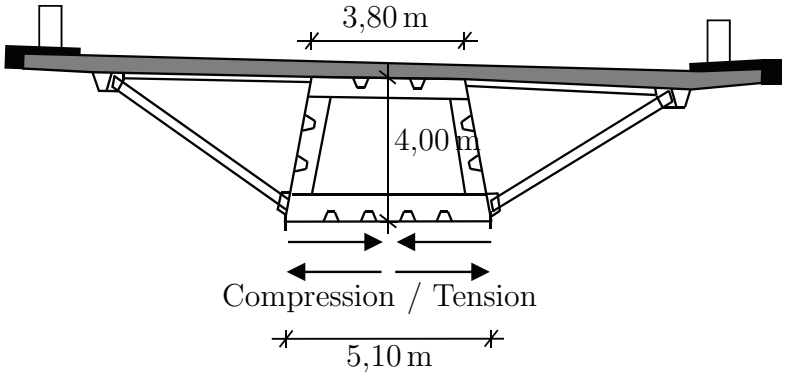

Figure 1.2: Multiaxial stress state on a box-girder bridge (cross-section of the Lennetal bridge in Hagen, Germany).

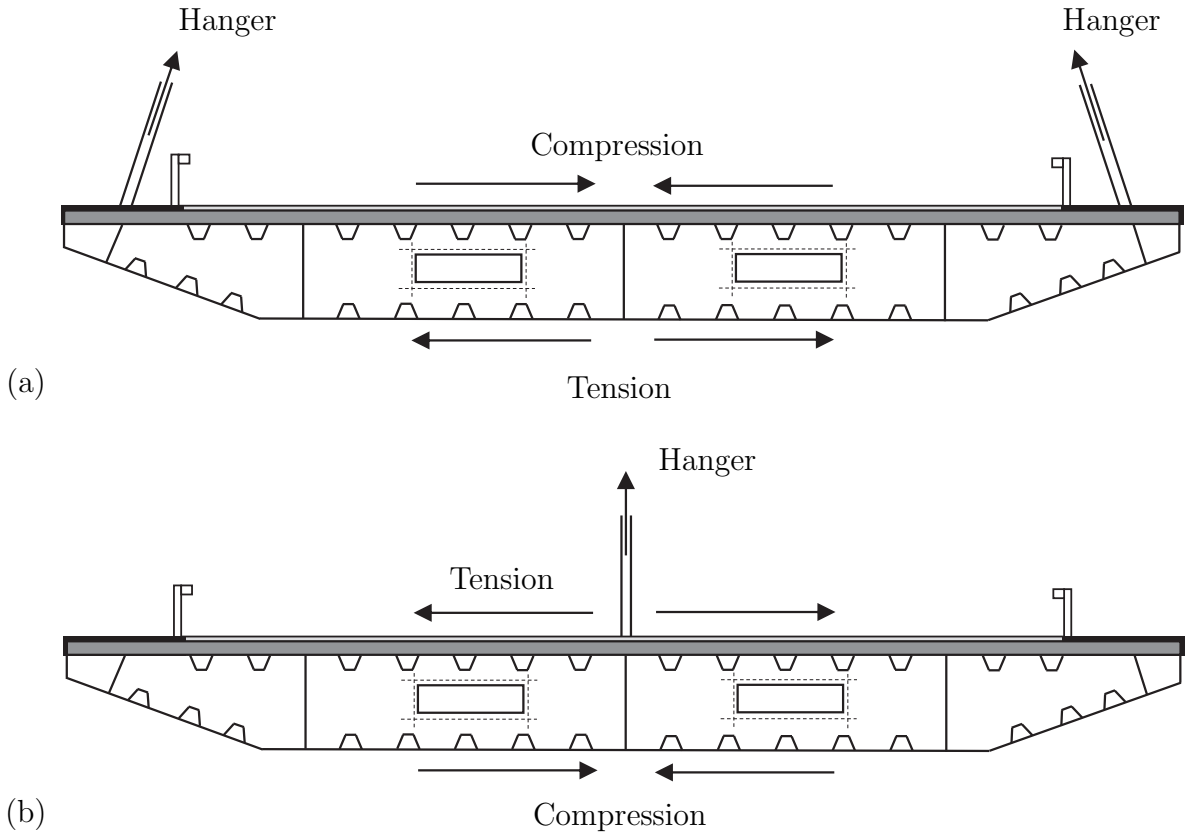

Figure 1.3: Transverse compression and tension for hanger bridges, based on [8].

1.2 Aim of this work and outline

The aim of this work is to analyse the buckling behaviour of multiaxially loaded plates in order to increase the insight and to allow the enhancement of the current design rules focusing on the reduced stress method according to Chapter 10, EN 1993-1-5 [36]. Therefore, the structure of this work is given in the following:

In **Chapter 2** the basis for the design is presented starting from the elastic buckling of flat plates and the effect of tension stresses on the buckling factor, which influences directly the plate slenderness when using the reduced stress method according to EN 1993-1-5 [36]. Furthermore the design procedure is presented in detail and notes are given on different interpretation possibilities, since the wording in the code is sometimes unclear. Some relevant existing studies are summarised in the context of the conducted investigations.

Chapter 3 shows the results of experimental investigations conducted on unstiffened and stiffened plates subjected to biaxial tension-compression and moment-shear interaction highlighting the effect of multiaxial stresses on the buckling behaviour in terms of the observed failure modes and resistances.

The numerical models used for further investigations on unstiffened and stiffened plates are presented in **Chapter 4**, while the parametric studies are arranged in the following **Chapter 5**. The investigations on unstiffened plates are conducted for the cases of tension-compression, tension-shear and bending-shear, while for stiffened plates the focus is on biaxial compression.

In **Chapter 6** the results from the numerical investigations are compared to the current design rules and an enhancement is proposed in order to take into account the positive effect of tension stresses. Additionally a statistical evaluation according to Annex D, EN 1990 [34] is conducted.

A summary of the conducted investigations is given in **Chapter 7** as well as an outlook for future work in this field.

2 Stability behaviour of flat plates

2.1 Elastic buckling of flat plates

The first approaches on describing the buckling behaviour of thin plates were developed to describe the linear buckling for linear material without the consideration of imperfections and yielding. They represent the bifurcation phenomena of thin plates.

During the first years of using thin plated structures in the last century, the design was conducted using the elastic critical load, which does not account for inevitable imperfections as well as any yielding of the panel. However, the positive effect of post-critical strength reserves is not taken into account. The later discovered so called column-like behaviour, which is present in plates with a high height-to-width ratio as well as for longitudinally stiffened plates, can reduce the capacity of the plate decisively and is treated more in detail in Sec.2.4.2.3. A detailed derivation of the differential equations can be found in [10].

Dubas & Gehri [30] summarise the linear buckling theory in a historical review, starting with de Saint-Venant [19], who established the differential equation of buckling of a plate loaded in its plane. The simplified formulation of the differential equation is shown in the following Eq.(2.1).

$$D \cdot \Delta\Delta(w) = N_x w'' + 2N_{xy} w'^{\star} + N_y w^{\star\star} \tag{2.1}$$

Herein w is the transverse displacement, w' its derivation in x direction and $w^{\star}$ the derivation in y direction respectively, $N_x = \sigma_x \cdot t$, $N_y = \sigma_y \cdot t$ and $N_{xy} = \sigma_{xy} \cdot t$ are the in-plane forces per unit length, t the plate thickness and D the flexural rigidity of the plate, which is defined according to Eq.(2.2).

$$D = \frac{E \cdot t^3}{12 \cdot (1 - \nu^2)} \tag{2.2}$$

where: $E = 210\,000\text{N/mm}^2$: elastic modulus
$\nu = 0.3$: Poisson's ratio

The solution of the differential equation Eq.(2.1) is found by an appropriate ap-

proach complying with the assumed boundary conditions leading to the critical buckling stresses, which usually is expressed as a product of the buckling coefficient and the Euler reference stress according to Eq.(2.3a) and Eq.(2.3b).

$$\sigma_{cr} = k_\sigma \cdot \sigma_E \tag{2.3a}$$

$$\tau_{cr} = k_\tau \cdot \sigma_E \tag{2.3b}$$

where: k_σ: buckling coefficient for direct stress
k_τ: buckling coefficient for shear stress
σ_E: Euler reference stress

The Euler reference stress is determined according to Eq.(2.4) showing also a common simplification.

$$\sigma_E = \frac{\pi^2 \cdot D}{b^2 \cdot t} = \frac{\pi^2 \cdot E}{12 \cdot (1 - \nu^2)} \left(\frac{t}{b}\right)^2 \cong 0.9 \cdot E \cdot \left(\frac{t}{b}\right)^2 \tag{2.4}$$

Furthermore, it is noted that in contrast to the Euler column formula, where the critical load refers to the column length, the Euler reference stress for plate buckling refers to the plate width b.

2.2 Effect of multiaxial stress states on the elastic buckling behaviour

2.2.1 General

Tension as well as compression stresses in transverse direction not only influence the post-critical buckling behaviour and the resistance but also have a great impact when calculating the critical buckling load. Therefore in Sec.2.2.2 a solution of the differential equation Eq.(2.1) for multiaxially loaded plates is shown according to Betten & Shin [7] and additionally the derivation of a formulation is presented to ignore the peaks between the transition points of the individual curves. These peaks for the linear bifurcation analysis result from the non-continuously differentiable functions obtained for the aforementioned solution of the differential equation. Lindner & Rusch [74] recommend not to account for these peaks when calculating the plate slenderness, as the effect is flattened out for high-grade non-linear calculations. Furthermore, in this section the effect of multiaxial stress states on plates subjected to shear as well as on stiffened plates is highlighted on the level of the elastic buckling behaviour.

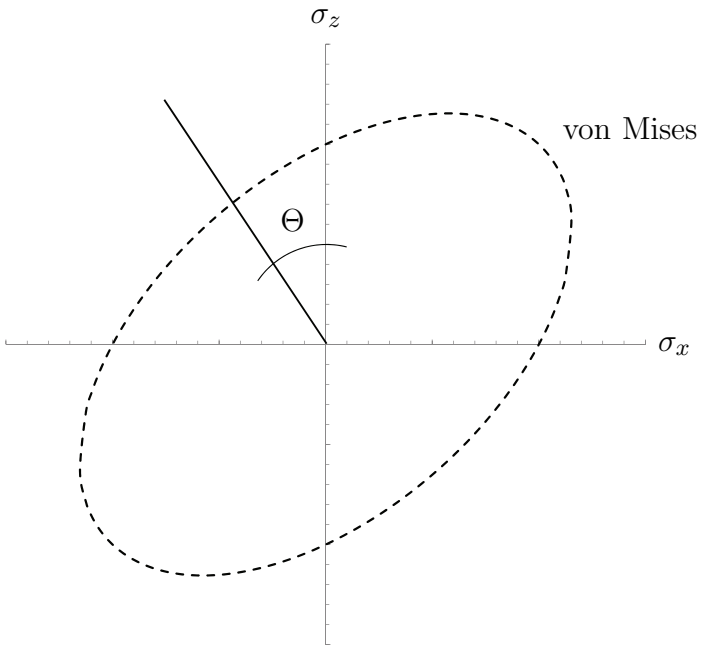

Figure 2.1: Definition of interaction angle Θ.

2.2.2 Direct stresses

In order to investigate the full parameter range of interaction between direct stresses σ_x and σ_z, the interaction angle Θ within this work is defined according to Fig.2.1. The interaction angle can also be expressed by the parameter β in order to describe the stress-ratio in the panel, see Eq.(2.5). Compression is denoted as positive direct stress.

$$\beta = \sigma_z/\sigma_x = -\tan(\Theta) \tag{2.5}$$

Betten & Shin [7] present a solution to the differential equation Eq.(2.1) for rectangular plates under biaxial loading and for hinged boundary conditions, see Eq.(2.6). The detailed derivation is omitted here with reference to [7].

$$k_\sigma = \left(\frac{m^2}{\alpha^2} + n^2\right)^2 \cdot \left(\frac{m^2}{\alpha^2} + n^2 \cdot \beta\right)^{-1} \tag{2.6}$$

In the presented equation the parameters m and n indicate the number of half-waves in x and y direction of the buckled shape, respectively. Fig.2.2 shows a set of curves for different β-values in dependence on the panel aspect ratio $\alpha = a/b$. Positive values for β mean that the plate is subjected to biaxial compression, while negative values result for biaxial tension–compression.

The buckling coefficient k_σ for calculating the critical buckling load strongly depends on the panel aspect ratio α as well as on the stress state, or in other words the ratio between the longitudinal and the transverse stress. It can be seen from Fig.2.2 how transverse compression stresses reduce the buckling coefficient and therefore the critical buckling load.

In contrast to this, transverse tensile stresses lead to increased buckling coefficients, showing clearly the positive effect. Since the critical buckling stress is used as an input parameter for the design according to EN 1993-1-5 [36] with an unique plate slenderness, the shown positive effect from tensile stresses can theoretically directly be integrated in the design of slender plates, see Sec.2.4.2. Nevertheless, no studies are known which systematically have investigated this issue until now.

As the buckling coefficient k_σ also depends on the number of half-waves in both directions, see Eq.(2.6), Fig.2.2 shows the lower envelope for $n = 1$ in x-direction and varying number of half-waves in z-direction m. For $\beta = 0$ (pure compression) the curve is well known to result in $k_\sigma = 4$ for plates where the panel aspect ratio has an integral number and to have peaks where the curves for different half-wave modes intersect with each other. The peaks become smaller and negligible with increasing panel aspect ratio α. While for biaxially compressed plates the buckling coefficient is reduced compared to plates under uniaxial compression and no peaks are visible in the regarded area, the plates loaded with tension–compression show pronounced peaks when the curves with different numbers of half-waves intersect each other. This effect increases with higher ratios of tension stresses.

Another observation from Fig.2.2 is that the mentioned peaks on the transition points of the buckling modes are reached for smaller panel aspect ratios α with increasing tension. Or, in other words, the buckling mode jumps to a multi-half-wave mode with increasing tension. In order to point out these peaks in the curves for the buckling coefficient, Fig.2.3 shows the buckling coefficients for different panel aspect ratios $\alpha =$ 1 to 3 in relation to the buckling coefficient for an infinitely long plate, where the interaction-angle is defined according to Eq.(2.5).

The peaks between the modes affect directly the slenderness and therefore the resistance of the regarded plate, so that already Lindner & Rusch [74] recommend not to account for them, as the effect is flattened out for high-grade non-linear calculations. It is noted that EN 1993-1-5 [36] gives formulations for the calculation of the buckling coefficient k_σ for several cases, while DIN 18800-3 [22] just referred to literature.

The formulations given in EN 1993-1-5 [36] for plates loaded with uniaxial compression are not dependent from the panel aspect ratio α, so that here the peaks are not accounted for. Especially with increasing tension stresses these peaks get more and more pronounced. Therefore in the following a simple formulation attempting for a safe determination of the slenderness for multiaxially loaded plates is derived. The basis is the solution of the differential equation according to [7], see Eq.(2.6).

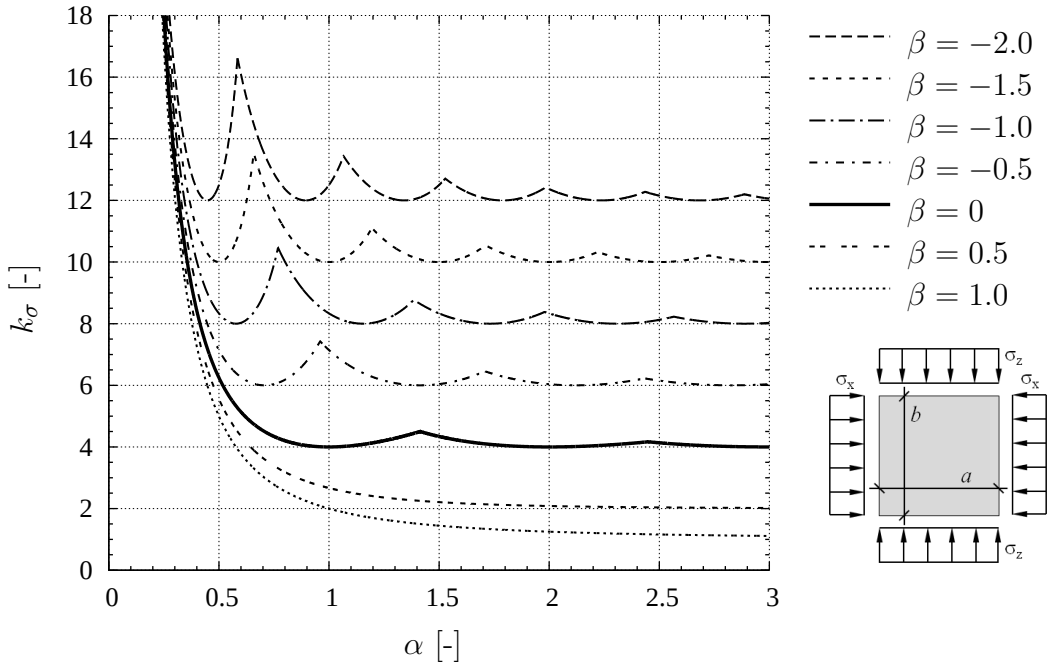

Figure 2.2: Buckling coefficient k_σ depending on the stress ratio $\beta = \sigma_z/\sigma_x$ and panel aspect ratio $\alpha = a/b$.

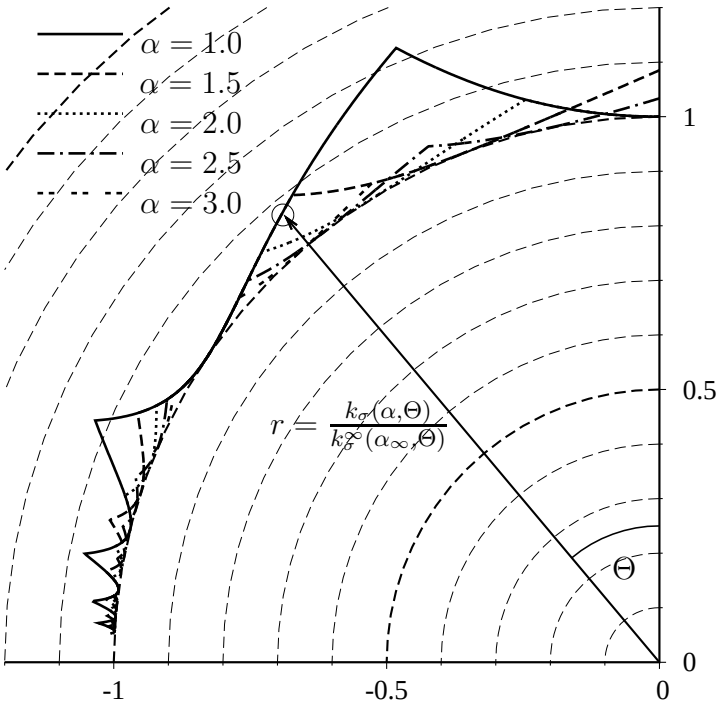

Figure 2.3: Ratio of buckling coefficient k_σ to the respective minimum buckling coefficient k_σ^∞.

Since the first minima of the buckling coefficient is aimed at , the parameters m and n are both set to 1:

$$\begin{aligned} k_{\sigma}^{m,\,n=1} &= \left(\frac{1}{\alpha^2}+1\right)^2 \cdot \left(\frac{1}{\alpha^2}+\beta\right)^{-1} \\ &= \frac{\alpha^4+2\alpha^2+1}{\alpha^4\beta+\alpha^2} \end{aligned} \tag{2.7}$$

The first derivation over the panel aspect ratio α is calculated according to Eq.(2.8).

$$\left(\frac{\partial}{\partial\alpha}\right) k_{\sigma}^{m,\,n=1} = -\frac{\left(4\alpha^4+4\alpha^2\right)\beta-2\alpha^4+2}{\alpha^7\beta^2+2\alpha^5\beta+\alpha^3} \tag{2.8}$$

For the determination of the minimum for the buckling coefficient, the counter is set to zero:

$$0 = \left(4\alpha^4+4\alpha^2\right)\beta-2\alpha^4+2 \tag{2.9}$$

and for the sake of simplification α^2 is substituted with ω, so that:

$$\begin{aligned} 0 = &\quad \left(4\omega^2+4\omega\right)\beta-2\omega^2+2 \\ = &\quad (4\beta-2)\,\omega^2+4\beta\omega+2 \end{aligned} \tag{2.10}$$

The positive solution of the quadratic Eq.(2.10) leads to Eq.(2.11).

$$\omega = -\frac{1}{2\beta-1} \tag{2.11}$$

By resubstituting ω by α^2 Eq.(2.12) shows the panel aspect ratio leading to the minimum buckling coefficient depending on the stress ratio $\beta < 0.5$.

$$\alpha^{k_{\sigma}^{min}} = \sqrt{\frac{-1}{2\beta-1}} \tag{2.12}$$

When inserting Eq.(2.12) into Eq.(2.7) the minimum buckling coefficient is determined according to Eq.(2.13).

$$k_{\sigma}^{min} = 4\,(1-\beta) \tag{2.13}$$

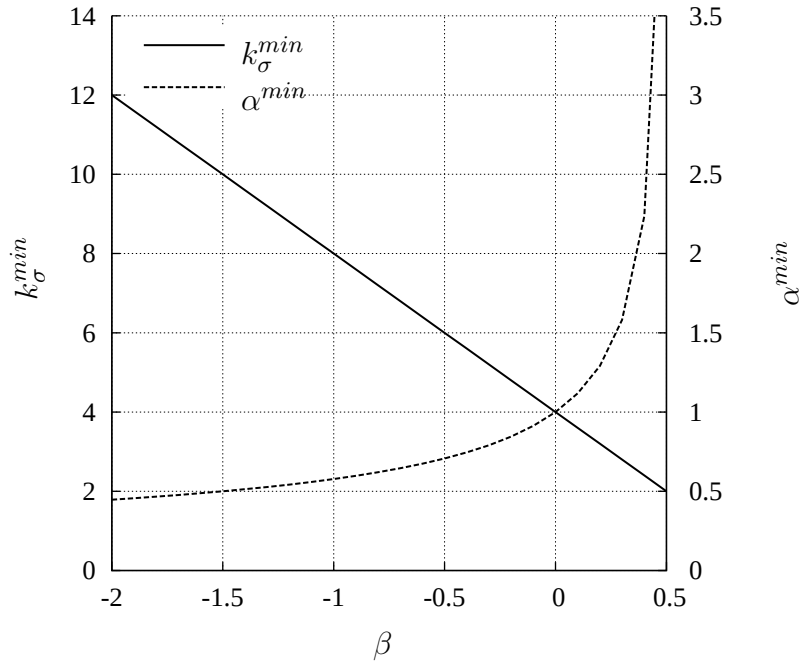

Figure 2.4: Influence of stress ratio β on the minimum buckling coefficient k_σ^{min} and the respective panel aspect ratio α^{min}.

Fig.2.4 shows the influence of the stress ratio β on the minimum buckling coefficient k_σ^{min} and the respective panel aspect ratio α^{min} calculated with Eq.(2.12) and Eq.(2.13). The diagram shows that with increasing tensile stresses (negative β) the panel aspect ratio α, where the minimum buckling coefficient occurs, is decreasing and the buckling coefficient increases linearly.

It is recommended to use the k_σ^{min} values according to Eq.(2.13) that allow for ignoring the peaks between the buckling modes, since these do not occur for non-linear calculations nor in reality, so that an underestimation of the plate slenderness may occur. A comparison between calculations with and without considering these peaks is shown in Sec.6.

2.2.3 Shear stresses

The elastic critical shear buckling stress can be calculated in analogy to the one for direct stress using Eq.(2.3b), where k_τ is the buckling coefficient of the shear buckling stress. This critical shear buckling stress coefficient has been evaluated for three different boundary conditions of edge support for plates subjected to pure shear [125]. Timoschenko [111], Bergmann & Reissner [6] and Seydel [102] developed solutions for the case of a plate subjected to pure shear simply supported on four edges, which is shown in Eq.(2.14a) and Eq.(2.14b).

Furthermore other solutions exist, such as for plates clamped on four edges and

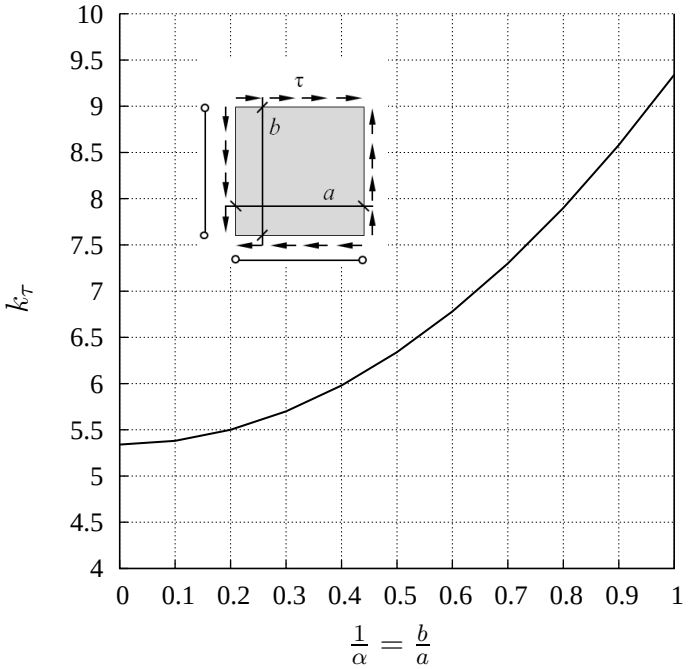

Figure 2.5: Plate buckling coefficients for plates in pure shear.

plates clamped on two opposite edges and simply supported on remaining two edges, see [125] for further information. The solution presented for simply supported edges is also included in Annex A, EN 1993-1-5 [36]. It should be noted here, that investigations by Kuhlmann et al. [66] have shown, that simple (hinged) boundary conditions have to be used when assessing the critical shear buckling stress according to design resistance of Eq.(5.2) in Chapter 5, EN 1993-1-5 [36], as the buckling curves derived by experimental tests already consider certain clamping effects, see also [67].

Fig.2.5 shows the shear buckling coefficient k_τ for plates with aspect ratios $\alpha > 1$ and hinged boundary conditions. Herein, the coefficient is plottet against $1/\alpha$ in order to show a larger range.

$$k_\tau = \begin{cases} 4.00 + \dfrac{5.34}{\alpha^2} & \text{for } \alpha \leq 1 \quad (2.14a) \\ 5.34 + \dfrac{4.00}{\alpha^2} & \text{for } \alpha \geq 1 \quad (2.14b) \end{cases}$$

Shear and direct stresses

Direct stresses have a significant influence on the shear buckling coefficient. Therefore, and also because this is a frequent case in practice, the combinations shear-compression and shear-bending are shown shortly in the following. A first interaction equation for the case of shear combined with longitudinal compression with all sides simply supported was given by Iguchi [50]. The problem of bending and shear was treated by Timoshenko [112] and an interaction formula was suggested by Chwalla [14]. Later,

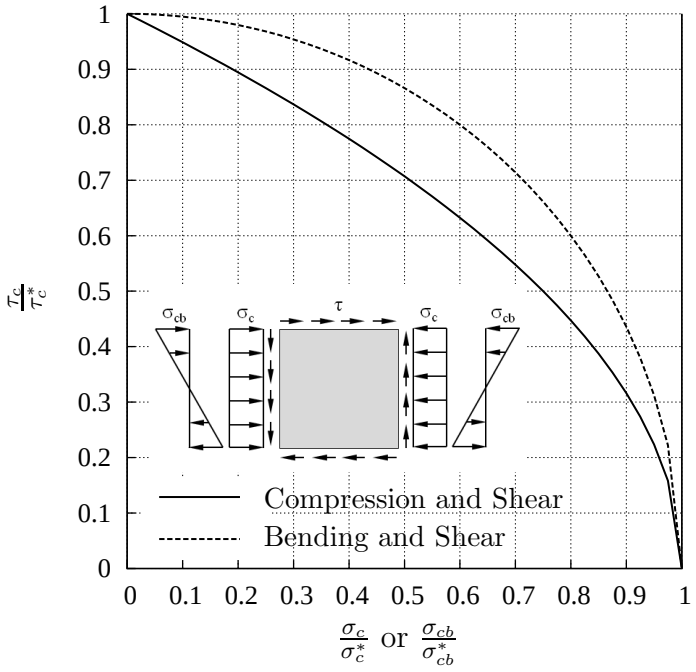

Figure 2.6: Interaction curves for buckling of flat plates under shear and uniform compression and bending.

Gerard & Becker [47] developed an interaction formula for the case of combined bending and direct stresses at the ends (of dimension b) acting together with pure shear, see Eq.(2.15), which is also illustrated in Fig.2.6.

$$\frac{\sigma_c}{\sigma_c^*} + \left(\frac{\sigma_{cb}}{\sigma_{cb}^*}\right)^2 + \left(\frac{\tau_c}{\tau_c^*}\right)^2 = 1 \tag{2.15}$$

where: σ_c^*: critical stress under compression alone
σ_{cb}^*: critical stress under bending alone
τ_c^*: critical stress under shear alone

It can be seen that compression and bending have a different influence on the shear buckling coefficient, so that in the later course of this work the investigations are conducted for several ratios of compression and bending interaction with shear.

2.2.4 Stiffened plates under direct stresses

In contrast to unstiffened plates the analytical determination of the elastic buckling stress for stiffened plates turns out to be much more complex, since many more parameters such as the cross-section or the location of the stiffeners are involved. Generally the following methods exist for the calculation of the buckling coefficient k_σ for longi-

tudinally stiffened plated, see also [51]:

- From charts or tables;
- From simplified expressions;
- By using appropriate software or numerical techniques.

Several charts and tables have been published in the past for determining the critical stress of longitudinally stiffened plates under uniaxial compression for instance from Seide & Stein [100], Bleich & Ramsey [9], and Timoshenko & Gere [113] . However, the most used buckling charts in practice are those from Klöppel [54], [55].

The stiffness of the stiffener is represented by the non-dimensional parameters γ (relative flexural stiffness), δ (relative axial stiffness) and Θ_s (relative torsional stiffness) according to Eq.(2.16), where the reference flexural stiffness D of the plate is defined as given in Eq.(2.17).

$$\gamma = \frac{EI_s}{bD}, \qquad \delta = \frac{A_s}{bt}, \qquad \Theta_s = \frac{GJ_s}{bD} \tag{2.16}$$

$$D = \frac{Et^3}{12\,(1-\nu^2)} \tag{2.17}$$

Herein, I_s, A_s and J_s represent the flexural inertia, the cross-sectional area and the torsion constant of the stiffener respectively. E is the elastic modulus ($210\,000\,\mathrm{N/mm^2}$ for steel), ν the Poisson's coefficient (0.3 for steel) and G the shear modulus ($G = E/2\,(1+\nu) = 80769\,\mathrm{N/mm^2}$ for steel).

Fig.2.7 shows an exemplary chart taken from Klöppel [55], where the buckling coefficients k_σ can be taken graphically for a plate with hinged boundary conditions under uniform compression and one stiffener with an axial rigidity of $\delta = 0.1$ in dependence on the panel aspect ratio α as x-coordinate and the flexural rigidity γ of the stiffener as curve parameter. However, drawbacks are usually the small number of charts and the limits of the graphs, which according to Johansson et al. [51] make them unpracticable in many situations encountered in practice. Furthermore, as the charts have been developed in former days when usually open stiffeners were used, the torsional rigidity of the stiffeners was neglected.

Simplified expressions for the determination of the critical buckling factor for stiffened plates are already implemented in Annex A, EN 1993-1-5 [36]. The procedure is shown in Sec.2.4.2. For the sake of completeness it is mentioned here additionally, that Schafer & Peköz [93] also provided a solution in a rather compact form for cold–formed steel members with multiple longitudinal intermediate stiffeners, which was adopted in the AISI standard [2]. As the critical buckling loads only depend from geometry, stiffness and loading, the expressions may be also applied for welded structures.

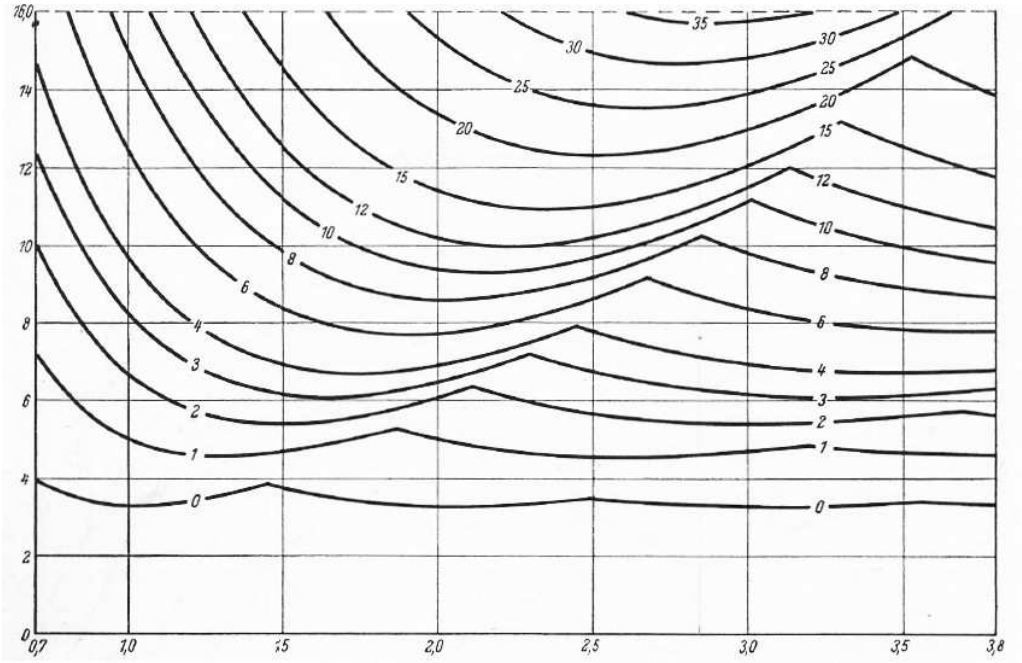

Figure 2.7: Buckling coefficients k_σ over the panel aspect ratio α for a stiffened plate with one stiffener and axial rigidity $\delta = 0.1$ dependent from the flexural rigidity γ of the stiffener according to [55].

Nowadays, the critical buckling coefficient can usually be calculated by appropriate software tools. One of these programs is EBPlate [16], which was developed in the frame of the RFCS-project COMBRI [66]. It allows for calculating the buckling coefficient for almost any kind of situation and even for different stresses acting at the same time for unstiffened as well as for stiffened plates. Furthermore the program has the possibility to run in batch mode, allowing to incorporate it into subroutines e.g. with Matlab [79] to generate and run input files for parametric studies.

The critical buckling stress σ_{cr} for a plate stiffened with one longitudinal stiffener calculated with EBPlate is shown in Fig.2.8, where the values are calculated exemplarily for the following dimensions: length $a = 3000\,\text{mm}$, width $b = 2000\,\text{mm}$ and thickness $t = 10\,\text{mm}$. The results show the influence of the bending stiffness γ of the stiffener and the applied load interaction-angle Θ on the critical buckling stress. Therefore the axial stiffness δ and the torsional stiffness are kept constant to 0.1 and 0.01 respectively.

It can be seen, that the critical buckling stress increases for positive interaction angles in the compression–tension domain and decreases for the biaxial compression domain, thus for negative interaction angles. With increasing flexural rigidity the critical buckling stress also increases until it reaches a plateau where local buckling of the subpanels prevails, so that a higher flexural rigidity of the longitudinal stiffener does not have an influence anymore. The flexural rigidity where the plateau starts is denoted as the minimum stiffness $\gamma^\star$. The critical buckling stress that corresponds to the first buckling mode (also known as "natural" mode) is called "natural critical stress", see [45]. It

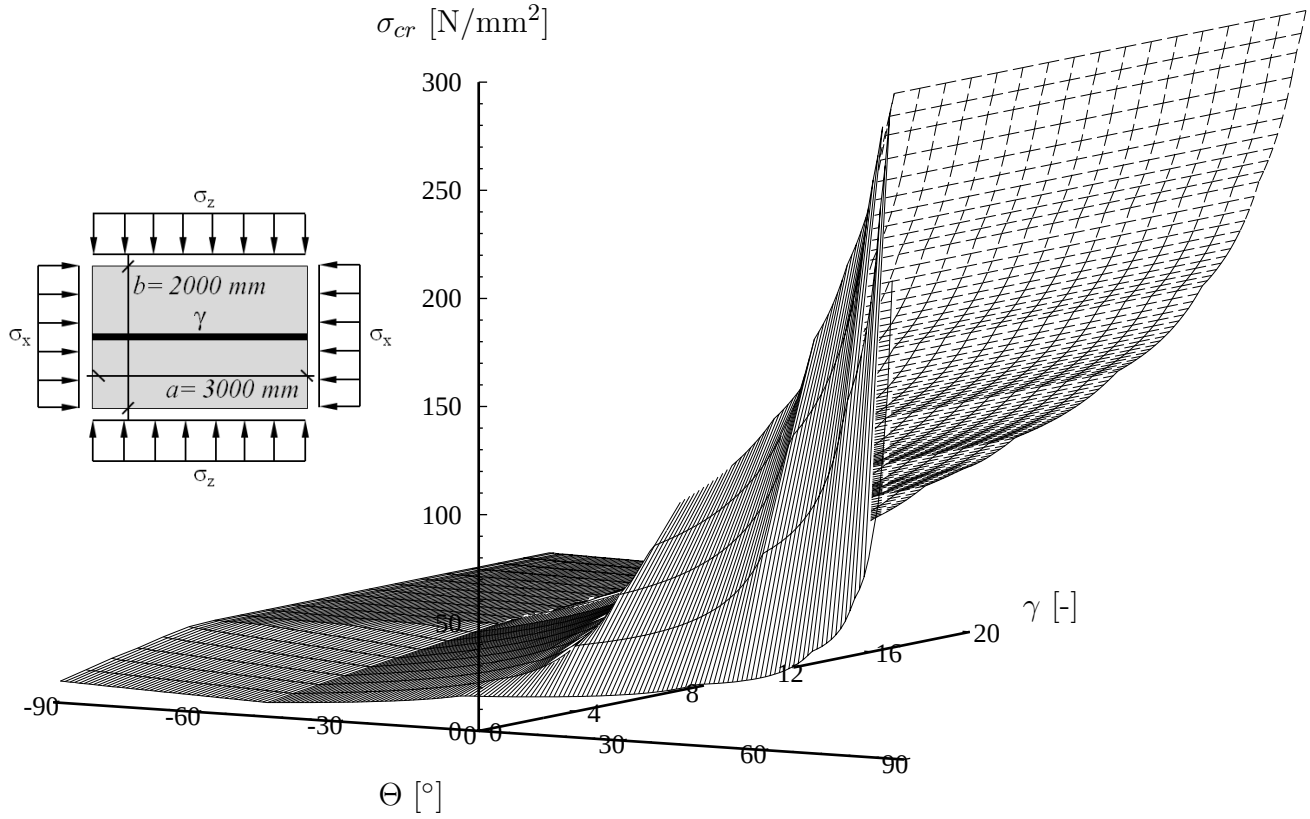

Figure 2.8: Influence of the load interaction angle Θ on the critical buckling stress in dependence on the relative flexural stiffness γ.

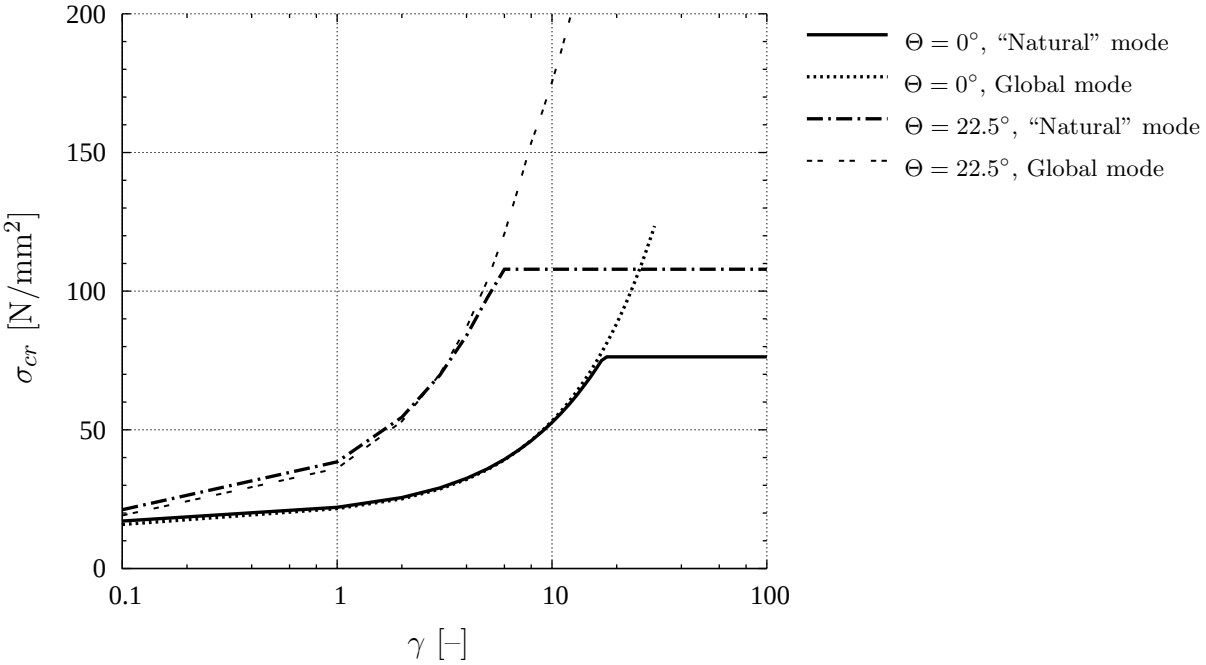

Figure 2.9: Buckling modes of a stiffened plate for $\Theta = 0°$ and $\Theta = 22.5°$.

can also be noticed from Fig.2.9 that the minimum stiffness $\gamma^\star$, where the natural critical stress is dominated by local buckling, varies with the interaction angle Θ. The exemplarily chosen cases highlight that the required stiffness of the stiffener to provoke local buckling for the natural mode decreases with increasing tensile stresses and that the natural critical stress also increses with increasing tensile stresses.

Fig.2.10 shows the critical buckling stress dependent on the interaction angle for different flexural stiffnesses, pointing out the complexity and sensitivity of the topic, since all parameters have a significant influence. Some exemplary eigenmodes, which have been determined using EBPlate, are shown in Fig.2.11 for the regarded example mentioned above, pointing out that for pure compression stronger stiffeners are needed to prevent global buckling compared to the case of tension-compression interaction, where even weak stiffeners are able to force local buckling.

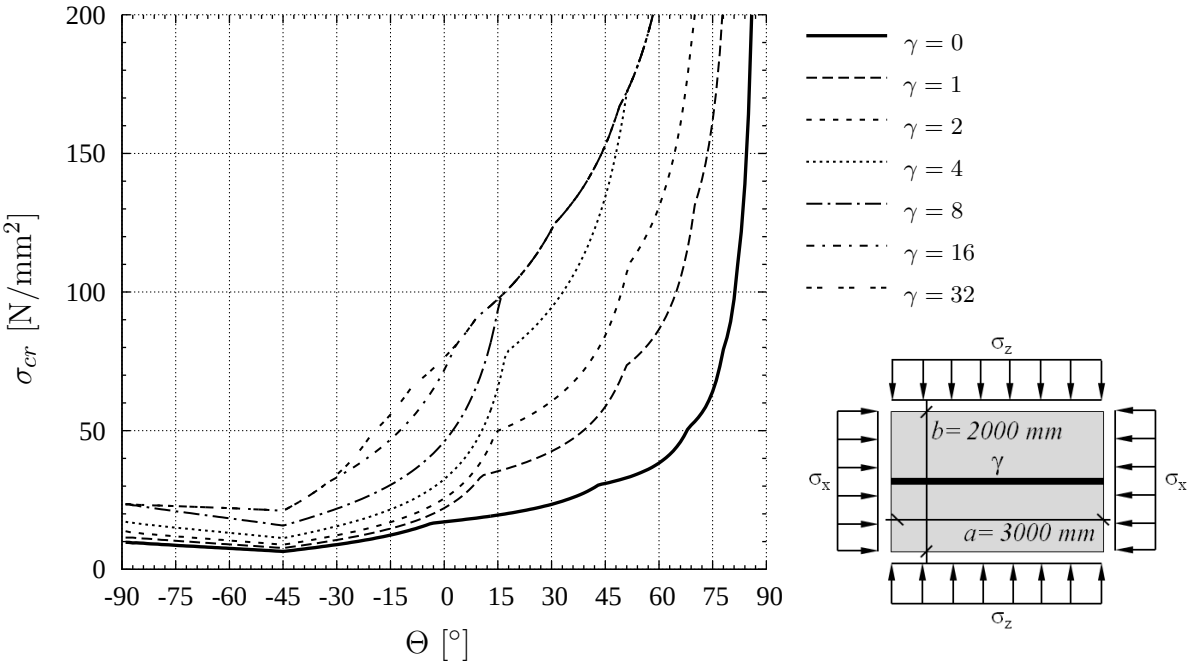

Figure 2.10: Influence of the load interaction angle Θ on the critical buckling stress in dependence of the relative flexural stiffness γ.

a) $\Theta = 0°$, $\gamma = 16$

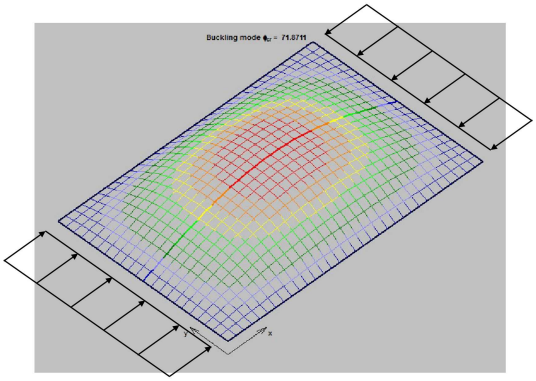

b) $\Theta = 45°$, $\gamma = 4$

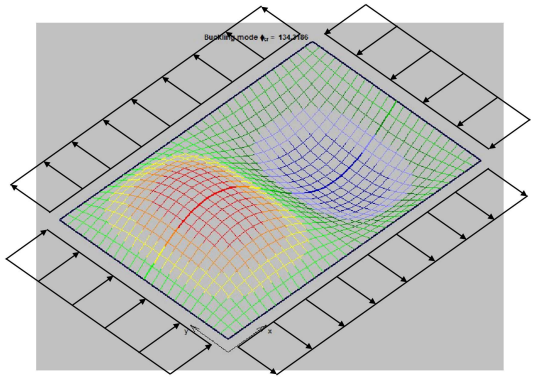

c) $\Theta = 0°$, $\gamma = 32$

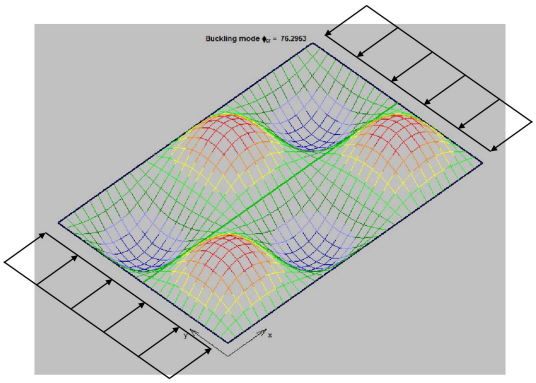

d) $\Theta = 45°$, $\gamma = 8$

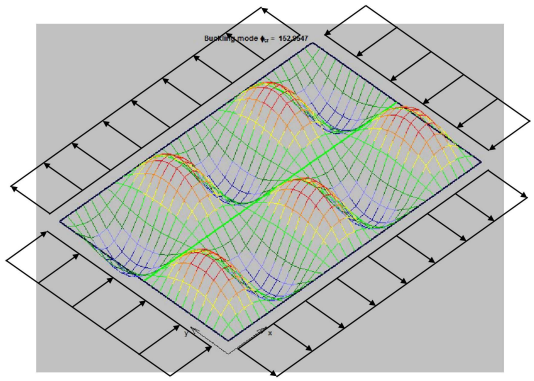

Figure 2.11: Eigenmodes from a linear buckling analysis using EBPlate.

2.3 Strength and postbuckling behaviour of flat plates

2.3.1 Direct stresses

While for columns, due to imperfections, the ultimate load is always lower than the elastic critical load, plates may possess a pronounced postcritical strength reserve, which results in ultimate loads being higher than the critical load, see Fig.2.12. This postcritical strength reserve comes from the development of a double curvature when the plate buckles and is illustrated in a descriptive way in [125] by the analogy to a simple grillage model. Thereby, the continuous plate is replaced by vertical struts in the load direction and horizontal ties in the perpendicular direction. As the struts buckle outwards, the ties are stretched and tend to restrain the motion and thus provide a postbuckling strength reserve. For plates this means that in perpendicular direction to the load tension stresses occur due to the activated extensional stiffness.

Furthermore, the simple grillage model visualises that the struts closer to the supported edges are restrained more by the ties than the struts in the middle of the plate, resulting in a redistribution of the longitudinal in-plane direct stresses, the so-called membrane stresses. Fig.2.13 shows the stress distribution before and after passing the

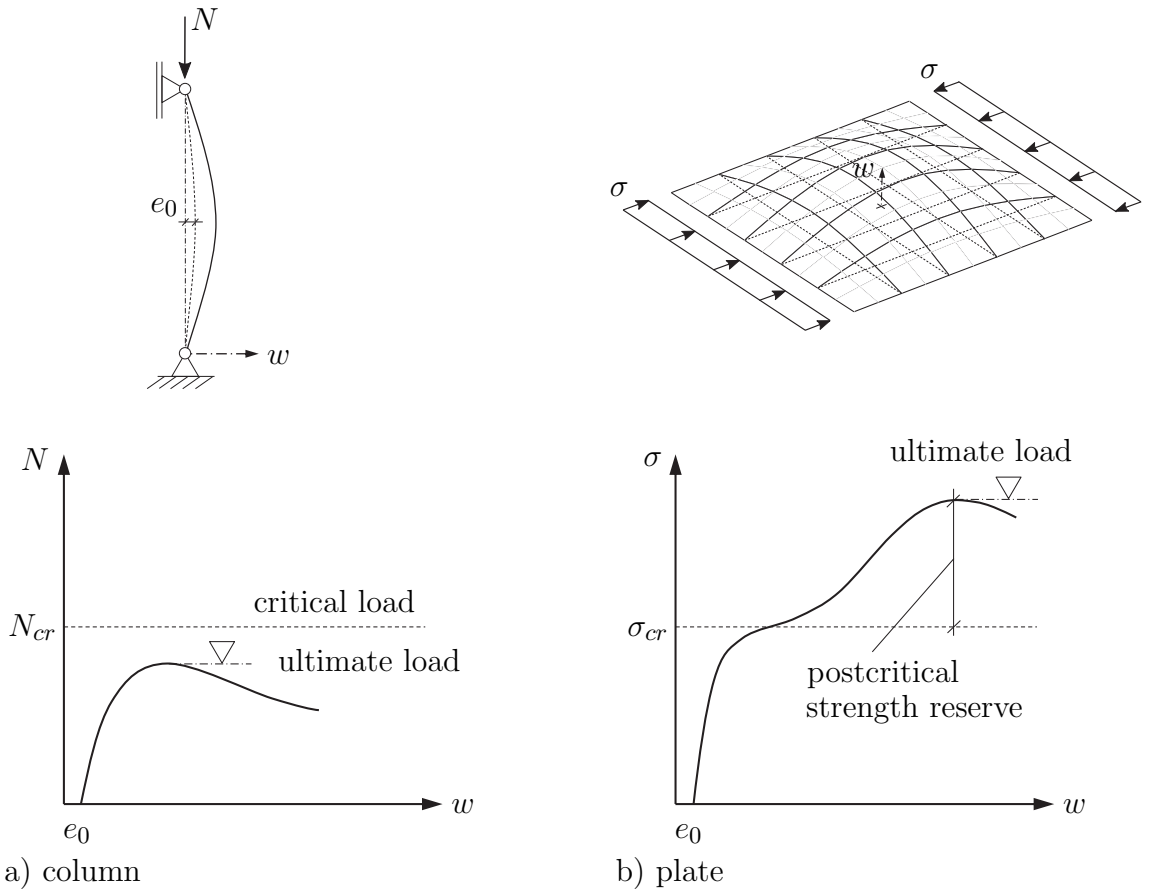

Figure 2.12: Comparison of column and plate buckling.

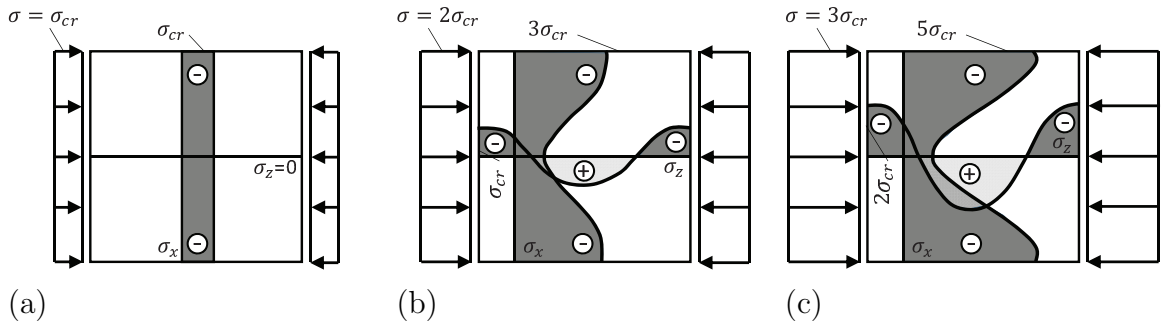

Figure 2.13: Stress distribution before and after passing the critical load, on the basis of [85].

critical load, highlighting on the one hand the stress redistribution to the edges in load direction and on the other hand the development of tension stress in perpendicular direction. Of course, the development of these tension stresses is dependent on the boundary conditions of the edges. If the unloaded edges are restrained, then the tension stresses are higher than if the edge is free to move in plane. Therefore different edge boundary conditions are investigated within this work, see Sec.4.

It should be noted here that the mentioned postcritical strength reserve can only be accounted for, if so-called "plate-like" behaviour prevails. In certain cases where "column-like" buckling is decisive, as the name implies, the plate behaves more like a column not taking into account the advantages of postcritical strength reserves, since the Gaussian curvature of the buckled plate becomes insignificant. However, for more information and on how this phenomena is accounted for in the design, reference is made to Sec.2.4.2.3.

2.3.2 Shear

Fig.2.14 shows the web of a girder subjected to shear load. For pure shear stress below the critical load ($\tau < \tau_{cr}$) the principal stresses by equilibrium are equal according to amount and inclined by 45° based on the girder axis. With increased shear load ($\tau > \tau_{cr}$) and for slender webs this stress state changes fundamentally. Due to shear buckling the principal tensile stresses increase faster than the principal compression stresses, leading to a rotation of the principal stresses for reasons of equilibrium, where the principal tensile stresses are in direction of the developed shear buckle. The shear stress field passes over to a tension field action, see Fig.2.14. This presumes boundary elements that provide a certain anchorage allowing to develop a tension diagonal. For the design rules according to EN 1993-1-5 [36] the so-called "modified rotated stress field method" from HÖGLUND [49] has been adopted. Additionally, when using the effective width method the possibility is given for taking into account the development of a plastic hinge mechanism in the flanges, which participate in the load bearing. However, when the reduced stress method is used, this effect is not taken into account, since in any case isolated panels are regarded.

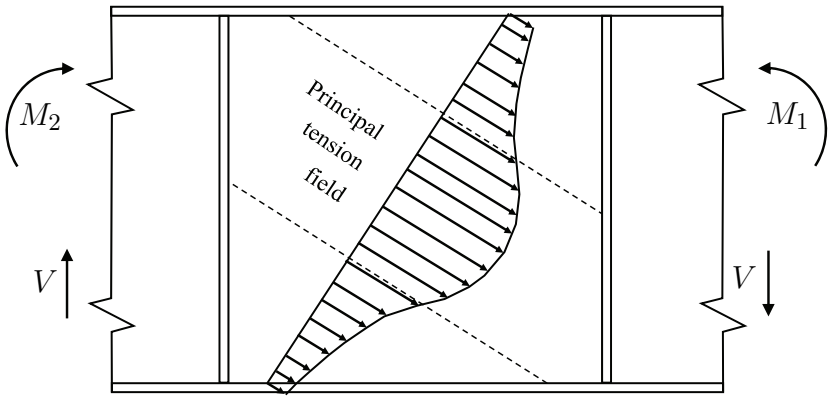

Figure 2.14: Tension field action, on the basis of [125].

2.4 Comparison of different design rules

2.4.1 Evolution of buckling rules in Germany

Theoretical but particularly experimental investigations on plates under multiaxial stress states are very limited. The design rules for multiaxially loaded plates prone to buckling are based on investigations, which have been conducted mainly in the 1970s on square plates.

As this work focuses on the reduced stress method, which was mainly developed in Germany during the last century and is of practical relevance ibidem, the evolution of the buckling rules in Germany is summarised in Tab.2.1 starting from DIN 4114 [23] in 1952. In the beginning, the design rules were meant for webs under primarily shear stresses. However, in the course of the development of box-girders the rules have been applied also for the design of longitudinally stiffened flanges. Since the phenomena of column-like behaviour was not yet sufficiently known, several cases of damage occurred in the late 1960s and early 1970s, especially during the launching of steel box-girder bridges. As a reaction at short notice in 1972 increased safety requirements have been defined in a supplemental decree [1] for steel bridges, which have been then later adopted within supplemental regulations in [24] for all steel constructions.

So far, the verifications have been conducted using critical loads and *Engesser* buckling curve without considering imperfections. For the determination of the shear resistance the increase coming from yielding was already taken into account. This changed in 1978 with the implementation of the DASt-Richtlinie 012 [17] resulting from a research programme undertaken by the DASt as a reaction on several cases of damage, where it became possible to determine the ultimate load from buckling curves, which included imperfections, using slenderness values. In 1990, with the introduction of the DIN 18800-3 [22], the design rules were completely revised and the determination of the stresses was carried out for the first time on a design level. The new buckling curves included the effect of imperfections as well as the effect of postcritical strength reserves,

which are of essential importance especially for plates with high slenderness. The calculation of the reduction was done for each load component separately using the respective slenderness.

As a further development of the buckling rules SCHEER & NÖLKE [96] in 2001 specified the following criteria for a "generalised equivalent stress design":

A. In the frame of the linear buckling theory only one decisive buckling shape result for a multiaxially loaded plate. Appertaining to it an equivalent critical buckling load $\sigma_{eq,cr}$ exists.

B. For the limit case of stocky plates not subjected to buckling the design check should merge into the von Mises criterion.

C. For the limit case of uniaxial loading the design check should merge with the respective verification.

D. The stabilising effect of tensile stresses should be taken into account.

E. The utilisation factor should be for direct reading from the results of the verification.

F. The design rules should be user-friendly and easily programmable.

G. The results should be plausible and sufficiently accurate.

H. Obviously a generalised form of the equivalent stress hypothesis is appropriate.

I. For biaxial compression the limiting stresses $limit\,\sigma_x$ should decline monotonously with increasing σ_y/σ_x-ratio.

The postulations **B**, **C**, **H** and **F** are fulfilled by the design rules in DIN 18800-3 [22], see [96]. The determination of the reduction factors was conducted for the respective load and the corresponding slenderness as input parameter separately. This means, that for each acting load the slenderness is calculated individually. This changed with the official introduction of EN 1993-1-5 [36] in 2010. The determination of the reduction factors using the reduced stress method now occurs with a unique plate slenderness, which includes the complete stress field fulfilling also the postulation **A**. The consideration of the stabilising effect of tensile stresses is possible in principle. However, systematic investigations are missing, so that the investigations of this work aim at fulfilling also postulation **D**.

Table 2.1: Evolution of buckling rules in Germany, extended table on the basis of [96].

Year	1952	1972	1978	1990	2010
Rule	DIN 4114 [23]	Decree [1]	DASt-Ri 012 [17]	DIN 18800-3 [22]	EN 1993-1-5 [36] (Chapter 10)
Application	webs	webs and flanges			
Loads	σ, τ (nominal loads)			σ, τ (design loads)	
Design basis	individual buckling stress σ_{Ki}, τ_{Ki}				equivalent buckling stress $\sigma_{v,cr}$
Correction	reduction for σ_{Ki} and $\sqrt{3} \cdot \tau_{Ki} > 0{,}8 \cdot \sigma_F$		-	-	-
Resistance functions	σ_{VK} and τ_{VK} from *Engesser* buckling curve		σ_{VK}, τ_{VK} from **one** buckling curve with $\bar{\lambda}_p = \sqrt{f_{y,k}/\sigma_{Ki}}$ or $\sqrt{f_{y,k}/\sqrt{3}\tau_{Ki}}$	σ_{PR}, τ_{PR} from individual buckling curves with $\bar{\lambda}_p = \sqrt{f_{y,k}/\sigma_{Ki}}$ or $\sqrt{f_{y,k}/\sqrt{3}\tau_{Ki}}$	reduction factors from **individual** buckling curves with **one single** slendeness $\bar{\lambda}_p = \sqrt{\alpha_{ult,k}/\alpha_{cr}}$
Check	$\sigma_{VK}/\sigma \geq \mathrm{req}\,\nu_{VK}$ and $\tau_{VK}/\tau \geq \mathrm{req}\,\nu_B$			$\sigma_{P,R,d}/\sigma \geq 1{,}0$ and $\tau_{P,R,d}/\tau \geq 1{,}0$	yield criterion with reduced parts
Utilisation of post-critical strength reserves by	smaller values for $\mathrm{req}\,\nu_B$	not accounted for	case dependent $\mathrm{req}\,\nu_B$	buckling curves	
Consideration of imperfections	no	no	in buckling curve	in buckling curves	

2.4.2 EN 1993-1-5

2.4.2.1 General design procedure

The design of slender plates in Europe is currently conducted according to EN 1993-1-5 [36], which gives, apart from the possibility of using the Finite Element Method, generally two different methods for the design of slender plates. The first method, called "effective width method", is based on the reduction of the cross-section area taking account of local buckling of the subpanels between the stiffeners and the global buckling. This verification is done for the individual actions, while for the interaction of different forces interaction formulas are used. The "effective width method" has the advantage of considering stress redistribution between the panels. But for the consideration of multiaxial stress states, such as biaxial compression or tension-compression, as well as for tension-shear there is no option for verification provided yet.

The second method which may be used for the design is the so–called "reduced stress method". It is a classic concept that limits the allowable stresses in the plate and uses a kind of von Mises criterion to check the combination of different stresses. This criterion was at first presented by Scheer & Nölke in [95] and [96]. The reduction of the allowable stresses in comparison with the full strength is a function of the slenderness of the regarded plate. For the reduced stress method according to EN 1993-1-5 [36] the determination of the plate slenderness is based on the complete stress field, resulting in a unique plate slenderness without the differentiation of the single acting forces.

In [82] Müller introduces "generalised buckling curves" with the aim of an harmonisation and reduction of the overall number. These are included in Annex B, EN 1993-1-5 [36]. Fig.2.15 shows the principle of the procedure for the buckling check according to Chapter 10, EN 1993-1-5 [36].

At first, the minimum load amplifiers for the design loads to reach the characteristic value of resistance on the most critical point of the plate $\alpha_{ult,k}$ and the minimum load amplifier for the design loads to reach the elastic critical stress state of the plate under the multiaxial stress field α_{cr} are determined. With these factors the system slenderness can be calculated, which serves as the input parameter for the calculation of the reduction factors used in the last step to carry out the design check. EN 1993-1-5 [36] thereby limits the application of the verification formula in case of panels with tension and compression only for the compressive parts.

It still remains unclear, if for the preceding steps $1-4$ in Fig.2.15 tension stresses may be considered or not in case of biaxially loaded plates in tension and compression. One possible interpretation of EN 1993-1-5 would be that tension stresses should not be considered for the last step, but could still be used for the determination of the slenderness in step 3. With increasing tension stresses this would lead to a decreasing slenderness leading in turn to higher reduction factors. If in this case the tension stresses remain disregarded for the last step 6, the resistance increases with increasing tension stresses without considering the plastic destabilisation in the verification formula.

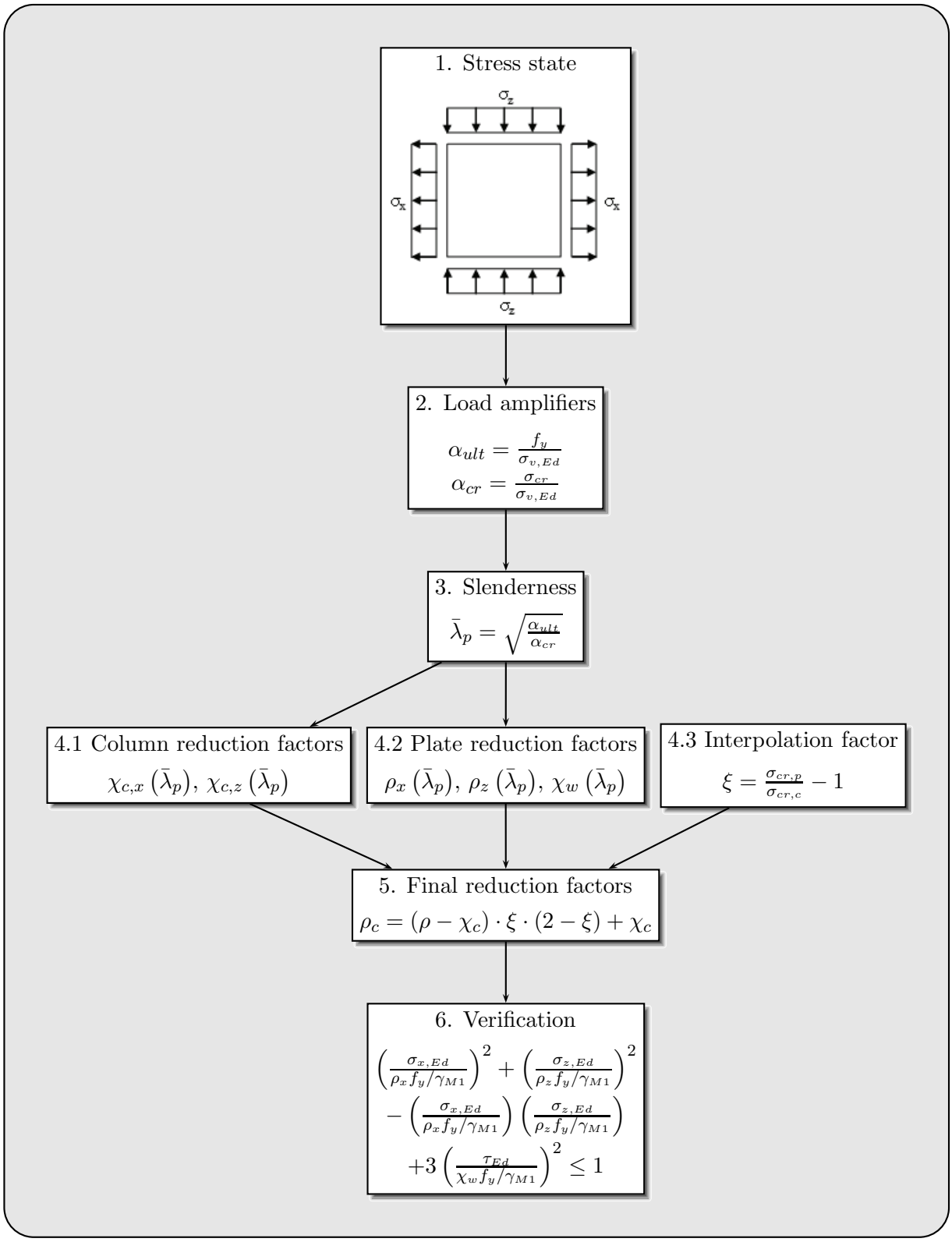

Figure 2.15: Design procedure according to Chapter 10, EN 1993-1-5 [36].

Eq.(2.18) shows the determination of the global slenderness, where $\alpha_{ult,k}$ is the minimum load amplifier for the design loads to reach the characteristic value of resistance on the most critical point of the plate and α_{cr} is the minimum load amplifier for the design loads to reach the elastic critical stress state of the plate under the multiaxial stress field.

$$\bar{\lambda}_p = \sqrt{\frac{\alpha_{ult,k}}{\alpha_{cr}}} \tag{2.18}$$

Fig.2.16 illustrates the development of the slenderness in dependence on the interaction-angle Θ presented in Sec.2.2.2 normalised to the slenderness for uniaxial compression $\overline{\lambda}_{p,0}$ for a square plate ($\alpha = 1$) and a long plate ($\alpha = 3$) in polar coordinates. It can be seen how the slenderness in the biaxial compression domain increases up to ≈ 1.4 times the slenderness for pure compression and ≈ 2.0 respectively for the regarded long plate. For the tension–compression interaction the slenderness diminishes approaching to zero for pure tension.

The verification according to Chapter 10, EN 1993-1-5 [36] is done with a kind of von Mises criterion, see Eq.(2.19). Within the shown equation ρ_x , ρ_z and χ_w are the reduction factors which reduce the yield stress due to plate buckling taking into account column-like behaviour where relevant, see Sec.2.4.2.3.

$$\left(\frac{\sigma_{x,Ed}}{\rho_x f_y/\gamma_{M1}}\right)^2 + \left(\frac{\sigma_{z,Ed}}{\rho_z f_y/\gamma_{M1}}\right)^2 - \left(\frac{\sigma_{x,Ed}}{\rho_x f_y/\gamma_{M1}}\right)\left(\frac{\sigma_{z,Ed}}{\rho_z f_y/\gamma_{M1}}\right) + 3\left(\frac{\tau_{Ed}}{\chi_w f_y/\gamma_{M1}}\right)^2 \leq 1 \tag{2.19}$$

where:	$\sigma_{x,Ed}$; $\sigma_{z,Ed}$; τ_{Ed}:	Acting stresses
	ρ_x; ρ_z; χ_w:	Reduction factors for each stress
	f_{yd}:	Yield strength
	γ_{M1}:	Partial safety factor

The determination of the reduction factors according to Chapter 10, EN 1993-1-5 [36] can be done by the buckling curves given in Chapter 4 and 5 or from Annex B as well. While the buckling curves in Chapter 4 (direct stresses) and Chapter 5 (shear stresses) take as much advantage as possible from the postcritical strength reserve, the buckling curves provided in Annex B, which were derived by MÜLLER [82] in a general format, are more conservative and do not account for the postcritical strength reserve as much as the aforementioned ones. However, BRAUN showed in [11] by numerical simulations that the recalculation of the buckling curves strongly depends on the chosen boundary conditions, see also Sec.4.6.2.

a) $\alpha = 1$

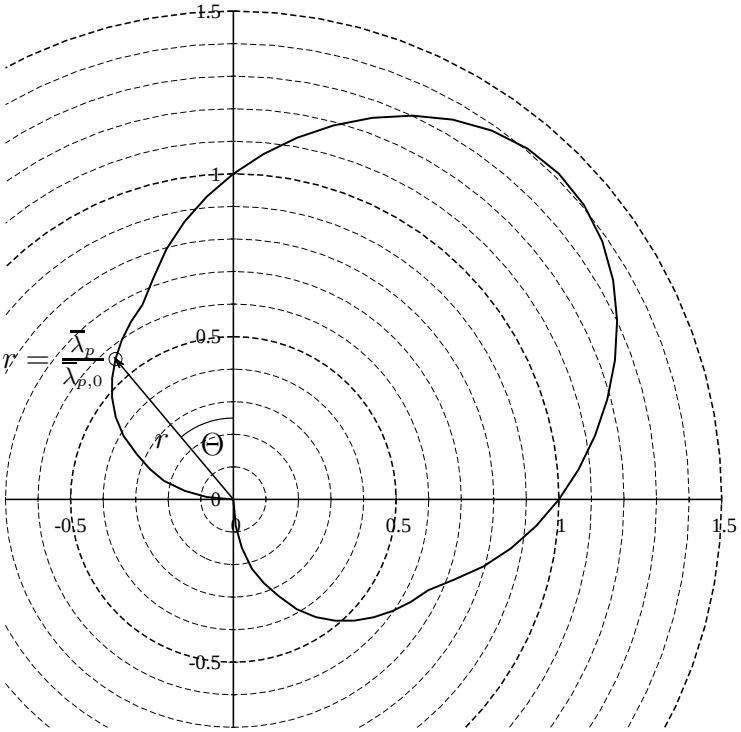

b) $\alpha = 3$

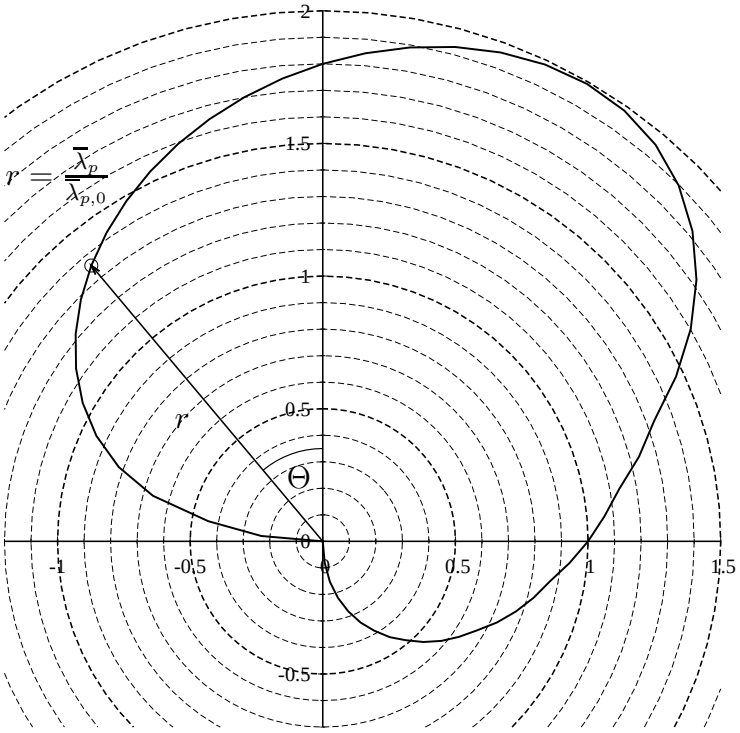

Figure 2.16: Normalised slenderness values over the whole interaction range of direct stresses considering the complete stress field.

2.4.2.2 Buckling curves for direct stresses

The buckling curve given in Chapter 4 is based on the Winter curve for longitudinal stresses, taking into account also the stress ratio, see Eq.(2.20).

$$\rho = \frac{\bar{\lambda}_p - 0.055 \cdot (3 + \psi)}{\bar{\lambda}_p^2} \leq 1.0 \tag{2.20}$$

for: $\bar{\lambda}_p > 0.5 + \sqrt{0.085 - 0.055 \cdot \psi}$
else: $\rho = 1.0$

where: ψ: Stress ratio (= 1 for pure compression; = −1 for pure bending)

The buckling curves in Annex B as mentioned before have a general format similar to the buckling curves for columns given in EN 1993-1-1 [35]. Even if they might look identical at the first sight, they differ, since the buckling curves are derived by Müller [82] as a solution of the Ayrton-Perry formulation. Grotmann [48] already proposed an expression with the Ayrton-Perry format in order to avoid different formulations, but the proposal was contested by Müller [82] and a formulation according to Maquoi & Rondal [77], [78] was derived as shown in Eq.(2.21).

$$(1 - \rho) \cdot (1 - \rho \cdot \bar{\lambda}_p^{\gamma}) = \alpha_p \cdot (\bar{\lambda}_p - \bar{\lambda}_{p,0}) \cdot \rho \tag{2.21}$$

Herein, the term $\alpha_p \cdot (\bar{\lambda}_p - \bar{\lambda}_{p,0})$ is the imperfection parameter depending on the slenderness, where the imperfection parameter α_p characterises the plate buckling curve and $\bar{\lambda}_{p,0}$ is the length of the plateau. While the column buckling curves in EN 1993-1-1 [35] are derived using the coefficient $\gamma = 2$, Müller uses the parameter $\gamma = 1$ for plate buckling leading to the solution given in Annex B of EN 1993-1-5 [36] shown in Eq.(2.22).

$$\rho = \frac{1}{\phi_p + \sqrt{\phi_p^2 - \bar{\lambda}_p}} \tag{2.22}$$

where: $\phi_p = \frac{1}{2} \cdot (1 + \alpha_p \cdot (\bar{\lambda}_p - \bar{\lambda}_{p,0}) + \bar{\lambda}_p)$

The values for $\bar{\lambda}_{p,0}$ and α_p for direct stresses according to Annex B, EN 1993-1-5 [36] are summarised in Tab.2.2. A distinction is made for different stress ratios $\psi \geq 1$ and $\psi < 1$ as well as for transverse stresses. All buckling curves for direct stresses are drawn in Fig.2.17 in comparison with the Euler curve.

Table 2.2: Values for $\bar{\lambda}_{p,0}$ and α_p for direct stresses according to Annex B, EN 1993-1-5 [36] for welded sections.

loading	α_p	$\bar{\lambda}_{p,0}$
longitudinal stresses for $\psi \geq 1$	0.34	0.7
longitudinal stresses for $\psi < 1$	0.34	0.80
transverse stresses	0.34	0.80

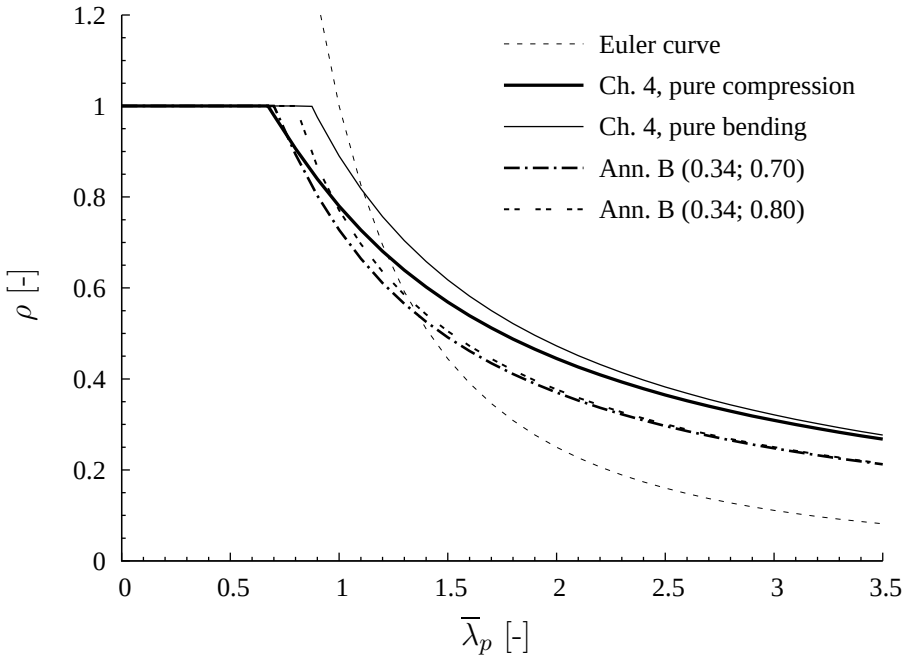

Figure 2.17: Buckling curves for longitudinal and transverse stresses according to EN 1993-1-5, Ch. 10.

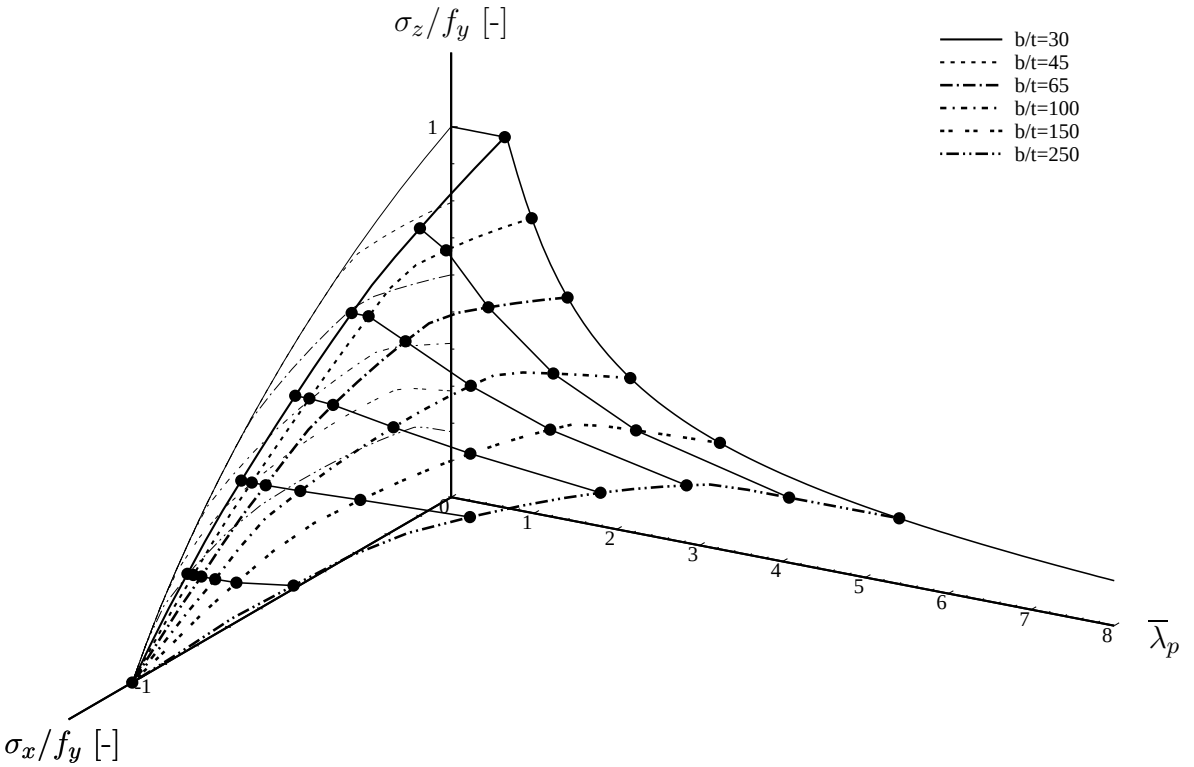

Figure 2.18: Isometrical illustration of the resistance interaction curves according to EN 1993-1-5, Chapter 10 ($\alpha = 1$).

The input parameter for the reduction factors is the plate slenderness, see Eq.(2.18), so that the consideration of tensile stresses leads to smaller slenderness values and therefore to higher reduction factors. The evaluation of the design equation with tension stresses and the development of the slenderness with increasing interaction-angle is shown for square plates in Fig.2.18 for different b/t-ratios using the buckling curves from Ch. 4, EN 1993-1-5 [36]. The investigated plates have a yield stress of $f_y = 355\,\mathrm{N/mm^2}$. A projection of the curves from the isometrical illustration in Fig.2.18 to the σ_x/f_y–σ_z/f_y plane leads to the interaction curves shown in Fig.2.19 for the considered b/t-ratios, so that the influence of tension stresses on the resistance for biaxially loaded plates as predicted by EN 1993-1-5 [36] can directly be identified.

2.4.2.3 Column-like behaviour

The development of a double curvature of the plate is of essential importance for the post-buckling strength reserve. Since the plate buckling curves consider the post-buckling strength reserve, a special treatment is needed for plates where a double curvature does not occur. The most obvious case is a plate without longitudinal supports as shown in Fig.2.20 a), which behaves completely like a column. Column-like behaviour occurs also for small aspect ratios α, where the restraints from the lateral supports do not influence the behaviour of the plate in the middle and therefore only a single curvature can develop, see Fig.2.20 b). The third case where column-like buckling can be observed depends on the stiffness ratio of both directions of the plate as for stiffened plates shown in Fig.2.20 c).

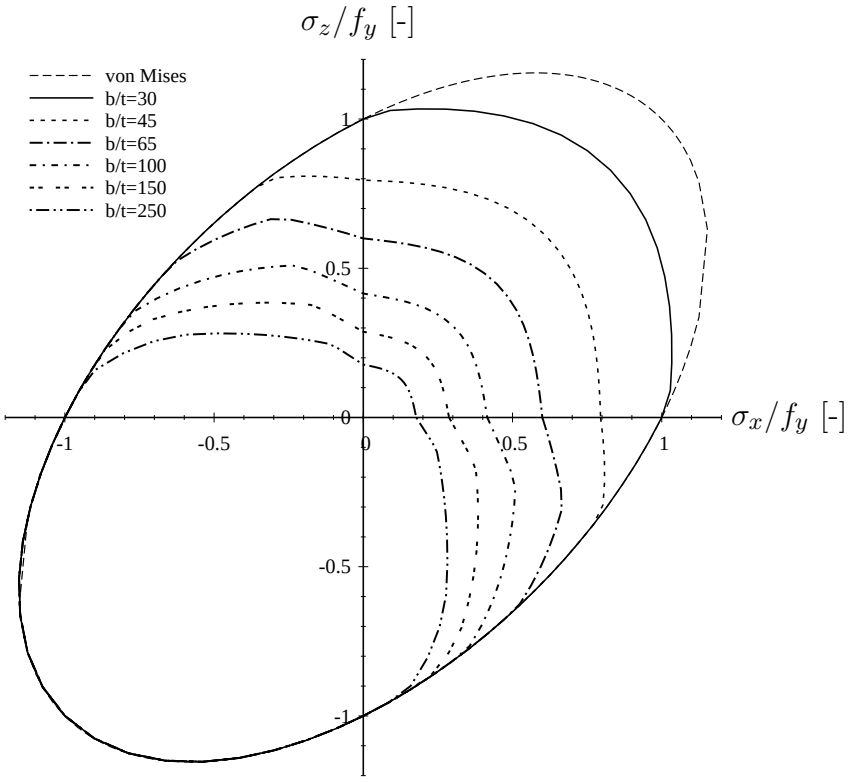

Figure 2.19: Resistance interaction curves according to EN 1993-1-5, Chapter 10 ($\alpha = 1$).

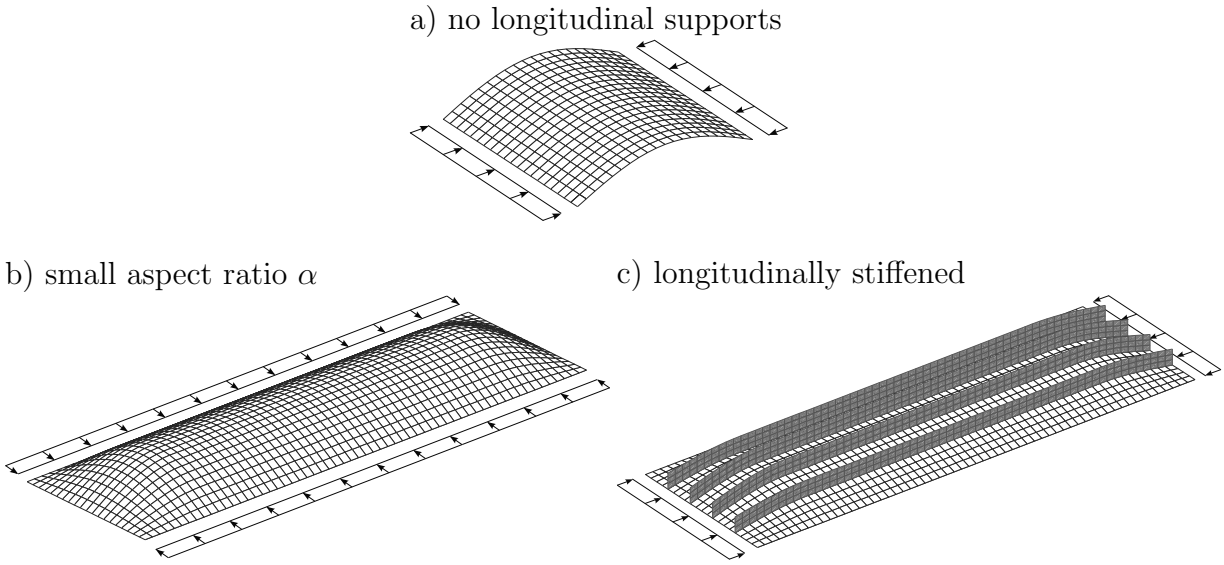

Figure 2.20: Cases for column-like buckling behaviour.

To take into account the column-like behaviour of a plate, an interaction between the plate buckling and column-buckling curves is conducted according to Eq.(2.23) leading to a final reduction factor ρ_c. It is noted here, that in the recent past a discussion arose on if the critical plate buckling stress $\sigma_{cr,p}$ should in this case be applied using the complete stress field or only the normal stresses in the regarded direction. The latter procedure is recommended in relevant literature as e.g. [12], [99], [116], [117] and also followed by BRAUN in [11]. This approach is also used for the present work, as the derivation of the formulation is conducted on uniaxially loaded plates with an aspect ration $\alpha \leq 1$, see [42] and [43].

$$\rho_c = (\rho - \chi_c) \cdot \xi \cdot (2 - \xi) + \chi_c \tag{2.23}$$

$$\text{where:} \quad \xi = \frac{\sigma_{cr,p}}{\sigma_{cr,c}} - 1 \quad \text{but} \quad 0 \leq \xi \leq 1$$

In case of an unstiffened plate the elastic critical column buckling stress $\sigma_{cr,c}$ is obtained with Eq.(2.24).

$$\sigma_{cr,c} = \frac{\pi^2 \, E \, t^2}{12 \, (1 - \nu^2) \, a^2} \tag{2.24}$$

For the determination of the reduction factor χ_c due to column-like behaviour the European buckling curve a (EBC a) from EN 1993-1-1 [35] is used for unstiffened plates, while for stiffened plates a distinction is made for closed-section stiffeners using EBC b and open-section stiffeners using EBC c. The equation for the general format European buckling curves is shown in Eq.(2.25).

$$\chi_c = \frac{1}{\phi + \sqrt{\phi^2 - \bar{\lambda}_c^2}} \tag{2.25}$$

$$\text{where:} \quad \phi = \tfrac{1}{2} \cdot (1 + \alpha \cdot (\bar{\lambda}_c - 0.2) + \bar{\lambda}_c^2)$$

Herein, using Chapter 10, EN 1993-1-5 [36] the slenderness $\bar{\lambda}_p$ according to Eq.(2.18) is taken as input parameter instead of $\bar{\lambda}_c$, see also [4], [12] and [51]. In case of longitudinally stiffened plates, the eccentricity of the stiffeners with respect to the plate needs to be accounted for by increasing the value of the generalised imperfection parameter α, see Eq.(2.26).

$$\alpha_e = \alpha + \frac{0.09}{i/e} \tag{2.26}$$

where: α = 0,34 (curve b) for closed section stiffeners
= 0,49 (curve c) for open section stiffeners
e = $\max(e_1, e_2)$ is the largest distance from the respective centroids of the plating and the one-sided stiffener (or of the centroids of either set of stiffeners when present on both sides) to the neutral axis of the effective column;
i = $\sqrt{\frac{I_{sl,1}}{A_{sl,1}}}$;
$I_{sl,1}$ is the second moment of area of the gross cross section of the stiffener and the adjacent parts of the plate, relative to the out-of-plane bending of the plate;
$A_{sl,1}$ is the gross cross-sectional area of the stiffener and the adjacent parts of the plate.

For the evaluation of long plates (e.g. $\alpha = 3$) shown in Fig.2.21 the interpolation between plate-like and column-like behaviour is evident looking at the $\sigma_z/f_y - \bar{\lambda}_p$ plane. The upper dashed curve denotes the plate-buckling curve from EN 1993-1-5 [36], while the lower curve is the column-buckling curve according to EN 1993-1-1 [35]. The interaction curves for long plates with $\alpha = 3$ are projected to the $\sigma_z/f_y - \sigma_x/f_y$ plane and shown for the complete interaction domain in Fig.2.22.

The first quadrant shows the interaction curves for biaxial compression, where σ_z is applied on the long side and σ_x is applied on the short side. The second quadrant denotes the tension–compression domain with compression applied on the long side, where a mixed plate–like and column–like behaviour is present, see also Fig.2.21. The fourth quadrant also shows the tension–compression interaction, but for the short edge being in compression. The interaction curve in this case is very similar to the interaction curve for a square plate, with the only difference being caused by different peaks of the buckling coefficients as described in Fig.2.3 of Sec.2.2.2.

2.4.2.4 Buckling curves for shear stress

The buckling curves for shear stress can be either determined by Chapter 5 or by Annex B. In Chapter 5 the buckling curves for shear stress are different for rigid end post and non-rigid end post, where the reduction factors χ_w are based on the rotated stress field method, but finally defined from test results to get a proper safety margin, see [51]. The equations for the determination of the reduction factors χ_w are summarised in Tab.2.3.

Herein η is the coefficient that includes the increase of shear resistance at smaller web slenderness. This coefficient is derived from tests on beams with stocky webs, where the ultimate resistance in shear was found to reach 0.7 to 0.8 times the yield strength in tension. In the commentary on EN 1993-1-5 [51] two reasons are given for this behaviour: The first one is due to strain hardening of the steel, which may be utilised because it does not give excessive deformations. The second reason is said to be probably due to a contribution from the flanges. Since these two effects cannot be easily separated, the

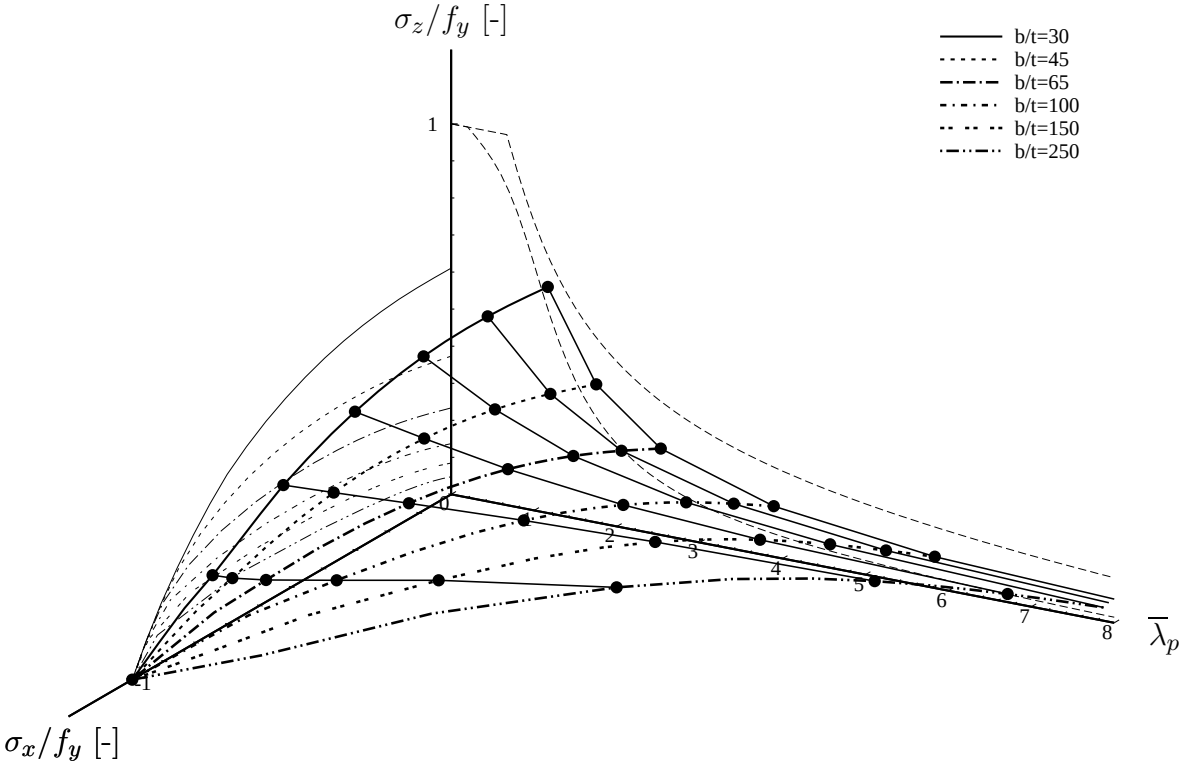

Figure 2.21: Interaction curves according to EN 1993-1-5, Chapter 10 ($\alpha = 3$).

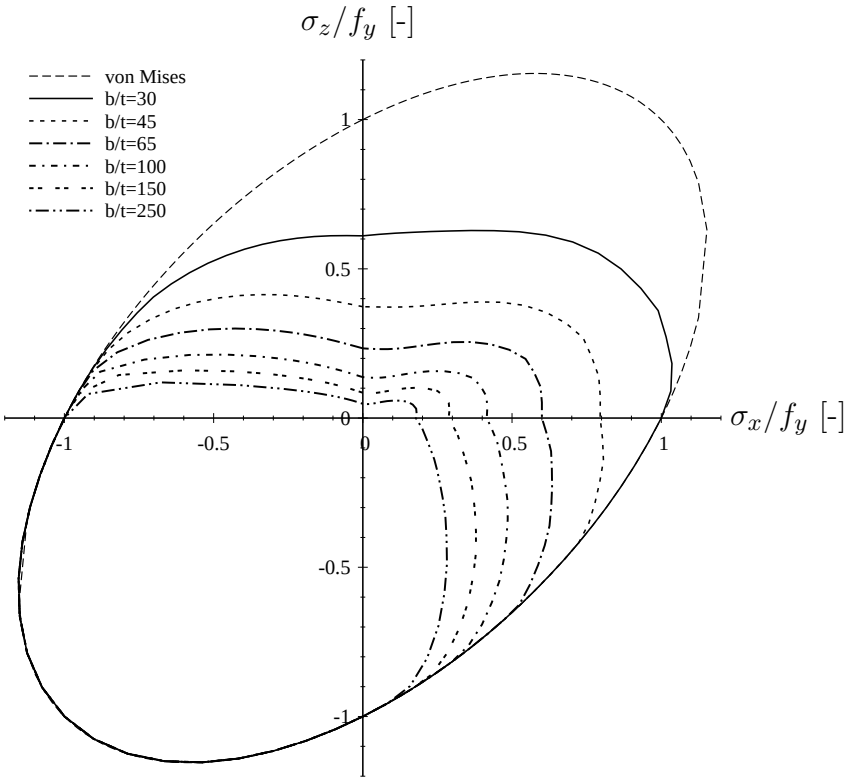

Figure 2.22: Interaction curves according to EN 1993-1-5, Chapter 10 ($\alpha = 3$).

Table 2.3: Reduction χ_w for shear buckling according to Chapter 5, EN 1993-1-5 [36].

	Rigid end post	Non-rigid end post
$\bar{\lambda}_p < 0.83/\eta$	η	η
$0.83/\eta \leq \bar{\lambda}_p < 1.08$	$0.83/\bar{\lambda}_p$	$0.83/\bar{\lambda}_p$
$\bar{\lambda}_p \geq 1.08$	$1.37/(0.7+\bar{\lambda}_p)$	$0.83/\bar{\lambda}_p$

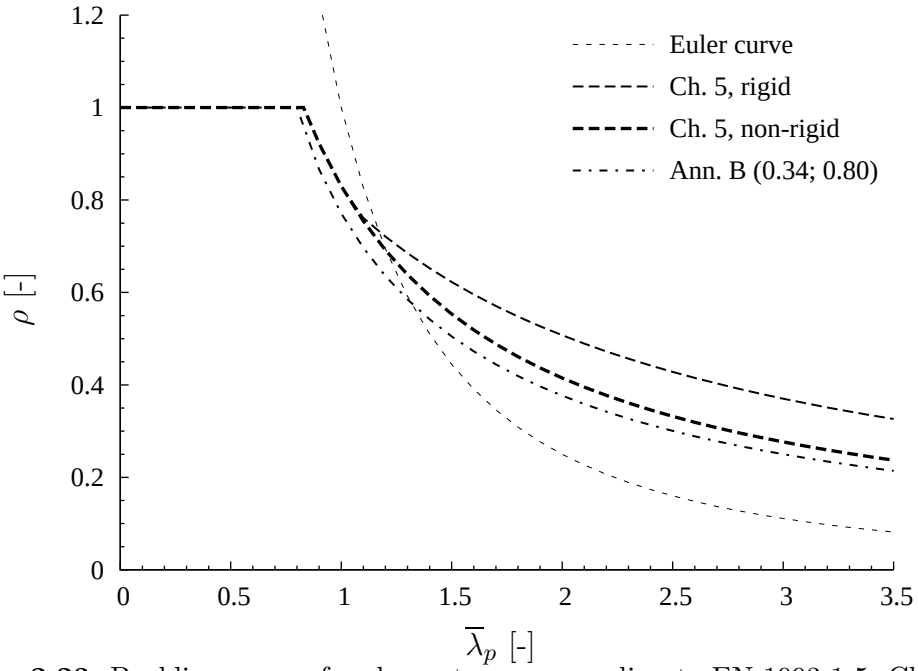

Figure 2.23: Buckling curves for shear stresses according to EN 1993-1-5, Ch. 10.

increase in resistance should not be taken into account for isolated shear panels that are not attached to flanges to form I-like cross sections. The tests have been conducted for steel grades up to S460, so that the increase can be considered for the mentiond cases by the coefficient $\eta = 1.2$.

The shear buckling reduction according to Annex B of EN 1993-1-5 [36] is done in the same format as given in Eq.(2.22) using the values for $\bar{\lambda}_{p,0} = 0.80$ and $\alpha_p = 0.34$, which are the same as for longitudinal stresses with $\psi < 0$ as shown in Tab.2.2. The shear buckling curves according to Chapter 5 and Annex B are shown in Fig.2.23 in comparison to the Euler curve.

For the case of interaction between direct stresses ($\psi = 1$) and shear stresses, the normalised slenderness over the whole interaction range is shown in Fig.2.24 and the interaction curves for different b/t-ratios are show in Fig.2.25. In contrast to the tension-compression interaction curves, the curves are obviously symmetric for positive and negative shear stresses. It is also noticeable, that the influence of tensile stresses have a larger influence on the shear buckling resistance than on the buckling resistance due to direct stresses as shown previously in Fig.2.19.

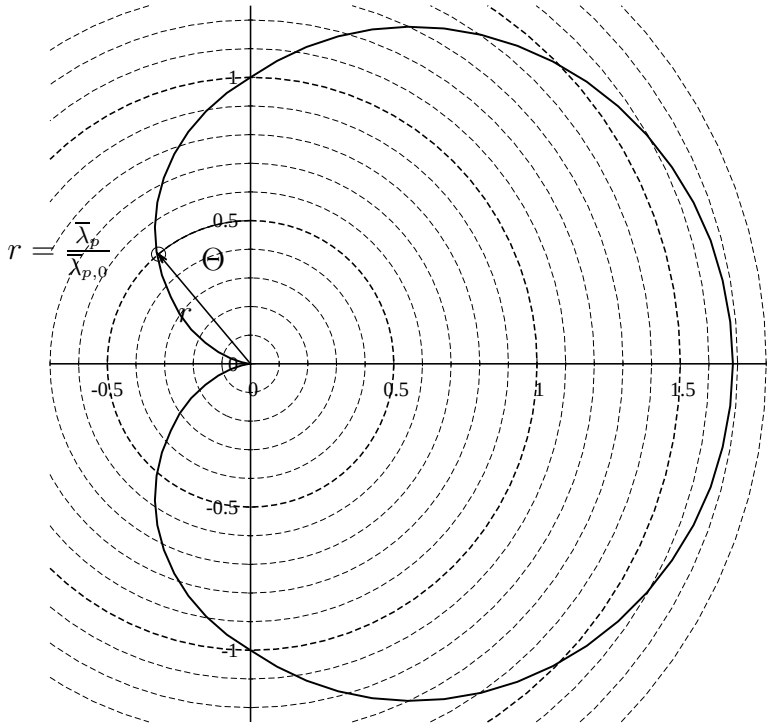

Figure 2.24: Normalised slenderness values over the whole interaction range of shear and direct stresses considering the complete stress field, $\alpha = 2$.

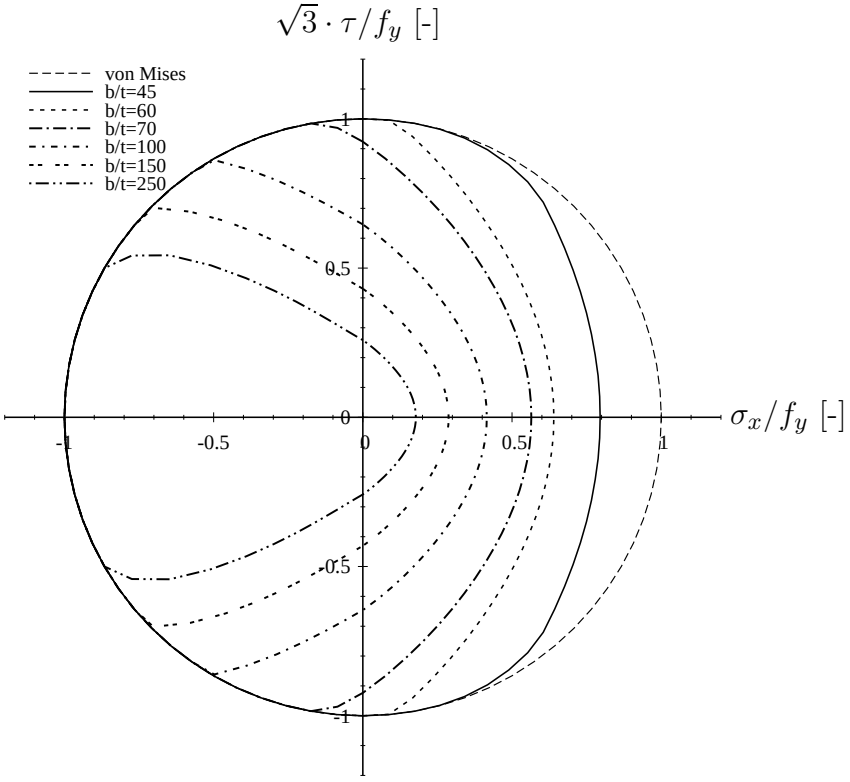

Figure 2.25: Resistance interaction curves according to EN 1993-1-5, Chapter 10 ($\alpha = 2$).

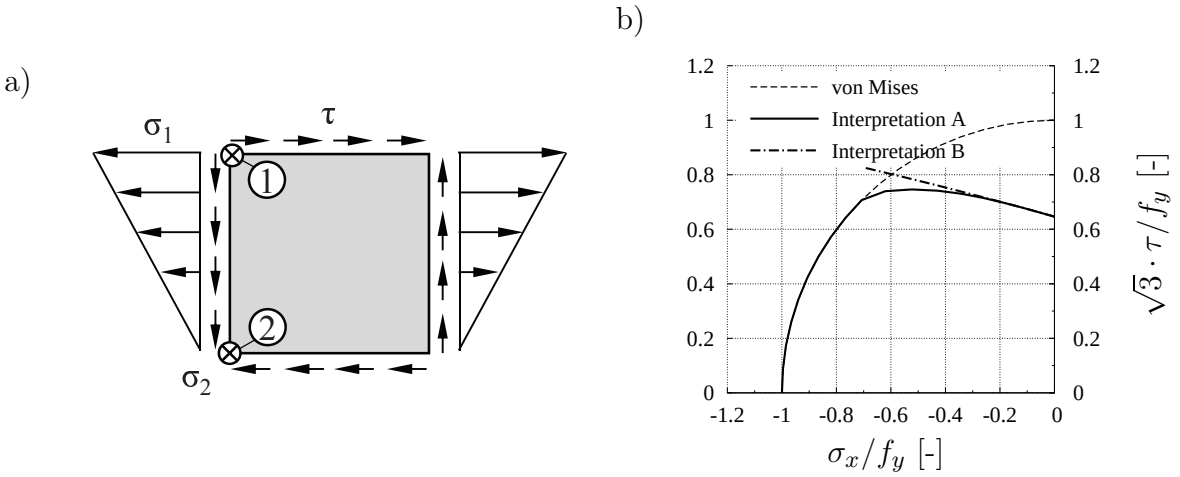

Figure 2.26: Interaction curves according to Interpretation A and B of EN 1993-1-5, Chapter 10 ($b/t = 100$, $\psi = 0$).

EN 1993-1-5 [36] gives in Sec. 10 (5) Note 2 the recommendation to apply the verification formula only for compressive parts within the buckling verification. The note might be interpreted as a recommendation not to account for the positive effect of tension stresses on the buckling behaviour because information on appropriate investigations are missing. However, Fig.2.19, Fig.2.22 and Fig.2.25 show the interaction curves considering the effect of the tension stresses in the determination of the critical buckling load for calculating the plate slenderness and using the design formula shown in Eq.(2.19).

Evaluations of the existing rules in Chapter 10, EN 1993-1-5 [36] conducted by Braun [11] for the biaxial case of compression show some pronounced interaction curve shapes where discrepancies are observed in comparison with numerical results leading to a modification of the current design rules. Therefore, similar results may also exist for the interaction of multiaxial stress states like biaxial tension–compression, tension–shear or compression–shear.

Furthermore, one question that occurs when applying the design approach to a plate subjected to a direct stress gradient ($\psi \neq 1$) and shear, is where to perform the design check, see exemplarily Fig.2.26 a). In interpretation **A** the buckling verification is conducted at point ①, while in interpretation **B** the buckling check is conducted at point ② and material yielding is verified at point ①. This means, that in interpretation **B** the two phenomena are regarded separately, while in interpretation **A** both are regarded at once, leading to a quicker procedure. Fig.2.26 b) shows exemplarily what this means for the interaction curves of the resistance. It can be seen, that interpretation **A** and **B** are almost the same and a difference can be observed just when approaching to the von Mises criterion, where in interpretation **A** the plastic destabilising effect of the tension stresses cause a stronger reduction of the applicable shear stress, while interpretation **B** proceeds until it reaches the von Mises criterion, where material yielding is decisive.

2.4.2.5 Stiffened plates

For assessing the global plate buckling stress of stiffened plates EN 1993-1-5 [36] provides a procedure within the informative Annex A. The calculation of the buckling stress is given separately for equivalent orthotropic plates with at least three longitudinal stiffeners (A.1), for plates with one or two stiffeners (A.2) and for stiffened plates subjected to shear (A.3). Alternatively the use of Klöppel-charts [54], [55] is possible for certain cases giving the buckling stress for longitudinally stiffened plates, see Sec.2.2.4. It should be noted, that these charts apply only for flexible stiffeners ($\gamma < \gamma^\star$) in so far as they allow only to enable the natural critical stresses to be determined [45], see also Fig.2.9.

However, nowadays software solutions are also available for this purpose such as EBPlate [16], a software tool that was developed in the frame of the European project COMBRI [66]. EBPlate calculates the natural buckling modes of unstiffened or stiffened plates, but can be used to also assess the global critical buckling stress of longitudinally stiffened plates. Therefore the longitudinal stresses which would cause local buckling in the subpanels are transferred to the stiffeners, by simulating a specific orthotropic behaviour of the plate.

If numerical software solutions like EBPlate [16] are used, a detailed procedure is described and demonstrated by several practical example calculations by Sedlacek et. al in [99]. The German National Annex DIN EN 1993-1-5/NA [25] gives a non-contradictory complementary information containing references, where the literature mentioned above is also included. Therein two models are used for the buckling checks, one discrete model to determine the local buckling behaviour and one orthotropic plate model with smeared stiffeners for the global buckling behaviour. As the code allows for several interpretations for multiaxially loaded stiffened panels, Pourostad [86] conducted an intense parametric study with different approaches for the assessment of the resistance curves, confirming that the procedure demonstrated by [99] gives the most plausible results.

In the following, the procedure for assessing the critical plate buckling stress is shown according to Annex A.2.2 of EN 1993-1-5 [36]. Therefore for the case of one and two stiffeners the stiffened plate is simplified by a fictitious isolated strut supported on an elastic foundation reflecting the plate effect in the direction perpendicular to this strut using Eq.(2.27).

$$\begin{aligned} \sigma_{cr,sl} &= \frac{1.05\,E}{A_{sl,1}}\frac{\sqrt{I_{sl,1}\,t^3\,b}}{b_1\,b_2} && \text{if} \quad a \geq a_c \\ \sigma_{cr,sl} &= \frac{\pi^2\,E\,I_{sl,1}}{A_{sl,1}\,a^2} + \frac{E\,t^3\,b\,a^2}{4\,\pi^2\,(1-\nu^2)\,A_{sl,1}\,b_1^2\,b_2^2} && \text{if} \quad a < a_c \end{aligned} \tag{2.27}$$

with: $a_c = 4.33\sqrt[4]{\frac{I_{sl,1}\,b_1^2\,b_2^2}{t^3\,b}}$

where: $I_{sl,1}$ is the second moment of area of the gross cross section of the stiffener and the adjacent parts of the plate, relative to the out-of-plane bending of the plate;
$A_{sl,1}$ is the gross cross-sectional area of the stiffener and the adjacent parts of the plate.

In case of a stiffened plate with two longitudinal stiffeners the elastic critical plate buckling stress should be taken as the lowest of those computed for the cases where at first it is assumed that one of the stiffeners buckles while the other one acts as a rigid support and secondly buckling of both the stiffeners simultaneously is accounted for by considering a single lumped stiffener that is substituted for both individual ones such that:

1. its cross-sectional area $A_{sl,1}$ and its second moment of area $I_{sl,1}$ are respectively the sum of that for the individual stiffeners and
2. it is positioned at the location of the resultant of the respective forces in the individual stiffeners.

It is worth mentioning that in Annex A.2.1 of EN 1993-1-5 [36] an alternative method is introduced, where global buckling of the stiffened plate is checked by a buckling verification of the most compressed stiffener. However, as the clauses A.2.1 (3) to (6) do not concern the topic mentioned in the title of Annex A.2 (critical plate buckling stress) and there is also some unclear and inconsistent wording, an amendment has been proposed for improving this issue, see [18].

Plates that are stiffened with three or more longitudinal stiffeners can be treated as equivalent orthotropic plates according to Annex A.1 of EN 1993-1-5 [36] taking the elastic critical plate buckling stress according to Eq.(2.28).

$$\sigma_{cr,p} = k_{\sigma,p}\,\sigma_E \tag{2.28}$$

where: $k_{\sigma,p}$ is the buckling coefficient according to orthotropic plate theory with the stiffeners smeared over the plate according to Eq.(2.29).

$$\begin{aligned} k_{\sigma,p} &= \frac{2\left(\left(1+\alpha^2\right)^2+\gamma-1\right)}{\alpha^2\left(\psi+1\right)\left(1+\delta\right)} && \text{if} \quad a \le \sqrt[4]{\gamma} \\ k_{\sigma,p} &= \frac{4\left(1+\sqrt{\gamma}\right)}{\left(\psi+1\right)\left(1+\delta\right)} && \text{if} \quad a > \sqrt[4]{\gamma} \end{aligned} \tag{2.29}$$

with: $\psi = \frac{\sigma_2}{\sigma_1} \ge 0.5$
$\gamma = \frac{I_{sl}}{I_p}$
$\delta = \frac{A_{sl}}{A_p}$
$\alpha = \frac{a}{b} \ge 0.5$

where: I_{sl} is the second moment of area of the whole stiffened plate
I_p is the second moment of area for bending of the plate
$= \frac{b\,t^3}{12(1-\nu^2)} = \frac{b\,t^3}{10.92}$
A_{sl} is the sum of the gross areas of the individual longitudinal stiffeners
A_p is the gross area of the plate $= b\,t$
σ_1 is the larger edge stress
σ_2 is the smaller edge stress

As mentioned before, stiffened plates can also have a pronounced column-like behaviour, see Fig.2.20, so that the interaction formula shown in Eq.(2.23) is used for calculating the final reduction factor taking into account these effects. It is worth mentioning, that an assumed "safe-sided" underestimation of the elastic critical column buckling stress leads to an increased factor ξ in the aforementioned formula and in turn to an underestimation of the column-buckling effect.

The elastic critical column buckling stress of a stiffened plate $\sigma_{cr,c}$ may be determined from a linear extrapolation of the elastic critical column buckling stress $\sigma_{cr,sl}$ of the stiffener closest to the panel edge with the highest compressive stress according to Eq.(2.30). For stiffened plates loaded with pure compression $\sigma_{cr,c} = \sigma_{cr,sl}$.

$$\sigma_{cr,sl} = \frac{\pi^2\,E\,I_{sl,1}}{A_{sl,1}\,a^2} \tag{2.30}$$

However, the code is somehow not clear in the description of the reduced stress method, so that difficulties may arise especially for stiffened plates when trying to apply the design rules, see [117]. Since there is no distinction between local and global buckling in the code, Timmers [110] picked up this issue comparing to possible interpretations:

- Method 1

The determination of the minimum load amplifier for the design loads to reach the elastic critical stress state of the plate is conducted numerically on a model including local buckling. The load amplifier is then defined as $\alpha_{cr} = \min\left(\alpha_{cr,gl};\, \alpha_{cr,loc}\right)$. This value is used for the calculation of the plate slenderness and for the reduction factors ρ and χ_c. The calculation of ξ is done according to Eq.(2.23) for global buckling. Afterwards one single verification is conducted for the complete plate.

- Method 2

This method consists of a verification against local buckling of the decisive panel (with $\alpha_{cr,loc}$) and a verification against global buckling excluding local buckling of the subpanels (with $\alpha_{cr,gl}$). The final reduction factor is then calculated as $\rho_c = \min\left(\rho_{c,loc};\, \rho_{c,gl}\right)$.

A comparison of numerical simulations with both methods conducted by TIMMERS in [110] showed that method 1 may give in some cases results that are considerably on the unsafe side (about 21.4 % to 31.6 %), while method 2 gave much better results leading to the conclusion, that method 2 should always be used. This approach will be used also for the present work and corresponds to example calculations from literature as e.g. [4], [12] and [99].

2.4.3 DIN 18800-3

2.4.3.1 General design procedure

In contrast to the procedure according to EN 1993-1-5 [36] described in Sec.2.4.2, in DIN 18800-3 [22] the slenderness $\bar{\lambda}_{xP}$ and $\bar{\lambda}_{zP}$ are calculated for each load direction separately, so that the reduction factors κ_x, κ_y and κ_τ are in a later step determined based on different slenderness values respectively. The reference strengths are then calculated according to Eq.(2.31).

$$\sigma_{P,R,d} = \kappa \cdot \frac{f_y}{\gamma_M}; \quad \tau_{P,R,d} = \kappa_\tau \cdot \frac{f_y}{\sqrt{3}\,\gamma_M} \tag{2.31}$$

where: κ; κ_τ: Reduction factors according to Tab.2.4 and Tab.2.5
f_y: Yield strength
γ_M: Material partial safety factor

Fig.2.27 shows exemplary buckling curves according to DIN 18800-3 [22]. It can be noticed, how for subpanels an increase of the reduction factor is obtained, as in-plane membrane restraints are accounted for. This is considered by the factor c, see Tab.2.4 and Tab.2.5. Another observation is that postcritical strength reserves in case of shear buckling are only accounted for unstiffened panels, while for stiffened panels with a slenderness $\bar{\lambda}_p > 1.38$ the buckling curve approaches the Euler curve. In case of multiaxially loaded plates the interaction criterion in Eq.(2.32) according to DIN 18800-3 [22] is applied.

$$\left(\frac{|\sigma_x|}{\sigma_{xP,R,d}}\right)^{e_1} + \left(\frac{|\sigma_y|}{\sigma_{yP,R,d}}\right)^{e_2} - V \cdot \left(\frac{|\sigma_x \cdot \sigma_y|}{\sigma_{xP,R,d} \cdot \sigma_{yP,R,d}}\right) + \left(\frac{\tau}{\tau_{P,R,d}}\right)^{e_3} \leq 1 \tag{2.32}$$

where: $e_1 = 1 + \kappa_x^4$
$e_2 = 1 + \kappa_y^4$
$e_3 = 1 + \kappa_x \cdot \kappa_y \cdot \kappa_\tau^2$
$V = (\kappa_x \cdot \kappa_y)^6$, when σ_x and σ_y are both compression, else $V = \frac{\sigma_x \cdot \sigma_y}{|\sigma_x \cdot \sigma_y|}$

Table 2.4: Plate-buckling reduction factors for subpanels and panels without longitudinal stiffeners according to DIN 18800-3 [22].

Loading	Slenderness	Reduction factor
Longitudinal stresses (subpanel)	$\bar{\lambda}_p = \sqrt{\frac{f_y}{\sigma_{cr}}}$	$\kappa = c \cdot \left(\frac{1}{\bar{\lambda}_p} - \frac{0.22}{\bar{\lambda}_p^2}\right) \leq 1$ where $c = 1.25 - 0.12 \cdot \psi_T$; ψ_T is the stress ratio of the relevant stiffened panel
Longitudinal stresses (panel without longitudinal stiffeners)	$\bar{\lambda}_p = \sqrt{\frac{f_y}{\sigma_{cr}}}$	$\kappa = c \cdot \left(\frac{1}{\bar{\lambda}_p} - \frac{0.22}{\bar{\lambda}_p^2}\right) \leq 1$ where $c = 1.25 - 0.25 \cdot \psi \leq 1.25$
Shear stresses	$\bar{\lambda}_p = \sqrt{\frac{f_y}{\tau_{cr} \cdot \sqrt{3}}}$	$\kappa_\tau = \frac{0.84}{\bar{\lambda}_p} \leq 1$

Table 2.5: Plate-buckling reduction factors for panels with longitudinal stiffeners according to DIN 18800-3 [22].

Loading	Slenderness	Reduction factor
Longitudinal stresses	$\bar{\lambda}_p = \sqrt{\frac{f_y}{\sigma_{cr}}}$	$\kappa = c \cdot \left(\frac{1}{\bar{\lambda}_p} - \frac{0.22}{\bar{\lambda}_p^2}\right) \leq 1$ where $c = 1.25 - 0.25 \cdot \psi$;
Shear stresses	$\bar{\lambda}_p = \sqrt{\frac{f_y}{\tau_{cr} \cdot \sqrt{3}}}$	$\kappa_\tau = \frac{0.84}{\bar{\lambda}_p} \leq 1$ for $\bar{\lambda}_p \leq 1.38$ $\kappa_\tau = \frac{1.16}{\bar{\lambda}_p^2} \leq 1$ for $\bar{\lambda}_p > 1.38$

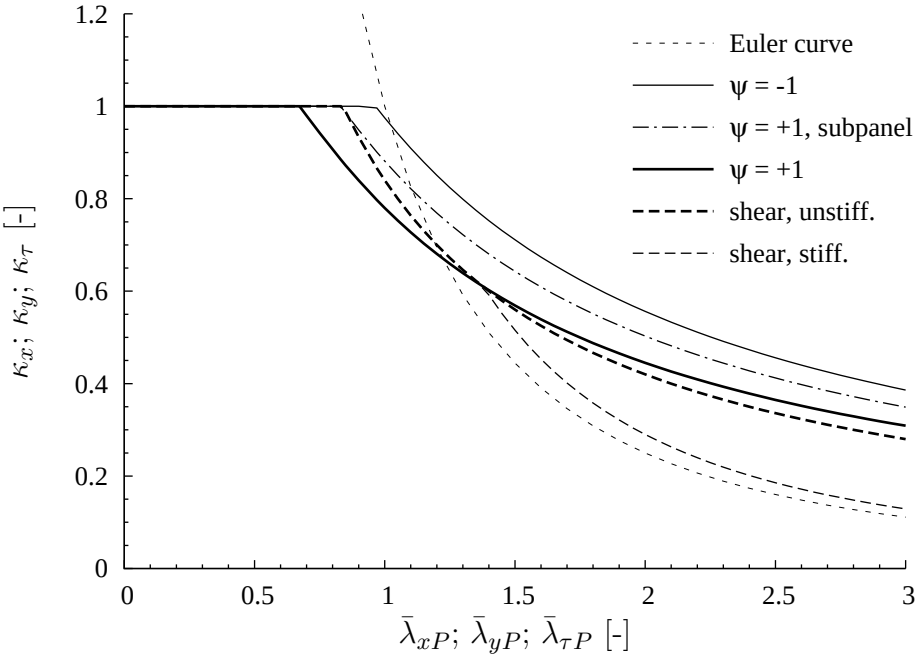

Figure 2.27: Reduction curves according to DIN 18800-3 [22].

Within Eq.(2.32) the exponents e_i and the factor V were calibrated with test results and numerical calculations, see Sec.2.5.4. The positive effect of tensile stresses is not taken into account by DIN 18800-3 [22] as the slenderness is determined for each loading separately.

Fig.2.28 shows a comparison of the σ_x–σ_z interaction curves according to DIN 18800-3 [22] and EN 1993-1-5 [36] pointing out the clear differences that are visible for the biaxial compression domain as well as for tension-compression. It can be seen that the curves according to DIN 18800-3 [22], which used the single slenderness for determining the reduction in each direction, have a monotonic falling character, while EN 1993-1-5 [36] takes into account the stabilising effect of tensile stresses. However, in how far this effect is correctly reflected by the rules was not yet investigated. Furthermore, the comparison of the σ_x–τ interaction curves in Fig.2.29 shows also differences for compression–shear as well as for tension-shear showing the need for investigations for the interaction domain.

2.4.3.2 Column-like behaviour

As already mentioned in Sec.2.4.2, plates may possess a pronounced column-like behaviour, when certain conditions dominate, where a double curvature of the plate can not develop. In these cases, according to DIN 18800-3 [22] column-like behaviour is

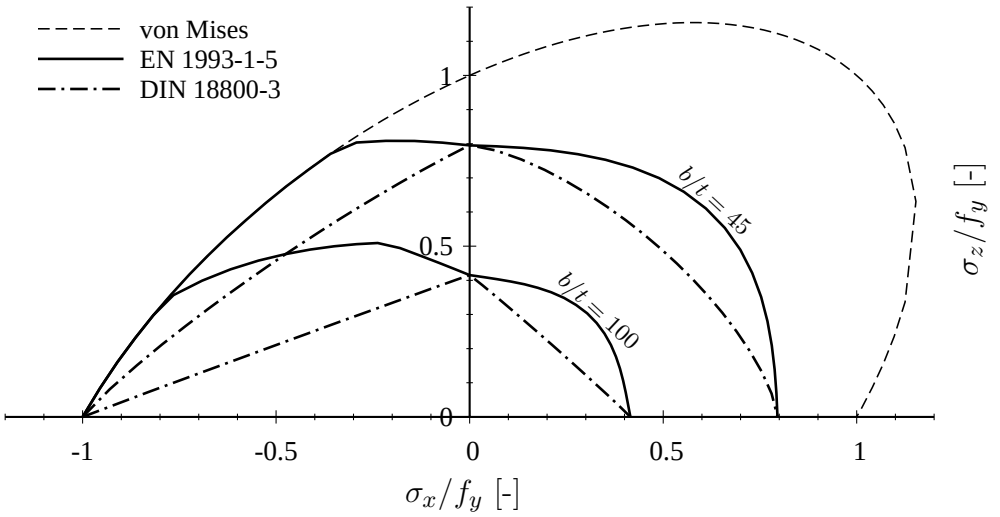

Figure 2.28: Comparison of σ_x–σ_z interaction curves according to DIN 18800-3 [22] and EN 1993-1-5 [36].

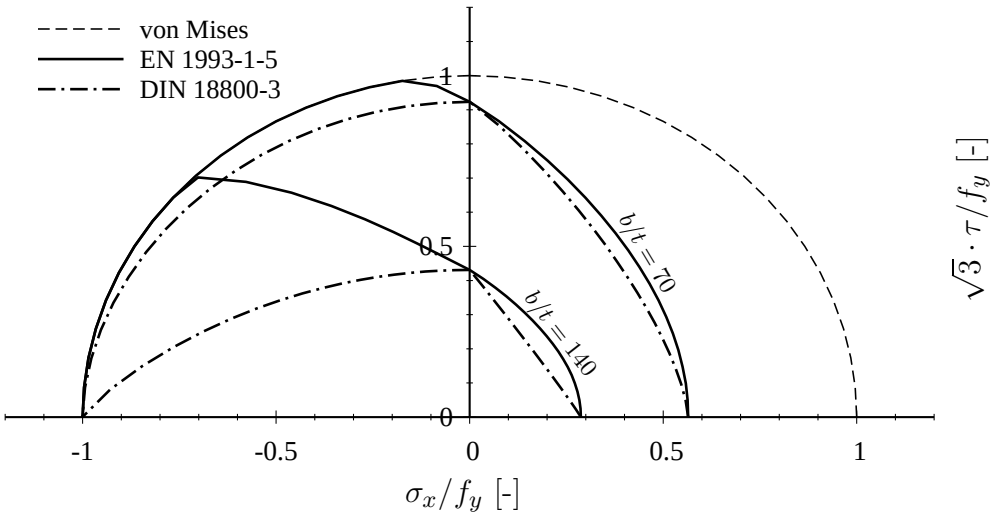

Figure 2.29: Comparison of τ–σ_x interaction curves according to DIN 18800-3 [22] and EN 1993-1-5 [36].

taken into account according to Eq.(2.33).

$$\kappa_{PK} = (1 - \rho^2) \cdot \kappa + \rho^2 \cdot \kappa_K \tag{2.33}$$

where: $\rho = \frac{\Lambda - \sigma_{Pi}/\sigma_{Ki}}{\Lambda - 1} \geq 0$ is a weighting factor,

$\Lambda = \bar{\lambda}_p^2 + 0.5$ but $2 \leq \Lambda \leq 4$

It can be seen that here the interpolation between plate-like and column-like behaviour depends on the slenderness. Therefore, the ratio $\sigma_{Pi}/\sigma_{Ki} \equiv \sigma_{cr,p}/\sigma_{cr,c}$ where only plate-like behaviour governs can vary from 2 to 4, while in EN 1993-1-5 [36] this ratio is fixed to 2. The reduction due to column-like behaviour is considered by the European Buckling Curve b. In Sec.2.5.7 different approaches for the interpolation are shown and discussed pointing out in a direct comparison of the interpolation rules of DIN 18800-3 [22] and EN 1993-1-5 [36] the discrepancies between them even though the general formulation is identical.

It is worth noticing that the format of the current formulation given in Eq.(2.23) goes back to the commentary of the supplemental decree on old DIN 4114 [23], see [43]. As DIN 4114 [23] was originally drafted just for the design of webs and column–like behaviour was not yet investigated, the supplementary decree [1] enlarged the scope also to flanges and added some notes on the consideration of the still missing column–like behaviour. However, a practical formulation was only presented later in the respective commentary, where it was assumed that for $\sigma_{cr,c}/\sigma_{cr,p} \leq 0.5$ plate buckling is decisive, while for $\sigma_{cr,c}/\sigma_{cr,p} > 0.5$ an interpolation with column-like behaviour needs to be considered, see [43]. The proposal was later adopted in a modified form by the "European Recommendations" in [39]. It should be noted here that the formulation was based on experimental investigations conducted on long unstiffened plates subjected to transverse loads, where the loaded edges remained straight in-plane, see [42]. And it should also be kept in mind that today the formulation is applied for considering the effect of column-like behaviour on long plates subjected to transverse loads (independently from the boundary conditions) as well as for stiffened plates, see Fig.2.20.

A comparison to the interpolation according to EN 1993-1-5 [36] shows that DIN 18800-3 [22] uses a more severe formulation for slender plates ($\bar{\lambda}_p > 1.22$) leading to a more column-like reduction for these cases. The reason for this is due to an adaption of the original formulation, which was based on DASt-Richtlinie 012 [17], as DIN 18800-3 [22] accounted for post-critical strength reserves for high slenderness, see [75]. For prEN 1993-1-5 [87] and respectively EN 1993-1-5 [36] this adaption has obviously not taken place. Later, Seitz [101] conducted investigations on long unstiffened plates subjected to transverse stress with deformable edges and proposed a new interpolation formula, see Sec.2.5.7.

2.5 Existing studies

2.5.1 General

During the past years, several investigations have been conducted leading to and dealing with the buckling rules of EN 1993-1-5 [36] identifying discrepancies between them and numerical simulations. In the following sections some relevant investigations are summarised concerning:

- numerical investigations on multiaxially loaded plates on the basis of the finite difference method (Dowling et al. [29] and Dier & Dowling [20])
- numerical investigations on multiaxially loaded plates on the basis of the finite element method (Dinkler & Kröplin [26])
- development of buckling rules for plates under multiaxial stress states (Lindner & Habermann [72], [73])
- further evolution of buckling rules for plates under multiaxial stress states (Scheer & Nölke [95], [96])
- discussion of different approaches for the design of plates under multiaxial stress states considering the analogy to shell buckling (Winterstetter [124])
- interpolation between plate–like and column–like behaviour (Seitz [101])
- proposal of a revised design formula for plates subjected to biaxial compression (Braun [11])
- influence of tension stresses on shear buckling and comparison to current design rules (Sinur [106])
- proposal of a set of reduction curves for multiaxially loaded plates (Jönsson & Bondum [53])

2.5.2 Dier and Dowling (1979/1980)

Large numerical studies on the buckling behaviour of long and square plates ($\alpha = 1$ and 3, $b/t = 20 - 120$, $f_y = 245\,\mathrm{N/mm^2}$, edges restrained in-plane) under biaxial loading have been conducted by Dowling et al. [29] and Dier & Dowling [20] using the finite difference method focusing on biaxial compression as well as on tension-compression. Fig.2.30 shows numerical results of the investigations, which were later presented by Dier & Dowling in [21]. The geometric imperfections have three half-waves in longitudinal direction and one half-wave in transverse direction, additionally the amplitude was varied in order to investigate the influence on the bucking behaviour. From the interaction curves for long plates the influence of column-like behaviour is clearly noticeable for transverse stresses on the long edge (y-direction), while for longitudinal stresses on the short edge (x-direction) plate-like buckling prevails.

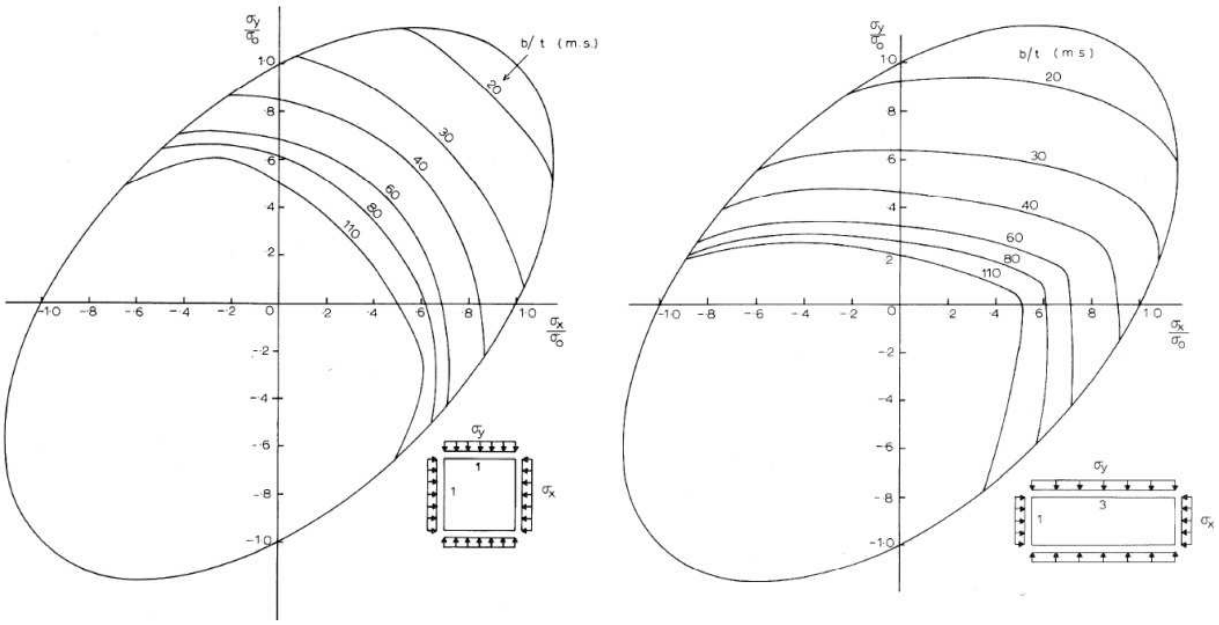

a) $\alpha = 1$ b) $\alpha = 3$

Figure 2.30: Numerical results by Dier & Dowling [21].

What is very interesting, is the fact that for pure compression in x-direction the square plate and the long plate give similar capacities, since the long plate with three half-waves in longitudinal direction behaves similar to a square plate. However, when looking at the tension-compression domain it may be noticed that for the square plate an increase of the capacity develops with increasing tension, which then later drops down again, while for the same range the long plate shows a monotonous decreasing curve. This behaviour is likely to be caused by changes in the failure modes, which occur on multiaxially loaded plates with tensile stresses. This effect was later investigated by Dinkler & Kröplin [26], see Sec.2.5.3.

Furthermore, the outcomes from Valsgard [119] have been confirmed, showing that a proportional loading of the plate is safe-sided as with other load sequences buckling pattern may develop, which are favourable and can increase the capacity. Hence, a proportional loading of the edges is adopted in the further investigations within this work.

2.5.3 Dinkler and Kröplin (1984)

Dinkler & Kröplin [26] conducted numerical investigations on square plates loaded with biaxial compression and tension-compression for b/t-ratios of 55 and 110 using a yield strength of $f_y = 240\,\mathrm{N/mm^2}$ and an initial geometrical imperfection of $w_0 = b/250$. The edge boundary conditions were restrained in-plane.

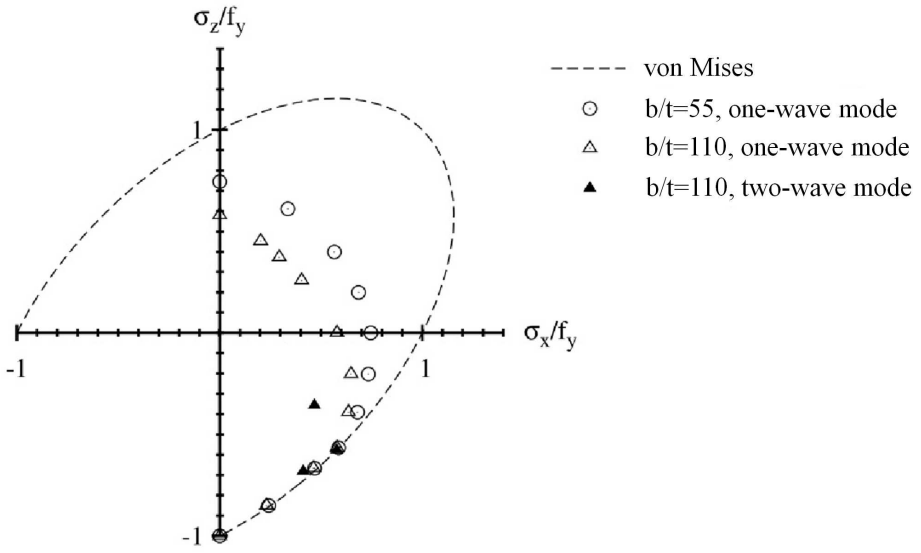

Figure 2.31: Numerical results from Dinkler & Kröplin [26], taken from [11].

The results show for the tension-compression domain the effect of the imperfection shape on the resistance. While for the case of biaxial compression for square plates the one-wave mode is always decisive, this changes when tensile forces are applied, leading to the conclusion that different imperfection shapes need to be considered when conducting investigations on multiaxially loaded plates with tensile stresses.

2.5.4 Lindner and Habermann (1988)

In [72] Lindner & Habermann describe the at that time new design procedure according to the draft code E DIN 18800-3 [31] for the multiaxial stress state with regard to plate buckling. The concept, which renounces for the instrument of the equivalent critical stress, was already presented by them in [71] and is shown in Sec.2.4.3 of this work. Compared to E DIN 18800-3 [31] the presented interaction formula in [72], which corresponds to DIN 18800-3 [22], was calibrated by a V-factor and modified exponents e_i for the different terms within the equation from comparisons with test results and numerical calculations.

Furthermore, Lindner & Habermann [72] give diagrams, which may be used for a simplified calculation for unstiffened long plates, helping the engineers in practice in design. However, due to errors these diagrams have been corrected and represented by them in [73]. In Fig.2.32 the interaction diagrams for compression-shear and bending-shear ($\psi = -0.5$) are shown exemplarily. The curves within the diagrams represent so–called “limit (b/t)”-ratios.

a)

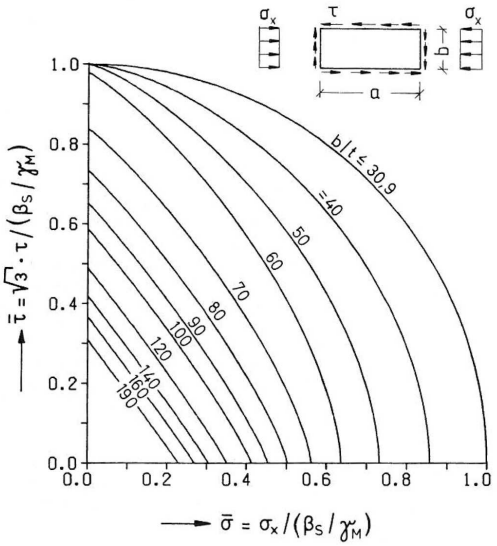

b)

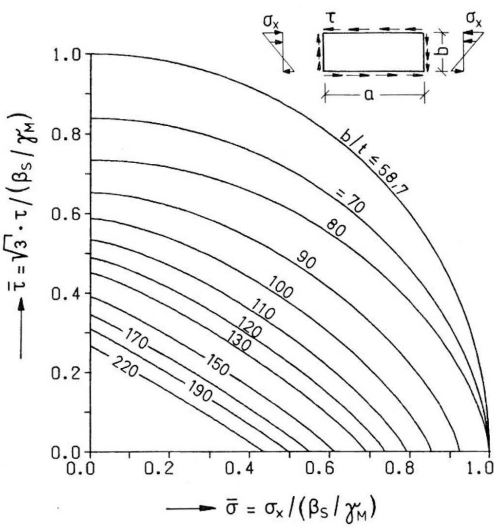

Figure 2.32: Interaction curves for St 52 (≡ S355) for a) $\psi = 1$ and b) $\psi = -0.5$ according to Lindner & Habermann [73].

2.5.5 Scheer and Nölke (2001)

Scheer & Nölke [95], [96] present a new design procedure based on a generalisation of the equivalent stress according to the von Mises criterion, which was later adopted in EN 1993-1-5 [36]. The procedure makes use of an unique plate slenderness and has been described in detail in Sec.2.4.2. The procedure theoretically allows accounting for the stabilising effect of tensile stresses, which is of great importance according to Scheer & Nölke [96] and a disadvantage of the earlier proceedings, which led to deficits e.g. for large girders, such as the over 10 m high beams used in shipyard cranes subjected in wide areas to shear and stabilising longitudinal tension stresses. The reliability is checked for some cases by a comparison to numerical results. However, later research by Winterstetter [124] pointed out, that in certain cases the procedure gives unsafe and unplausible results leading to subsequent modifications as shown in the following sections.

2.5.6 Winterstetter (2002)

In [124] Winterstetter discussed different approaches for accessing the resistance of slender plates subjected to multiaxial loadings showing also the analogy between plate and shell buckling. According to [124], the two approaches generally can be subdivided into:

- combining the respective load carrying capacity predictions for the combined fundamental load cases or
- calculating combined loading bifurcation loads and applying reduction factors derived directly from them ("direct" approach).

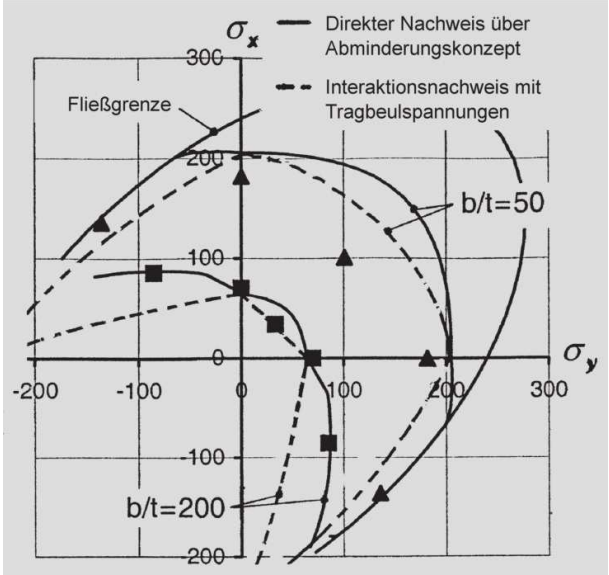

Figure 2.33: Interaction curves calculated by the "direct" approach and by the combination of the fundamental load cases compared to numerical simulations according to Winterstetter [124].

Furthermore Winterstetter notes that a consistent format for all buckling cases (plates as well as shells) would be mechanically correct and desirable. It is also pointed out, that in case of biaxial compression the slenderness is increased making pronounced use of post-buckling strength reserves, which is doubted for real cases. Several approaches are presented for taking into account the different sensitivity to imperfections of the individual buckling cases. It is mentioned that an advantage of the "direct" approach is that the positive effect of tension stresses can also be taken into account. However, it is also noted on the other side, that the interaction curves are somehow not plausible. Furthermore, numerical calculations are qualitatively compared to both approaches leading to the conclusions that the "direct" approach may lead to unsafe results, see Fig.2.33. This case has been later picked up by Braun [11] and is discussed in Sec.2.5.8 of this work.

2.5.7 Seitz (2005)

For the case of long plates loaded with compression on the long edges Seitz [101] investigated the interpolation between plate-like and column-like buckling, as a direct comparison of the interpolation rules of DIN 18800-3 [22] and prEN 1993-1-5 [87] (same rules for interpolation as EN 1993-1-5 [36]) showed some discrepancies in the results, even though the general formulation is identical, see Sec.2.4.3.2.

Therefore, in order to analyse the buckling behaviour of plates subjected to transverse stresses prone to column-like behaviour Seitz [101] conducted a large parametric study on long plates with the loaded edges free to move in-plane proposing a modified

interpolation criterion for the evaluation of the buckling behaviour, where Eq.(2.23) can be rewritten as Eq.(2.34) with $f = \xi(2 - \xi)$.

$$\rho_c = \chi_c + (\rho - \chi_c) \cdot f \tag{2.34}$$

Herein, f is an interpolation factor which has been calibrated with numerical simulations and a function of the slenderness and of the ratio $\sigma_{cr,p}/\sigma_{cr,c}$ using the following approach in Eq.(2.35).

$$f = A \cdot \ln \left(\frac{\sigma_{cr,p}}{\sigma_{cr,c}} \right)^B \tag{2.35}$$

The evaluation of the numerical results using the least-squares-method for the case of compression of both long edges of a plate led to the formulation for the interpolation between column-like and plate-like buckling shown in Eq.(2.36).

$$f = 0.95 \cdot \bar{\lambda}_p^{-0.45} \cdot \ln \left(\frac{\sigma_{cr,p}}{\sigma_{cr,c}} \right)^{-0.15 \cdot \bar{\lambda}_p^2 + 0.75 \cdot \bar{\lambda}_p - 0.025} \leq 1.0 \tag{2.36}$$

For a better application of the calibrated formulation, the simplified expression shown in Eq.(2.37) has been proposed.

$$f = \bar{\lambda}_p^{-0.5} \cdot \ln \left(\frac{\sigma_{cr,p}}{\sigma_{cr,c}} \right)^{0.9} \leq 1.0 \tag{2.37}$$

Fig.2.34 shows the different interpolations according to DIN 18800-3 [22] ($\bar{\lambda}_p \geq 1.87$), EN 1993-1-5 [36], which also corresponds to DIN 18800-3 [22] for $\bar{\lambda}_p \leq 1.22$ and the proposed simplified modification by Seitz [101]. The curve from Seitz [101] gives generally smaller interpolation factors f leading to more column-like behaviour when determing the resistance.

2.5.8 Braun (2010)

According to EN 1993-1-5 [36] it is now possible to deal with multiaxially loaded plates considering a unique slenderness value based already on the level of critical load on the complete stress field. However, it has been shown by Braun [11] that in some cases interaction curves may result, where it is questionable if they make physically sense. Therefore the requirement **I** is not fulfilled, see Sec.2.4.1.

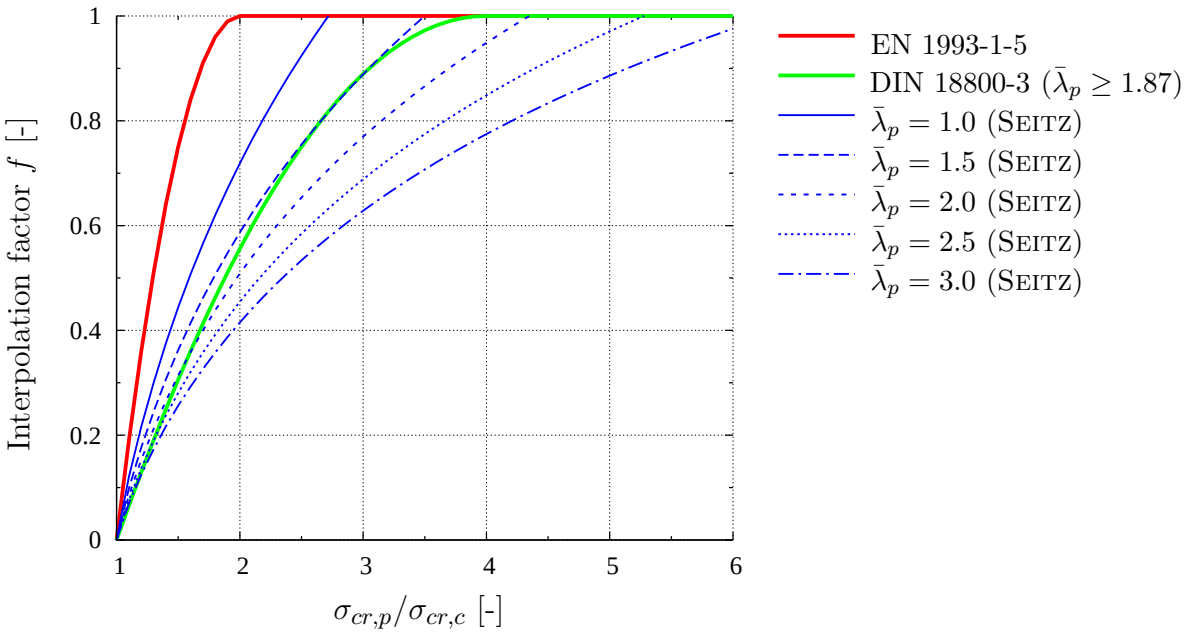

Figure 2.34: Approaches for the interpolation between column–like and plate–like behaviour.

The interaction curves according to EN 1993-1-5 [36], especially for long plates, show a pronounced bend for uniaxial compression σ_z and an increasing resistance in the biaxial compression domain, which is clearly above the resistance according to DIN 18800-3 [22]. Also in the tension–compression domain it can be seen that the curve is above both DIN 18800-3 [22] and DnV RP-C201 [27], which is applied for shipbuilding and offshore engineering, see Fig.2.35.

Furthermore, Braun [11] identified cases where the current design approach gives results, which are on the unsafe side when comparing them to numerical simulations. For these reasons a modification of the design formula for biaxial compression was proposed by an additional "V-factor" (see Eq.(2.38)), which accounts for existing uncertainities to meet also the requirement **G** mentioned in Sec.2.4.1. However, the investigations focused only on the case of biaxial compression and Braun [11] remarked, that for the case of biaxial tension–compression in EN 1993-1-5 [36] it is theoretically possible to account for the stabilising effect of tensile stresses, but also that there is almost no experimental research on that to justify it.

$$\left(\frac{\sigma_x}{\rho_x \cdot f_y}\right)^2 + \left(\frac{\sigma_z}{\rho_z \cdot f_y}\right)^2 - V \cdot \left(\frac{\sigma_x}{\rho_x \cdot f_y}\right) \cdot \left(\frac{\sigma_z}{\rho_z \cdot f_y}\right) \leq 1 \tag{2.38}$$

where: $V = \rho_x \cdot \rho_z$, if σ_x and σ_z are both compression, else $V = 1$

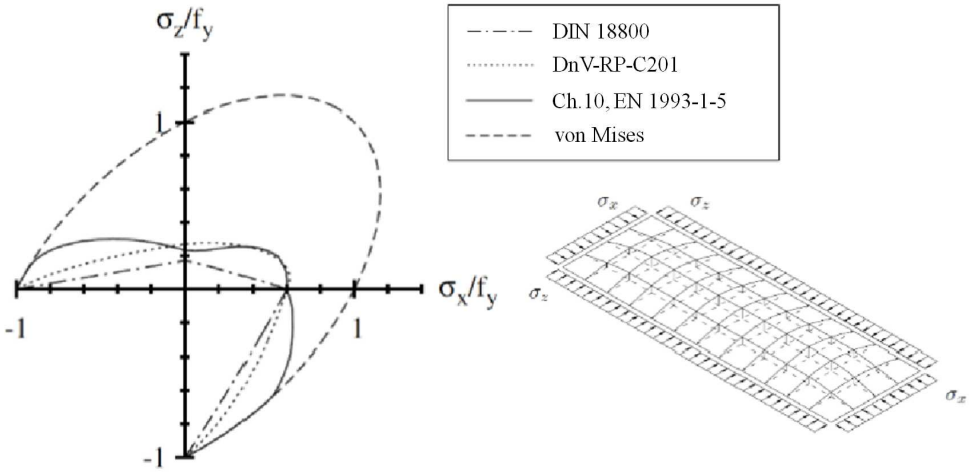

Figure 2.35: Comparison of different code rules, $\alpha = a/b = 3$ for biaxial compression [11].

2.5.9 Sinur (2011)

Sinur [106] conducted some numerical investigations on square plates subjected to compression-shear and tension-shear interaction, comparing them to the design approaches given in EN 1993-1-5 [36] and considering the effective width method (EWM) as well as the reduced stress method (RSM), see Fig.2.36. While for the compression-shear interaction both methods give quite similar results, Sinur [106] highlighted the fact that the effective width method is not capable to include the positive effect of tensile stresses on the shear resistance. However, even though the reduced stress method is able to consider this effect some inconsistencies were found. Since the main focus of Sinur [106] was on the bending moment-shear interaction of longitudinally stiffened steel girders according to the effective width method, the investigations on steel panels subjected to compression-shear and tension-shear were only meant as a small accompanying study to point on the buckling behaviour and the limits of the effective width method, which does not account for the positive effect of tensile stresses.

Since these uncertainties have been found in case of tension-shear interaction, further investigations are required to validate and if necessary to enhance the code rules.

2.5.10 Jönsson and Bondum (2012)

Numerical investigations conducted by Jönsson & Bondum [53] concerned on the buckling behaviour of plates subjected to biaxial compression as well as on tension–compression and propose a new set of curves, see Fig.2.37, which depend from the b/t-ratio and the ratio of the applied loads leading to a reduction of the von-Mises criterion as $\sigma_{vm} \leq \rho_b \cdot f_y$.

The format of the resulting verification is similar to the reduced stress method but with a "global" reduction factor, which is applied to the applicable yield stress. However,

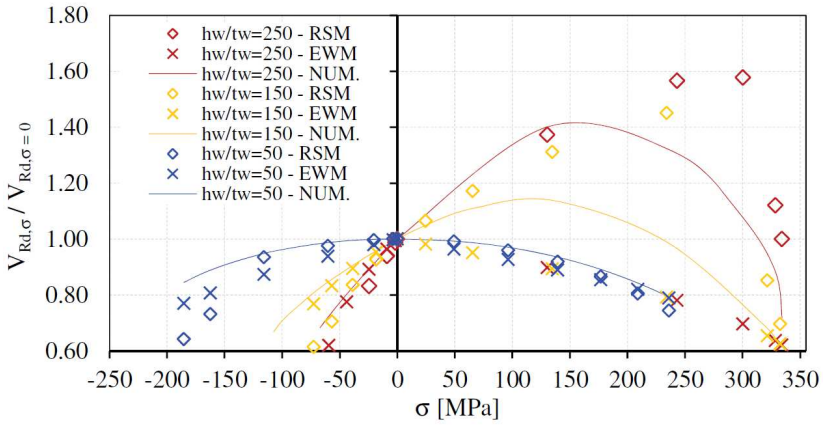

Figure 2.36: Comparison of numerical simulations (NUM) to the reduced stress method (RSM) and the effective width method (EWM) [106].

the calculation of the reduction factor is done without the use of a global slenderness value as usually done in EN 1993-1-5 [36], but uses instead only the b/t-ratio of the regarded plate. Consequently, the approach, which is very interesting from a clear scientific point of view, does not really harmonise with the current design rules and would therefore result in an additional design approach. This is not in compliance with current tendencies to harmonise the code rules and to reduce the number of alternatives rather than creating new ones.

The investigations give an interesting insight in the buckling behaviour of slender plates and raise the question on the application of imperfections for multiaxially loaded plates. While Braun [11] used imperfection shapes with a maximum of three half-waves according to findings from Dow [29], Jönsson & Bondum [53] considered imperfection shapes with up to ten half-waves. It is correctly argued that this approach leads to conservative results, but findings from Fischer [41] found out that in practice usually one-wave imperfections prevail and even the three half-wave imperfection is rarely observed for long plates with $\alpha = a/b > \sqrt{2}$.

2.6 Summary

The foregoing sections of this chapter give an overview on the buckling phenomena for slender plates on the level of elastic critical stress as well as on the ultimate load according to the selected code rules EN 1993-1-5 [36] and DIN 18800-3 [22]. Furthermore, the outcomes of relevant existing studies are summarised.

In a first step the elastic buckling of flat plates and the effect of multiaxial stress states are described. The buckling coefficient for unstiffened panels is given as a function of the panel aspect ratio and the stress state resulting in significantly elevated values if tensile stresses are acting. However, the evaluation of the buckling coefficient shows

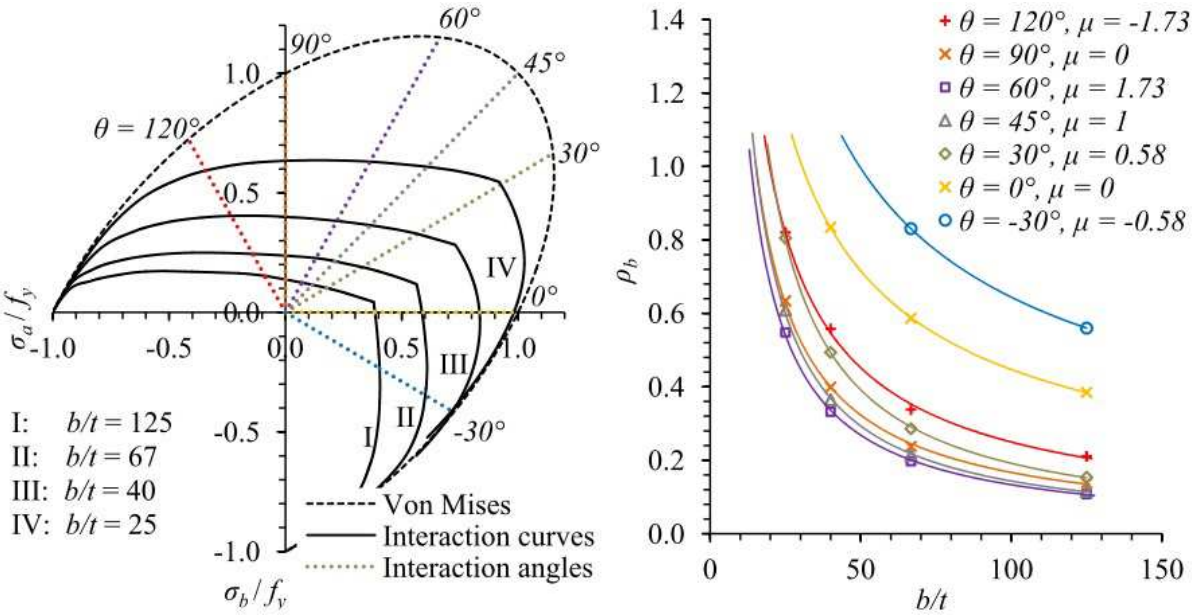

a) Selected interaction angles b) Buckling reduction curves

Figure 2.37: Interaction angles and corresponding buckling reduction curves ($\alpha = 4$) [53].

pronounced peaks for certain cases, where it is questionable if they should be taken into account for the design. Therefore, a formulation is presented ignoring these peaks. For the assessment of the buckling coefficient in case of stiffened plates several possibilities are explained. The complexity in the determination of the buckling coefficient, which involves a variety of parameters, leads to the conclusion that nowadays numerical techniques are the most appropriate approaches. Especially if numerical parametric studies have to be conducted, the numerical determination of the buckling coefficient is the most suited procedure, as it allows for assessing the values for a wide parametric range, while a graphical determination is limited and very labour intensive. The analytical solutions are limited to uniaxial loading.

As this work focuses on the reduced stress method, which was mainly developed in Germany, an overview on the evolution of the German buckling rules is given. The current rules according to EN 1993-1-5 [36] are explained in detail with a particular look on multiaxially loaded plates showing the impact of the stress state on the plate slenderness and therefore on the interaction curves. The interaction curves according to EN 1993-1-5 [36] allow a systematic utilisation of the favourable effect of tensile stresses on the buckling behaviour, especially compared to the rules according to DIN 18800-3 [22]. However, studies to justify this beneficial effect are missing. Therefore, in the following chapters experimental and numerical investigations are conducted to give an insight in the buckling behaviour of multiaxially loaded plates.

The analyses of relevant investigations from the past years shows the attempts to take into account the benefits from tensile stresses on the buckling behaviour. However, the existing investigations are limited to certain cases and in parts do not consider mode-

transitions due to multiaxial stress states. Recent investigations on plates subjected to biaxial compression revealed cases, where the current design approach gives results, which are on the unsafe side when comparing them to numerical simulations and led to a modifications of current rules. Other investigations on plates subjected to shear and tension also found cases where the current formulation may give unsafe results, so that further analyses are needed to clear this issue. Furthermore, recent investigations focused on the formulation of the interpolation of plate-like and column-like behaviour in case of transverse stress, which is adopted and compared in the following studies.

3 Experimental investigations

3.1 General

Experimental investigations on slender plates subjected to multiaxial stress states have been conducted in the frame of several research projects and are presented in the following. The investigations are therefore subdivided in investigations on unstiffened plates subjected to the multiaxial loading case tension–compression in Sec.3.2 and in investigations on stiffened girders subjected to bending–shear interaction in Sec.3.3.

3.2 Tests on multiaxially loaded plates

3.2.1 Overview

Experimental investigations on unstiffened plates subjected to multiaxial stress states have been conducted in order to study the effect of tensile stresses on the buckling behaviour. Existing experimental investigations known to the author dealt only with uni-axial loading and biaxial compression. The experimental studies were supported by a grant from the "Deutscher Ausschuß für Stahlbau – DASt" (German Committee for Steel Structures) in the frame of the "Arbeitsgemeinschaft Industrieller Forschungsvereinigungen Otto von Guericke e.V." (AiF), which is financed by funds of the Federal Ministry for Economic Affairs and Energy (BMWi) as well as experimental studies supported by the European Research Fund for Coal and Steel (RFCS). In the frame of this work the results of the investigations from the German project are included, since the European research project focuses on the use of high strength steel, which is not further investigated here.

This chapter aims at showing the main outcomes of the experimental studies in a compact way. For further information reference is made to the reports of the projects "Beulen mehrachsig beanspruchter Platten" (DASt–AiF, engl.: "Buckling of plates under multiaxial loading") [68] and "Optimal use of High Strength Steel grades within bridges"(RFCS) [69].

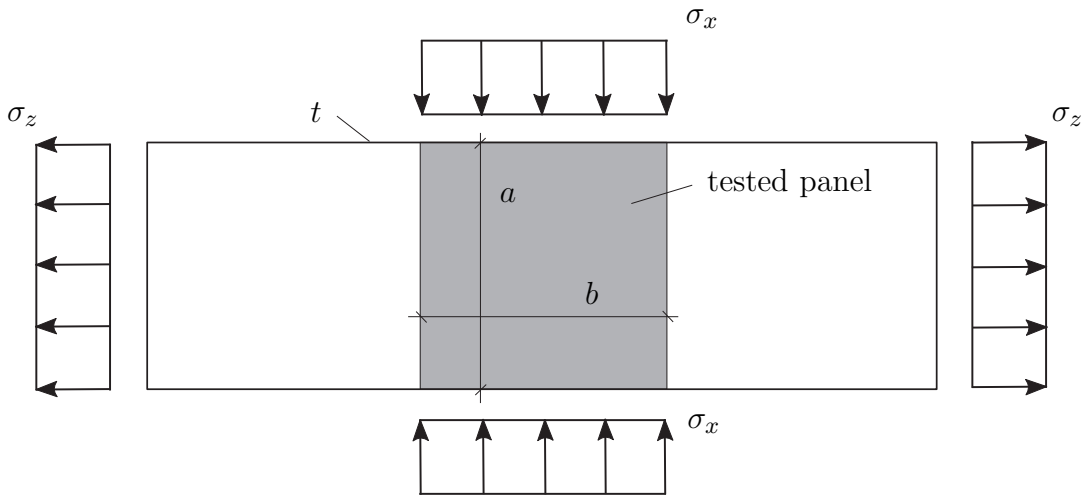

Figure 3.1: Schematic layout of the multiaxially loaded plates.

Table 3.1: Dimensions and stress-ratio of the tested steel panels.

Test	a (mm)	b (mm)	t (mm)	b/t	$\beta = \sigma_z/\sigma_x$
C1	900	900	6	150	0
C2	900	900	6	150	-0.5
C3	900	900	6	150	-1
D1	1500	1500	6	250	0
D2	1500	1500	6	250	-0.5
D3	1500	1500	6	250	-1

3.2.2 Test specimens

3.2.2.1 Dimensions and test parameters

For the experimental investigations simple isolated steel panels are regarded, which are loaded by tension (σ_z) in horizontal and compression (σ_x) in vertical direction. The general test specimen layout is shown in Fig.3.1. The dimensions and the stress-ratios $\beta = \sigma_z/\sigma_x$ are summarised in Tab.3.1. In order to investigate different b/t-ratios the plate dimensions a and b have been varied keeping the plate thickness $t = 6$mm constant, so that the same hinged bearing could be used for all tests, see Sec.3.2.3.

3.2.2.2 Material properties

Uniaxial tensile coupon tests according to EN 10025-2 [32] have been conducted in order to determine the mechanical steel properties. The tests were done on each of the three specimens taken in longitudinal and transverse direction. The mean values of the results in both directions of the tensile coupon tests are summarised in Tab.3.2.

Table 3.2: Results of tensile coupon tests.

tests	yield strength f_y [N/mm^2]	ultimate strength f_u [N/mm^2]	elastic modulus E [N/mm^2]
C1-C3, D1-D3	287	414	200 458

Figure 3.2: Placement of cameras for photogrammetric measurements.

3.2.2.3 Geometric imperfections

The initial geometric imperfections of the tested plates have been measured by the Institute for Photogrammetry of the University of Stuttgart using the photogrammetric method. To obtain the data, four industrial cameras (μEye 2280SE-M, 8 mm lenses) were placed in front of the area of interest, see Fig.3.2. A scale-bar was included in the scene to determine scaling. One axis of the reference plane had to be aligned to the zenith axis in space. For this purpose a plumb-line was installed and measured in the images.

The general procedure and functionality of the photogrammetric method is described briefly in the following. For a better overview the approach is shown using only two cameras. However, the measurements in the frame of this work have been conducted with four cameras in order to increase the accuracy that results from the redundancy in the determination of the 3D coordinates from several pictures.

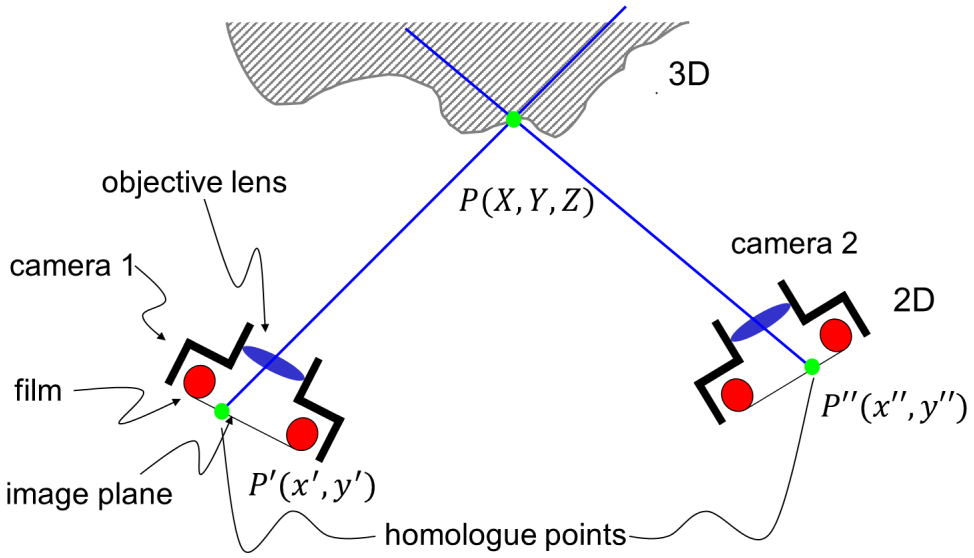

Figure 3.3: General procedure for photogrammetric methods [15].

The principle of the photogrammetric method is based on the so-called spatial intersection, which is also used for field measurements in applied geodesy. Fig.3.3 shows a configuration with two cameras, where a 3D point in space with the coordinates $P(X,Y,Z)$ is projected to the image planes of the cameras through the objective lenses resulting in the homologue 2D points $P'(x',y')$ for camera 1 and $P''(x'',y'')$ for camera 2 respectively.

The relationship of the points can be expressed by so-called collinearity equations, which are the essential equations for the photogrammetric method. These equations represent the mathematical implementation of the central projection. The collinearity equations shown in Eq.(3.1a) and Eq.(3.1b) describe the relationship of the object to the projected image for camera 1. The relationship of the object to the projected image for camera 2 is analogically given in Eq.(3.2a) and Eq.(3.2b).

$$x' = x'_0 - c \cdot \frac{r_{11} \cdot (X - X_{01}) + r_{12} \cdot (Y - Y_{01}) + r_{13} \cdot (Z - Z_{01})}{r_{31} \cdot (X - X_{01}) + r_{32} \cdot (Y - Y_{01}) + r_{33} \cdot (Z - Z_{01})} \tag{3.1a}$$

$$y' = y'_0 - c \cdot \frac{r_{21} \cdot (X - X_{01}) + r_{22} \cdot (Y - Y_{01}) + r_{23} \cdot (Z - Z_{01})}{r_{31} \cdot (X - X_{01}) + r_{32} \cdot (Y - Y_{01}) + r_{33} \cdot (Z - Z_{01})} \tag{3.1b}$$

$$x'' = x''_0 - c \cdot \frac{r_{11} \cdot (X - X_{02}) + r_{12} \cdot (Y - Y_{02}) + r_{13} \cdot (Z - Z_{02})}{r_{31} \cdot (X - X_{02}) + r_{32} \cdot (Y - Y_{02}) + r_{33} \cdot (Z - Z_{02})} \tag{3.2a}$$

$$y'' = y''_0 - c \cdot \frac{r_{21} \cdot (X - X_{02}) + r_{22} \cdot (Y - Y_{02}) + r_{23} \cdot (Z - Z_{02})}{r_{31} \cdot (X - X_{02}) + r_{32} \cdot (Y - Y_{02}) + r_{33} \cdot (Z - Z_{02})} \tag{3.2b}$$

where:	c:	constant of the camera ($\approx$ focal length of the objective)
	r:	matrix for defining the line of vision of the camera
	$(X_0, Y_0, Z_0)^T$:	vector for defining the point of origin

By transformation of the equations, the relationship of the projected image to the object can be gained. The parameter b is furthermore introduced for simplifying the equations leading to the expressions given in Eq.(3.3a) and Eq.(3.3b) for camera 1. The analogous procedure is applied also for the second camera leading to to the expressions given in Eq.(3.4a) and Eq.(3.4b).

$$X = X_{01} + (Z - Z_{01}) \cdot \frac{r_{11} \cdot (x' - x'_0) + r_{12} \cdot (y' - y'_0) + r_{13} \cdot c}{r_{31} \cdot (x' - x'_0) + r_{32} \cdot (y' - y'_0) + r_{33} \cdot c} = X_{01} + (Z - Z_{01}) \cdot bx' \tag{3.3a}$$

$$Y = Y_{01} + (Z - Z_{01}) \cdot \frac{r_{21} \cdot (x' - x'_0) + r_{22} \cdot (y' - y'_0) + r_{23} \cdot c}{r_{31} \cdot (x' - x'_0) + r_{32} \cdot (y' - y'_0) + r_{33} \cdot c} = Y_{01} + (Z - Z_{01}) \cdot by' \tag{3.3b}$$

$$X = X_{02} + (Z - Z_{02}) \cdot \frac{r_{11} \cdot (x'' - x''_0) + r_{12} \cdot (y'' - y''_0) + r_{13} \cdot c}{r_{31} \cdot (x'' - x''_0) + r_{32} \cdot (y'' - y''_0) + r_{33} \cdot c} = X_{02} + (Z - Z_{02}) \cdot bx'' \tag{3.4a}$$

$$Y = Y_{02} + (Z - Z_{02}) \cdot \frac{r_{21} \cdot (x'' - x''_0) + r_{22} \cdot (y'' - y''_0) + r_{23} \cdot c}{r_{31} \cdot (x'' - x''_0) + r_{32} \cdot (y'' - y''_0) + r_{33} \cdot c} = Y_{02} + (Z - Z_{02}) \cdot by'' \tag{3.4b}$$

Using Eq.(3.3a) and Eq.(3.4a) the coordinate Z can be calculated according to Eq.(3.5).

$$Z = \frac{X_{02} - Z_{02} \cdot bx'' + Z_{01} \cdot bx' - X_{01}}{bx' - bx''} \tag{3.5}$$

From Eq.(3.3a) and Eq.(3.4a) furthermore the coordinate X can be calcuated by Eq.(3.6a) and Eq.(3.6b) leading to the identical values.

$$X = X_{01} + (Z - Z_{01}) \cdot bx' \tag{3.6a}$$

$$X = X_{02} + (Z - Z_{02}) \cdot bx'' \tag{3.6b}$$

Eq.(3.3b) and Eq.(3.4b) can be used for determining the coordinate Y with Eq.(3.7a)

Table 3.3: Comparison of measured geometric imperfections and tolerances according to EN 1090-2 [33].

geometric imperfection	C1	C2	C3	D1	D2	D3
measured	$b/900$	$b/281$	$b/225$	$b/268$	$b/333$	$b/242$
measured/allowable	11 %	36 %	44 %	37 %	30 %	41 %

or as a control with Eq.(3.7b).

$$Y = Y_{01} + (Z - Z_{01}) \cdot by' \tag{3.7a}$$

$$Y = Y_{02} + (Z - Z_{02}) \cdot by'' \tag{3.7b}$$

Additionally the arithmetic average can be calculated according to Eq.(3.8).

$$Y = \frac{1}{2}\left[Y_{01} + Y_{02} + (Z - Z_{01}) \cdot by' + (Z - Z_{02}) \cdot by''\right] \tag{3.8}$$

Using the described procedure of the photogrammertic method with four cameras a standard deviation of the internal errors of approximately 0.1 mm is achieved. For further information on the photogrammetric method reference is made to [60] and [76].

The measured initial imperfections are shown in Fig.3.4 to Fig.3.9 with reference to a x/y-plane, which is defined by the lower left and right point as well as the direction of the plumb-line. All imperfection shapes posses a one half-wave mode, except for test C1, where almost no initial imperfection is observed. For the other test specimens the imperfection amplitudes vary from 3.2mm to 6.2mm being all in accordance to the allowable tolerances according to EN 1090-2 [33] ($b/100$), see Tab.3.3.

3.2.3 Test setup

The test setup of the experiments is presented in Fig.3.10. As shown schematically in Fig.3.1, the tensile loads are applied in horizontal direction. The load introduction is carried out by special load introduction devices, which are attached to the test specimen with pre-stressed bolt connections and visible at the right side of Fig.3.10. The load introduction device is then connected with two pin connections to the hydraulic jacks, which lay horizontally in an anchored support.

The compression force is applied on the top of the test specimens by a hydraulic jack connected to a portal frame and distributed by a stiff girder, which is retained by the lateral support construction in order to prevent rotation. The lateral support construction consists of two C-sections on each side that are connected on top to each

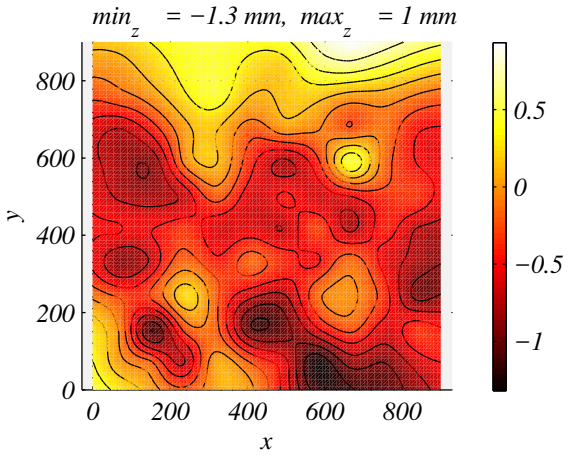

Figure 3.4: Initial imperfections - C1.

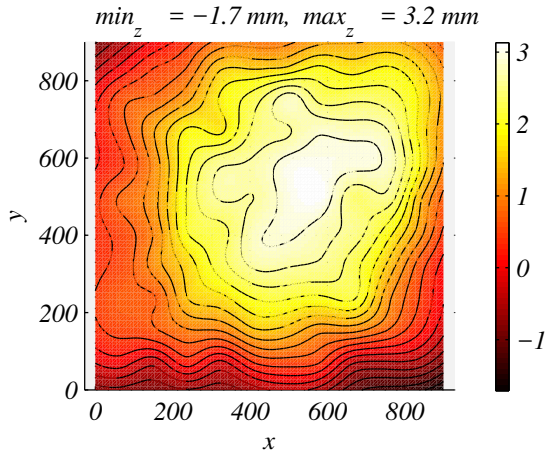

Figure 3.5: Initial imperfections - C2.

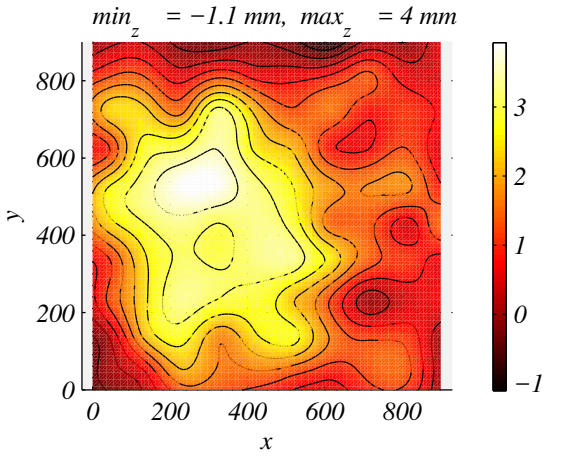

Figure 3.6: Initial imperfections - C3.

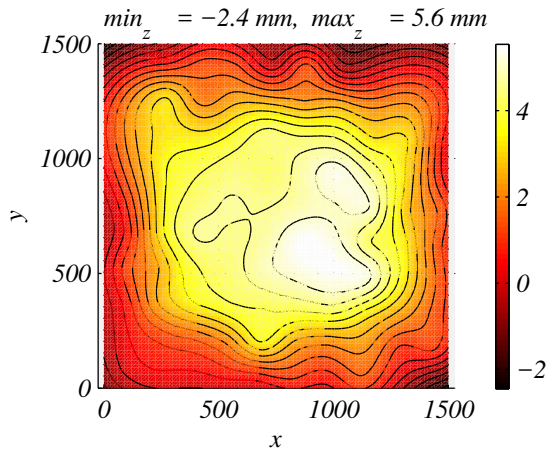

Figure 3.7: Initial imperfections - D1.

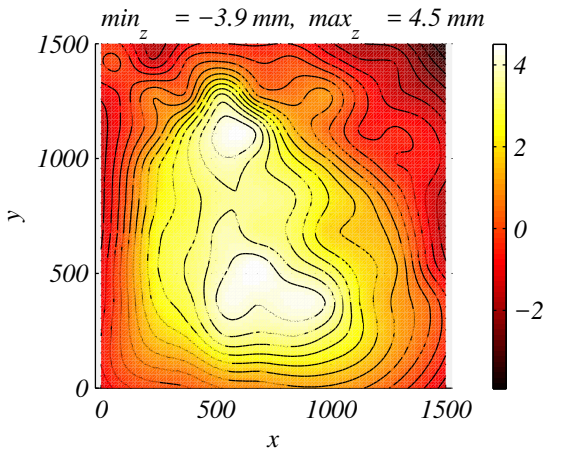

Figure 3.8: Initial imperfections - D2.

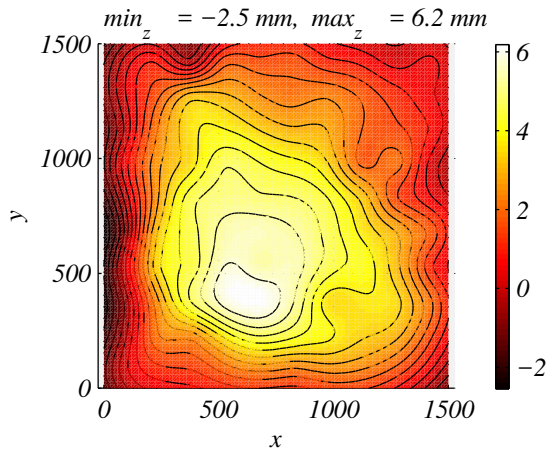

Figure 3.9: Initial imperfections - D3.

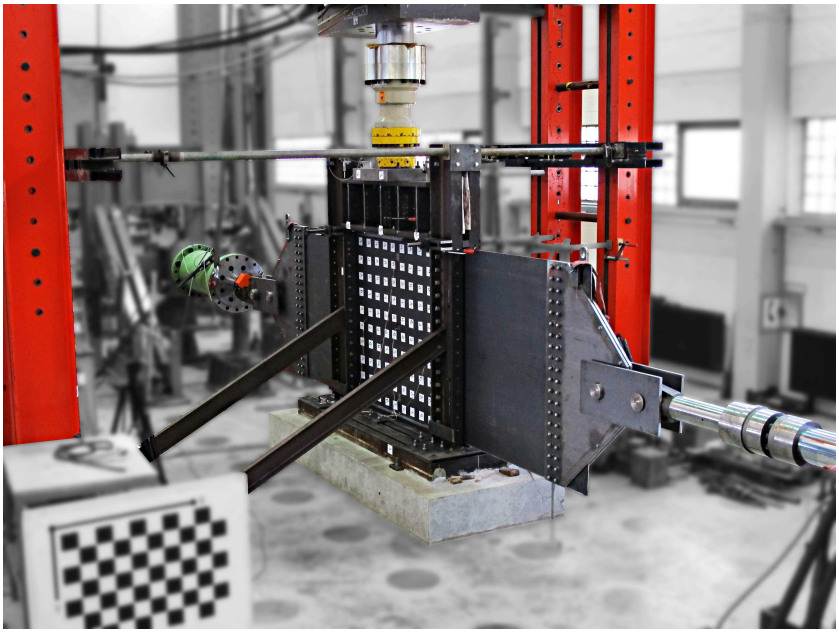

Figure 3.10: Test setup for multiaxially loaded plates.

other and are stabilised additionally with bars to the portal frame both on top and also in the middle. Chamfered plates are connected to the C-sections on both sides to give a linear support and hinges are provided on the bottom and top side of the plate to guarantee pinned boundary conditions, see Fig.3.11 a). On several points linear variable displacement transducers (LVDT) and triaxial rosette strain gauges are placed to measure deformations and strains, see Fig.3.11 b). The locations of the linear variable displacement transducers are shown basically in Fig.3.12. Additionally to the machine way of the hydraulic jack, the movements on top of the stiff girder are measured in order to receive the clean deformation without the distortion of the portal frame. The deformation on the bottom is also measured in case of possible settling of the base.

Forces, displacements and strains are recorded during the whole test procedure. Additionally at certain load increments of 50 kN the test is stopped and the out-of-plane deformations are measured with photogrammetric methods as also used for the initial geometric imperfections, see Sec.3.2.2.3.

3.2.4 Test procedure

The test specimens are preloaded with approximately 15 % of the estimated ultimate load before the beginning of the "real" loading phase. The loading is applied load-controlled until the ultimate resistance is reached and displacement-controlled afterwards. The used displacement-rate is chosen to 0.005 mm/sec in order to have static loading conditions. Every 50 kN the loading is stopped and the out-of-plane deformations are measured. After reaching the ultimate load the displacement rate is raised to

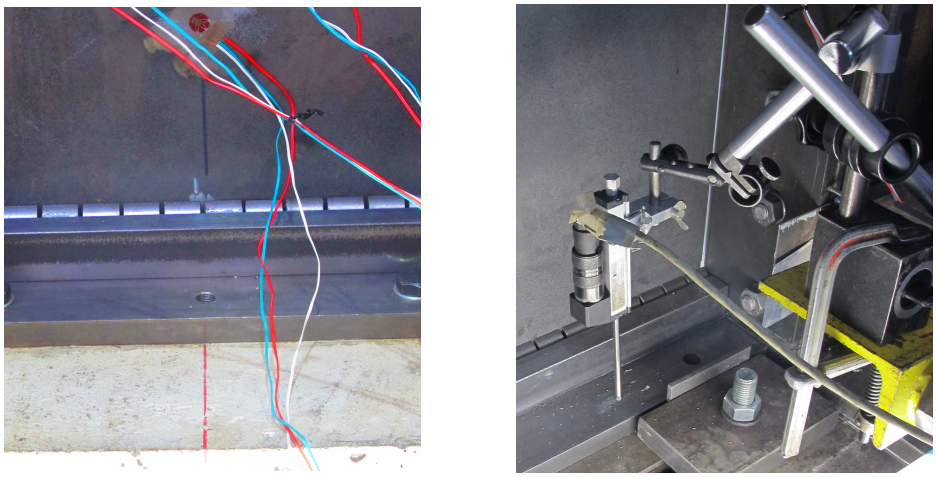

(a) (b)

Figure 3.11: Test setup – a) Hinges to allow for edge rotation b) Placement of a linear variable displacement transducer (LVDT).

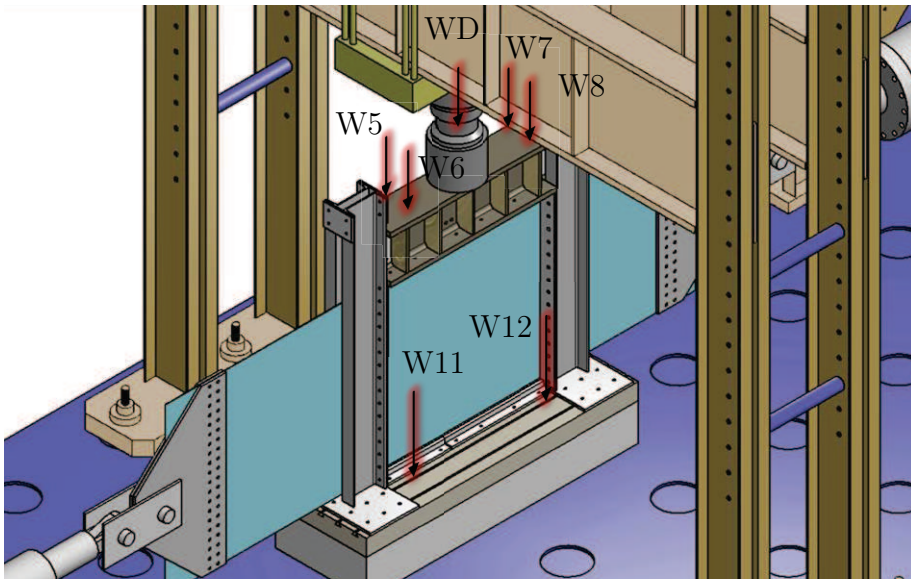

Figure 3.12: Location of linear variable displacement transducers (LVDT).

0.01 mm/sec and the out-of-plane measurements took place every 0.5 – 1.0 mm.

As it was technically not possible to couple the hydraulic jacks to each other in order to apply the tensile force while introducing the compression force, the procedure was chosen as follows: first the tension increment was applied and secondly the respective compression increment. This allowed for an almost proportional load application with a constant σ_z/σ_x–ratio.

3.2.5 Test results

The out-of-plane deformations of the plates at ultimate load are presented in Fig.3.13 – Fig.3.18 together with the respective load-displacement curves. The continuous curve denotes the compression force, while the dashed curve is the simultaneously applied tensile force. It is obvious how for the uni-axially loaded plates a one half-wave failure mode develops and the multiaxially loaded plates failure modes are observed with two and three half-waves. Especially for the test series "D" the effect is clearly visible, where at uni-axial loading (D1) one half-wave develops, with $\beta = -0.5$ (D2) two half-waves and with $\beta = -1$ (D3) three half-waves, so that the influence of the tensile forces for the failure mode is evident and mode transitions can be depicted clearly.

The influence of the tension stresses on the buckling behaviour can be seen not only on the failure mode but also on the load-displacement curves. For test series "C" though the ultimate compression load is similar with and without tensile forces, a much more unfavourable behaviour with a sharp drop is observed without tension (C1), while for the other tests (C2 and C3) of the series the curve is smoother with increasing tension and more gentle characteristic is obtained. The comparatively high capacity of C1 can also be explained by the very small geometric imperfection in this test. The curves of the compression force from test series "C" are summarised and compared in Fig.3.19 a).

In case of test series "D" a distinct increase of the ultimate load is observed, when tensile stresses act at the same time. The curves are summarised in Fig.3.19 b) and highlight this effect. Furthermore especially the curve of test D3 shows a noticable bend at approximately 700 kN where the mode transition from one half-wave to the three half-wave shape occurred.

3.2.6 Summary

Six tests on isolated steel plates have been conducted and presented giving an insight into the buckling behaviour of multiaxially loaded panels. While for the uni-axially loaded reference tests one half-wave failure modes were observed, mode transitions occurred when additional tensile stresses were applied in transverse direction. This fits well with the behaviour for linear elastic buckling analyses (LBA), where tensile stresses also lead to multi-wave buckling shapes, see Sec.2.2.2.

In Fig.3.20 the test results are related to the yield strength by means of a **L**oad

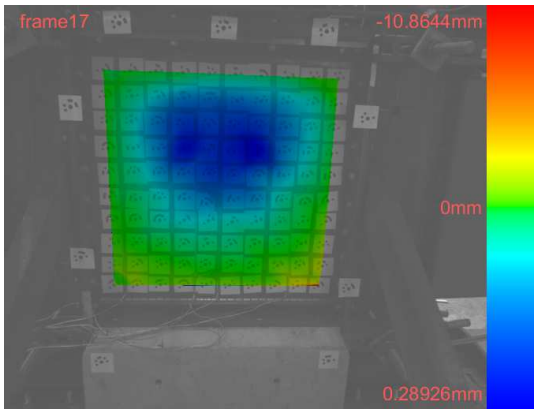

(a)

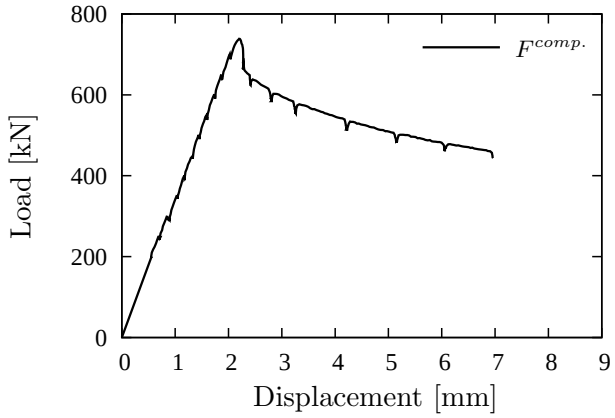

(b)

Figure 3.13: Panel C1: (a) Out-of-plane measurements, (b) Load-displacement diagram.

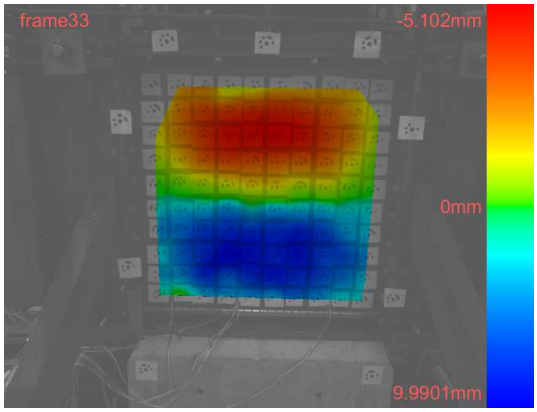

(a)

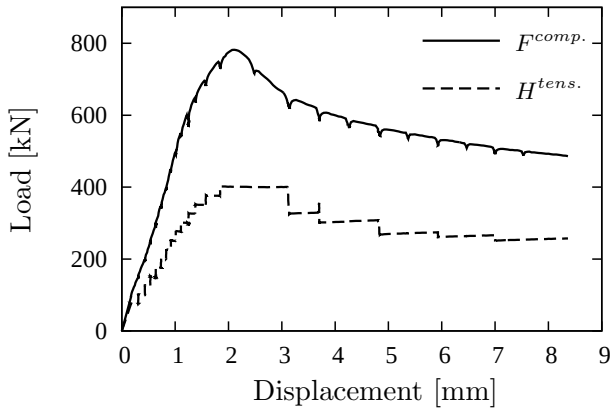

(b)

Figure 3.14: Panel C2: (a) Out-of-plane measurements, (b) Load-displacement diagram.

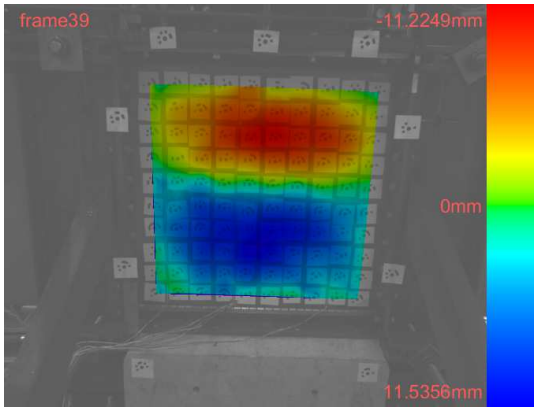

(a)

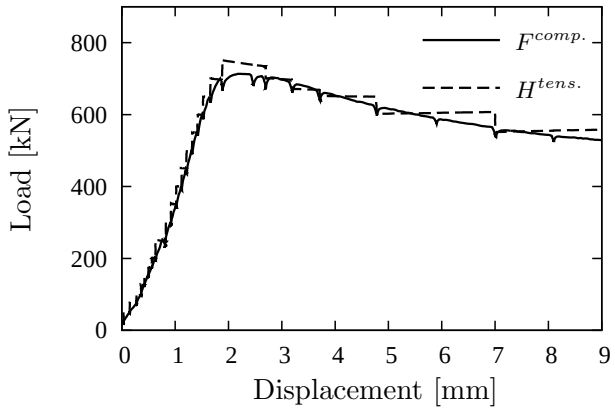

(b)

Figure 3.15: Panel C3: (a) Out-of-plane measurements, (b) Load-displacement diagram.

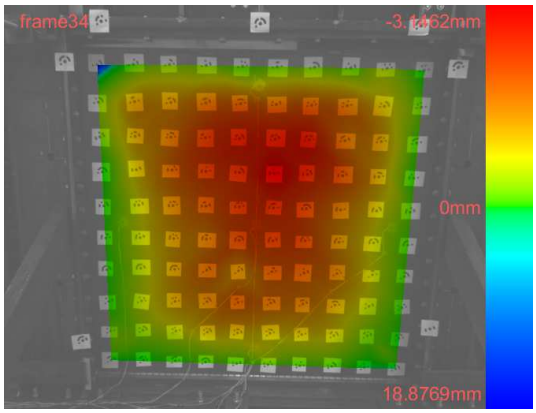

(a)

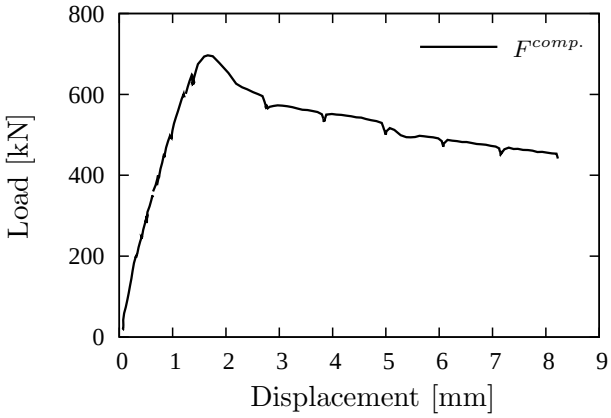

(b)

Figure 3.16: Panel D1: (a) Out-of-plane measurements, (b) Load-displacement diagram.

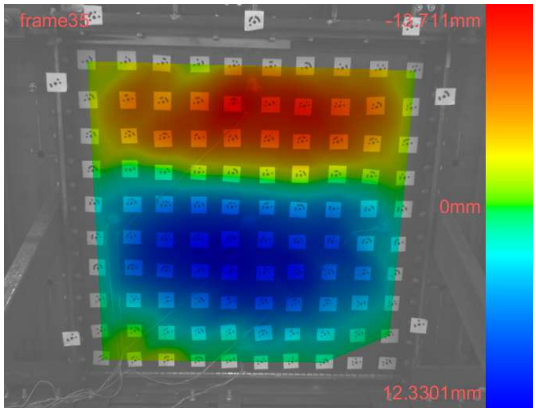

(a)

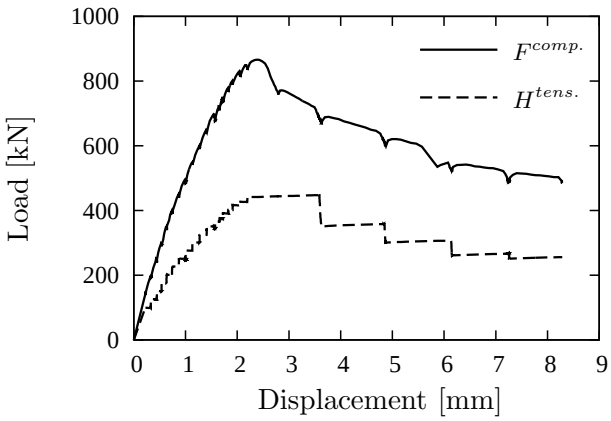

(b)

Figure 3.17: Panel D2: (a) Out-of-plane measurements, (b) Load-displacement diagram.

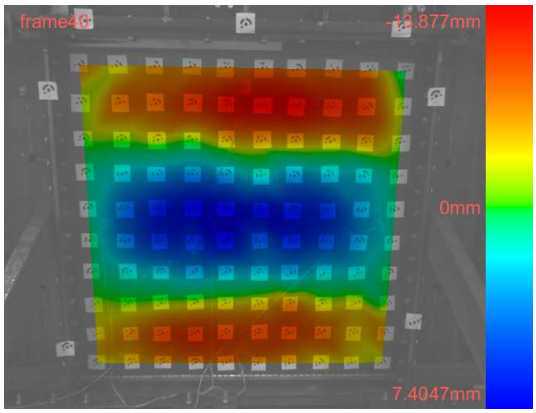

(a)

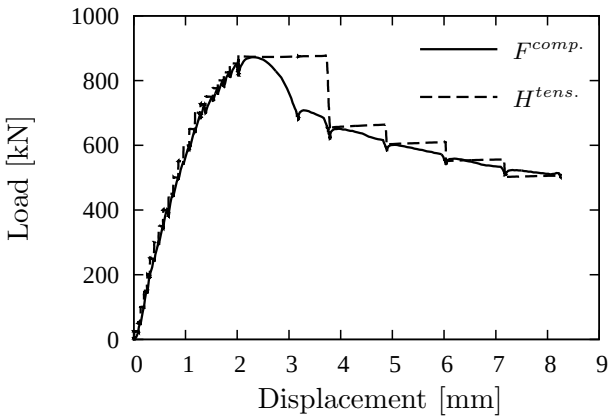

(b)

Figure 3.18: Panel D3: (a) Out-of-plane measurements, (b) Load-displacement diagram.

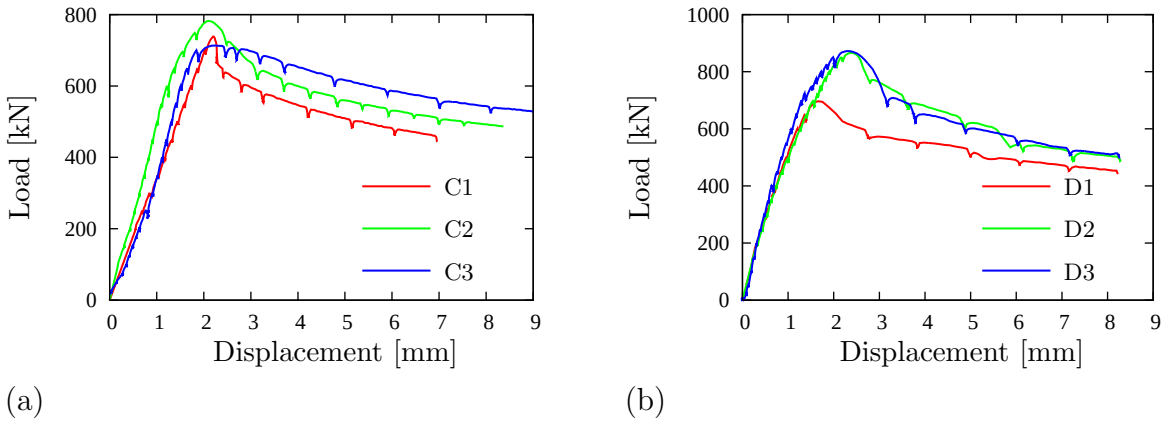

Figure 3.19: Compression load-displacement curves (a) C1–C3 (b) D1–D3.

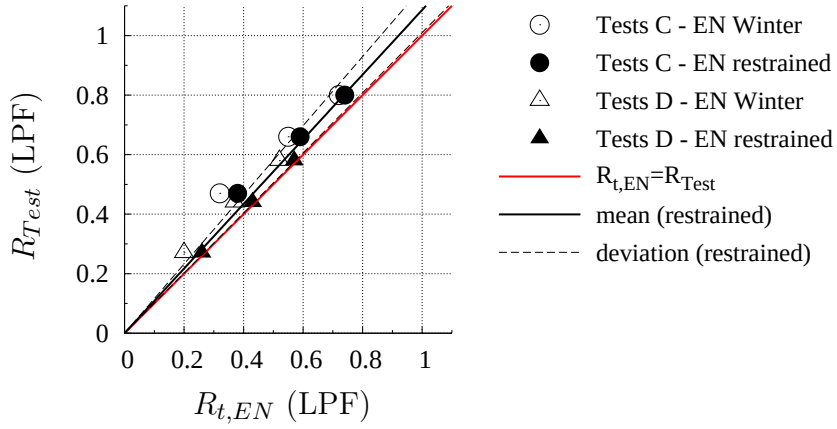

Figure 3.20: Comparison of tests and design according to EN 1993-1-5 [36] using the Winter-curve and the buckling curve according to Fig.4.22 for restrained edges.

Proportionality **F**actor (LPF $= \sigma_v / f_y$) and compared to the resistance according to the current rules of Chapter 10, EN 1993-1-5 [36]. In addition to the determination of the resistance using the Winter curve, anticipating the numerical investigations conducted in Sec.4, also a further buckling curve is adopted here, which is gained with a simplified numerical model using boundary conditions where the edges remain straight in-plane, see Sec.4.6.4.2, since this model represents the test situation in a more suitable way as the Winter-curve assumes the unloaded edges to move free in-plane.

It can be seen that the current rules match quite well to the test results, especially when using the buckling curve which considers straight edge boundary conditions, so that at this point it seems reasonable to take into account tensile stresses in the design of multiaxially loaded plates. However, the test basis is very limited, so that further numerical investigations are conducted in order to consider a wider parametric range.

3.3 Tests on longitudinally stiffened plates

3.3.1 Overview

In the frame of a research project on the load bearing behaviour of longitudinally stiffened steel plates, within the field of bending-shear interaction, tests were conducted on six welded girders, see [64], [63], [108], [128]. The tests served for the validation of a numerical model in order to conduct a wide parametric study leading to an enhancement of the M-V interaction formula given in EN 1993-1-5 [36] for the design according to the effective width method. However, the tests are presented here to show the influence of multiaxial stress states on the buckling behaviour of slender plates, especially since the girders are highly subjected to bending-shear interaction.

The main outcomes of the experimental investigations are presented in this section in a short and compact way. For further details and information reference is made to [64].

3.3.2 Test specimens

3.3.2.1 Dimensions

To avoid size effects, the girders have been realised in dimensions which are also used in practical situations such as for bridge constructions. The tests focused specifically on the field of interaction between bending moment and shear. The general shape of the girder and the stiffener section are shown in Fig.3.21.

The main dimensions of the cross-section, which remained the same for all tested girders, are shown in Tab.3.4, while the varied parameters are given in Tab.3.5. All tested girders were stiffened longitudinally with a closed trapezoidal stiffener and the global height-to-length ratio of the stiffened panel is $\alpha = 1.0$ for all of them, see Fig.3.22 exemplarily for girder A1.

Table 3.4: Main dimensions of the tested girders.

h_w (mm)	a (mm)	b_f (mm)	H_{st} (mm)
1500	1500	300	200

In Sec.A of the Annex the dimensions of all tested girders are gathered. Due to the limited maximum load of the hydraulic jack being 2000 kN, the test setup was realised as a cantilever system with an unsymmetric girder, which can be seen from the figures in the Annex A.

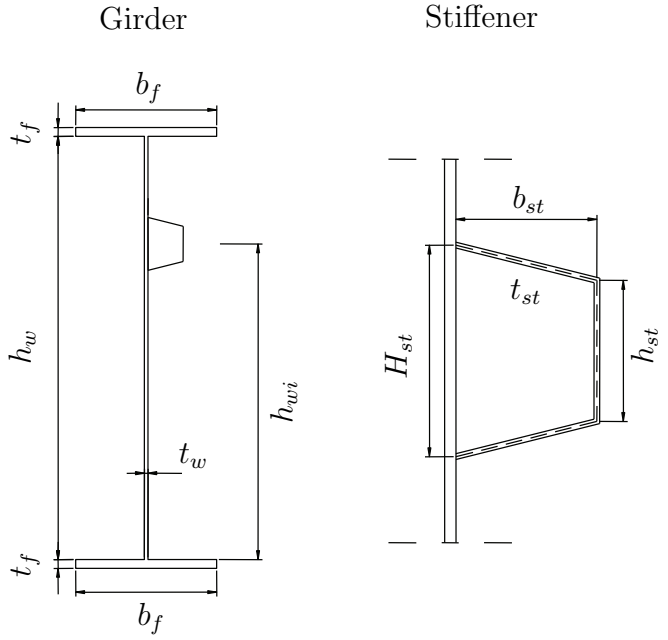

Figure 3.21: Cross-section of the tested girders.

Table 3.5: Varied parameters of the tested girders.

Girder	t_f (mm)	t_w (mm)	h_{st} (mm)	b_{st} (mm)	t_{st} (mm)	h_{wi} (mm)
A1	25	8	120	100	6	750
B1	25	6	100	84	4	750
A2	20	8	100	100	5	375
B2	20	6	85	80	4	375
A3	20	6	110	63	4	375
B3	20	6	110	70	3	375

The transversal stiffeners were 20 mm thick plates on both sides of the web where the load was applied and also at the support points. All other transversal stiffeners were one-sided and 15 mm thick. The girder was dimensioned in a way that the decisive panel was the one next to the vertical mid support at the cantilever.

3.3.2.2 Material properties

For the longitudinal stiffeners of the same thickness the plates were taken from the same melt. The same was done also for the flanges. For the web it was not possible to use steel from the same melt, due to their sizes, so for the 6 mm webs the material was used from two different melts. For all different plates tensile coupon tests were taken to determine the material properties.

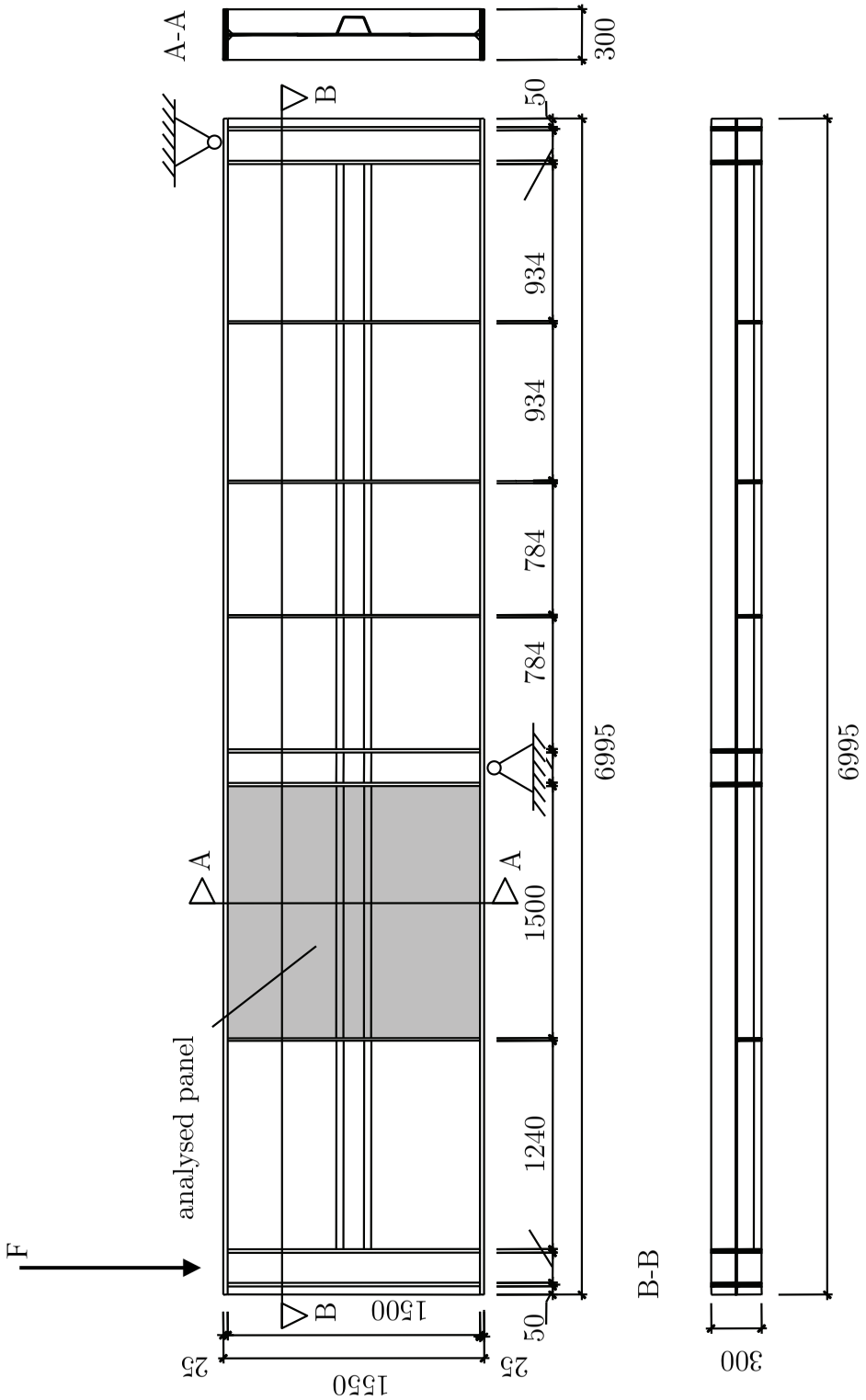

Figure 3.22: Test girder A1.

The results from the tensile coupon tests are summarised in Tab.3.6. The material for the transverse stiffeners was not tested and for numerical simulations it was assumed as bilinear with a nominal yield strength of $355\,\mathrm{N/mm^2}$.

Table 3.6: Results of tensile coupon tests.

Cross-sectional element	Girder	Yield strength $f_y\,[\mathrm{N/mm^2}]$	Ultimate strength $f_u\,[\mathrm{N/mm^2}]$	Elastic modulus $E\,[\mathrm{N/mm^2}]$
Flange	A1, B1	328	488	196 542
	A2, A3, B2, B3	332	499	198 537
Web	A1	255	361	195 771
	A2	249	362	196 324
	A3, B1	275	364	198 000
	B2, B3	308	395	197 749
Long. stiffener	A1	276	396	186 514
	A2	233	352	197 447
	A3, B1, B2	288	393	199 340
	B3	246	360	197 052

3.3.2.3 Geometric imperfections

The initial imperfections of the tested panels were measured using photogrammetric method. The measured shapes and amplitudes are plotted in Fig.3.23 to Fig.3.28. The shapes of the web panels stiffened with a longitudinal stiffener at the mid web depth are shown in Fig.3.23 (girder A1) and Fig.3.24 (girder B1). The web plate is deformed in two waves orientated in the same direction. Along the edges and the longitudinal stiffener the web plate is almost straight. The amplitudes are higher in case of the slender web plate. The amplitudes of the stiffener and the subpanel imperfections are always smaller than the allowable tolerances according to EN 1090 - 2 [33], where the maximum amplitude for the subpanel imperfection is limited to $h_{wi}/100$ and for the longitudinal stiffener to $a/400$, where h_{wi} denotes the subpanel height and a is the panel length.

The imperfection shapes of the panels stiffened with a longitudinal stiffener in the compression zone are shown in Fig.3.25 to Fig.3.28. The initial shape is defined with one wave in the larger subpanel. In the smaller subpanel a significant imperfection might be found only for girders A2 and B3. As in the previous cases A1 and B1 the amplitudes of the slender web plates with $t_w = 6\,\mathrm{mm}$ are much higher than those with $t_w = 8\,\mathrm{mm}$. The geometric imperfections result from the cooling phase after the girder is assembled

by welding. In case of stocky plates the plates are stiffer. Consequently, higher residual stresses might be obtained for stocky plates than for slender plates where the residual stresses are released with the transformation of the initial geometry of the plates.

Furthermore, residual stresses, which are mainly caused by the welding process, might have an influence on the behaviour and the resistance of plated girders. However, for quite similar studies Sinur [106] showed that for the regarded cases the influence of residual stresses in slender plate girders is rather small and can therefore be neglected in the numerical model.

3.3.3 Test setup

The girder tests were performed using the setup shown in Fig.3.29. The setup consisted of two large portal frames, a supporting structure and lateral supports. One of the portal frames included the hydraulic jack, with a capacity of 2000 kN. The stamp of the hydraulic jack received a calotte in order to apply the load always in vertical direction and without any restraining forces. The second portal frame was necessary, because it was intended to have a cantilever situation. The lifting force was then carried by the second portal frame. The large force coming from the middle support required a special support construction, which also allowed certain flexibility in the position of the support point being in fact different for each test girder.

Below the load application point of the girder and at each vertical support lateral brackets were provided in order to avoid lateral torsional failure mode. Teflon layers were used to reduce friction forces. The buckling support below the load application point is exemplarily shown in Fig.3.30.

Vertical transducers were applied at the bottom side of the lower flange at both ends of the girder (W1 and W7) as well as at the end of the tested panel (W2). At the middle support the transducer was applied on the support (W6). These transducers allowed the calculation of the deflection of the girders excluding the deformation of the portal frames and middle support. Due to some deformations of the portal frames and of the middle support the measured vertical deformations had been corrected according to Eq.(3.9) in order to receive the real vertical displacement w_1^{corr}:

$$w_1^{corr} = w_1^{meas} - \left(\frac{w_6 + w_7}{l_2}\right) \cdot (l_1 + l_2) + w_7 \tag{3.9}$$

where the variables are defined according to Fig.3.31 using for l_1 and l_2 the values given in Tab.3.7.

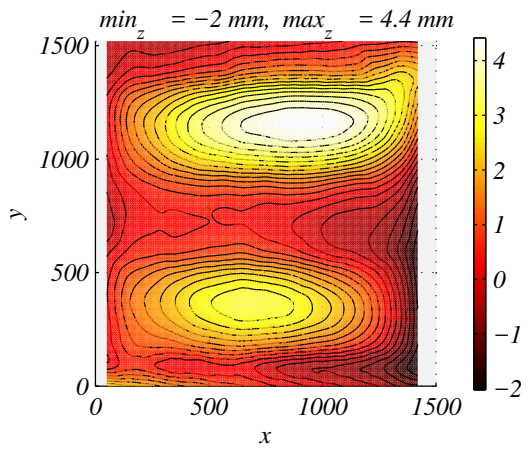

Figure 3.23: Initial imperfections - A1.

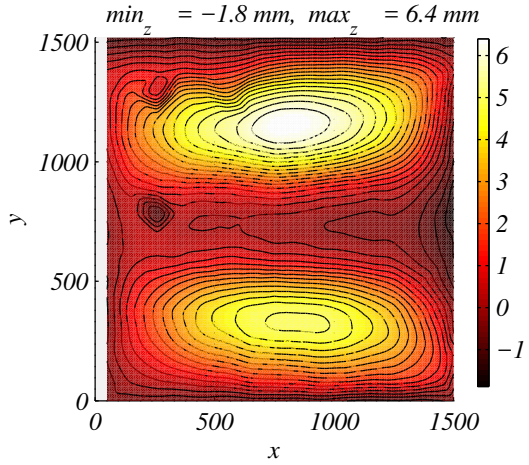

Figure 3.24: Initial imperfections - B1.

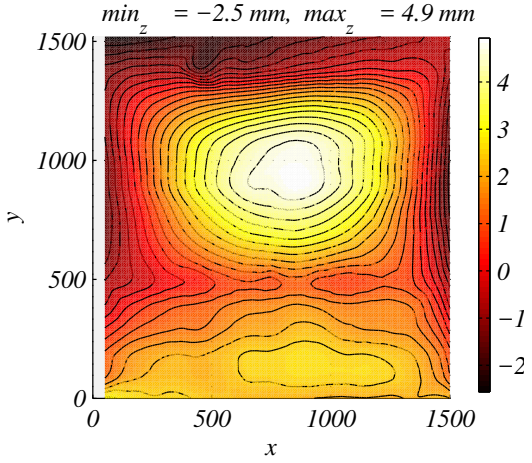

Figure 3.25: Initial imperfections - A2.

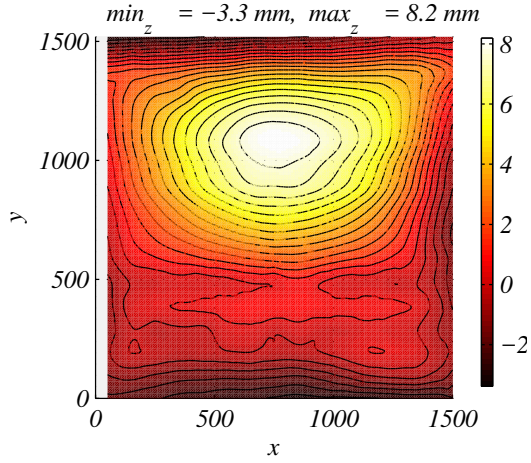

Figure 3.26: Initial imperfections - B2.

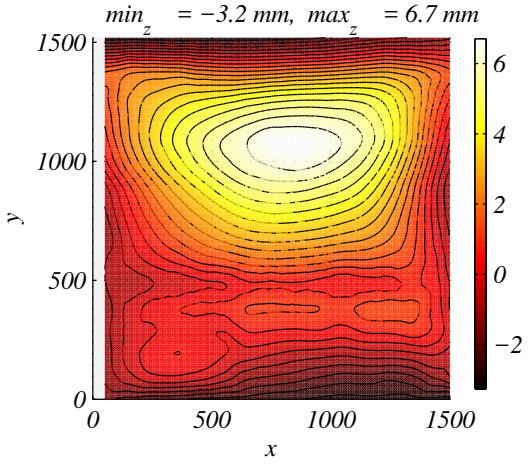

Figure 3.27: Initial imperfections - A3.

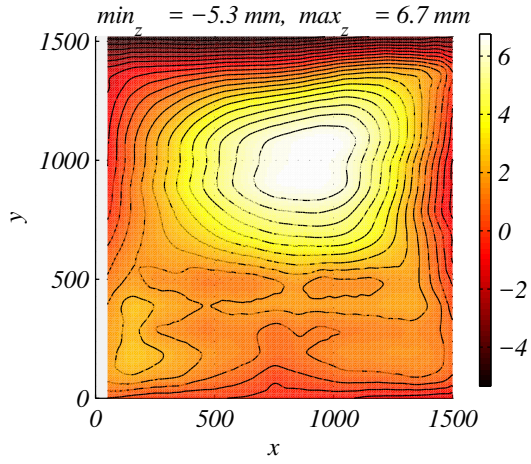

Figure 3.28: Initial imperfections - B3.

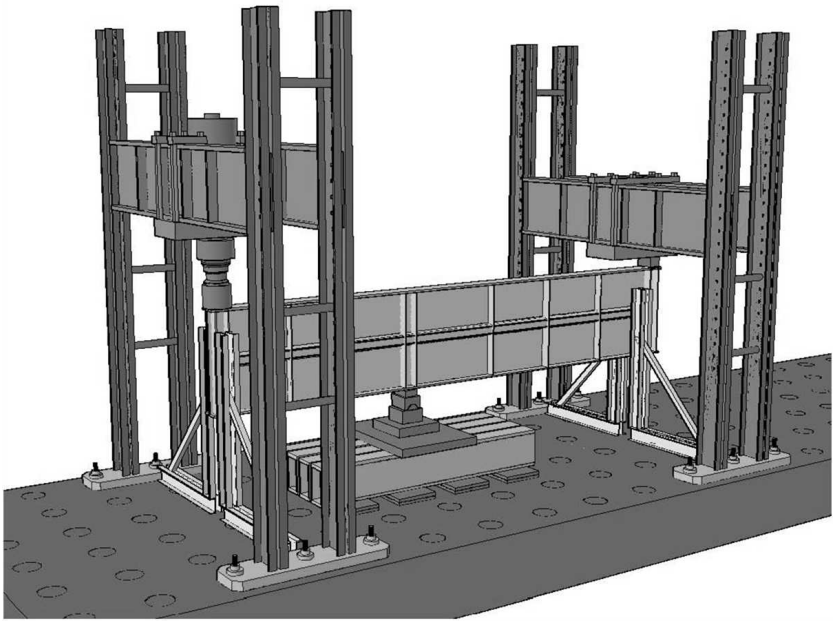

Figure 3.29: Test setup.

Figure 3.30: Buckling supports.

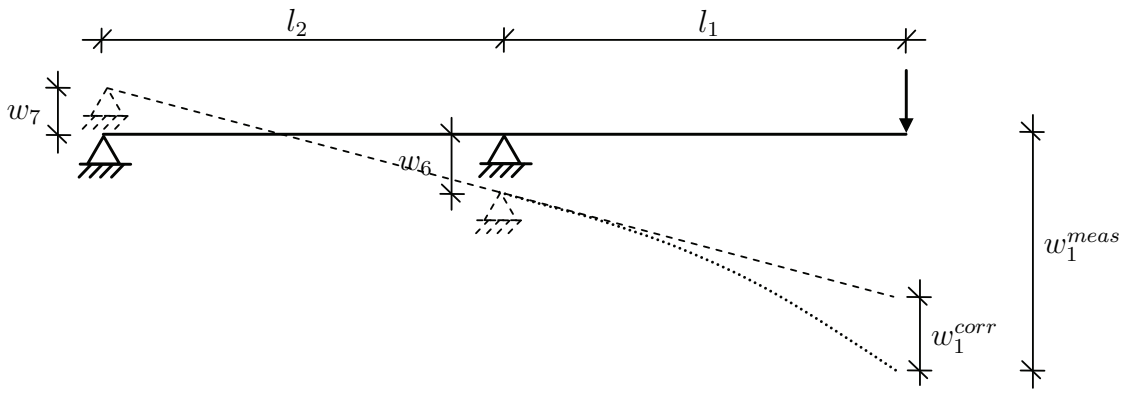

Figure 3.31: Correction of the measured vertical displacements.

Table 3.7: Global dimensions of the tested girders for the calculation of the corrected vertical deformations.

Girder	l_1 (mm)	l_2 (mm)
A1	2975	3700
A2	3510	3610
A3	5133	2605
B1	4315	3205
B2	5203	3205
B3	5100	2605

3.3.4 Test procedure

Before loading the girders to reach the maximum loads, the initial imperfections have been measured and a test load of approximately 15 % of the expected maximum load was applied. After the test load was removed the initial imperfection was measured again. The load was applied displacement controlled with a constant velocity of 0.5 mm/sec.

In specific intervals the loading was stopped for measuring the horizontal deformations. The intervals for the photogrammetric method were shorter, since the measurement took much less time than the measuring fork, which was used in longer intervals and served to confirm the results gained by the photogrammetric method.

3.3.5 Test results

In the following the out-of-plane measurements as well as the load-displacement curves are shown for all tested girders. The load-displacement diagrams include also the corrected values of w_1^{meas} and w_2^{meas} - the measured values - according to Eq.(3.9), which consider the frame deformations of the test setup. These corrected values are nominated as w_1^{corr} and w_2^{corr} respectively.

For girders A1 and A2, both with $h_w/t_w = 187.5$, the deformations clearly indicates the development of local tension fields, see Fig.3.32(a) and Fig.3.33(a). Also B1 showed local buckling, especially for the lower panel which was in the compression zone where the main failure for this girder occurred and the flange buckled into the web, see Fig.3.35(a). Although the γ/γ^*-ratio was smaller than for the other girders, no buckling failure of the longitudinal stiffeners of girders A1 and B1 happened.

Girder A2 and B2 also showed local buckling of the panels, see Fig.3.33(a) and Fig.3.36(a). While for girder A2 the tension field caused by shear was very pronounced and the local buckling in the lower compression panel only moderate, girder B2 showed a very pronounced compression buckling of the lower panel also with a failure of the longitudinal stiffener near to the transverse stiffener, causing failure in the upper panel due to compression. Girder A2 had $h_w/t_w = 187.5$ and girder B2 had $h_w/t_w = 250$.

For girders A3 and B3 global buckling was observed, see Fig.3.34(a) and Fig.3.37(a). In both cases the longitudinal stiffener failed and caused this buckling mode. Especially for girder B3, which had a class 4 longitudinal stiffener, the stiffener failure was very distinctive, while for girder A3 a slight tension field in the larger subpanel could be observed.

In the following figures Fig.3.32 – Fig.3.37 the local buckling of the flange can also be noticed, which mainly occurred after the maximum capacity had been reached. Local flange buckling can clearly be observed for girders B1, B2, B3 and A2. Nevertheless, flange buckling was also observed as a secondary failure for girders A1 and A3.

The maximum resistance and the failure mode of the conducted experimental investigations are summarised in Tab.3.8. For further details and information reference is made to [64].

Table 3.8: Summarised test results.

Girder	V_{max} (kN)	Failure mode
A1	1678	local buckling of the lower subpanel
A2	1431	local buckling of the upper subpanel
A3	940	global buckling of the stiffened panel
B1	1148	local buckling of the lower subpanel
B2	931	local buckling of the upper subpanel and buckling of the longitudinal stiffener
B3	926	global buckling of the stiffened panel

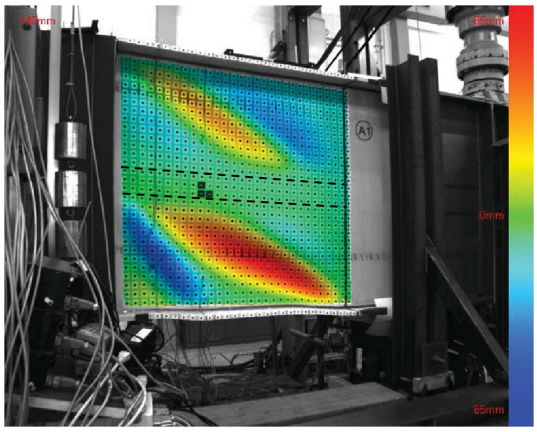

(a)

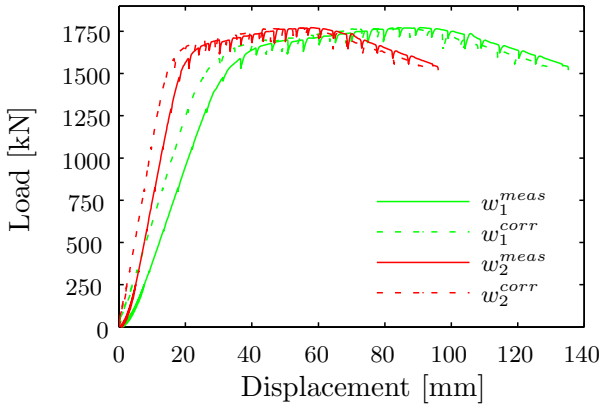

(b)

Figure 3.32: Girder A1: (a) Out-of-plane measurements, (b) Load-displacement diagram.

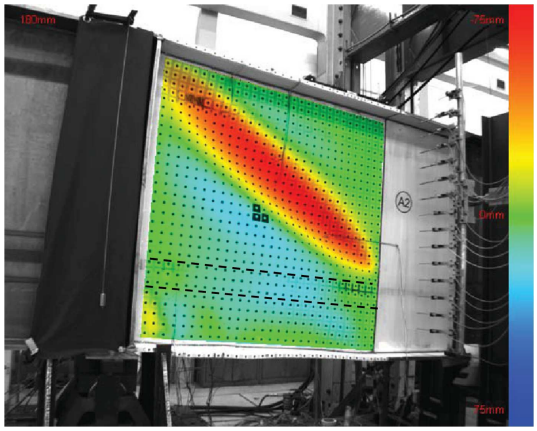

(a)

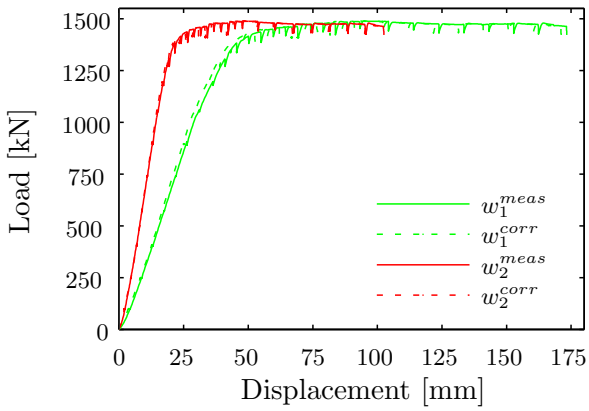

(b)

Figure 3.33: Girder A2: (a) Out-of-plane measurements, (b) Load-displacement diagram.

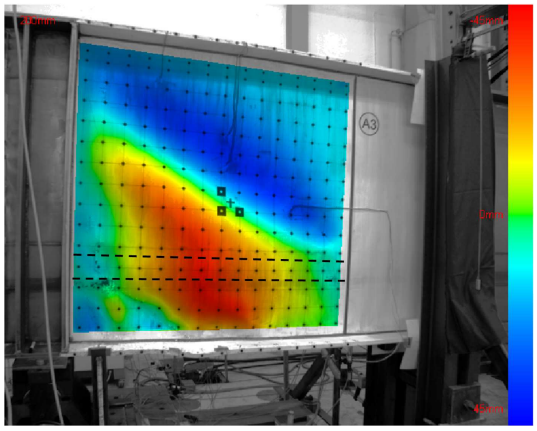

(a)

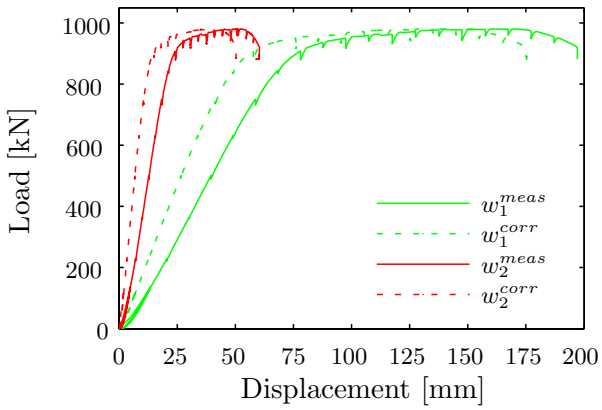

(b)

Figure 3.34: Girder A3: (a) Out-of-plane measurements, (b) Load-displacement diagram.

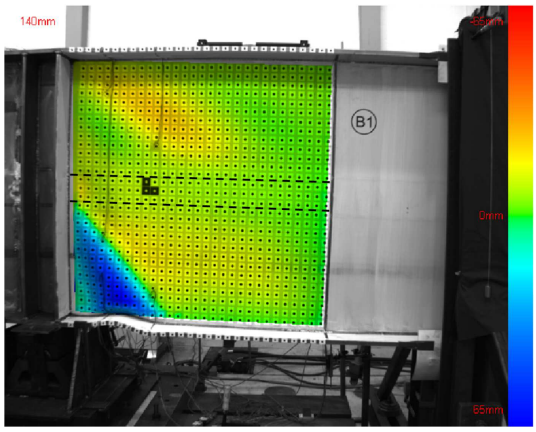

(a)

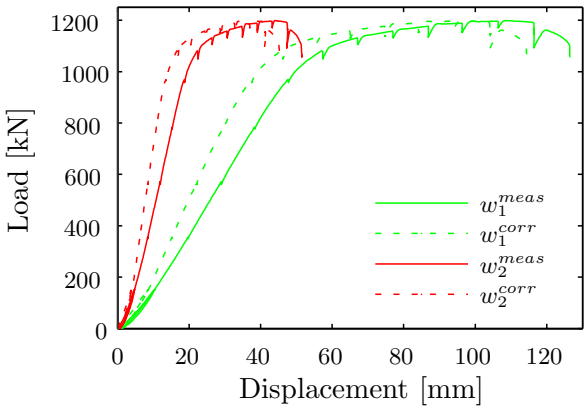

(b)

Figure 3.35: Girder B1: (a) Out-of-plane measurements, (b) Load-displacement diagram.

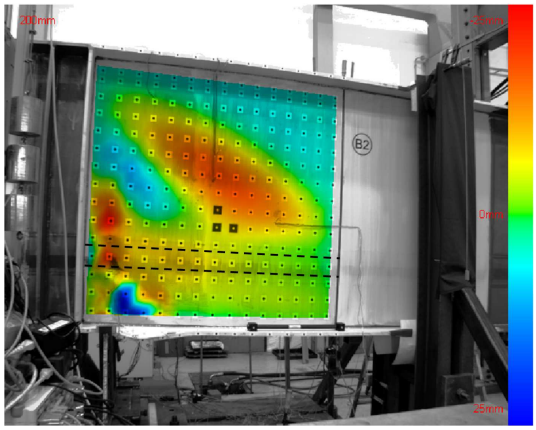

(a)

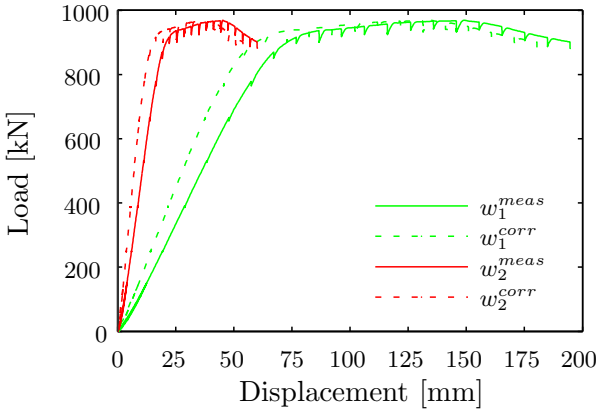

(b)

Figure 3.36: Girder B2: (a) Out-of-plane measurements, (b) Load-displacement diagram.

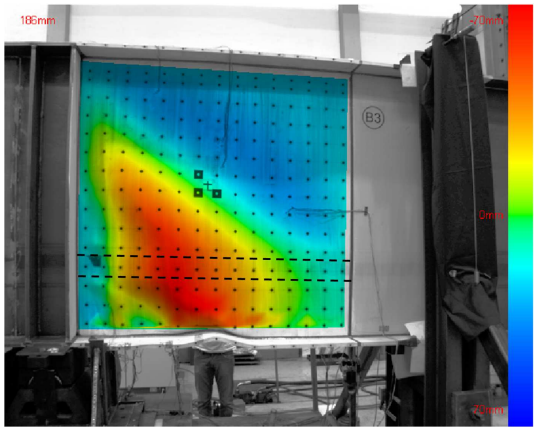

(a)

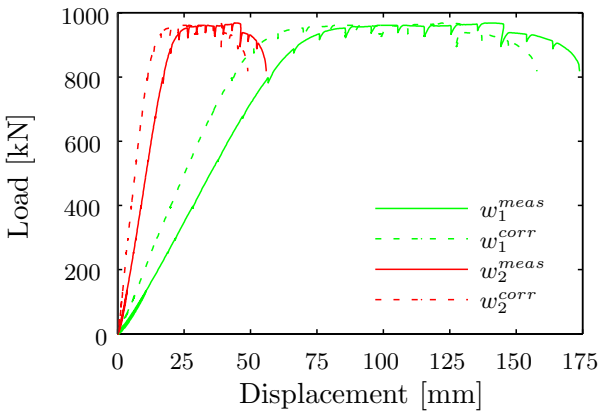

(b)

Figure 3.37: Girder B3: (a) Out-of-plane measurements, (b) Load-displacement diagram.

3.3.6 Summary

Six full scale plate girders stiffened with transverse and longitudinal stiffeners were tested for interaction of high bending moment and shear force. For the girders stiffened in the compression zone (A2, A3, B2 and B3) the first buckling appeared in the largest subpanel, which was subjected to bending with a stress ratio of $\psi = \sigma_{compression}/\sigma_{tension} \approx -0.5$ and shear. By increasing the applied displacement the direct stresses in the stiffener caused flexural buckling of the stiffener and consequently global shear buckling appeared over the whole web.

Pure local buckling was obtained for the girders stiffened at the mid-web depth (A1 and B1). In these cases the stiffener was not subjected to normal forces and the stiffness of the stiffener was sufficiently high to prevent global buckling due to shear stresses. The interaction of bending and shear force can be seen from the inclination of the tension field. For high compressive stresses the inclination of the tension field is increased. After the maximum capacity had been obtained, local buckling of the flange was always observed as a secondary failure. For these cases the subpanels were subjected to bending with a stress ratio of $\psi = \sigma_{compression}/\sigma_{tension} \approx 0$ and shear, where the upper subpanel is subjected to pure tension, while the lower one is under pure compression.

Here the positive effect of tension stresses on the buckling behaviour of slender plates can clearly be seen, as the panel subjected to compression and shear was obviously the decisive one and the panel subjected to tension and shear showed only very slight out-of-plane deformations due to shear.

4 Numerical investigations

4.1 General

The rapid development of data processing during the last decades opened the door to a lot of new possibilities for many engineering applications. While in former days the study of physical effects needed experimental investigations, nowadays it is possible to run numerical simulations allowing to analyse the effect of certain parameters, while otherwise many tests would be required boosting the costs. Furthermore, numerical simulations may be used in preliminary phases of a product development in order to reduce the needed iterations. However, numerical models can be very sensitive to certain assumptions such as e.g. boundary conditions, loadings or imperfections so that they should still be verified by appropriate experimental investigations. In the frame of this work numerical analyses have been conducted using the so-called **F**inite **E**lement **M**ethod (FEM). In the following a conceptional overview on the method is given, for further information appropriate literature is recommended such as e.g. [3], [109], [126] and [127].

The universal formulation of the FEM allows for the use in a wide field of applications such as e.g. structural analysis, heat transfer or even magnetic fields. Simulations according to the FEM consist in generally of three main parts: pre-processor, solver and post-processor.

During the pre-processing phase the real structural element is modelled and idealised using finite elements with specific material properties. Boundary conditions as well as loads $\mathbf{F}$ are afterwards applied to the model. In the solver phase the element stiffness matrix ${}^{e}\mathbf{K}$ is generated for each single finite element and superposed additively to a global stiffness matrix $\mathbf{K}_g$. This matrix represents the coefficient matrix for solving the system of equations of the sought deformations $\mathbf{u}$, see Eq.(4.1).

$$\mathbf{K}_g\mathbf{u} = \mathbf{F} \tag{4.1}$$

Based on the deformations it is possible to determine stresses and reaction forces in the regarded system. Since the results are principally just a huge amount of data and numbers it is necessary to post-process this data in order to graphically visualise them to have an overview on the deformation behaviour as well as on the stresses.

A general-purpose software that comprises the complete mentioned steps is ABAQUS [104], which is used in the release 6.11 for the present work for conducting the numerical investigations.

Table 4.1: Overview on selected assumptions for FE-methods.

Theory	Material behaviour	Geometric behaviour	Imperfections	Example of use
LA	linear	linear	no	elastic resistance
LBA	linear	linear	no	critical plate buckling load
GMNIA	non linear	non linear	yes	elastic-plastic resistance in ULS

4.2 Analyses and assumptions

In Annex C, EN 1993-1-5 [36] a guidance on the use of the FEM is given, which is followed also in the present work and commented where required. Generally, the mentioned annex gives several assumptions for conducting numerical analyses. The relevant assumptions for the numerical investigations in the frame of this work are listed in Tab.4.1. The linear analysis (LA) is only used to check if the model generally works correctly (boundary conditions and loading) as also recommended by Timmers [110].

The elastic buckling of flat plates especially for multiaxially loaded plates is treated in Sec.2.1. While for unstiffened plates subjected to multiaxial loading it is possible to use analytic formulations for determining the critical load, this is not the case for stiffened plates. Therefore, linear buckling analyses (LBA) need to be conducted to solve the classical eigenvalue problem. For this purpose the software EBPlate [16] is used within the present work. Of course, also ABAQUS allows for conducting linear buckling analyses, however, since in the carried out parametric studies, for reasons of practicality, the imperfections are applied using analytical sine-functions, there is no need for exporting the geometry of the eigenmodes, so that the specifically for LBA developed EBPlate has been utilised.

For determining the elastic-plastic resistance so-called geometric and materially non-linear analyses with imperfections (GMNIA) have been conducted, which represent the most sophisticated way of modelling and comes the closest to the real behaviour of slender plates. Due to the non-linearities in geometry, which arise from the large deformation when buckling occurs and the need to recalculate the equilibrium in each step at the deformed shape, the solution of Eq.(4.1) requires an incremental and iterative solution strategy.

A common strategy, which is implemented in ABAQUS, is the Newton-Raphson method, where the correct solution is approximated by linear steps. The tangent stiffness is therefore used for the "direction" of the increment, where based on the imbalance between the applied loads and the evaluated loads equilibrium several iterations are conducted until the imbalance reaches a defined threshold value. For the full Newton-Raphson method, which is used for large deformations, the tangent stiffness is determined for each iteration.

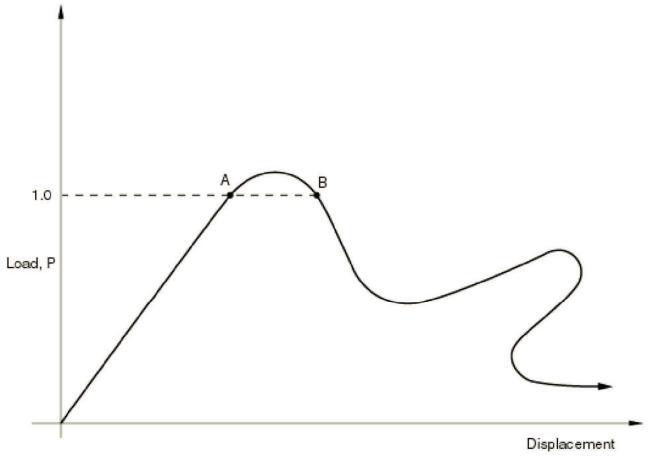

Figure 4.1: Proportional loading with unstable response [104].

In general, the analysis can either be controlled by displacements or by loads. A displacement-controlled analysis allows to follow the descending path of the load-displacement curve, while per se in a load-controlled analysis the tangent stiffness becomes zero when the maximum load is reached, so that regular full Newton-Rhapson methods fail to converge. However, since for the investigated parameter studies it is necessary to have constant load ratios (e.g. σ_z/σ_x) a displacement-controlled approach would lead to permanent variations of the stress-ratios, so that a load-controlled approach is required. A way to overcome this issue is the so-called arc-length method solution strategy. In contrast to the Newton-Raphson method, it allows to follow the descending path of the load-displacement curve using proportional loading and thus keeping the stress-ratios always constant.

The modified Riks method [89] is one of the several proposed arc-length methods and implemented in ABAQUS for the increments, whereas the Newton-Raphson method is still used for the iterations. The method is able to provide solutions even in cases of complex, unstable response such as shown in Fig.4.1.

According to [104] the loads are applied always proportional in each step, where a defined reference load P_{ref} is amplified by a load proportionality factor λ resulting in the current load magnitude P_{total} and including also a dead load P_0 if necessary for the case of a previous history, see Eq.(4.2). However, dead loads do not occur in the conducted investigations, so that the current load is directly defined by the reference load and the load proportionality factor.

$$P_{total} = \cancelto{0}{P_0} + \lambda \left(P_{ref} - \cancelto{0}{P_0} \right) = \lambda \cdot P_{ref} \tag{4.2}$$

To avoid missunderstandings in the following sections the load proportionality factor is denoted as "LPF".

4.3 Numerical modelling (GMNIA)

4.3.1 Geometry and Imperfections

When numerically calculating the ultimate load of a plate subjected to buckling with a geometrically and materially non-linear analysis and imperfections included (GMNIA), the application of the initial imperfections plays a decisive role. Generally two types of imperfections are distinguished: the geometrical and the structural imperfections. Some typical geometrical imperfections are for example the initial deformations, shrinkage at weldings, differences of the real geometrical values from the nominal ones and loading inaccuracies, while structural imperfections include e.g. residual stresses due to the fabrication process or inhomogeneities of the material causing a scatter of the yield strength. As it can be seen by the manifoldness of the mentioned imperfections, the realistic implementation of all of them is neither feasible nor possible, especially for the practical designer, who does not know what the imperfections will be for the built structure. Instead of considering all these effects it is common to apply idealised imperfections to a structure. These consist of initial deformations and in some cases also of residual stresses.

The application of initial deformations to a structure is usually subdivided into local and global imperfections, as for example done in Annex C, EN 1993-1-5 [36]. Local imperfections imply the application of buckles to a subpanel and the twist to the stiffeners or the flanges. This can be done by using e.g. sine-functions or the respective buckling-modes showing the desired deformation. Global imperfections are considered by the application of initial deformations over the whole structure, including also stiffeners if present. The initial deformations may be described by the imperfection shape and amplitude. In the frame of this work unstiffened as well as stiffened plates are investigated, so that the initial deformations applied to the model are both local and global imperfections. The definition of the applied imperfection shape and amplitude is of utmost importance, since it influences the buckling behaviour decisively. Schmidt [98] and Winterstetter [123] therefore classify the initial deformations referring to shell buckling. In [92] it is noted that this classification may be applied also for plate buckling analyses. The classification is summarised in the following:

- **Realistic imperfections:** Shape and amplitude should correspond as much as possible to the real imperfections of the structure. Since these imperfections inevitably depend from the fabrication process and the assembly operation, these realistic initial deformations are unknown when performing the structural design.
- **Worst case imperfections:** The imperfection shape that leads together with a given amplitude to the lowest resistance. Usually an imperfection shape affine to the first buckling mode is used. Brune [13] shows cases where the utilisation of this assumption does not lead to the lowest resistance. Nevertheless, the assumption of the eigenmode-affine imperfections usually lead to higher reductions

than the usage of realistic or stimulating imperfections. Another imperfection type which can be categorised to the worst case imperfections are the collapse-affine imperfections. Here the imperfection shape corresponds to the deformed shape at collapse. The procedure for this imperfection type is very laborious, since a nonlinear buckling analysis has to be performed previously itself.

- **Stimulating imperfections:** The applied initial deformations should allow to cover the real behaviour of the structure with the numerical model in principle. Stimulating imperfections can be for instance eigenmode-affine or fabrication-oriented imperfections.

For the recalculation of the experimental investigations, the realistic imperfections are used, since they have accurately been measured. For the numerical parametric studies, it is decided to use stimulating imperfections, see discussion in Sec.4.6.4.

4.3.2 Material

For recalculation of the tests, the material properties are taken from the tensile coupon tests and modified into true stress-strain curves according to Eq.(4.3).

$$\sigma_{true} = \sigma\,(1+\varepsilon) \tag{4.3a}$$

$$\varepsilon_{true} = \ln\,(1+\varepsilon) \tag{4.3b}$$

When the stress-strain curve is not known, assumptions must be made. This can be done for mild structural steel by a bi-linear material model. In Annex C, EN 1993-1-5 [36] several possibilities are listed for the modelling of material behaviour. In the frame of this work, for the numerical parametric studies a bi-linear material without strain hardening is used. The investigations are conducted with nominal values for structural steel S 355 with an elastic modulus $E = 210\,000\,\mathrm{N/mm^2}$, Poisson's Ratio $\nu = 0.3$, a yield strength $f_y = 355\,\mathrm{N/mm^2}$ and a plateau slope of $E/10\,000$ to avoid numerical problems.

4.3.3 Discretisation

When using FEM, as the name implies, the structural system is idealised by finite elements, which have to be chosen according to the respective purpose. For the numerical investigations in the following the so-called "S4R" element is used, which accounts for finite membrane strains as well as for arbitrarily large rotations and is therefore suitable for large-strain analyses. The element is a 4-node element with each six degrees of freedom and reduced integration. Reduced integration usually provides more accurate results and reduces running time significantly, especially in three dimensions [104].

4.4 Recalculation of experimental investigations on multiaxially loaded plates

4.4.1 General

The numerical recalculation of the experimental investigations, which were carried out in the frame of the DASt–AiF project [68] and are shown in Sec.3.2, is presented in the following. The numerical simulations are conducted to verify the procedure for the modelling and especially to compare the behaviour in dependence on the applied tensile stresses, as clear mode changes have been observed during the experiments, see Sec.3.2.5. In the frame of this work, only the main outcomes are presented in order to keep this chapter manageable. For further details reference is made to the technical report of the research project "Beulen mehrachsig beanspruchter Platten" (DASt–AiF) [68].

4.4.2 Numerical model

The numerical model is built up following the principles described in the foregoing sections using the multi purpose code ABAQUS [104]. The material properties are derived from tension coupon tests and modified to true stress–strain values according to Eq.(4.3). The measured initial imperfections presented in Sec.3.2.2.3 are applied to the model and "S4R" elements are used as described in Sec.4.3.3.

In Fig.4.2 the numerical model is shown exemplarily for test D3. The loads are applied in reference points, which are coupled with the respective edges via equation constraint in order to apply a constant displacement as during the tests. The lateral restraints for defining the tested area are applied as boundary conditions in y–direction. The boundary conditions of the compressed edges are assumed to be hinged, as for the tests special pivot bearings have been used, see Fig.3.11 a). The boundary condition on the edges where tensile forces are introduced are modelled as clamped, as the load introduction device is connected with a two–row bolt connection.

4.4.3 Global response

The global responses are compared by the load–displacement curves obtained from the tests and the numerical simulations allowing to evaluate the maximum forces, the initial stiffness as well as the descending paths of the curves.

The results of the numerical simulations are presented and compared to the experimental results in Fig.4.4. The diagrams show the load–displacement curves for the compressed edge. Fig.4.3 and Tab.4.2 show that the numerically obtained maximum loads match with the experimental ones, while the curves from the experiments show a less stiff behaviour. However, it should be noted here that the vertical displacements are in such a small range, that deformations of the test setup also play a role. Even though

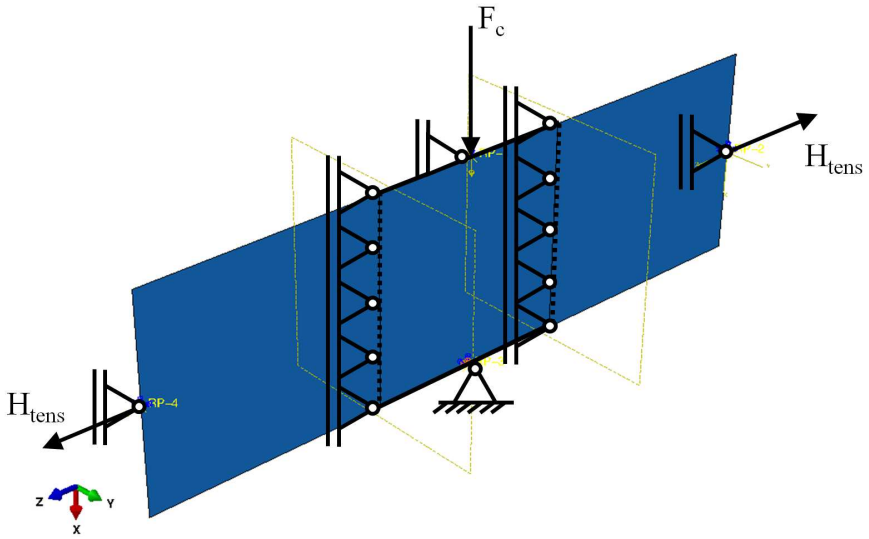

Figure 4.2: Numerical model for test D3.

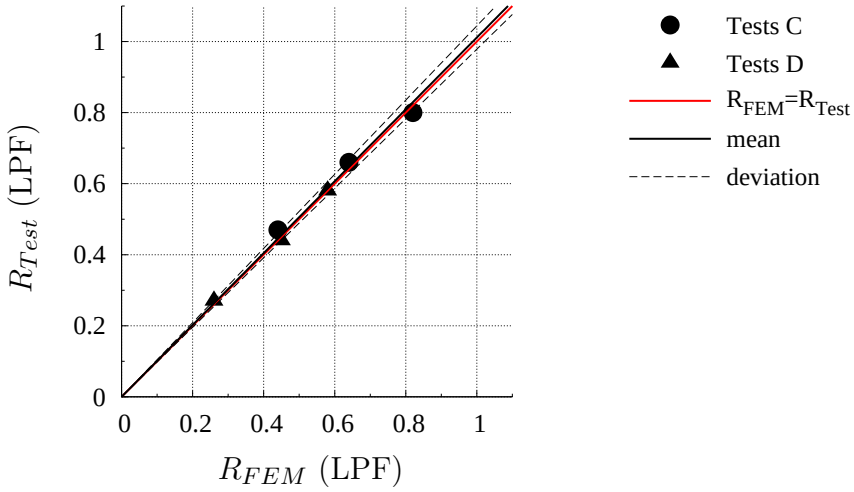

Figure 4.3: Comparison of tests and simulations.

the deformation of the portal frame as well as the deformation of the support have been measured and are already considered for the presented curves, it was practically not possible to measure the deformations in the hinges and the load introduction devices, see Fig.3.11 so that in Fig.4.4 the numerical load–displacement curves are additionally shifted to compare the stiffness just before buckling, as during the beginning of the tests the stiffness is influenced in part by the test setup. These curves are denoted as "FEM*".

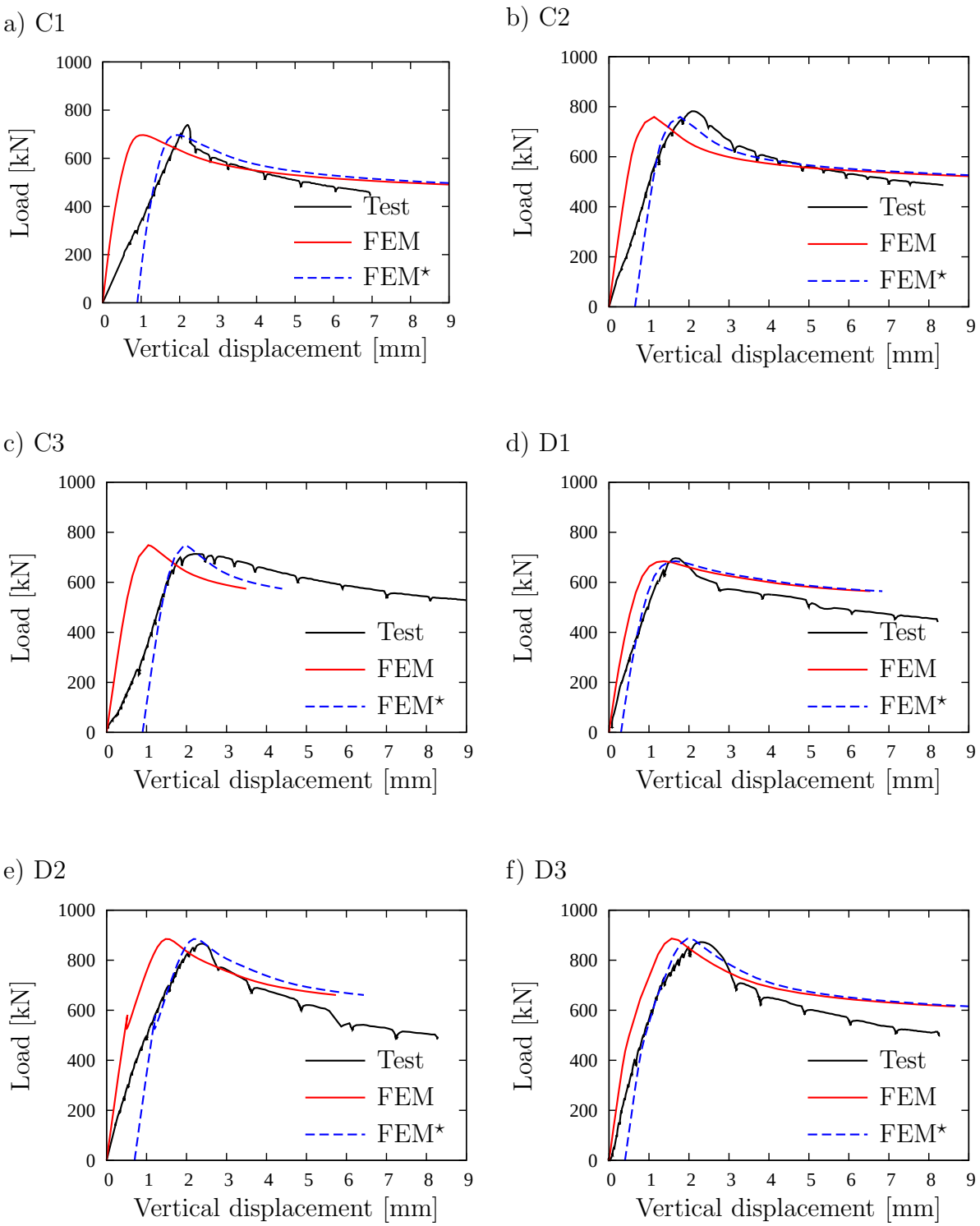

Figure 4.4: Comparison of force-displacement curves from tests and numerical simulations.

Table 4.2: Experimental and numerical maximum loads of the multiaxially loaded plates.

Test	C1	C2	C3	D1	D2	D3
$F_{c,test}$ [kN]	738.5	781.8	713.4	696.7	866.3	872.1
$F_{c,FEM}$ [kN]	703.6	759.5	748.5	684.1	885.0	886.7
$\frac{F_{c,FEM}-F_{c,test}}{F_{c,test}} \cdot 100\,\%$	−4.7	−2.9	+4.6	−1.8	+2.1	+1.6

4.4.4 Local response (out-of-plane deformations)

The out-of plane deformations of the tests are compared to the deformations from the numerical simulations in Fig.4.5 to Fig.4.10. For the numerical recalculations of the experimentally investigated plates under multiaxial stress state the same phenomena can be observed for the buckling shapes. While for the plates under pure compression the failure mode shows a one half–wave mode for both C1 and D1 ($\beta = 0$), for all plates influenced by tensile stresses more half–waves are observed in the direction of the compressive stresses. The tests C2 ($\beta = -0.5$) and C3 ($\beta = -1$) both show a two half–wave failure shape. The same is also observed for D2 ($\beta = -0.5$), while for higher tensile stresses D3 ($\beta = -1$) a three half–wave failure shape develops.

Therefore, from the comparisons of the numerical simulations with the experimental investigations it can be concluded that the adopted procedure for assessing the ultimate load of slender plates under multiaxial stress state gives reliable results and correctly takes into account also the development of multi–wave failure shapes in dependence on tensile stresses. Nevertheless, for practical reasons the model is further simplified as described in Sec.4.6.

a) Test

b) Numerical simulation

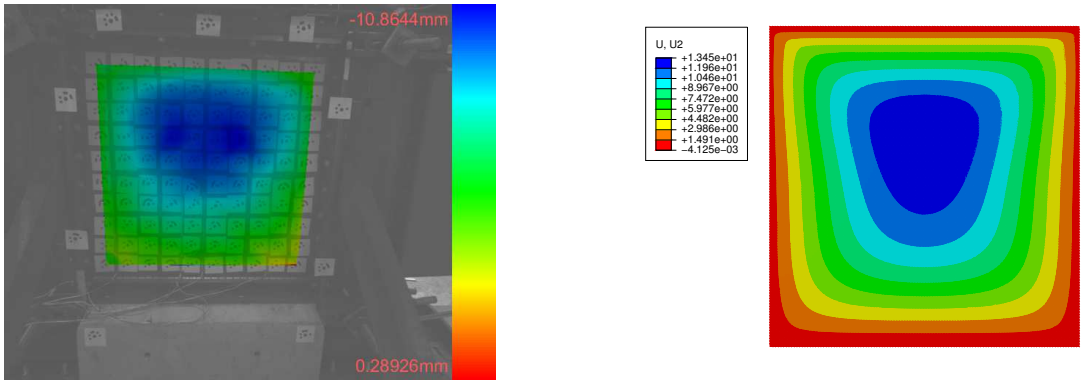

Figure 4.5: Panel deformation [mm] - test C1; a) Test, b) Numerical simulation.

a) Test

b) Numerical simulation

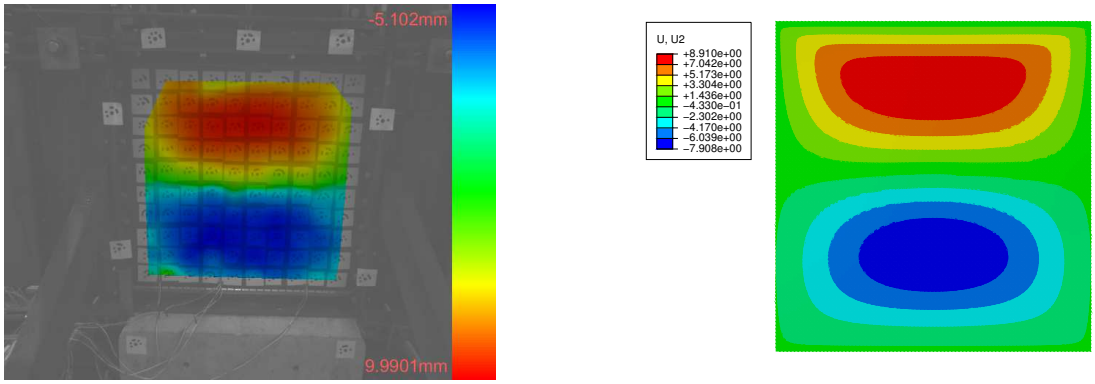

Figure 4.6: Panel deformation [mm] - test C2; a) Test, b) Numerical simulation.

a) Test

b) Numerical simulation

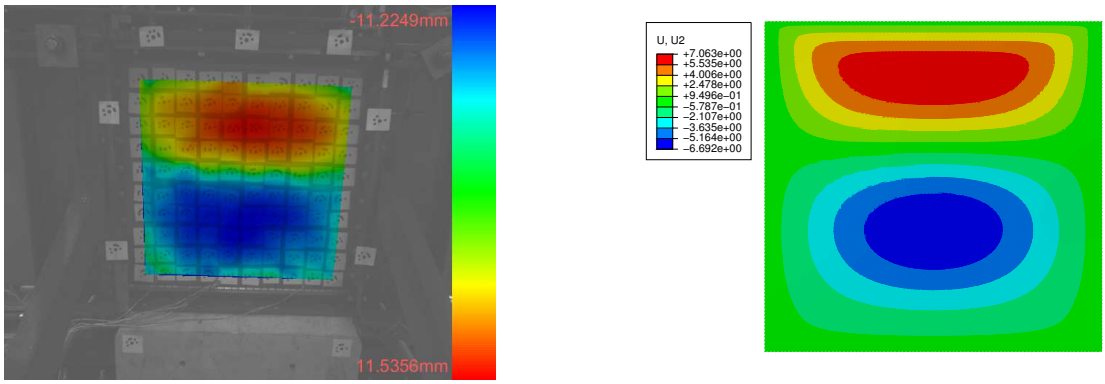

Figure 4.7: Panel deformation [mm] - test C3; a) Test, b) Numerical simulation.

a) Test

b) Numerical simulation

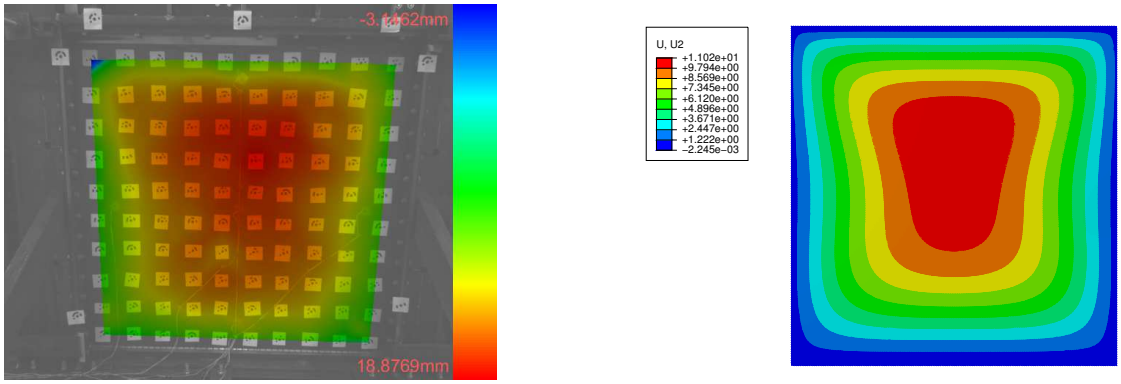

Figure 4.8: Panel deformation [mm] - test D1; a) Test, b) Numerical simulation.

a) Test

b) Numerical simulation

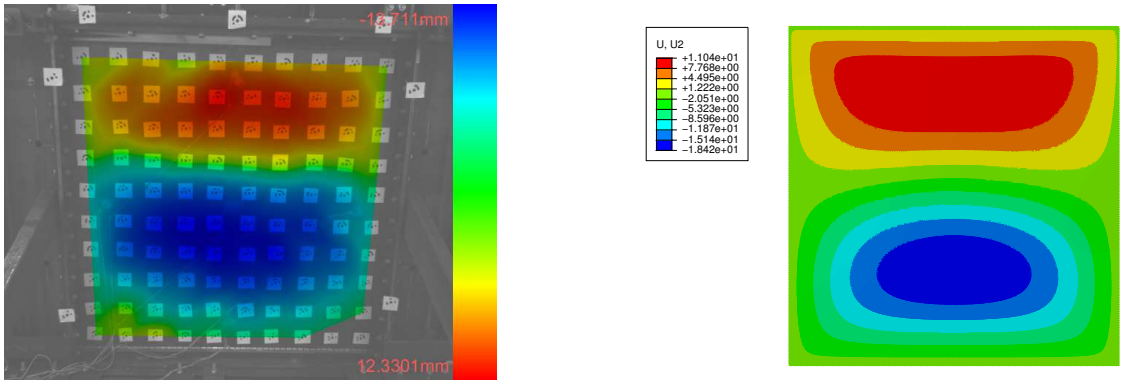

Figure 4.9: Panel deformation [mm] - test D2; a) Test, b) Numerical simulation.

a) Test

b) Numerical simulation

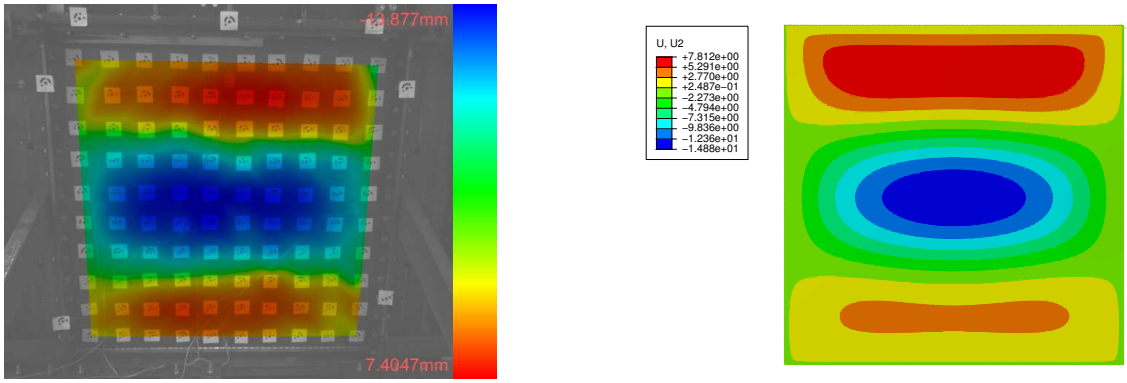

Figure 4.10: Panel deformation [mm] - test D3; a) Test, b) Numerical simulation.

4.5 Recalculation of experimental investigations on longitudinally stiffened plates

4.5.1 General

The experimental investigations, which were carried out in the frame of a DFG project [64] are presented in Sec.3.3 and have shown the interaction of direct and shear stresses on the buckling behaviour. In the following, the numerical results of the recalculation of these tests, which were conducted in close collaboration with Dr. Franc Sinur, are presented to demonstrate the performance of the finite element method using the assumptions described in the foregoing sections when dealing with multiaxial stress states. For overview purposes in this work only the main outcomes are presented in a compact way. For further details reference is made to the full report [64].

4.5.2 Numerical Model

The numerical model is built up following the principles described in the foregoing sections using the multi purpose code ABAQUS [104]. The plates are meshed with "S4R" elements as well as with "S3R" elements, which are a degenerated version of the "S4R" element and fully compatible with them. The material properties are derived from tension coupon tests, modified to true stress-strain values according to Eq.(4.3) and the measured initial geometric imperfections are applied. Investigations conducted by Sinur and Beg in [106] and [107] concluded that for the regarded case the influence of residual stresses is rather negligible and can be ignored in the numerical studies. Therefore the results of simulations calculated only with geometrical imperfections and with the combination of residual stresses and geometrical imperfection were compared differing for just 0.7 %. Fig.4.11 shows exemplarily the numerical model for girder A1, where also the load application point as well as the supports are marked.

4.5.3 Global response

The global response is compared by the load-displacement curves obtained from the tests and the numerical simulations allowing to evaluate the maximum forces, the initial stiffness as well as the descending paths of the curves.

In Fig.4.12 a) the results for girder A1 are shown. The numerically obtained response of the girder is slightly different to the experimental response. The main difference is obtained in the plastic area. Loss of load is obtained at lower vertical displacement in case of numerical simulation as in the test. Hardening can be clearly seen in the test, while in case of numerical simulation no hardening was observed. The stiffness, as expected, is slightly higher in the numerical model as in the test, but this difference is not significant.

The results for girder A2 are shown in Fig.4.12 b). The global response of the numerical simulation follows the response from the test. The initial stiffness is very similar in both cases as well as the behaviour of the yield plateau.

The global response of girder A3 is plotted in Fig.4.12 c). For this girder the numerical response fits very well the response obtained in the test in all aspects. The initial stiffness and behaviour in the yield plateau is very similar.

In Fig.4.12 d) the results obtained for girder B1 are compared. The elastic response is similar while the response in the yield plateau differs. In the test, hardening is observed, while within the numerical simulation no such response is found.

Fig.4.12 e) shows the comparison of the global response obtained by the test and numerical simulation for girder B2. As in case of girders A2 and A3 also for girder B2 a very similar response obtained by numerical simulation is found. The elastic response obtained from the numerical simulation follows the test results. The response in the yield plateau follows the test response.

The results for girder B3 are shown in Fig.4.12 f). The numerical simulation fits very well with the results from the test in all three aspects: initial stiffness, behaviour in the yield plateau and maximum resistance.

The results of the numerical simulations are summarized and compared to the experimental results in Tab.4.3.

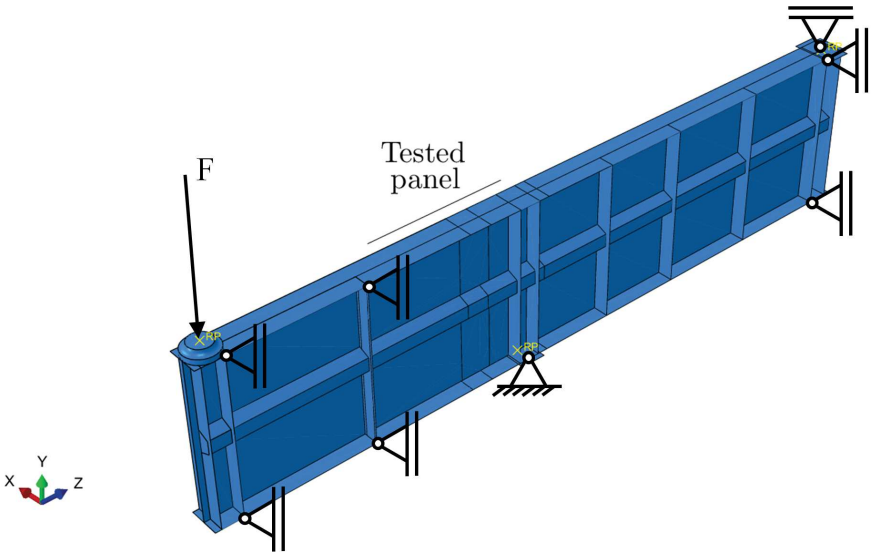

Figure 4.11: Numerical model for girder A1.

a) A1

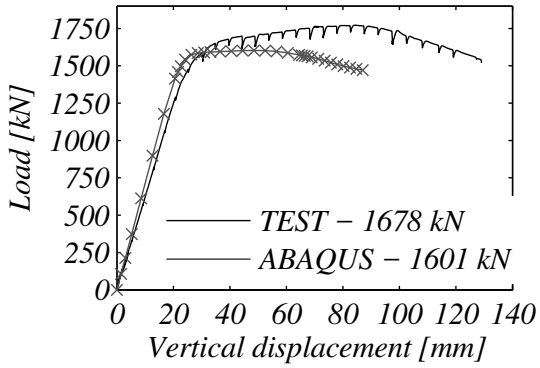

b) A2

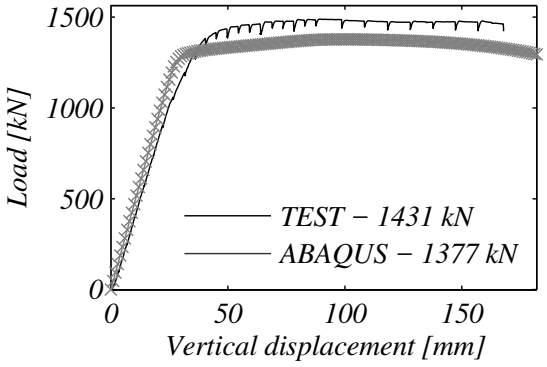

c) A3

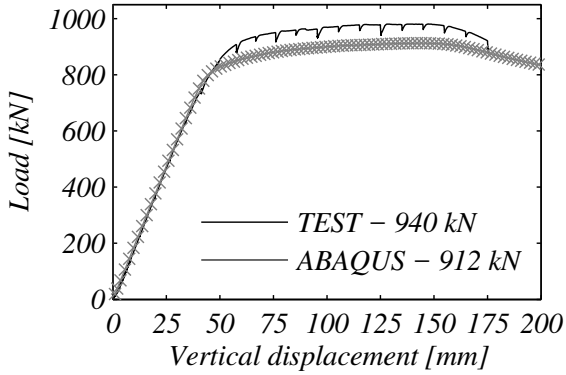

d) B1

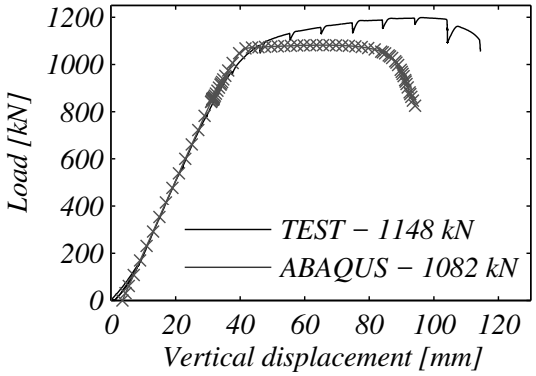

e) B2

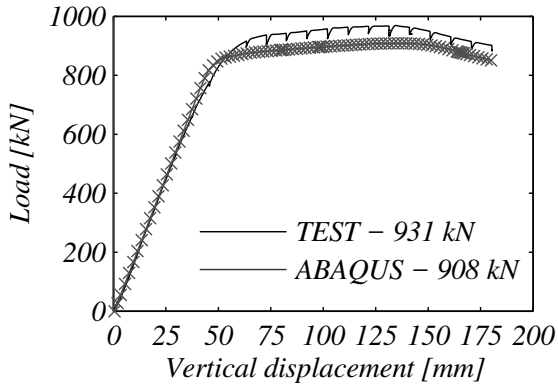

f) B3

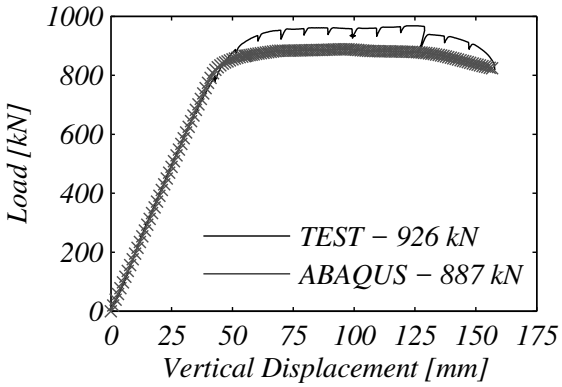

Figure 4.12: Comparison of force-displacement curves from tests and numerical simulations.

Table 4.3: Experimental and numerical maximum loads of the longitudinally stiffened plates.

Test	A1	A2	A3	B1	B2	B3
$F_{c,\,test}$ [kN]	1678	1431	940	1148	931	926
$F_{c,\,FEM}$ [kN]	1601	1377	912	1082	908	887
$\frac{F_{c,\,FEM}-F_{c,\,test}}{F_{c,\,test}} \cdot 100\,\%$	−4.6	−3.8	−3.0	−5.7	−2.5	−4.2

4.5.4 Local response (out-of-plane deformations)

The out-of-plane deformations of the tested girders are compared to the numerical results in Fig.4.13 to Fig.4.18. Despite that the out-of-plane deformation is a very sensitive parameter, the numerical model gives comparable results to the ones obtained from the tests. The numerical model sufficiently describes the behaviour of the real tests. With appropriate consideration of significant parameters such as real material model and actual initial imperfections the numerical results are very close to the real behaviour of experimental test, as in the presented situations. By the comparisons of the experimental and the numerical results it can therefore be shown that the selected assumptions for the numerical modelling lead to a realistic reproduction of the real buckling behaviour.

a) Test

b) Numerical simulation

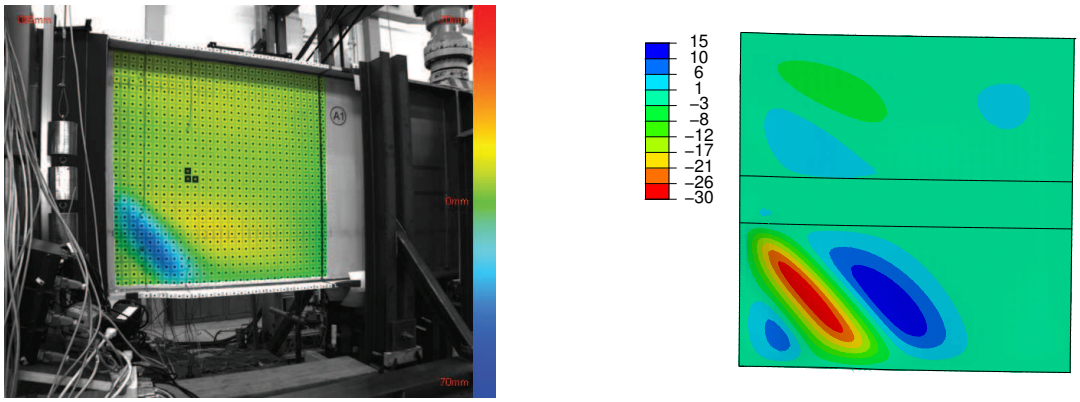

Figure 4.13: Panel deformation [mm] - girder A1; a) Test, b) Numerical simulation.

a) Test

b) Numerical simulation

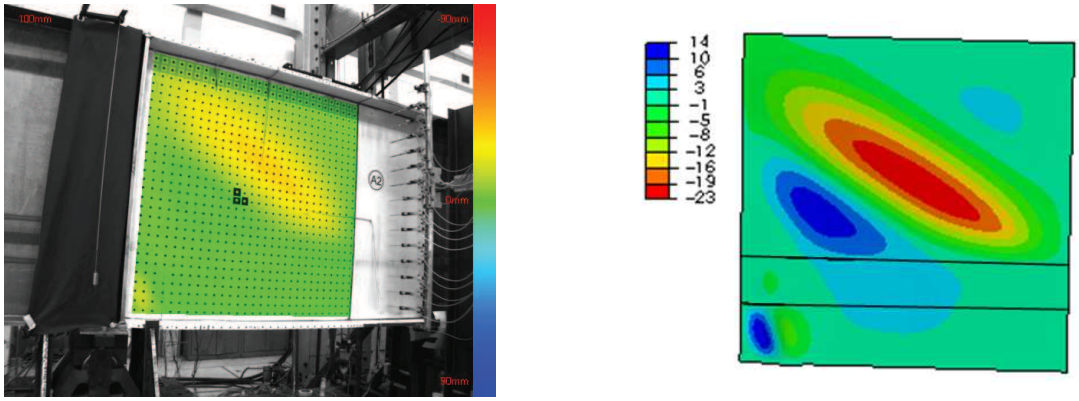

Figure 4.14: Panel deformation [mm] - girder A2; a) Test, b) Numerical simulation.

a) Test

b) Numerical simulation

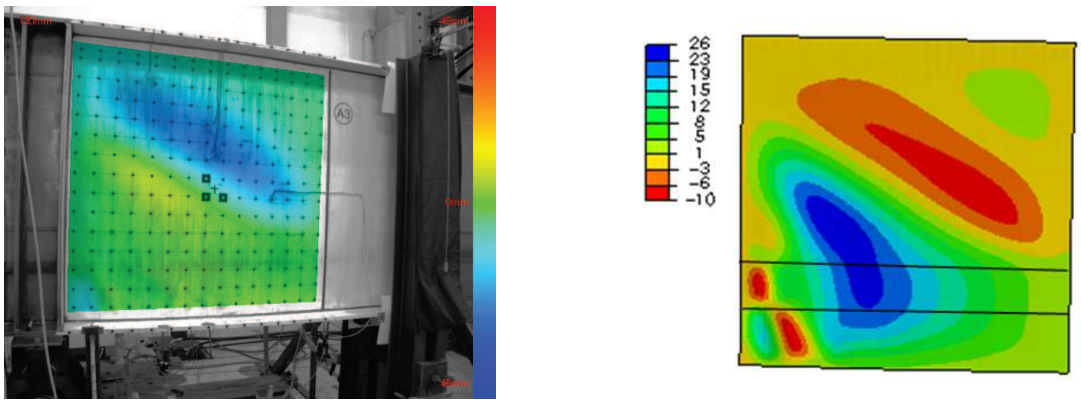

Figure 4.15: Panel deformation [mm] - girder A3; a) Test, b) Numerical simulation.

a) Test

b) Numerical simulation

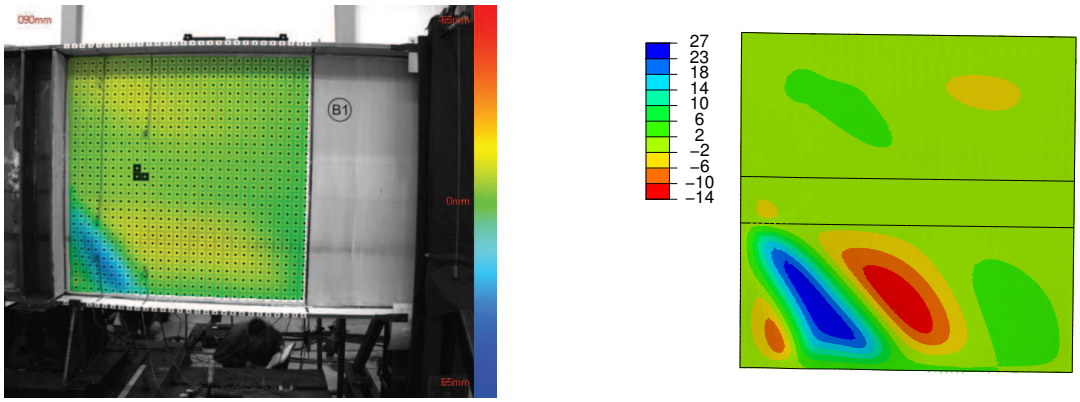

Figure 4.16: Panel deformation [mm] - girder B1; a) Test, b) Numerical simulation.

a) Test

b) Numerical simulation

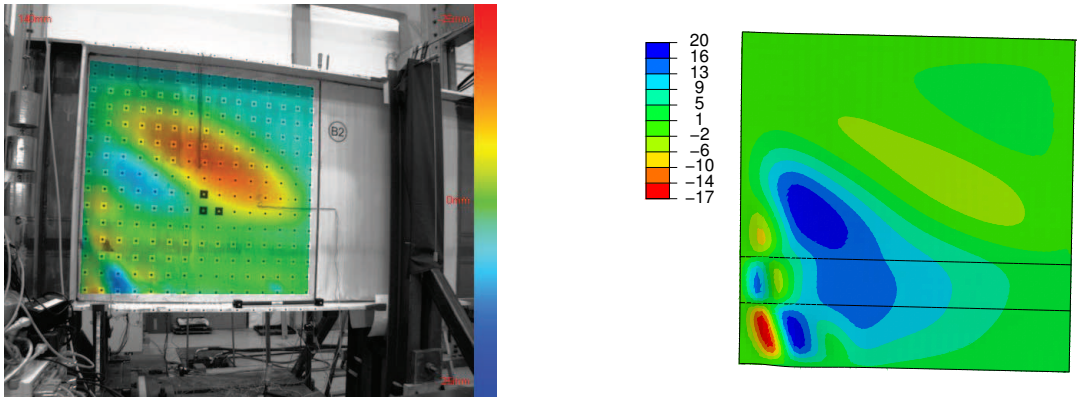

Figure 4.17: Panel deformation [mm] - girder B2; a) Test, b) Numerical simulation.

a) Test

b) Numerical simulation

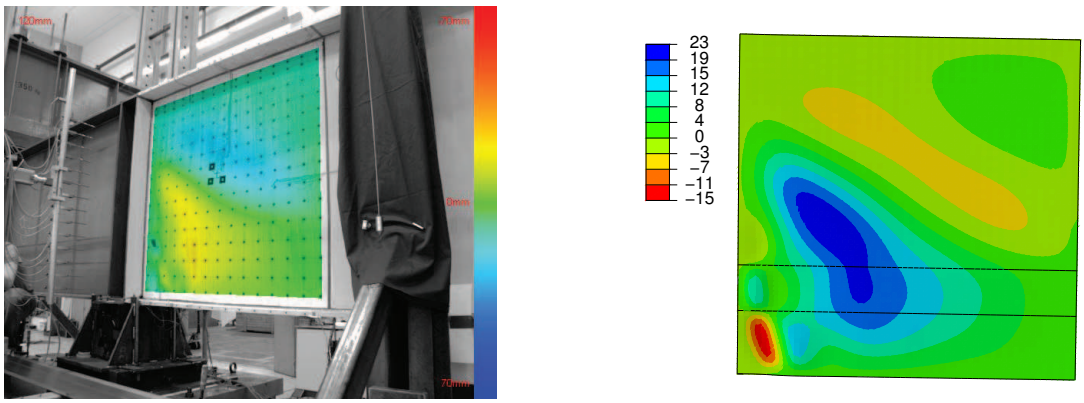

Figure 4.18: Panel deformation [mm] - girder B3; a) Test, b) Numerical simulation.

4.6 Numerical model for unstiffened plates

4.6.1 General

The numerical model for unstiffened plates is developed for conducting a wide parametric study in Sec.5. In general, the model is the same as used for the recalculation of the tests shown in Sec.4.4. However, it is simplified by eliminating the unloaded parts of the plate, as they are not of importance for the further numerical investigations. The model therefore consists of a simple plate, which represents a local web or flange panel cut out from a whole structure. This allows to analyse the behaviour of the buckling phenomena with a wide range of parameters and to evaluate in a later step the current design rules in EN 1993-1-5 [36].

4.6.2 Boundary conditions

An important parameter for the analysis of plate buckling effects are the applied boundary conditions. Therefore, different types of boundary conditions are investigated for the validation of the simplified model as well as for the undertaken parametric study in Sec.5. For the analysis on plates subjected to direct stresses, the assumptions from Braun [11] are included in the models. These are named here as the boundary conditions BC-A, BC-B and BC-C, see Fig.4.19. BC-A assumes that in the case of uniaxial compression the loaded edges remain straight, while the unloaded edges are free to move in plane. In the case of biaxial compression-tension, the edges loaded with compression remain straight and the edges loaded with tension are free to move. With boundary condition BC-B all edges remain straight, while in contrast to this with BC-C all edges are free to move in plane.

The edge boundary conditions for the straight edges are realised by so-called linear multi-point constraint equations. These type of constraint requires that a linear combination of nodal variables is equal to zero, see [104]. The equation is then applied to the degree of freedom which is constrained to be constant along the desired edge. The equation constraint is applied only in perpendicular direction of the respective edge, while the nodes remain always free to move in the longitudinal direction.

a) BC-A b) BC-B c) BC-C

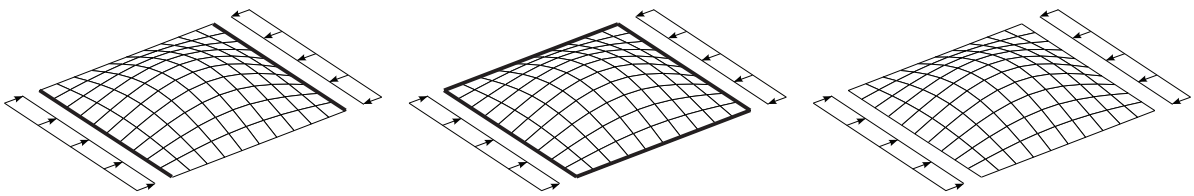

Figure 4.19: Boundary conditions.

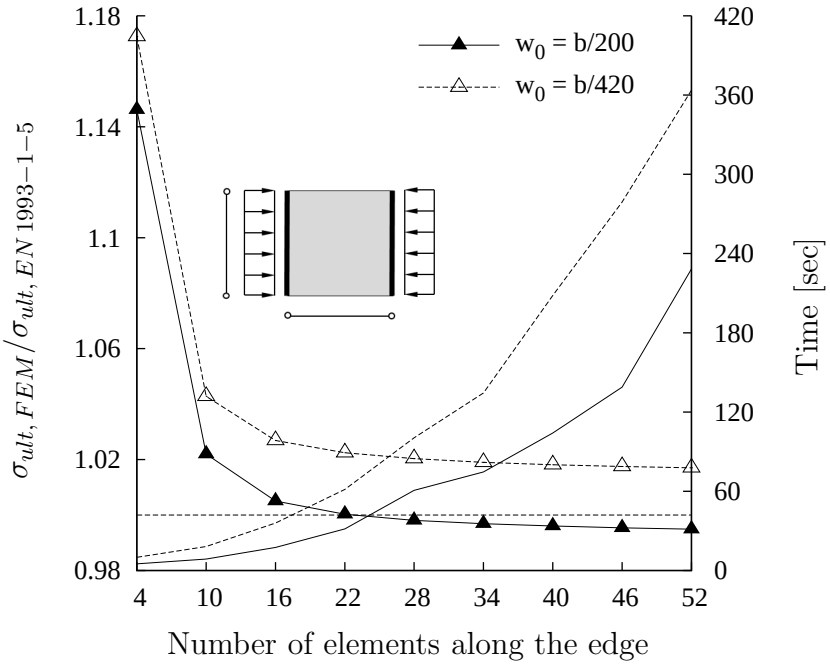

Figure 4.20: Study of the mesh convergence for uniaxial direct stresses (GMNIA).

4.6.3 Mesh convergence

To identify the required mesh density, a sensitivity analysis has been conducted showing the influence of the number of elements on the ultimate resistance of a plate ($b/t = 83$) loaded with direct stresses as well as on the computing time. The comparison is conducted for both imperfection amplitudes $w_0 = b/200$ and $w_0 = b/420$ and it can be noticed, that both curves are parallel and a sufficient accuracy with an acceptable calculating time can be reached for 40 elements along the edge.

4.6.4 Verification

4.6.4.1 General

In the following sections the known buckling resistance curves shown in Sec.2.4 both for compression and shear are recalculated with the numerical models previously presented. Since a frequent case for multiaxial loading is combined bending and shear for webs, the numerical model is calculated under several compression–bending combinations ($\psi = 0.5; 0; -0.5$ and -1.0), especially as here the buckling curves according to EN 1993-1-5 [36] and DIN 18800-3 [22] differ noticeably.

This procedure allows to confirm the suitability of the models for the further parametric studies conducted on multiaxially stressed plates.

4.6.4.2 Plates in uniaxial compression

The buckling curves used in Chapter 4, EN 1993-1-5 [36] are based on tests and studies of postcritical strength conducted by Winter [122] and evaluated and confirmed among others later by Scheer [94]. Since then several investigations analysed the behaviour of uniaxial compressed plates subjected to buckling. During the turn of the millennium some doubts arose on the validity of the Winter curve. Ruff & Schulz [90], induced by different questions such as among others the geometric imperfections of real structures often exceeding the manufacturing tolerances, conducted numerical investigations on plates under pure compression. The relation between the ultimate load and the applied imperfections where therefore investigated. They came to the conclusion that using eigenmode-affine imperfections with amplitudes according to the manufacturing tolerances would give ultimate loads up to 20 % below the Winter curve and proposed a new reduction curve with additional reductions due to residual stresses and not perfectly parallel edges.

Although, due to several replies, this was then later relativised in a supplemental statement [91], it gave reason for further investigations conducted by Lindner & Rusch [74], especially because in [91] residual stresses were not considered. The outcomes from the project were later published in [92]. The contradictions between numerical and empirical results for the ultimate load were resolved by using stimulating imperfections instead of worst-case imperfections. A modification of the buckling curves used in the codes and already proven in reality for many years was not considered as necessary.

Winterstetter [123] came to similar conclusions for shell structures, where fabrication oriented stimulating imperfections were used for performing a wide parametric study. Lindner & Rusch [74] transferred this approach to plate structures giving generally the following two options for applying stimulating imperfections:

1. Definition of fabrication oriented imperfection shapes according to Winterstetter [123]
2. Using eigenmode-affine imperfection shapes with reduced amplitudes and residual stresses compared to the worst-case assumption

Since option 1 has a rather subjective character, Lindner & Rusch [74] performed their studies following option 2. The investigations confirmed the results from Usami [118] that the Winter curve can be recalculated with a reduced amplitude and without residual stresses. If also residual stresses are considered, the amplitude is reduced once more as well as the applied residual stresses. In Tab.4.4 these two options are shown.

Since the eigenmode-affine imperfection with reduced amplitude and without residual stresses showed to give reliable results in [11], the recalculation of the buckling curves is conducted with this type of imperfections to verify the numerical model used for the parametric studies in the following sections. Additionally, the imperfection amplitude is set to $b/200$ according to EN 1993-1-5 [36] in order to identify the effect on the ultimate load, depending on the plate slenderness.

Table 4.4: Stimulating imperfections according to [74].

Imperfection (eigenmode-affine)	Amplitude w_0	Residual stresses (compression $\sigma_{res,c}$)	Residual stresses (tension $\sigma_{res,t}$)
A	$b/420$	-	-
B	$b/500$	$0.1\, f_y$	$0.5\, f_y$

Lindner & Rusch [74] also spotted that the boundary conditions of the non-loaded edges have a significant influence on the ultimate load, while the length of the plate has only a minor effect, if the same imperfection amplitude is applied. Also Braun [11] investigated the effect of the boundary conditions, concluding that the edge constraints have a large influence on the buckling behaviour especially for slender plates. The effect of the boundary conditions is also regarded in the present work in order to verify the numerical model, since the effect of the boundary conditions on the buckling interaction study is also regarded. Therefore, for the recalculation of the buckling curves the boundary conditions BC-A, BC-B and BC-C are used see Fig.4.19.

In Fig.4.21 the calculated reduction factors for the numerical model with BC-A are drawn against the Winter curve. In general it is visible that the Winter curve is recalculated sufficiently well with both imperfection amplitudes, although in the medium to high slenderness range the $b/420$ is slightly closer and for stocky plates the model with $b/200$. As expected, the influence of the imperfection amplitude vanishes for high slenderness. For the parametric studies both amplitudes are applied to the numerical model. Since the assumed boundary condition is on one hand conservative for inner subpanels, where all edges remain straight providing that the neighbouring panels are stiff sufficiently, and on the other hand may be unsafe for panels loaded with patch loading where the edges do not necessarily remain straight, the case of pure compression is also studied for the boundary conditions BC-B and BC-C.

In Fig.4.22 the results are shown analogically for the boundary condition BC-B. The numerical results for stocky plates lie close to the Winter curve and for slender plates noticeably above. This behaviour arises from the increased tension stresses in perpendicular direction to the applied load caused by the constrained edges. This effect is more pronounced for high slenderness since due to buckling the edges in the middle would tend to move inwards but are forced to remain straight, so additional stabilising tension stresses occur. Fig.4.23 shows the results for boundary condition BC-C i.e. for all edges free to move in-plane. The numerically calculated reductions are in good agreement with the reduction curve given in Annex B, EN 1993-1-5 [36] for the parameters $\alpha_p = 0.34$ and $\overline{\lambda}_p = 0.70$ derived by Müller [82].

The recalculations of the buckling curves are conducted on a square plate, which as discussed by Braun [11], can be considered as the worst case. From the shown results it can be concluded that the developed numerical model performs sufficiently well and can be used for further parametric studies. Fig.4.24 shows the sound performance of the simulations in a statistical comparison of the simulations and the Winter curve.

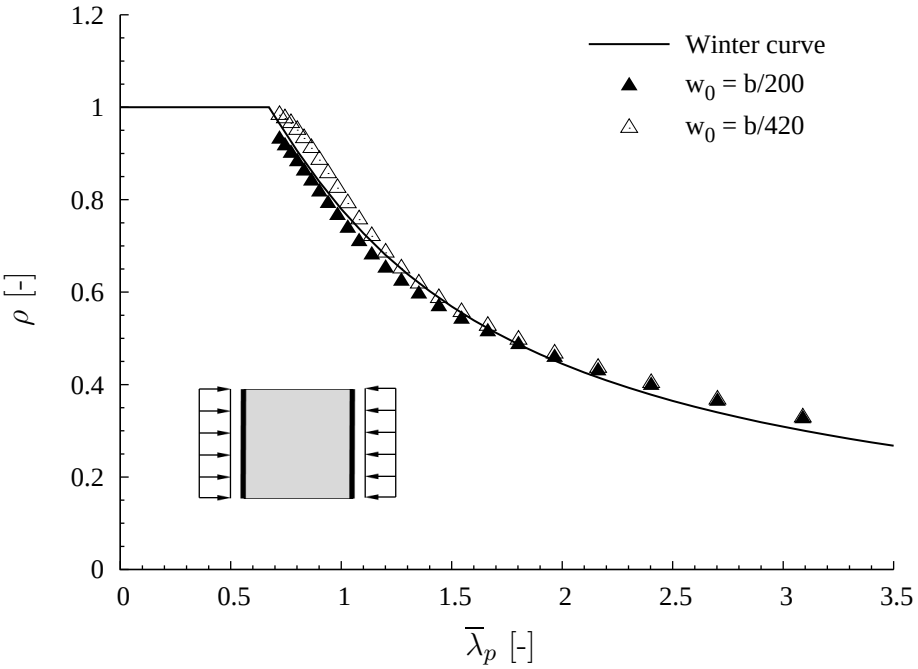

Figure 4.21: Comparison of simulations and the Winter curve (BC-A, $\alpha = 1$, all edges hinged, loaded edges constrained and unloaded edges unconstrained).

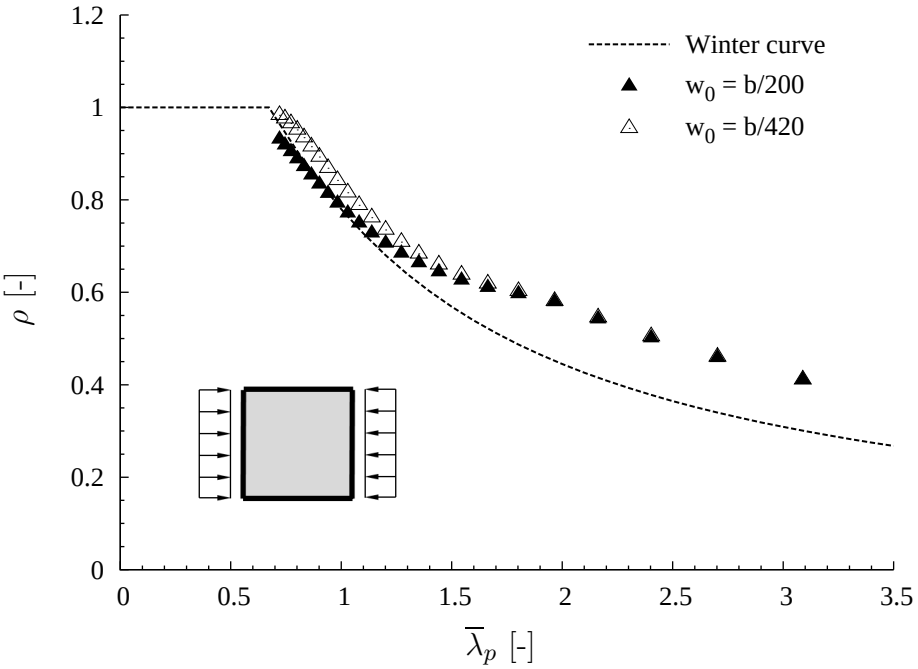

Figure 4.22: Results of simulations in case of a plate with constrained edges (BC-B, $\alpha = 1$, all edges hinged and constrained).

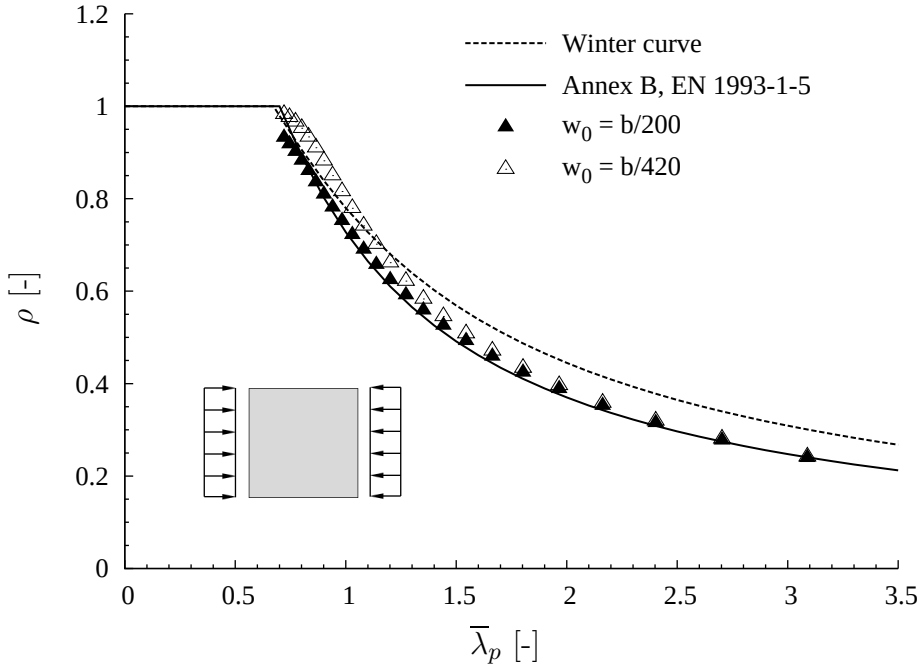

Figure 4.23: Comparison of simulations and the buckling curve according to Annex B, EN 1993-1-5 (BC-C, $\alpha = 1$, all edges hinged and unconstrained).

a) $w_0 = b/200$ b) $w_0 = b/420$

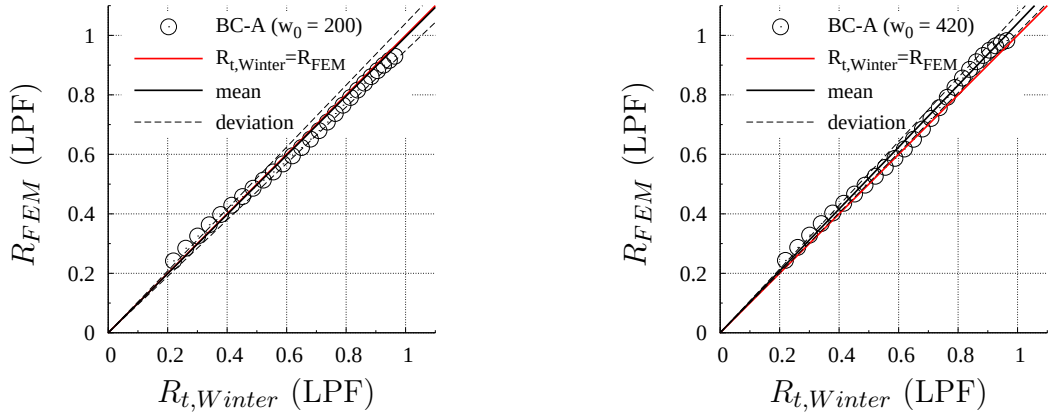

Figure 4.24: Statistical comparison of simulations and the Winter curve (BC-A, $\alpha = 1$, all edges hinged, loaded edges constrained and unloaded edges unconstrained).

Since for the parametric study concerning the interaction of direct and shear stress, the stress gradient is of practical importance, a recalculation of the buckling curves with linear stress gradients including stress ratios of $\psi = 0.5; 0; -0.5$ and -1.0 is conducted additionally. For the following recalculations the model with the boundary conditions BC-A is used, since the model successfully correlates with the Winter curve, which is the basis for the buckling curves considering stress gradients, see Eq.(2.20) and Tab.2.4. Furthermore, the model with the boundary condition BC-A shows a very good agreement when recalculating the shear buckling curves, see Sec.4.6.4.3.

Fig.4.25 shows the results from the numerical simulations on the recalculation of the buckling curve with a stress ratio of $\psi = 0.5$. In addition to the buckling curve according to EN 1993-1-5 [36] also the buckling curve according to DIN 18800-3 [22] presented in Sec.2.4.3 is shown. It can be seen that the buckling curve according to EN 1993-1-5 [36] gives for all cases smaller reduction factors than the numerical calculations, while DIN 18800-3 [22] matches very well with the approach according to USAMI [118] ($w_0 = b/420$). The same conclusion can be drawn also for the case of $\psi = 0$, where DIN 18800-3 [22] again matches very well with the approach from USAMI [118], while EN 1993-1-5 [36] gives smaller reduction factors, see Fig.4.26. For this case the same behaviour was already observed by KUHLMANN & BRAUN in [65], where also the influence of residual stresses was investigated showing only a small influence within the shown bandwidth of results. Therefore, in [65] the approach from USAMI [118] was adopted for the evaluation of further analyses. Also for stress gradients containing tension stresses from bending ($\psi = -0.5$ and -1) the buckling curves from EN 1993-1-5 [36] lead to smaller reduction factors while DIN 18800-3 [22] matches with the numerical calculations, see Fig.4.27 and Fig.4.28.

The buckling curve depending on the direct stress distribution for internal compression elements used in EN 1993-1-5 [36] is presented by JOHANSSON ET AL. in [51] with reference to DUBAS [30], where in turn, referring to WATANABE [121], it is pointed out that it is generally accepted that the influence of imperfections is less severe for bending than for pure compression. Therefore, as a modification of the Winter curve, an equation including the effect of the stress gradient was presented and later adopted in EN 1993-1-5 [36]. However, it is quite astonishing that the buckling curves from DIN 18800-3 [22] match almost perfectly with the numerical simulations, while the buckling curves from EN 1993-1-5 [36] give conservative results when a stress gradient is considered, in particular having in mind that both curves merge into the Winter curve for the "extreme" case of pure compression ($\psi = 1.0$).

Fig.4.29 shows a comparison of the different buckling curves from EN 1993-1-5 [36] and DIN 18800-3 [22] for different stress ratios. It can be seen that both codes take into account the positive effect of stress ratios $\psi \leq 1$. But while in EN 1993-1-5 [36] the effect is mainly indicated by an elongation of the yield plateau and all curves approach to each other for high slenderness, the curves in DIN 18800-3 [22] are additionally "shifted" up. Furthermore DIN 18800-3 [22] gives the same buckling curves for all cases with $\psi \leq 0$, see also Tab.2.4 for panels without longitudinal stiffeners.

4.6.4.3 Plates under shear

The model for shear calculations is the same as the one for direct stresses with BC-A, see Sec.4.6. However, in order to reduce the influence of the lateral edges on the resistance, the panel aspect ratio is increased to $\alpha = 2$. Fig.4.30 points out the influence of the panel aspect ratio α on the ultimate resistance τ_{ult}, showing that this effect is more pronounced for higher slenderness, while almost no difference is noticeable for small to medium slenderness.

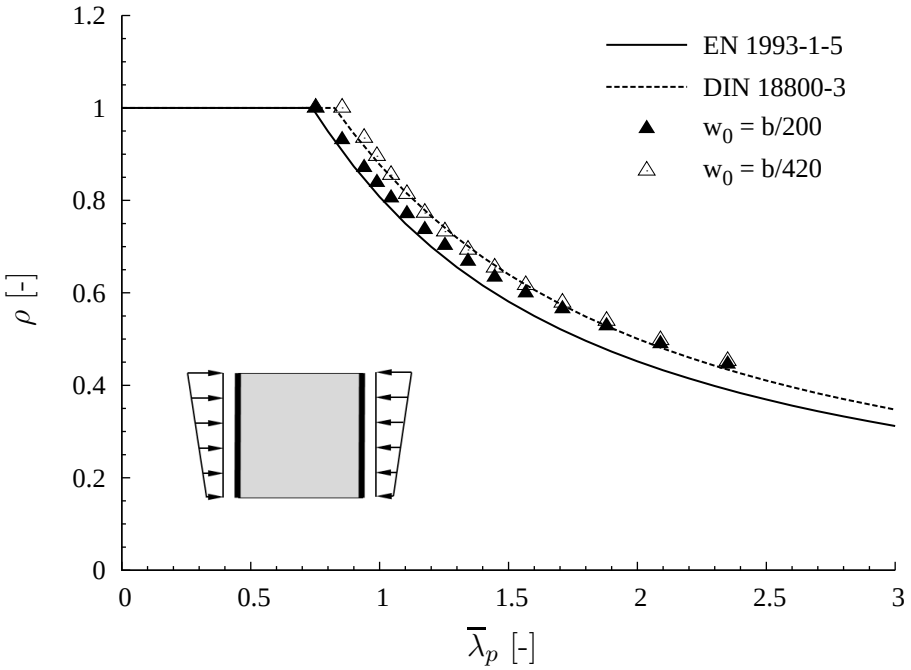

Figure 4.25: Comparison of simulations and the buckling curves according to EN 1993-1-5 [36] and DIN 18800-3 [22] ($\psi = 0.5$, $\alpha = 1$, all edges hinged, loaded edges constrained and unloaded edges unconstrained).

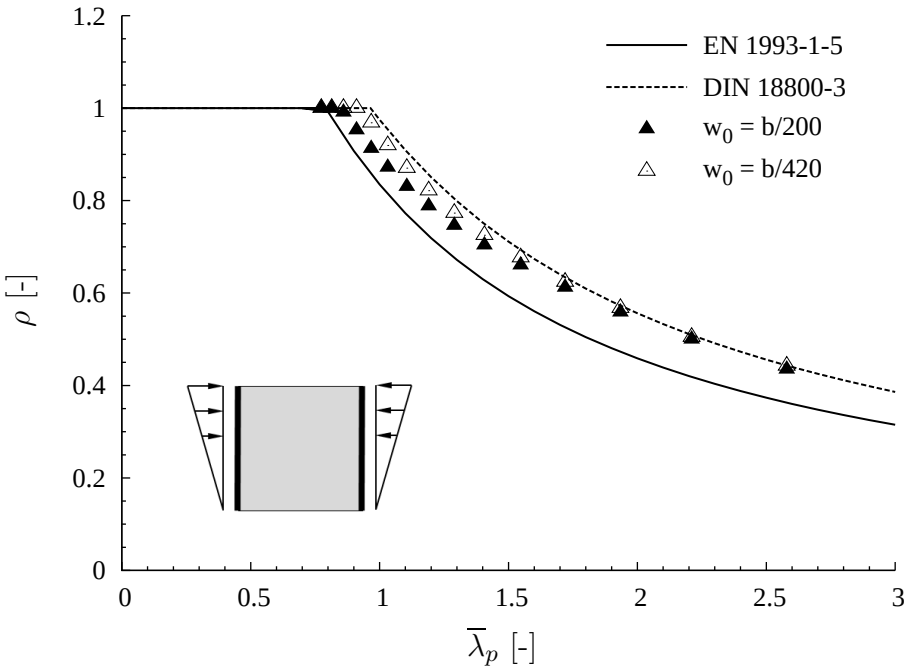

Figure 4.26: Comparison of simulations and the buckling curves according to EN 1993-1-5 [36] and DIN 18800-3 [22] ($\psi = 0$, $\alpha = 1$, all edges hinged, loaded edges constrained and unloaded edges unconstrained).

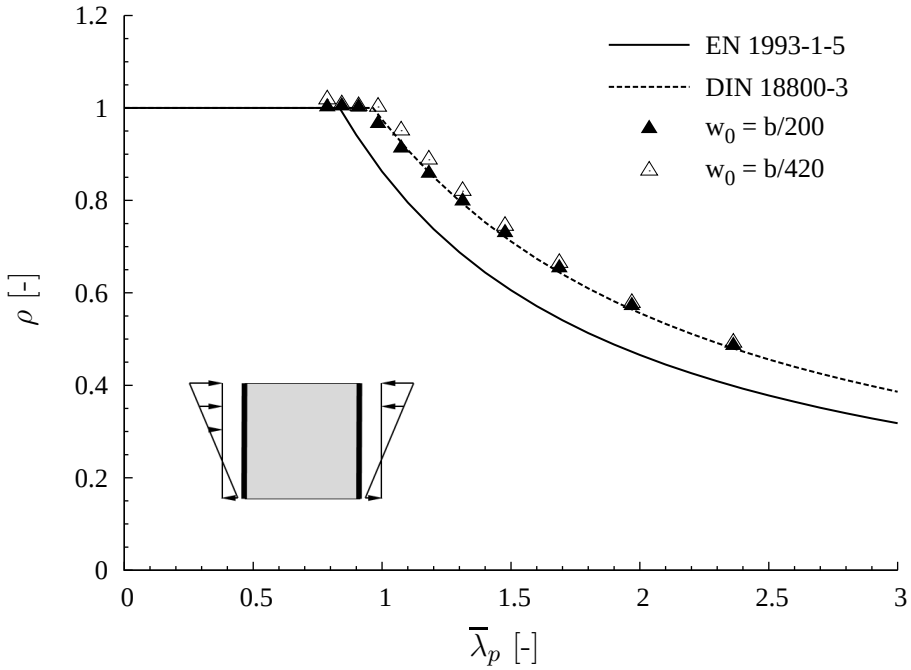

Figure 4.27: Comparison of simulations and the buckling curves according to EN 1993-1-5 [36] and DIN 18800-3 [22] ($\psi = -0.5$, $\alpha = 1$, all edges hinged, loaded edges constrained and unloaded edges unconstrained).

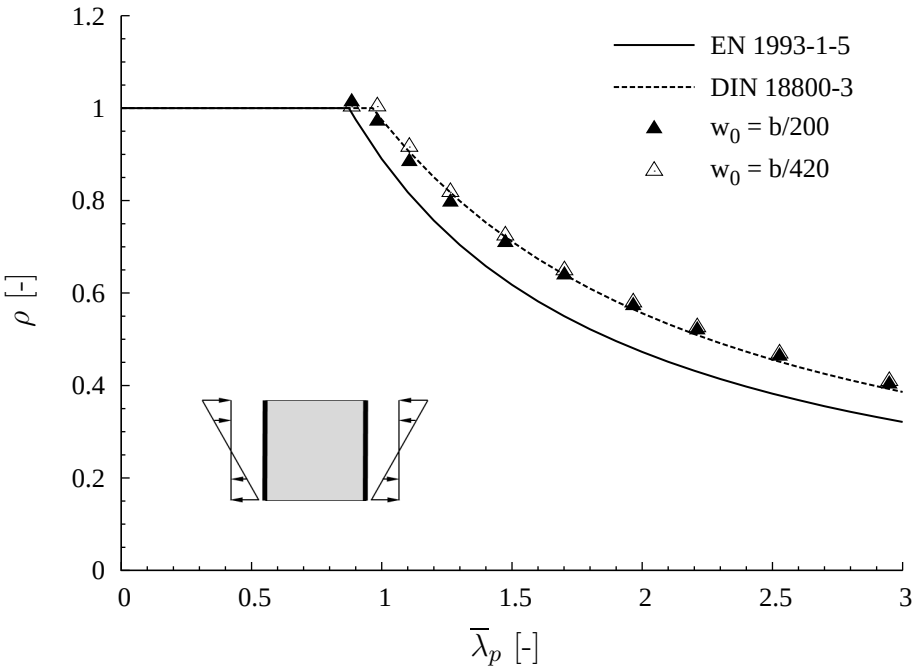

Figure 4.28: Comparison of simulations and the buckling curves according to EN 1993-1-5 [36] and DIN 18800-3 [22] ($\psi = -1$, $\alpha = 1$, all edges hinged, loaded edges constrained and unloaded edges unconstrained).

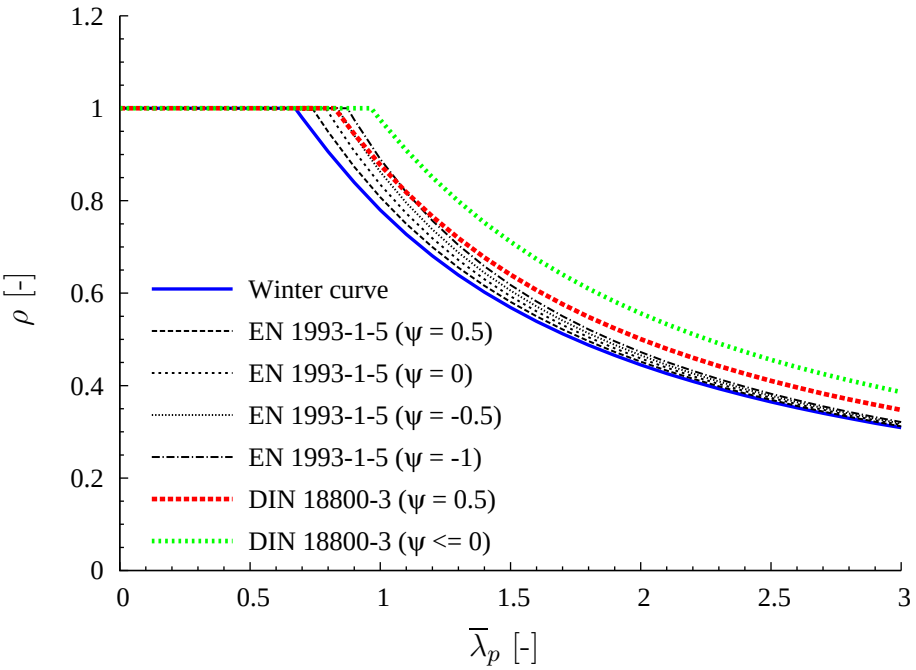

Figure 4.29: Comparison of the buckling curves according to EN 1993-1-5 [36] and DIN 18800-3 [22] with different stress ratios ψ.

The imperfections are applied following the principles presented in Sec.4.6.4.2 for a compatible procedure allowing for conducting investigations on plates subjected to direct stresses and shear in a later step. In Fig.4.31 the results of the numerical study are compared to the shear buckling curve given in Chapter 5 of EN 1993-1-5 [36] and the statistical comparison of the simulations and the buckling curves is shown in Fig.4.32. The influence of the imperfection amplitude w_0 is rather small and only visible for slenderness $\bar{\lambda} \lesssim 1.2$. The numerical results match very well with the buckling curve, so that the approach, which has also been succesfully used in [65], can be regarded as suited for futher parametric studies.

4.7 Numerical model for stiffened plates

4.7.1 General

For investigating the buckling behaviour of longitudinally stiffened plates under direct stresses, a numerical model is developed based on the outcomes from Sec.4.6. Therefore, the edges are modelled to be hinged and free to move in plane, so that the results are in a later step compared to the design rules according to EN 1993-1-5 [36] using the buckling curve from Annex B, since the model corresponds to the "BC-C-model" presented in Sec.4.6.2. The boundary conditions of the model correspond to the design example for finite element analysis conducted in [4]. The load is applied on the plate as well as

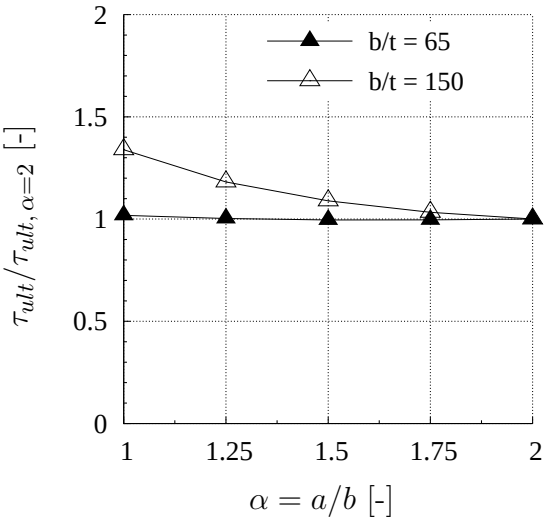

Figure 4.30: Influence of the plate length on the shear buckling resistance τ_{ult}.

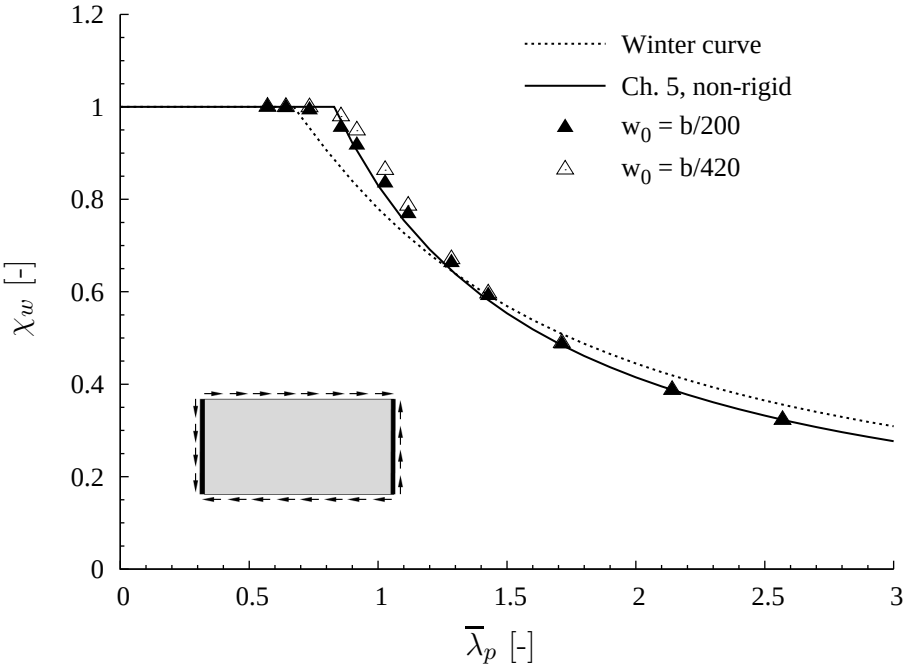

Figure 4.31: Comparison of simulations and buckling curves (BC-A, $\alpha = 2$, all edges hinged).

a) $w_0 = b/200$ b) $w_0 = b/420$

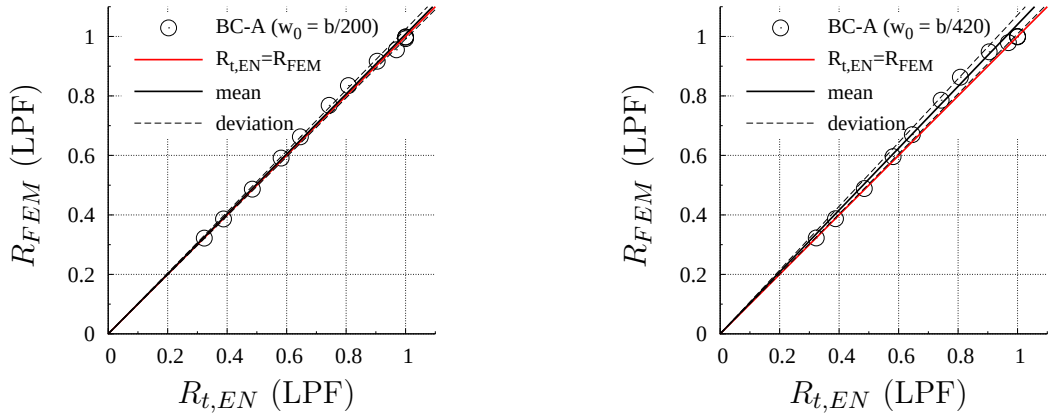

Figure 4.32: Statistical comparison of simulations and buckling curves (BC-A, $\alpha = 2$, all edges hinged).

on the stiffeners to represent the situation of continuous longitudinal stiffeners. Open stiffeners are investigated in the frame of this work.

4.7.2 Parameters

In order to exclude torsional buckling of the longitudinal stiffeners, Chapter 9.9.2, EN 1993-1-5 [36] provides minimum requirements for stiffeners. Therein, two criteria of the minimum requirements for transverse stiffeners are referred to in order to check torsional buckling also for longitudinal stiffeners. Only for open longitudinal stiffeners, if necessary, the torsional buckling has to be checked, see also [67]. Unless a more advanced method of analysis is carried out in order to prevent torsional buckling of stiffeners with open cross-sections the first criteria may be applied by checking the ratio of the St. Venant torsional constant for the stiffener alone (I_T) and the polar second moment of area of the stiffener alone around the edge fixed to the plate (I_p) according to Eq.(4.4).

$$\frac{I_T}{I_p} \geq 5.3 \frac{f_y}{E} \tag{4.4}$$

If the warping stiffness is taken into account, stiffeners should either fulfil the above criterion or the criterion according to Eq.(4.5).

$$\sigma_{cr} \geq \Theta \, f_y \tag{4.5}$$

Herein, σ_{cr} is the elastic critical stress for torsional buckling not considering rotational restraint from the plate and Θ is a parameter to ensure class 3 behaviour, which is

recommended to $\Theta = 6$ in EN 1993-1-5 [36]. As mentioned above, for trapezoidal or similar closed sections these criteria are not required. According to JOHANSSON ET. AL [51] and BEG ET. AL [4] for a flat bar with the dimensions b_{st} for the height and t_{st} for the thickness the criterion shown in Eq.(4.4) can be simplified to Eq.(4.6).

$$\frac{b_{st}}{t_{st}} \leq \sqrt{\frac{E}{5.3\, f_y}} = 10.6 \qquad \text{for S 355} \tag{4.6}$$

The numerical investigations are carried out for a steel grade S 355, so that the criterion in Eq.(4.6) results in $b_{st}/t_{st} \leq 10.6$. Therefore, for all numerical simulations with open stiffeners the height to thickness ratio is set to $b_{st}/t_{st} = 10$. The verification of the stiffeners themselves is carried out indirectly by the verification of the global buckling of the stiffened plate and by determination of the buckling coefficients considering the stiffeners, see [67].

For the sake of completeness it is mentioned that current investigations conducted by KÖVESDI & DUNAI [59] deal with the stiffness requirements for cross girders on orthotropic plates subjected to pure compression. The starting point of the investigations was the torsional stiffness criteria, which cannot be fulfilled by the designers in case of T-section cross girders. The investigations led to a modification of the current "deflection limit" criterion and to a new "support rigidity" criterion as well as the elimination of the "torsional stiffness" criterion. However, it should be noted that the investigations deal explicitly with T-section cross girders not directly loaded with normal stresses. The deduced criteria therefore apply for transverse stiffeners in order to provide a rigid support for a plate with longitudinal stiffeners. Therefore, in the present work the criteria for the torsional stiffness according to Eq.(4.4) and Eq.(4.6) are applied nevertheless for the geometry of the longitudinal stiffeners.

In order to also investigate the influence of the stiffness of the stiffener on the plates, three levels are regarded. In BEG ET AL. [4] a classification for the stiffening is given, where $\gamma = 5$ or 10 means lightly stiffened and for $30 \leq \gamma \leq 100$ the plate is normally stiffened. For the following investigations on stiffened plates the values of $\gamma = 7$, 25 and 65 are applied to the stiffeners in order to cover the lightly and normally stiffened plates as well as the transition area between them. It should be noted here that the stiffness $\gamma = 25$ is selected from the classification of longitudinal stiffeners done in [4] and not from the minimum stiffness requirement $\gamma_{min} = 25$, which was derived in COMBRI [66] for the effective with method, as the reduced stress method allows for accounting for any type of stiffness of longitudinal stiffeners.

Additionally, to include the interaction of column- and plate-like behaviour, three length to width ratios α are investigated. The panel aspect ratio α as well as the stiffness of the stiffener γ have a decisive influence on the behaviour of the plate. With increasing panel aspect ratio the behaviour is governed by plate-like buckling, while increased stiffness of the stiffeners lead to a more column-like governed behaviour. Therefore in

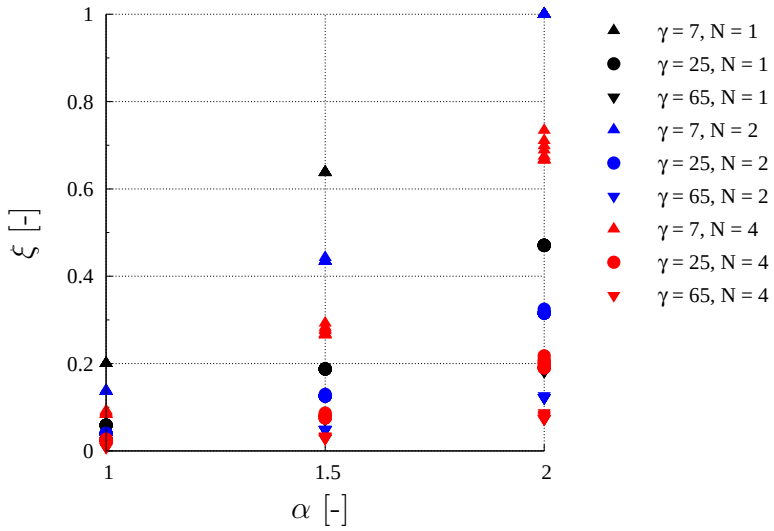

Figure 4.33: Effect of panel aspect ratio (α), stiffness of the stiffener (γ) and number of the stiffeners (N) on the interaction parameter (ξ).

addition to the different stiffness of the stiffeners the panel aspect ratios $\alpha = 1$, 1.5 and 2 are regarded. The effect of the panel aspect ratio and the stiffness of the stiffener on the interaction parameter ξ for column- and plate-like buckling behaviour is shown in Fig.4.33 for the investigated cases of one to four stiffeners ($N = 1$, 2 and 4).

Therefore, the interpolation formula for the influence of column-like behaviour according to EN 1993-1-5 [36] is evaluated for the regarded cases. It should be noted here that this does not represent the "real" buckling behaviour of the plates but aims at covering a wide range for the current formulation. According to Eq.(2.23) almost pure column-like behaviour ($\xi = 0$) is found for $\alpha = 1$, except for weak stiffeners, where a small interaction with plate-like buckling occurs. The plates with $\alpha = 1.5$ result in a mixed behaviour for all stiffeners, where the weak stiffeners are more influenced by plate-like behaviour, while the stronger stiffeners are more influenced by column-like buckling. The longer plates with $\alpha = 3$ show mainly plate-like behaviour for the weak stiffeners and a mixed behaviour for the stronger ones. As mentioned before, these basic parameters are chosen to represent a wide range for the buckling behaviour within the parametric study on combined loading.

The parameters used for the validation of the numerical model are summarised in Tab.4.5 resulting in a total of 270 possible combinations. Of course, the total number of numerical calculations are far more, since several possible imperfections and imperfection combinations need to be considered, see Sec.4.7.3.

4.7.3 Imperfections

In the frame of a DFG research project [64] for stiffened plates an advanced method for the direct determination of the most unfavourable imperfection shape by means

Table 4.5: Varied parameters for the validation of the numerical model for stiffened plates.

Panel aspect ratio α	Stiffness of the stiffener γ	Slenderness b/t	Number of stiffeners N
1, 1.5, 2	7, 25, 65	65, 80, 90, 100 115, 130, 150 180, 210, 250	1, 2, 4

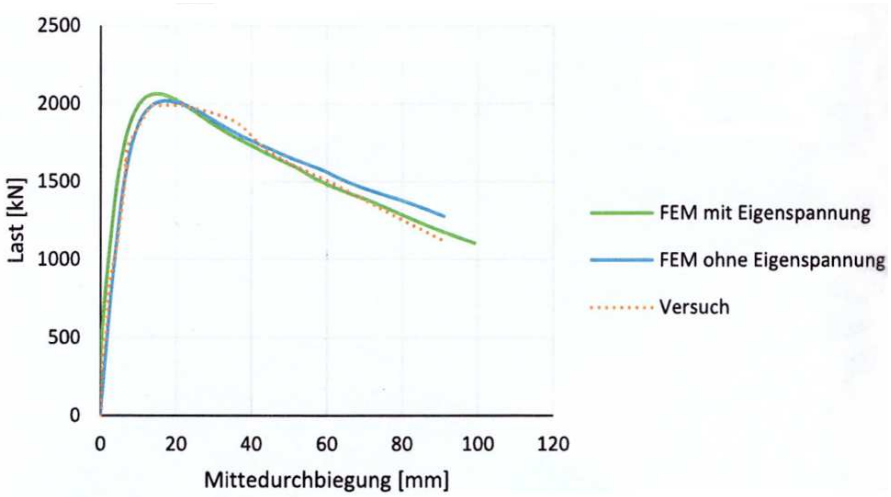

Figure 4.34: Comparison of Test-No.: E50-70 from [97] and simulations with and without residual stresses according to [86].
(translation from German language: Last = Load, Mitteldurchbiegung = Deflection in the centre of the panel, mit Eigenspannung = with residual stresses, ohne Eigenspannungen = without residual stresses, Versuch = Test)

of ultimate limit states was presented using an exact sensitivity analysis according to [56], [57], [61] and [62]. Even though the method works well in the examined examples, it showed to be very complex and not practicable for a larger parametric study, so that for further investigations the initial imperfections are applied as equivalent geometric imperfections according to Annex C, EN 1993-1-5 [36], see Tab.4.6. It is noted here that for the calculation of the global imperfection amplitude $b = b_{gl}$ and for the local imperfection amplitude $b = b_{loc}$ are taken. As shown by Pourostad in [86], the influence of residual stresses on stiffened plates under pure compression is very marginal compared to the influence of geometrical imperfections, so that the application of equivalent geometric imperfections is regarded as absolutely sufficient for the evaluation of the buckling rules and further parametric studies. Fig.4.34 shows an exemplary comparison of a test from [97] and simulations with and without residual stresses according to [86].

In Fig.4.35 a) - c) the components of the applied imperfections for a single stiffened plate with an open stiffener are exemplarily shown. In a later step they are combined

Table 4.6: Equivalent geometric imperfections according to EN 1993-1-5 [36].

Type	Component	Shape	Magnitude
global	longitudinal stiffener with length l	bow	$\min(a/400, b/400)$
local	panel or subpanel with short span a or b	buckling shape	$\min(a/200, b/200)$
local	stiffener or flange subject to twist	bow twist	1/50

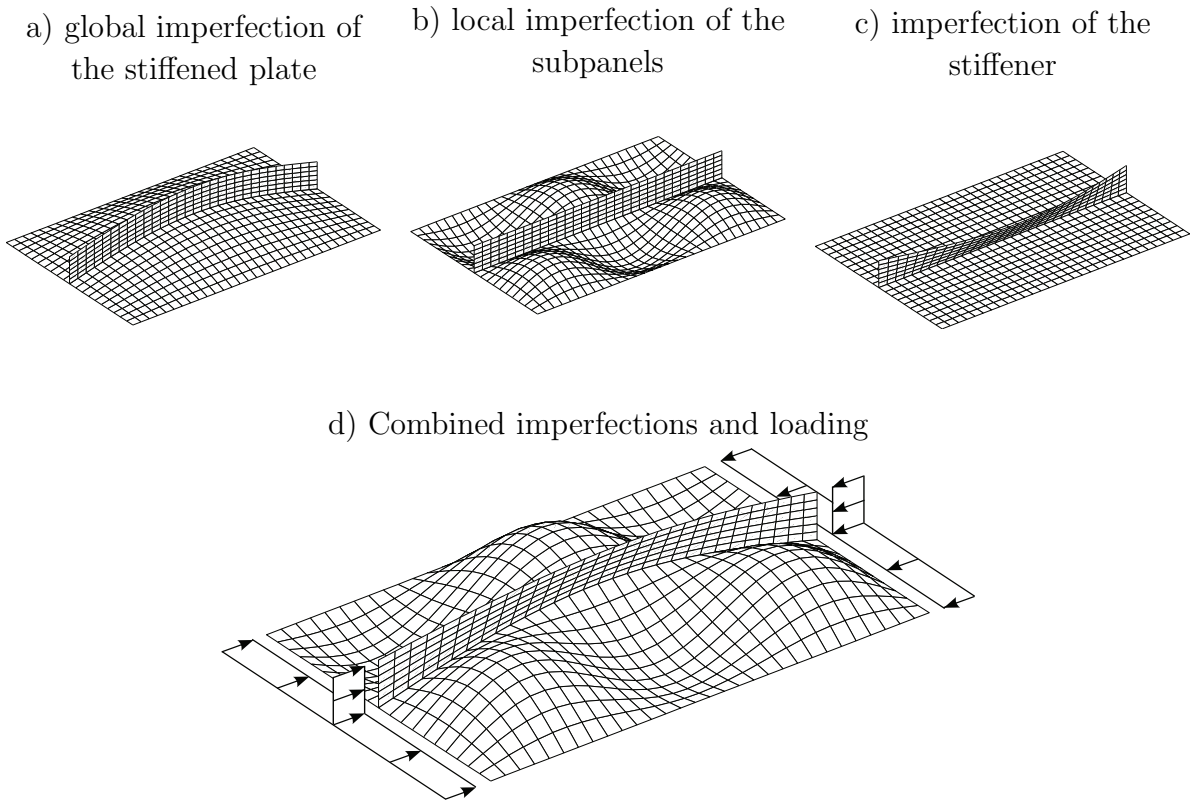

Figure 4.35: Applied imperfections and loading of a stiffened plate.

according to Sec. C.5(5), EN 1993-1-5 [36] to perform the numerical simulations, see Fig.4.35 d). Therefore, a leading imperfection is chosen and the accompanying imperfections are reduced to 70 %. Even though in literature such as e.g. [4] it is shown that usually the global imperfection as the leading one gives the smallest resistance, for the sake of completeness within this work all possible combinations are taken into account.

Annex C, EN 1993-1-5 [36] illustrates the global imperfection shape for stiffened panels according to Fig.4.36. One question that arises when applying the global imperfection to a plate stiffened with more than one longitudinal stiffener is where the magnitude for the imperfection amplitude should be measured. Fig.4.37 shows three different possible interpretations of Tab.4.6 on the example of a plate stiffened with four longitudinal stiffeners. In interpretation **1** the maximum amplitude is applied for the middle of the

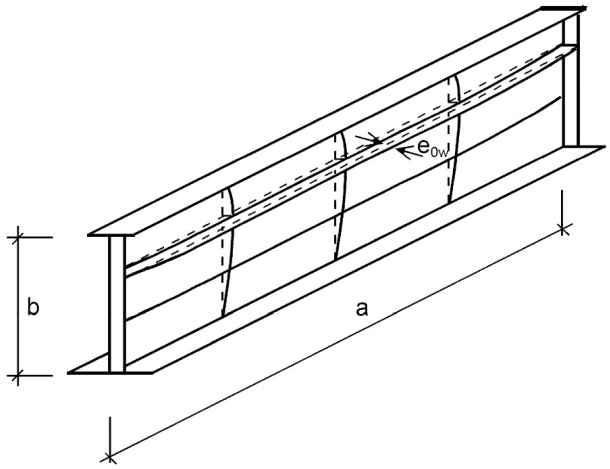

Figure 4.36: Global imperfection shape according to Annex C, EN 1993-1-5 [36].

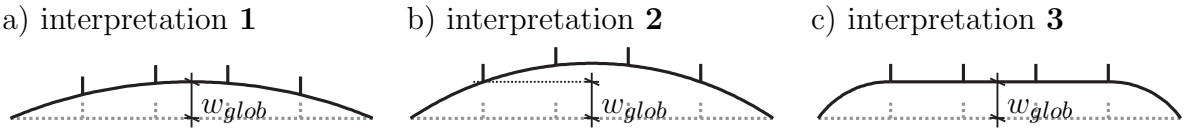

Figure 4.37: Applied imperfection types on a stiffened plate.

plate. This approach is the one often found in literature, as e.g. [4] and [110]. However, this may lead to very small imperfections for stiffeners near the edge. For this reason in interpretation **2** the maximum amplitude of the global imperfection is defined for the stiffener, which is close to the edge, leading in turn to increased amplitudes in the middle of the plate.

The imperfections are applied by adding sine functions to the perfect geometry. In case of interpretation **1** the maximum amplitude of the imperfection is as defined in EN 1993-1-5 [36], while for interpretation **2** the maximum amplitude, as mentioned above, is increased according to Eq.(4.7).

$$w_{0,\,max} = \frac{w_{0,\,EN\,1993-1-5}}{\sin\left(\frac{\pi \cdot b_{loc}}{b}\right)} \tag{4.7}$$

Herein, b_{loc} is the distance between the equally spaced stiffeners. Tab.4.7 shows a comparison of the maximum amplitude for interpretation **1** and **2** for equally spaced longitudinal stiffeners. While for only one stiffener the two approaches lead of course to the same amplitude, this changes with increasing number of stiffeners, leading to a difference in the maximum amplitude of up to 70 %.

In the third approach, denoted as interpretation **3**, the maximum amplitude is defined as for interpretation **2**, but is assumed constant between the longitudinal stiffeners. This approach leads to a more realistic imperfection shape, which is also similar to the failure

Table 4.7: Comparison of the maximum amplitudes according to interpretation 1 and 2.

No. of stiffeners	b_{loc}	$w_{0,max}^{int.\,2}$	$\frac{w_{0,max}^{int.\,2}}{w_{0,max}^{int.\,1}} \cdot 100\%$
1	$b/2$	$b/400$	100%
2	$b/3$	$b/346$	115%
4	$b/5$	$b/235$	170%

shape, where the outermost panels in general fails and the stiffeners move almost parallel. Interpretation **3** is therefore used for the following investigations.

4.7.4 Verification

Fig.4.38 a) shows all numerical results for plates with one, two and four single sided open stiffeners in comparison with the design rules according to EN 1993-1-5 [36] using EBPlate [16] for the determination of the critical buckling stress. For the sake of convenience the presented numerical results are already the minimum resistances for all regarded combinations of imperfections according to Annex C, EN 1993-1-5 [36]. Generally, it can be noted that the design rules and the numerical results are in a very good agreement. Of course, due to different influences and the complexity of the load bearing behaviour, a perfect match on the bisecting line ($R_{FEM} = R_{t,EN}$) cannot be found as in the case of the buckling curves for unstiffened plates. Nevertheless, the developed model can be regarded as suited for further parametric studies. It is noted here that for the analyses the boundary condition is chosen as BC-C according to Fig.4.19 and compared to the design procedure using the buckling curve according to Annex B, EN 1993-1-5 [36], see Sec.4.6, as the investigation of all boundary conditions would have gone beyond the scope of this work. Additionally, the resistance according to EN 1993-1-5 [36] is calculated also using Annex A for the determination of the critical buckling stress and marked with blue crosses. It can be noticed that, compared with the results gained by using EBPlate [16], slightly more conservative values are obtained. In Fig.4.38 b) - d) the results are also shown separately for plates stiffened with one, two and four stiffeners. While for plates with one stiffener the numerical results match very well with the code rules, the results scatter more to the conservative side when more than one stiffener is considered. Similar conclusions can also be found in [5] and the Background Document to Work Package 1.1 of the COMBRI-project [66].

Some lower resistances are found for plates stiffened with one longitudinal stiffener, see Fig.4.38 b) and Fig.4.39 a). A further break down of the results in different panel aspect ratios α in Fig.4.39 b) - d) shows a very narrow distribution for $\alpha = 1$, while for longer plates the scatter is slightly higher. Some lower results are only found for the cases with the weak stiffener $\gamma = 7$ and high b/t-ratios. The results with the stiffeners $\gamma = 25$ and 65 are found higher than with the design procedure according to Chapter 10, EN 1993-1-5 [36].

a) all results

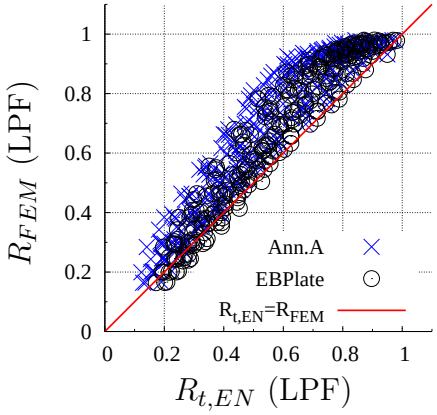

b) one stiffener

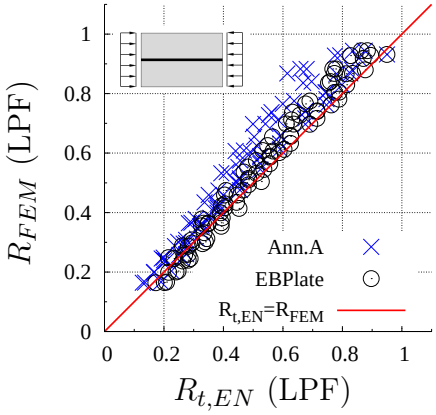

c) two stiffeners

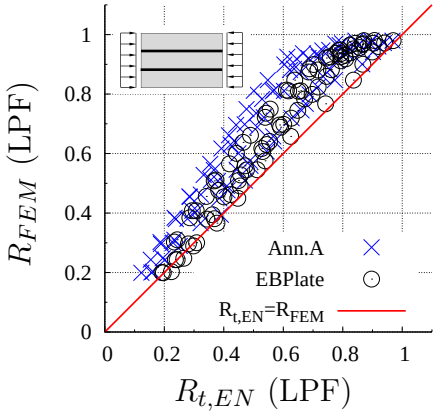

d) four stiffeners

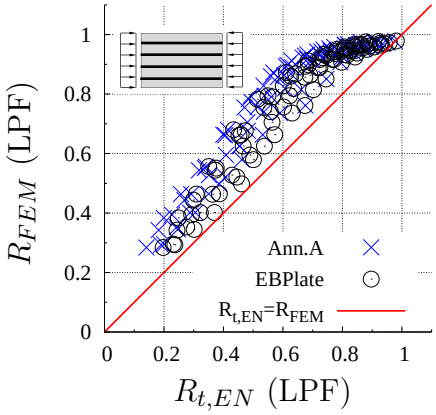

Figure 4.38: Statistical comparison of simulations and design according to EN 1993-1-5 [36] for stiffened plates.

a) all results

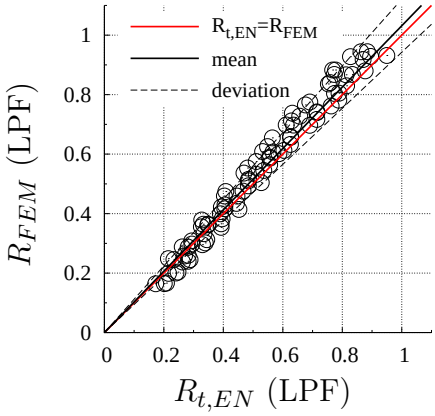

b) $\alpha_{glob} = 1.0$, $\alpha_{loc} = 2.0$

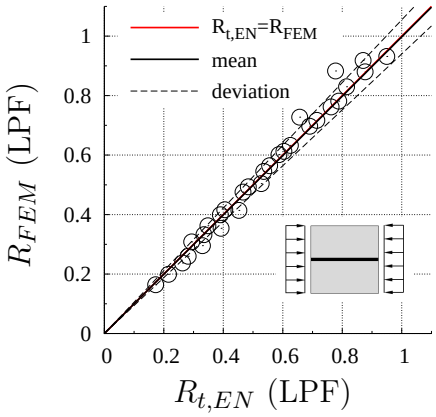

c) $\alpha_{glob} = 1.5$, $\alpha_{loc} = 3.0$

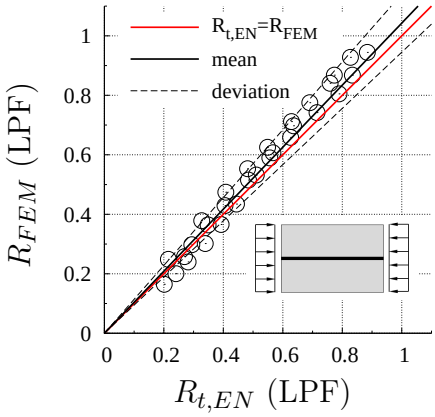

d) $\alpha_{glob} = 2.0$, $\alpha_{loc} = 4.0$

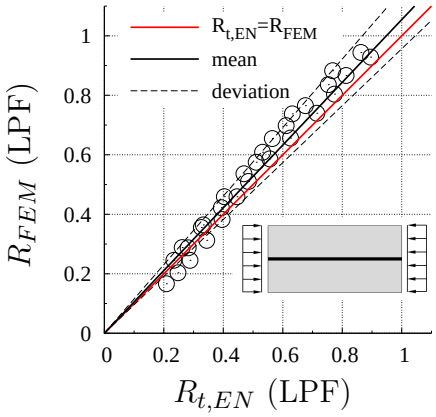

Figure 4.39: Statistical comparison of simulations and design according to EN 1993-1-5 [36] for stiffened plates (one stiffener).

4.8 Summary

In order to investigate a wide parametric range for analysing the buckling behaviour of multiaxially stressed plates the Finite Element Method is adopted within this work. After an overview on the method and the assumptions in accordance to Annex C, EN 1993-1-5 [36] the recalculations of the experimental investigations presented in Sec.3 are conducted, showing an appropriate agreement between the experimental and the numerical investigations in sense of global and local response, so that the applied procedure for conducting the numerical investigations can be regarded as verified. However, for the realisation of the parametric studies in the following chapter, simplified models are generated considering several kinds of boundary conditions. The models are validated by prior knowledge from the buckling curves using the approach from Usami [118] recommended by Lindner & Rusch [74] and also adopted by Braun [11]. While for pure compression $\psi = 1$ the numerical simulations showed almost perfectly the Winter curve, in case of stress gradients $\psi < 1$ the numerical simulations met the buckling curves from DIN 18800-3 [22]. In this case the curves from EN 1993-1-5 [36] give more conservative results. These results are quite interesting, as both approaches merge into the Winter curve for the "extreme" case of pure compression.

For investigating the buckling behaviour of longitudinally stiffened plates, a numerical model is developed based on the outcomes from the numerical investigations on unstiffened plates. The longitudinal stiffeners are applied as open sections and the dimensions are chosen to avoid torsional buckling of the stiffeners. In order to cover a wide parametric range, three different relative stiffness are applied to the plate as well as different panel aspect ratios and numbers of the stiffeners. For the validation of the model the results of the numerical simulations are compared to the design rules according to EN 1993-1-5 [36] using the buckling curve from Annex B, EN 1993-1-5 [36] for pure compression. Even though the scatter of the results is larger than for unstiffened plates, which is in the nature of the problem and was already observed in the COMBRI-project [66], the model shows to perform properly, so that the model can be regarded as suited for further investigations on stiffened plates subjected to biaxial compression.

5 Parametric studies on multiaxially loaded plates

5.1 General

In order to obtain an adequate database for the further step of evaluating or improving the current design rules given in EN 1993-1-5 [36] a large number of simulations has been conducted in the frame of the following parametric studies. The study on unstiffened plates is subdivided into two parts. In the first part the effect of tensile stresses on the buckling behaviour under direct stresses is investigated and in the second part the effect of tensile and compressive direct stresses on shear buckling considering also stress gradients. The simulations are conducted for the whole range of interaction and for different boundary conditions as well as imperfection shapes, which allows the identification of their influences. Sec.5.5 – Sec.5.7 focus on unstiffened plates, which represent the basic case for the application of the buckling rules, which should therefore reproduce the buckling behaviour under multiaxial stress states as accurate as possible. Stiffened plates are treated in a further step in Sec.5.8.

All the regarded load combinations and variations of the boundary conditions and imperfection shapes have been conducted for different width-to-thickness ratios b/t as well as for different length-to-width ratios α. The material used for the parametric study has a yield strength of $f_y = 355\,\mathrm{N/mm^2}$ and no strain hardening has been accounted for, thus a yield plateau according to EN 1993-1-5 [36] has been applied, see Sec.4.

5.2 Imperfections

As described in Sec.4.3.1 in general the imperfections can be distinguished into realistic, worst case and stimulating imperfections. Since the imperfection shape has a decisive impact on the buckling behaviour as already shown for example by Dow & Smith [28] or Ueda et al. [115], a special attention is paid to this issue. The aim of the parametric study is to obtain preferably realistic and also safe sided results considering mode transitions, see Sec.3.2. This can only be achieved when applying imperfection shapes, which are likely to be found in real structures rather than applying high-frequent imperfection shapes which result e.g. from a linear buckling analysis (LBA). Jönsson & Bondum [53] e.g. used in their analyses imperfection shapes with up to ten half

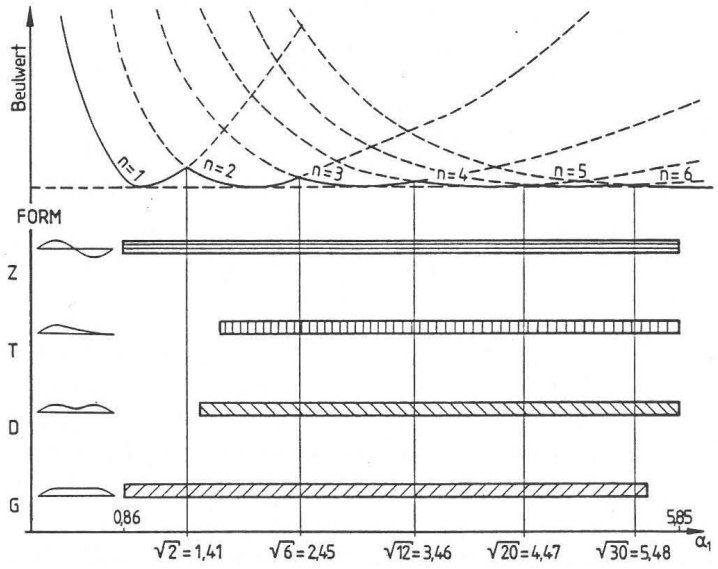

Figure 5.1: Measured imperfection shapes plotted against the length-to-width ratio α, [41].

waves for a length-to-width ratio of $\alpha = 4$. This assumption led to conservative results, which were used in a further step in defining reduction curves. Real measurements have been conducted by FISCHER ET AL. [41] on stiffened and unstiffened slender steel bridge plates with length-to-width ratios $0.86 \leq \alpha = a/b \leq 7.08$. The results show that for ratios $\alpha > \sqrt{2}$ the measured imperfections differ from the first eigenmode, so that for $\alpha = 3$ the "three-wave mode" was practically never observed. The measured imperfection shapes from [41] are plotted against α in Fig.5.1 (where "Beulwert" is the German term for buckling coefficient). It can be seen that for short plates one- and two-wave imperfections were found, while for longer plates additionally "drop"-shapes (T) and three-wave imperfections (D) were observed. It should be mentioned, that the observed three-wave imperfection in [41] is a superposition of a one- and a three-wave mode, so that a numerical approach with a pure three-wave imperfection shape is on the safe side.

BRAUN [11] conducted investigations on slender plates in the range of biaxial compression for $\alpha = 1$ and 3, where the three-wave mode has been used in order to aim at a lower bound. For the further studies within this work a similar approach is chosen, as the experimental investigations in Sec.3.2 and also the numerical investigations in Sec.4.4 revealed mode transitions for the failure modes. These mode-jumps are also observed for the parametric study, so that especially with increasing b/t-ratios, the three-wave imperfection is able to eliminate increased ultimate loads due to suppressed mode-jumps. This can be explained by the fact that, depending from the applied parameters, the plate tends to buckle in a certain failure mode. As the initial imperfection may not correspond to this mode, the ultimate load is then increased by the stiffness of the plate until the maximum load is exceeded and a mode transition occurs, leading to a sudden drop in the load-displacement curve. This effect is shown more in detail in Sec.5.5.2.

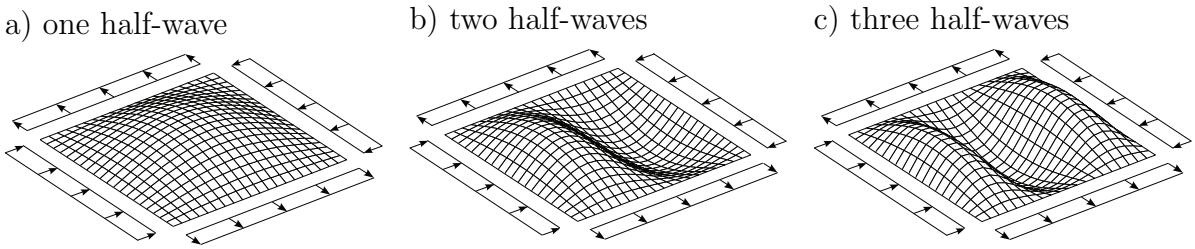

Figure 5.2: Imperfections for the parametric study on direct stresses for $\alpha = 1$.

In the compression–tension investigations for square plates as well as for long plates the imperfections have been applied as sine-functions with one to three half-waves, see Fig.5.2. The three-wave mode does in this case of course not represent a realistic initial imperfection, but is used for aiming at a lower bound for the before mentioned reasons. The tension–shear as well as compression-shear investigations are conducted on plates with a length-to-width ratio of $\alpha = 2$ using one- and two-wave imperfection shapes. Both imperfection amplitudes $b/200$ and 420 are used to observe the sensitivity on the buckling behaviour.

As Braun [11] showed that residual stresses do not significantly increase the quality of the recalculations of the buckling curves, and geometric imperfection and residual stresses have to be adjusted in every case such that a good agreement with the relevant buckling curve can be achieved, also in the parameter studies within this work equivalent geometric imperfections are considered as fully sufficient.

5.3 Loading

The loading of the model is performed using so-called "shell edge loads" that are applied as line loads along the edges. The ratio of the stresses in both directions (σ_z/σ_x) is defined and adjusted using the interaction angle presented in Eq.(2.5). In order to investigate the interaction domain accurately, the individual angle steps $\Delta\Theta$ are set to 5°, where Θ is defined according to Fig.2.1. The amounts of the applied stresses are calculated with a transformation of the von Mises criterion according to Eq.(5.1), where the equivalent stress σ_v is set equal to the yield stress f_y.

$$\begin{aligned} \sigma_v = \sqrt{\sigma_x^2 + \sigma_z^2 - \sigma_x \cdot \sigma_z + 3 \cdot \tau^2} &\stackrel{!}{=} f_y \\ \Rightarrow \sigma_x^2 + \beta^2 \cdot \sigma_x^2 - \beta \cdot \sigma_x^2 &= f_y^2 \\ \Rightarrow \sigma_x = \frac{f_y}{\sqrt{\beta^2 - \beta + 1}} & \end{aligned} \tag{5.1}$$

where: $\sigma_z = \beta \cdot \sigma_x$ (see also Eq.(2.5))

For the investigations on the interaction of direct stresses and shear the analogue procedure is conducted using the interaction parameter $\beta_\tau = \tau/\sigma_x$ and the interaction angle Θ_τ, which is varied as well in small steps of $\Delta\Theta_\tau = 5°$ to precisely cover the interaction domain. The transformation of the von Mises criterion leads to the stress relations given in Eq.(5.2).

$$\begin{aligned} \sigma_v &= \sqrt{\sigma_x^2 + \sigma_z^2 - \sigma_x \cdot \sigma_z + 3 \cdot \tau^2} \quad \stackrel{!}{=} f_y \\ &\Rightarrow \sigma_x^2 + 3 \cdot \beta_\tau^2 \cdot \sigma_x^2 \qquad\qquad\quad = f_y^2 \\ \Rightarrow \sigma_x &= \frac{f_y}{\sqrt{3 \cdot \beta_\tau^2 + 1}} \end{aligned} \tag{5.2}$$

where: $\tau = \beta_\tau \cdot \sigma_x$

By referencing the applied load with respect to the von Mises criterion as shown in Eq.(5.1) and Eq.(5.2) the LPFs resulting from the numerical simulations represent directly the global reduction factors, see also Eq.(4.2) in Sec.4.2.

5.4 Implementation of the model

The implementation of the numerical model is done with the use of the ABAQUS-intern Python interpreter [105] and several Matlab subroutines [79]. Fig.5.3 shows an overview of the applied procedure. The models, which have been verified in Sec.4.6 and Sec.4.7 are described by the respective parametrised models in the programming language Python. For further information on the programming language Python reference is made to [88].

The parameters are then modified by Matlab subroutines using the specified input parameters such as the geometry and the loading of the plate. Afterwards the input files are generated using the ABAQUS-intern Python interpreter. These input files are still without imperfections, so that the next Matlab subroutines add the defined imperfections to the model according to Sec.5.2. The generated input files are then queued in ABAQUS and executed one after the other by batch processing.

After conducting the numerical simulation on the model including imperfections, the results are evaluated using another subroutine exporting the load proportionality factor (LPF), the displacements as well as figures of each simulation, which allows for monitoring them in case of convergence problems.

The applied procedure is clearly structured and allows for analysing a large parameter range. As the input is always derived from the verified model and the output is monitored for all simulations the gained data from the parametric studies can be regarded as consistent. The same approach is adopted in principle for all realised parametric studies including also the investigations on stiffened plates presented in Sec.5.8.

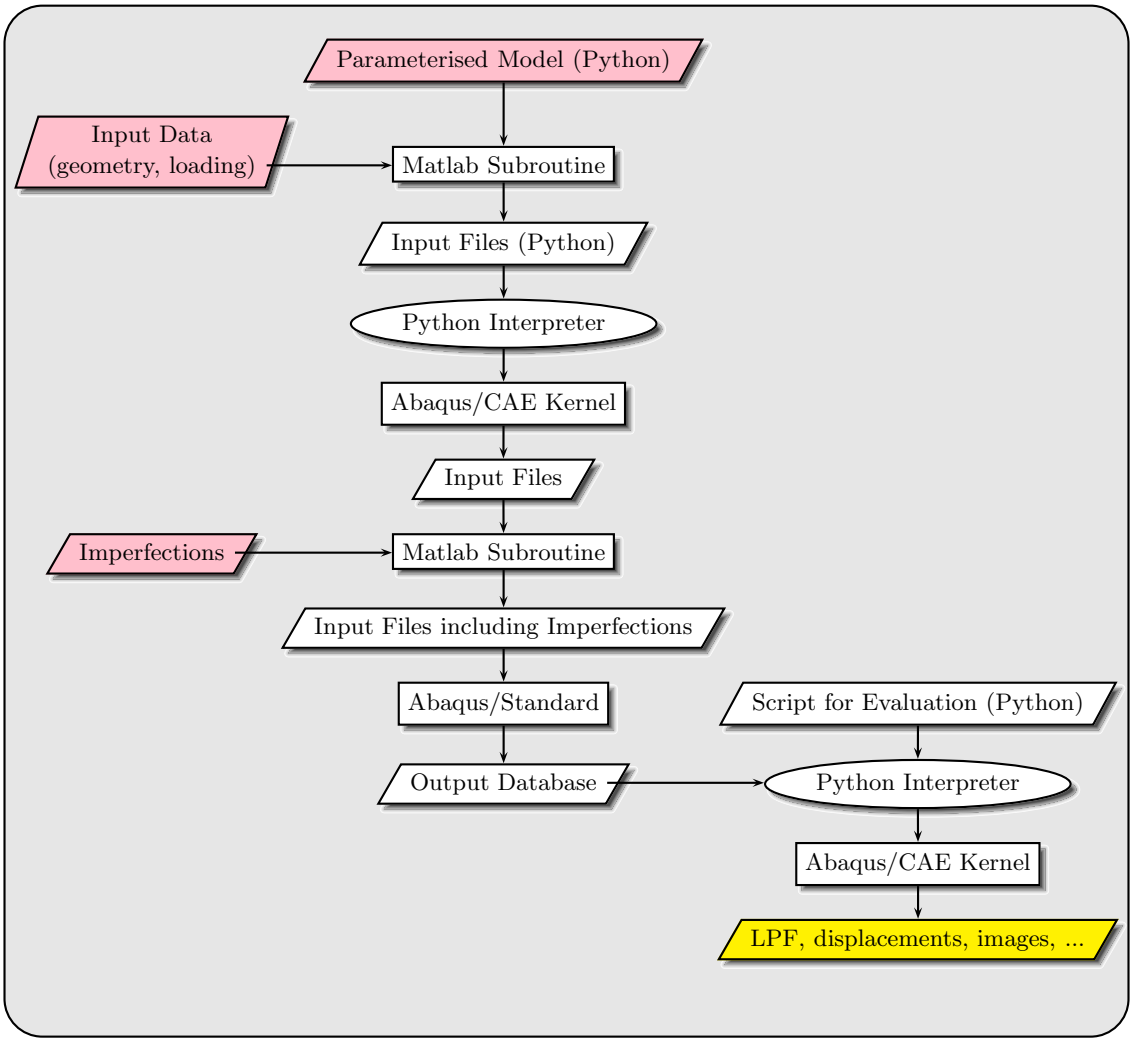

Figure 5.3: Implementation of the model and procedure for the parametric study.

5.5 Tension–Compression

5.5.1 Overview

For evaluating the buckling behaviour of slender plates subjected to tension–compression a large parametric study is presented in the following sections. A variation of the listed effecting parameters is conducted:

- Tension–compression ratios over the whole range (steps of $\Delta\Theta = 5°$, see Sec.5.3)
- Slenderness $b/t = 30, 45, 65, 100, 150$ and 250
- Panel aspect ratios $\alpha = 1$ and 3
- Imperfection shapes and amplitudes (one, two and three half-waves, $w_0 = b/200$ and $b/420$)
- Edge boundary conditions (free to move in-plane vs. restrained, hinged vs. clamped)

The results on square plates $\alpha = 1$ are presented in Sec.5.5.2 and the ones for long plates $\alpha = 3$ in Sec.5.5.3.

5.5.2 Investigations on square plates

The results of the parametric study on square plates subjected to tension–compression are for the sake of clarity subdivided by the type of edge boundary conditions, see Fig.4.19 (BC-A, BC-B, BC-C with hinged and BC-Ac with clamped edges). Additionally, for BC-A the results are subdivided by the applied imperfection shape (one, two and three half-waves) in order to highlight the effect on the buckling resistance in dependence on the interaction angle Θ, see Fig.2.1. Therefore Fig.5.4 to Fig.5.7 show the results for boundary condition BC-A, which has the compressed edges constrained to remain straight in-plane, while the edges loaded with tension are free to move in-plane. To reduce the volume of this section, the results for the other boundary conditions are presented already as the minimum from all investigated imperfection shapes and compared to BC-A.

Effect of Imperfections

In Fig.5.4 with the one half-wave imperfection shape for the b/t-ratios up to 100 an increase of the applicable compression stresses can be observed just until slightly before the curve reaches the von Mises criterion. In the case of $b/t = 150$ and 250 a sudden drop of the curves can be observed. This is due to failure-mode transitions, where the shape changes from a one half-wave to a three half-wave shape. The increased resistance that occurs just before the drop is due to the fact that the imperfection shape "forces" the plate to buckle in a one half-wave mode. For the lower b/t-ratios, where the drop does not occur, the stiffness of the plate is sufficient to keep it in the predetermined buckling shape, while for the more slender plates the stiffness is not sufficiently high and so a mode transition takes place. This can also be observed by the earlier drop of resistance for the plate with $b/t = 250$ compared to $b/t = 150$. This effect has also been observed during the experimental investigations as shown in Sec.3.2.5.

For the stockier plates a different behaviour is observed using a two half-wave imperfection shape, see Fig.5.5. The increase of the applicable compression stresses do not develop as for the one half-wave imperfection shape, so that the curve falls with increasing tension. On the other hand the curve starts at a higher level for pure compression compared to the one half-wave curve, resulting in an intersection between both curves. For the more slender plates a similar behaviour for both imperfection shapes can be observed. The plate with $b/t = 250$ again shows a drop in the curve. Here the failure mode jumps from a two half-wave mode to a four half-wave mode.

Fig.5.6 shows the interaction curves for the plates using a three half-wave imperfection shape. It can be noticed for $b/t = 65$, 100 and 150, that the interaction curves possess sharp bends where the interaction curve changes from increasing to decreasing with the amount of tension and the interaction curve of the plate with $b/t = 250$ does not show a sudden drop anymore. Another observation is the influence of the imperfection amplitudes $b/200$ and $b/420$ when comparing the curves. While generally it can be found, as also shown in Sec.4.6.4 for the recalculation of the buckling curves, that with increasing b/t-ratio and therefore higher slenderness the imperfection amplitude has a rather minor influence, for the compression–tension interaction the influence of the imperfection amplitude on the buckling behaviour becomes noticeable.

In order to get a safe-sided design procedure the lower envelopes of the interaction curves are used for further analyses. Fig.5.7 shows the decisive interaction curves for the boundary condition BC-A for all regarded plates. The curves have a monotone character and the sudden drops observed for the very slender plates are eliminated, so that no increase of the capacity due to suppressed mode transitions is accounted for.

The effect of the imperfection shape is illustrated exemplarily for selected cases in Fig.5.8 ($b/t = 150$) and Fig.5.9 ($b/t = 250$), where the load-proportionality-factor is plotted against the displacement of the compressed edge. In case of the plate with $b/t = 150$ shown in Fig.5.8 the curve is smooth and the failure-mode has one half-wave up to the interaction angle $\Theta = 25°$, see Fig.2.1. For higher interaction angles the curve has a sharp bend (marked with a circle) where the mode changes from one half-wave to three half-waves leading to reduced load-proportionality-factors. The sharp bend occurs earlier for the smaller imperfection amplitudes, which is obvious since the "obstacle" for the plate to buckle in the three half-wave mode is lower. In case of the plate with $b/t = 250$ the curve shows a snap-through behaviour for the interaction angle $\Theta = 65°$, where the buckling mode jumps from two half-waves to four half-waves, see circles in Fig.5.8 and Fig.5.9. For the evaluation of the results the second peak marked with triangles is considered as relevant. In Fig.5.10 the numerical results based on the decisive imperfection are normalised, or in other words, related to the results for pure compression showing the influence of the tensile stresses on plates with different slenderness. It is noticeable, that with increasing b/t-ratio the influence increases leading to elevated allowable compression stresses of up to over 30 % for $b/t = 250$ compared to the pure compression case.

a) $b/t = 30$

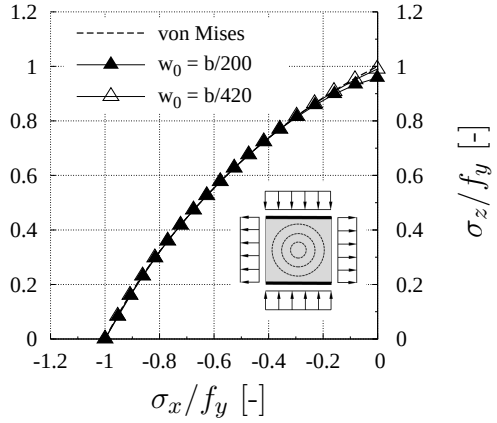

b) $b/t = 45$

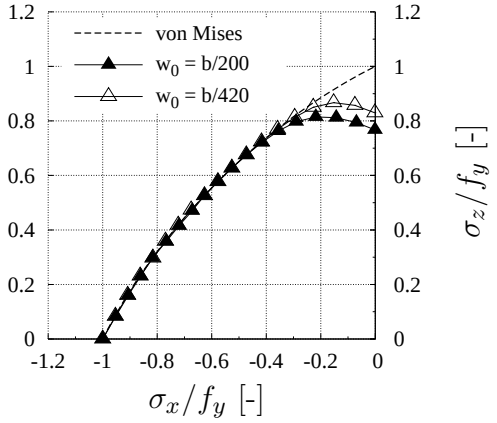

c) $b/t = 65$

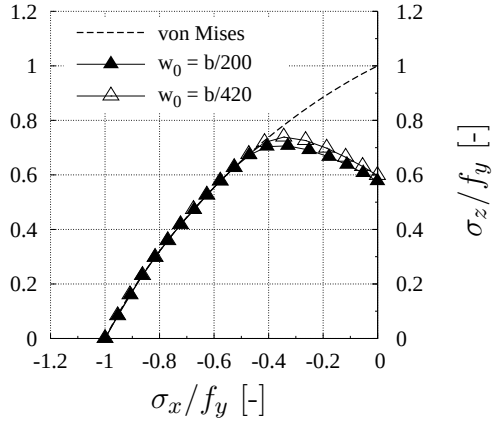

d) $b/t = 100$

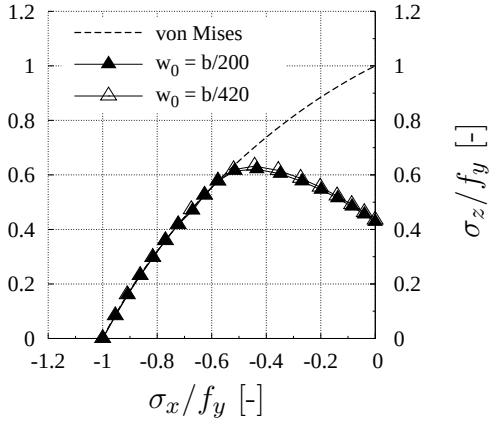

e) $b/t = 150$

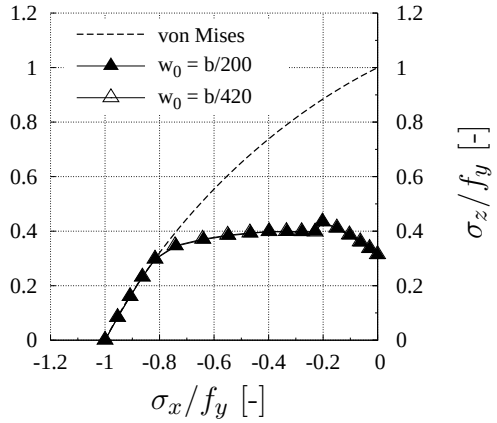

f) $b/t = 250$

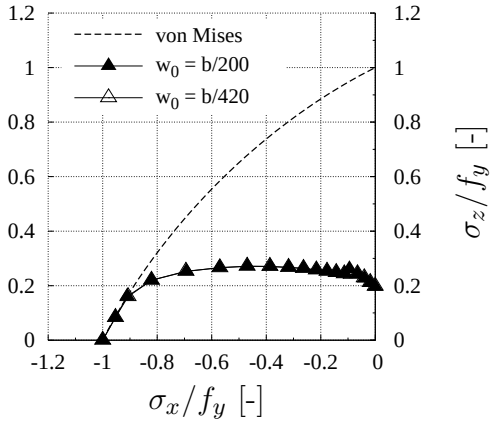

Figure 5.4: Numerical results for edges loaded with compression being constrained (BC-A, $\alpha = 1$, all edges hinged, 1-half-wave imperfection).

a) $b/t = 30$

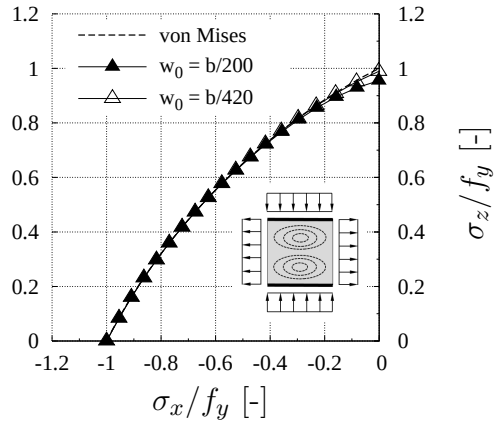

b) $b/t = 45$

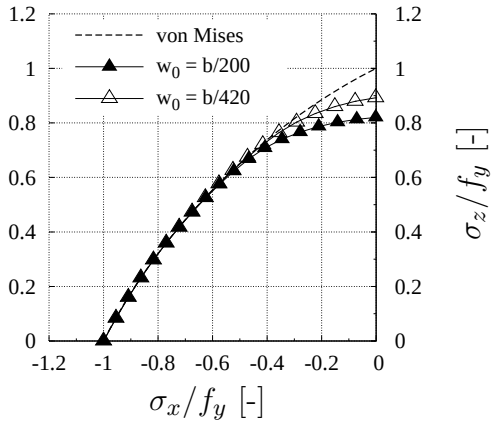

c) $b/t = 65$

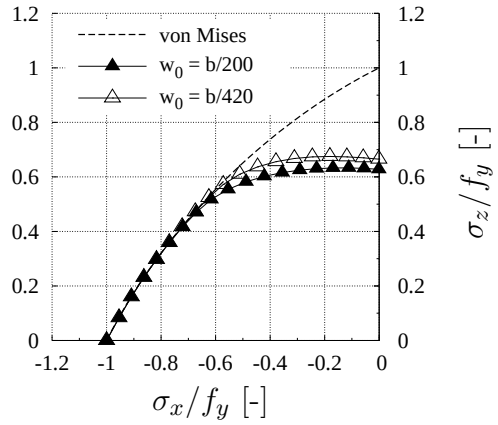

d) $b/t = 100$

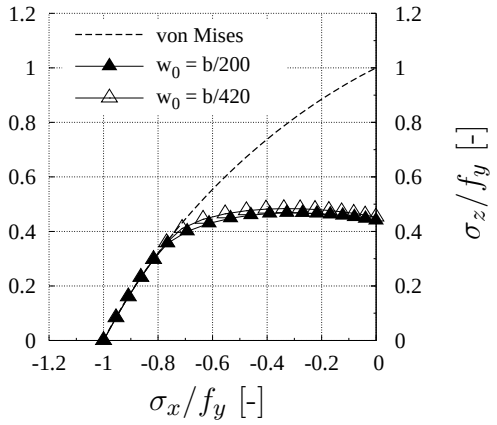

e) $b/t = 150$

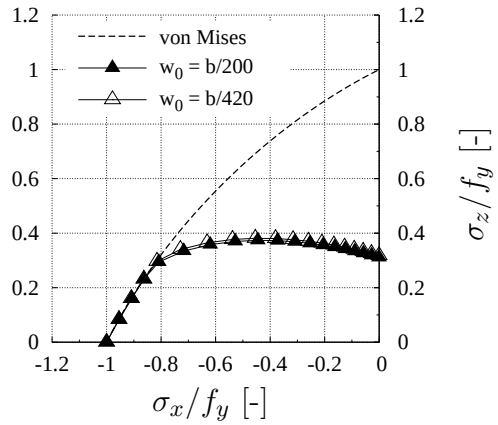

f) $b/t = 250$

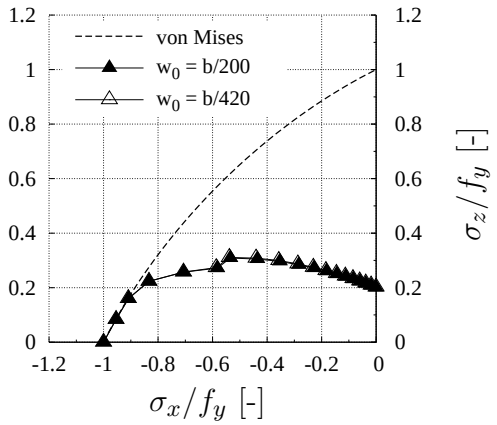

Figure 5.5: Numerical results for edges loaded with compression being constrained (BC-A, $\alpha = 1$, all edges hinged, 2-half-waves imperfection).

a) $b/t = 30$

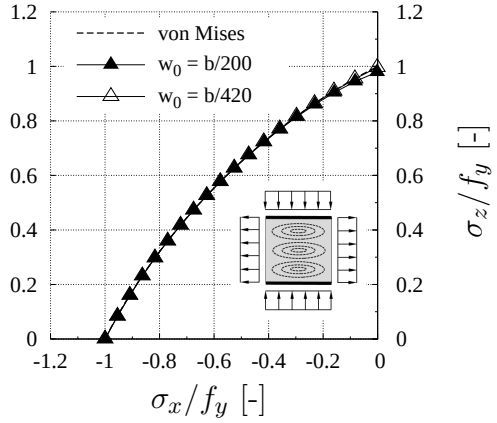

b) $b/t = 45$

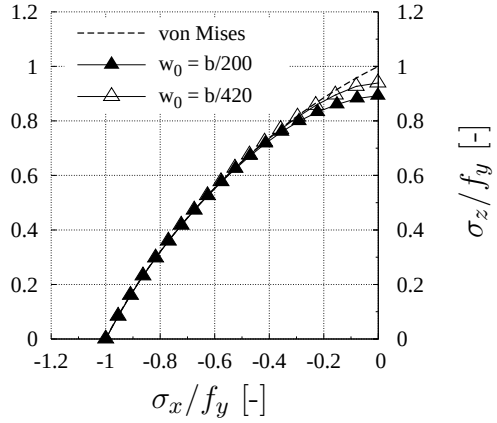

c) $b/t = 65$

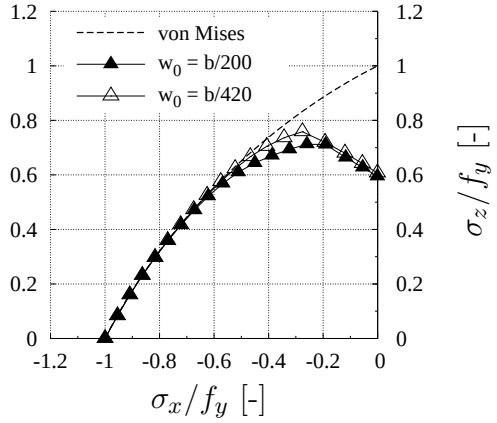

d) $b/t = 100$

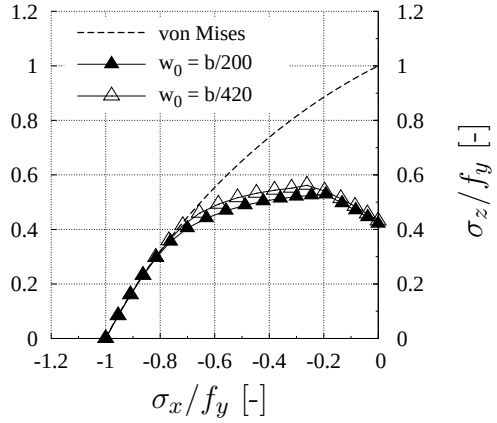

e) $b/t = 150$

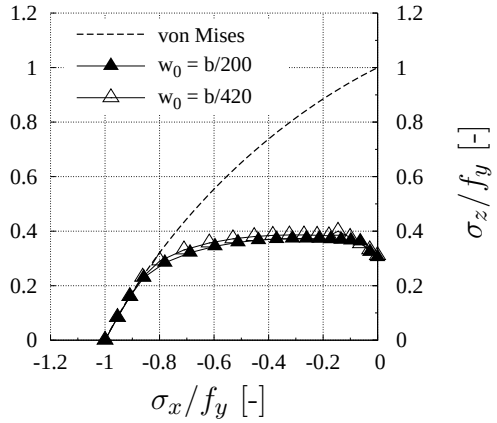

f) $b/t = 250$

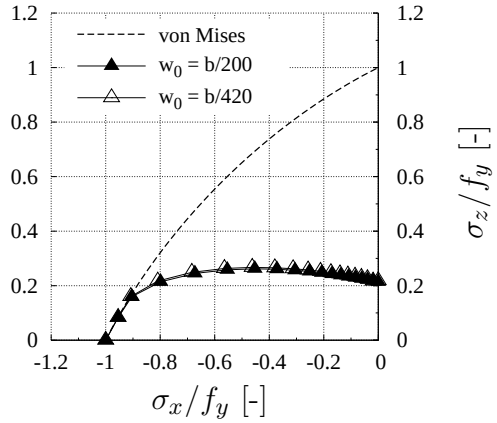

Figure 5.6: Numerical results for edges loaded with compression being constrained (BC-A, $\alpha = 1$, all edges hinged, 3-half-waves imperfection).

a) $b/t = 30$

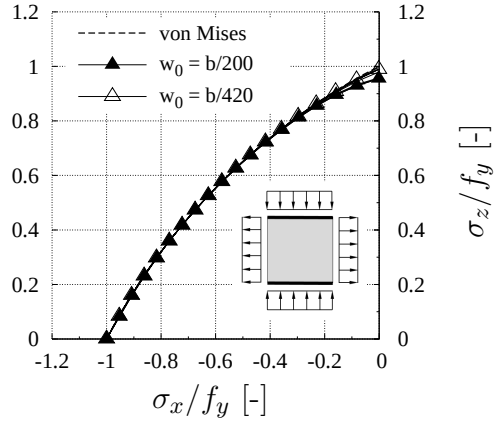

b) $b/t = 45$

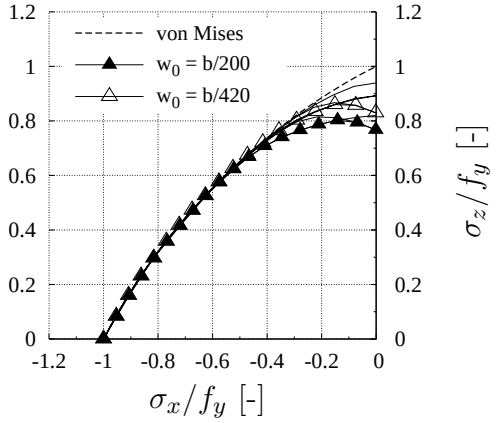

c) $b/t = 65$

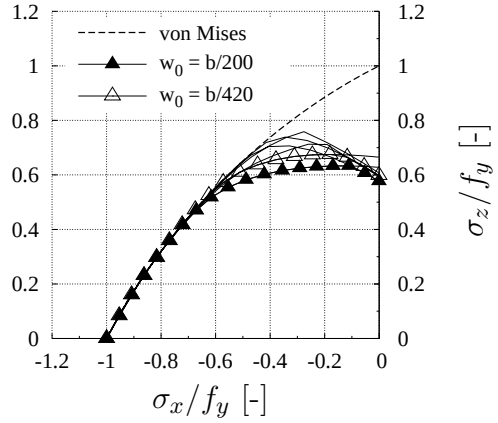

d) $b/t = 100$

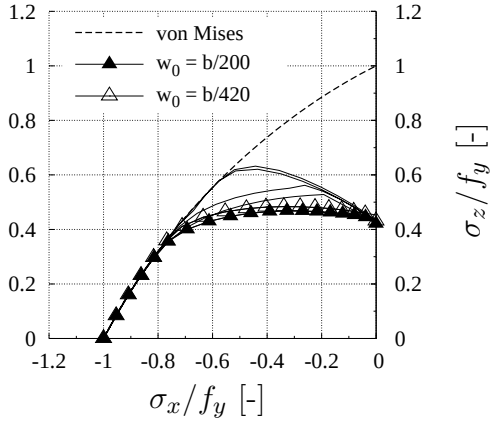

e) $b/t = 150$

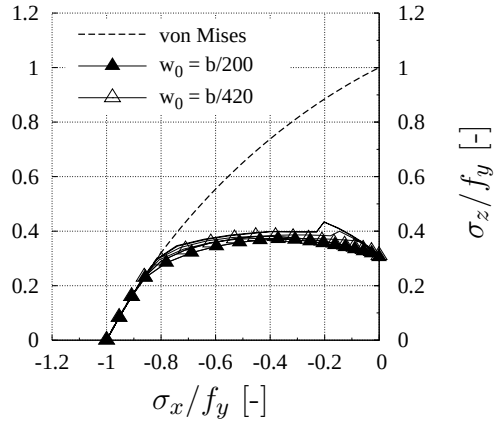

f) $b/t = 250$

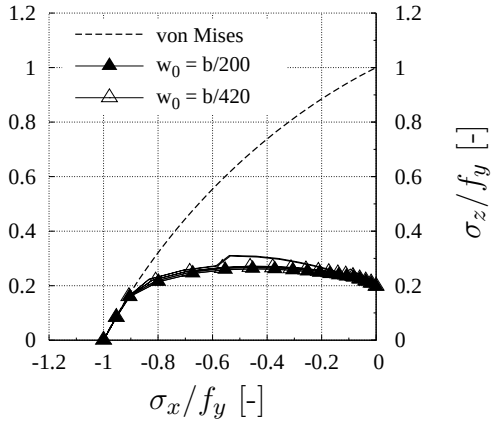

Figure 5.7: Numerical results for edges loaded with compression being constrained (BC-A, $\alpha = 1$, all edges hinged, decisive imperfection).

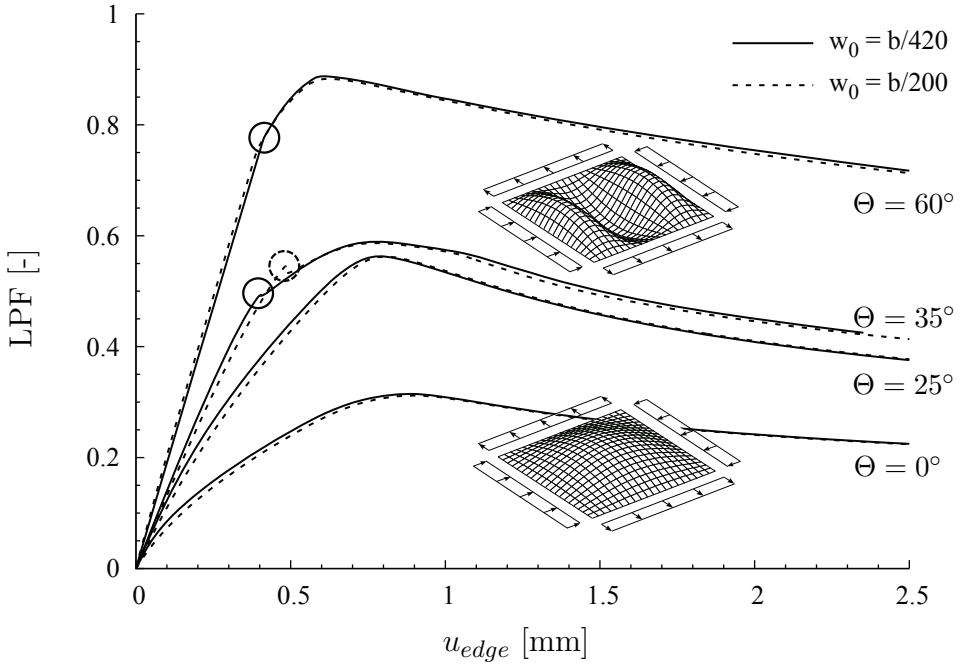

Figure 5.8: Load-Proportionality-Factor (LPF) against displacement of loaded edge (BC-A, $\alpha = 1$, $b/t = 150$, 1-half-wave imperfection).

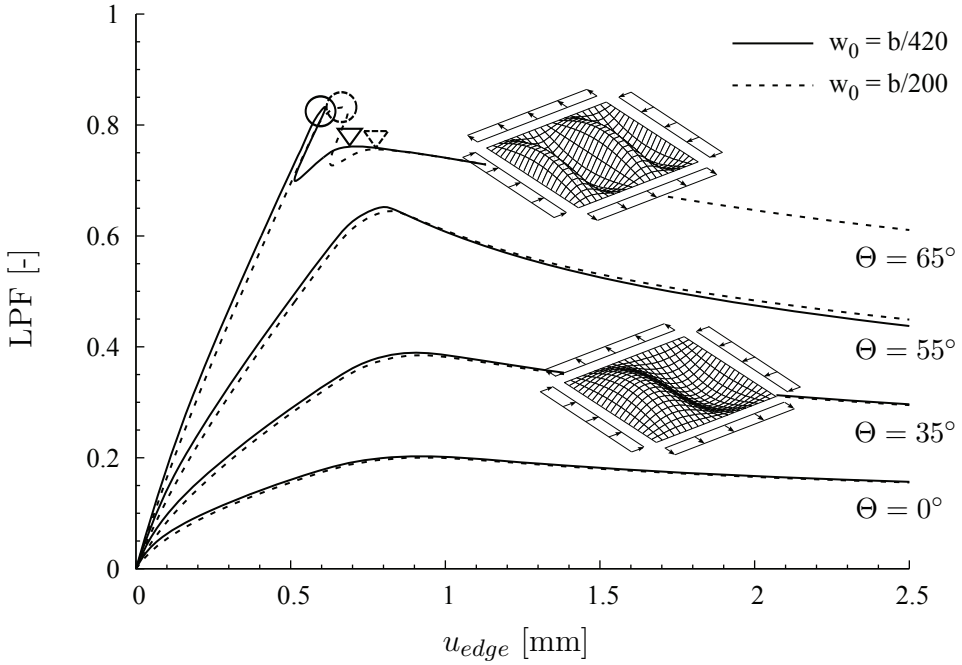

Figure 5.9: Load-Proportionality-Factor (LPF) against displacement of loaded edge (BC-A, $\alpha = 1$, $b/t = 250$, 2-half-wave imperfection).

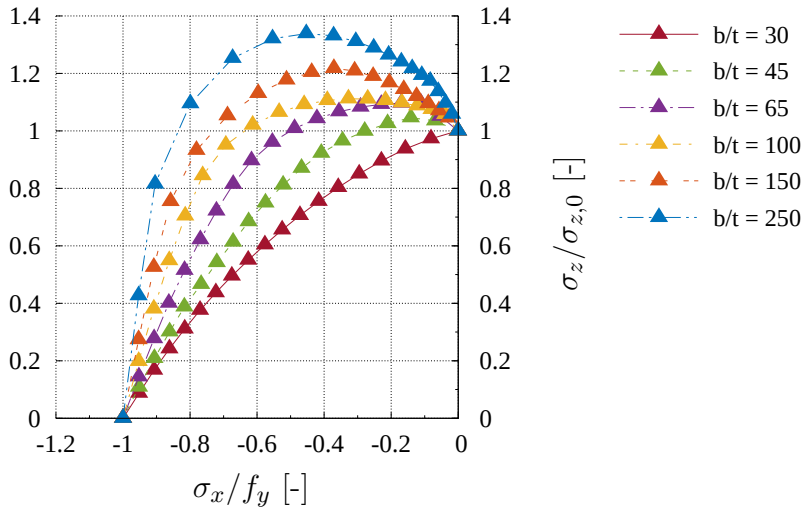

Figure 5.10: Numerical results for edges loaded with compression being constrained, normalised values (BC-A, $\alpha = 1$, $w_0 = b/200$, all edges hinged, decisive imperfection).

Effect of boundary conditions

As the buckling behaviour depends on the chosen boundary conditions, which was shown in the recalculation of the buckling curves in Sec.4.6.4 and also by Braun [11], the investigations for the compression–tension range are conducted for various boundary conditions. Thereby of course the same procedure is followed as described for the model with boundary condition BC-A concerning e.g. the application of the initial imperfections and the loading of the model. The following curves show already the curves gained by the decisive imperfection in order to keep this section manageable.

At first, the effect of the rotational edge restraints is investigated and compared to the hinged edges in Fig.5.11. Therefore the results for the **c**lamped edges are named as BC-A**c**. The increase of the resistance for pure compression is clearly noticeable and around 40 %. Comparisons of the curves for the clamped plates approach to the curves for the hinged plates show with increasing tensile stresses that the influence of the edge clamping vanishes. This means that the increase of the resistance due to rotational edge restraints, which usually provides a strength reserve since the design is done using hinged boundary conditions and partially clamped conditions are present in reality, is not given over the whole interaction range for the same amount. It can also be seen that all curves reach the von Mises criterion at the same interaction angle Θ, independently from the rotational boundary condition. Furthermore no noticeable increase in the applicable compression stresses is observed over the whole interaction range, except for $b/t = 250$ where a small increase takes place. The interaction curve is

nearly monotonically decreasing with higher tensile stresses.

The effect of the in-plane edge restraints is investigated in a next step with the boundary conditions used in Sec.4.6.4 for the recalculation of the buckling curves. The results using boundary condition BC-B according to Fig.4.19 are shown in Fig.5.12 in comparison to BC-A. The effect is rather small and concentrated in the region of pure compression. With increasing tension the results of BC-B approach quickly to the ones of BC-A, showing that the in-plane edge restraints in direction of the tension stresses do not play an important role.

In contrast to this, the results using the boundary condition with all edges free to move in-plane (BC-C), show that the in-plane edge restraints in the direction of compression influence the buckling behaviour almost over the whole interaction range until reaching the von Mises criterion. For the plates with $b/t = 30$ and 45 there is almost no difference between BC-A and BC-C, which is obvious since the buckling curve from Annex B, EN 1993-1-5 [36] also approaches the Winter curve for small slenderness. Nevertheless, for all regarded plates the curves again reach the von Mises criterion at the same interaction angle Θ, see Fig.2.1.

The results are referred to pure compression (normalised) and summarised in Fig.5.14 for all boundary conditions. The most influencing parameters for the compression–tension interaction behaviour, when referred to the pure compression resistance, are the in-plane edge restraints in the direction of compression. For boundary condition BC-C the increase of the applicable compression stresses is up to about 50 %, while the increase in case of boundary conditions BC-B and BC-Ac is negligible. The latter two have a similar influence on the buckling behaviour with increasing slenderness.

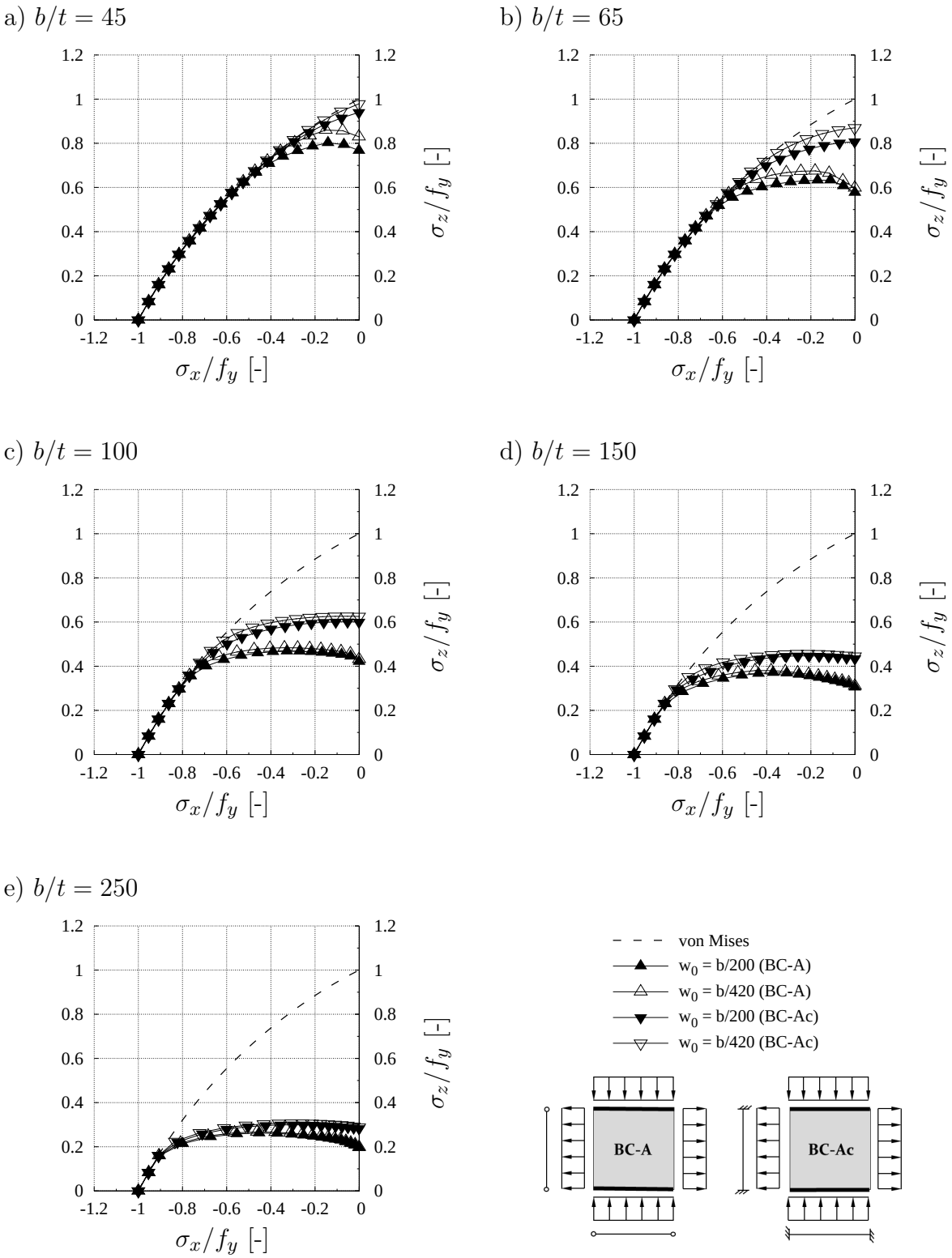

Figure 5.11: Comparison of hinged edge (BC-A) to clamped edge (BC-Ac) in the tension-compression interaction domain.

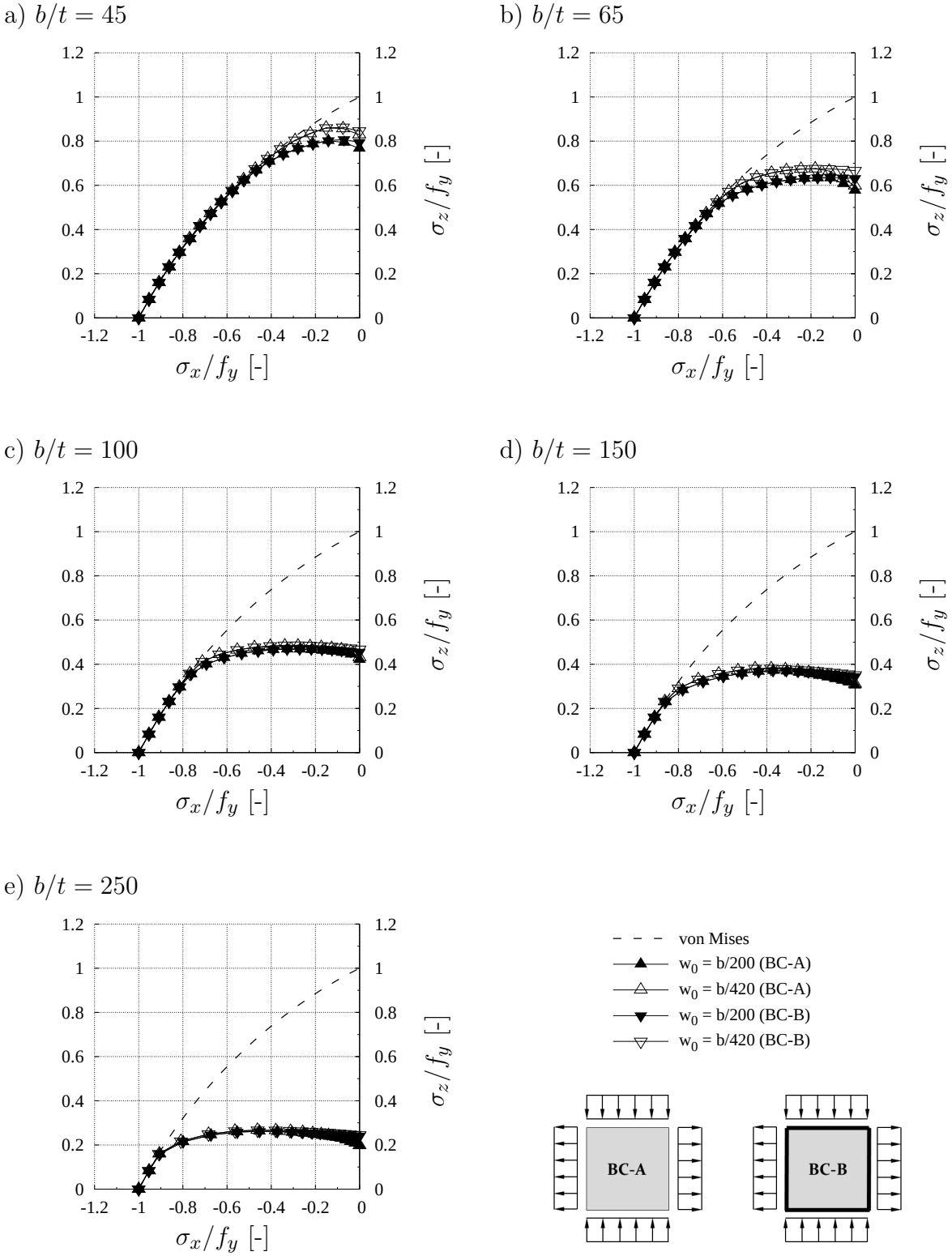

Figure 5.12: Comparison of BC-A to BC-B in the tension-compression interaction domain.

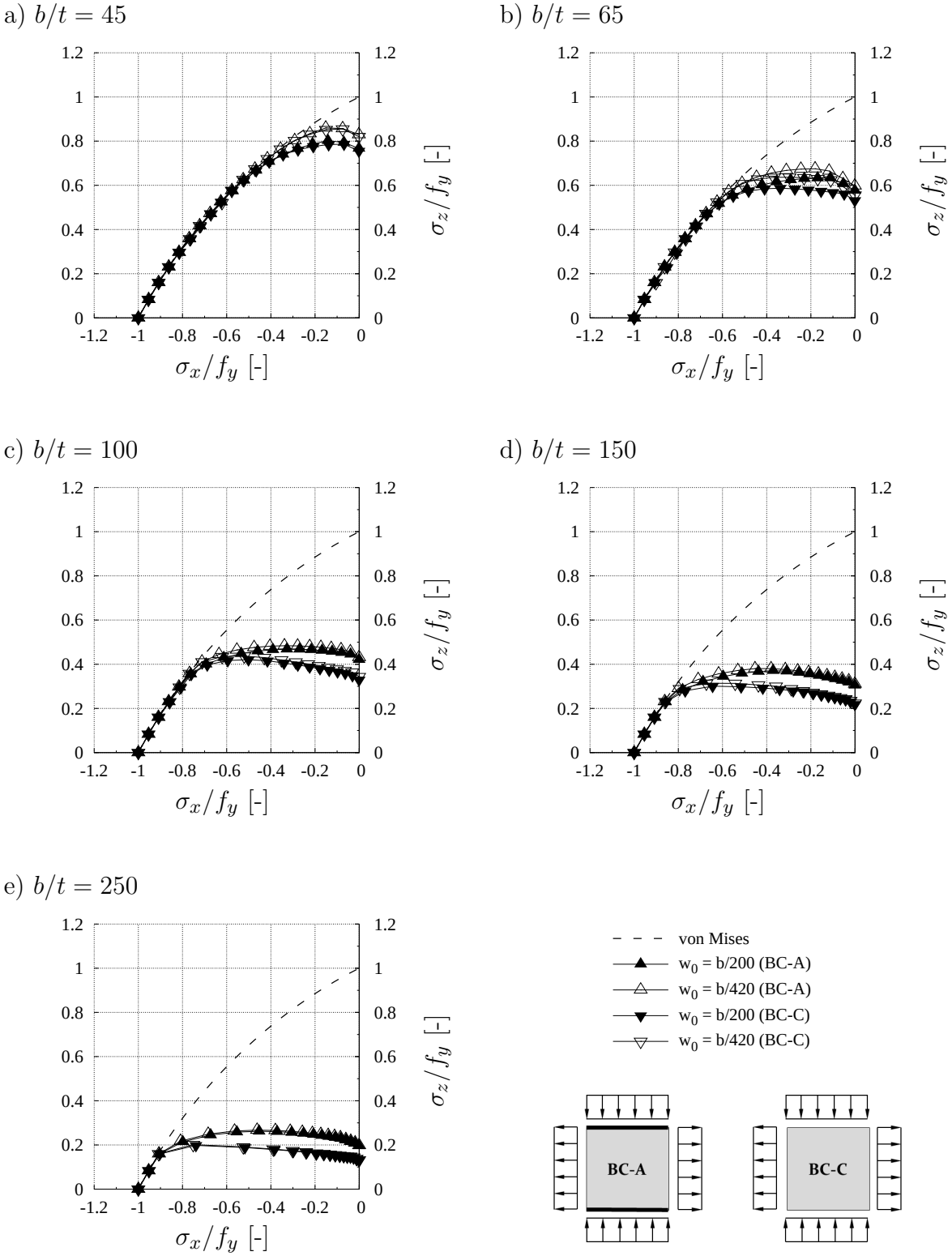

Figure 5.13: Comparison of BC-A to BC-C in the tension-compression interaction domain.

a) $b/t = 45$

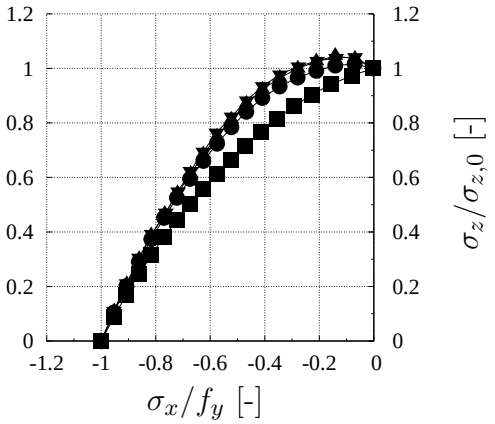

b) $b/t = 65$

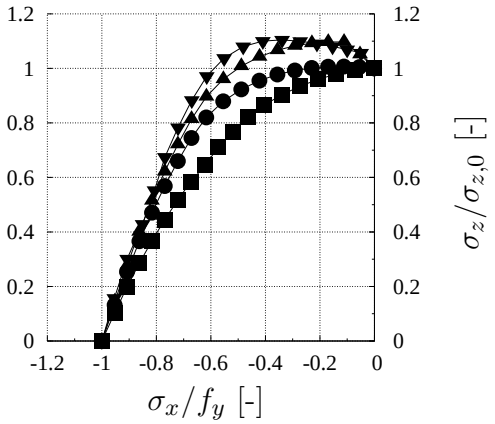

c) $b/t = 100$

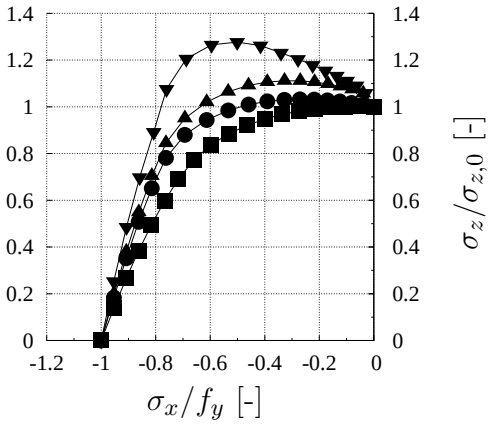

d) $b/t = 150$

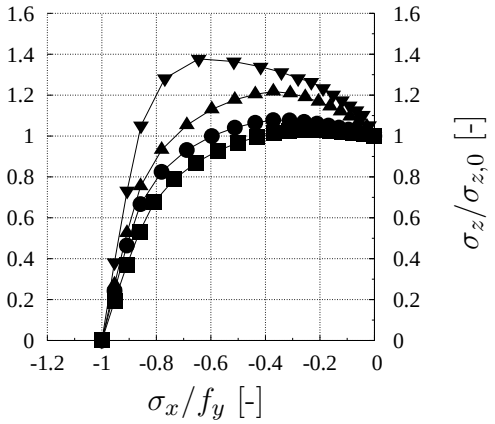

e) $b/t = 250$

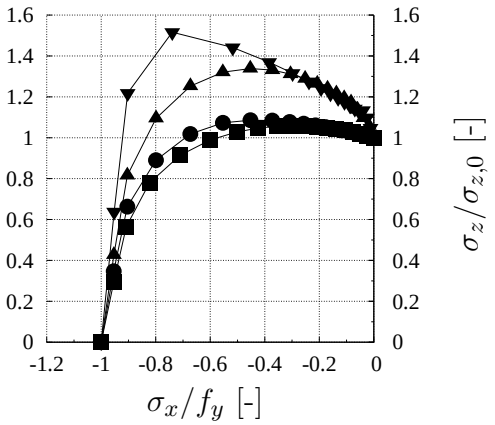

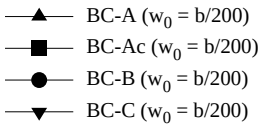

Figure 5.14: Effect of boundary conditions, values referred to pure compression ($\alpha = 1$, decisive imperfection).

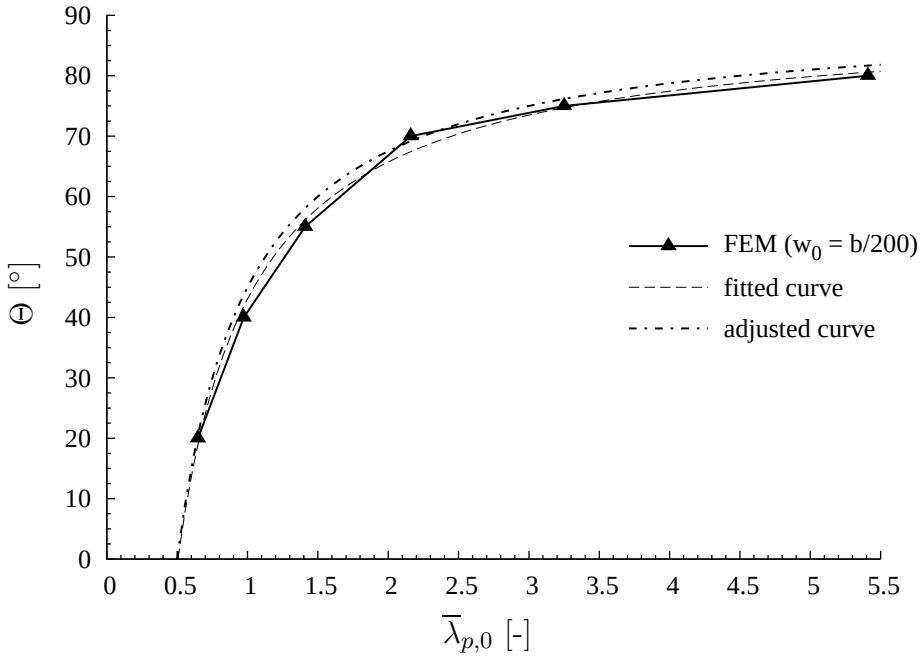

Figure 5.15: Limit angles for buckling ($\alpha = 1$).

Intersection of the interaction curves with the von Mises criterion

As observed from the foregoing investigations, all interaction curves determined by the numerical simulations conducted on square plates have the same intersection point with the von Mises criterion, independently from the edge boundary condition and assuming the same imperfection amplitude. Or, in other words, the effects of the boundary conditions vanish with increased tensile stresses and the intersection with the von Mises criterion remains only dependent on the b/t–ratio, thus the slenderness.

This fact can be utilised in defining a limit interaction angle Θ_{lim} for a quick estimation of whether the plate is subjected to buckling or not. The interaction angle is defined according to Fig.2.1. Thereby, the engineer in practice may identify directly, if the buckling design may be skipped by a simple stress check. The limit interaction angle is therefore put against the plate slenderness under uniaxial compression and a curve is fitted with the method of the least-squares [81], see Fig.5.15. In order to give a more practical solution the determined factors are simplified resulting the proposed adjusted curve, which can be expressed in degrees with Eq.(5.3). For defining the proposed equation, conservatively the intersection points resulting with an imperfection amplitude $w_0 = b/200$ are used.

$$\Theta_{lim} = 90 \cdot \left(1 - \frac{1}{2 \cdot \overline{\lambda}_{p,0}}\right) \tag{5.3}$$

It should be highlighted here that this option does only account for plates subjected to pure plate–like behaviour without the effects of column–like buckling, see Sec.2.3.

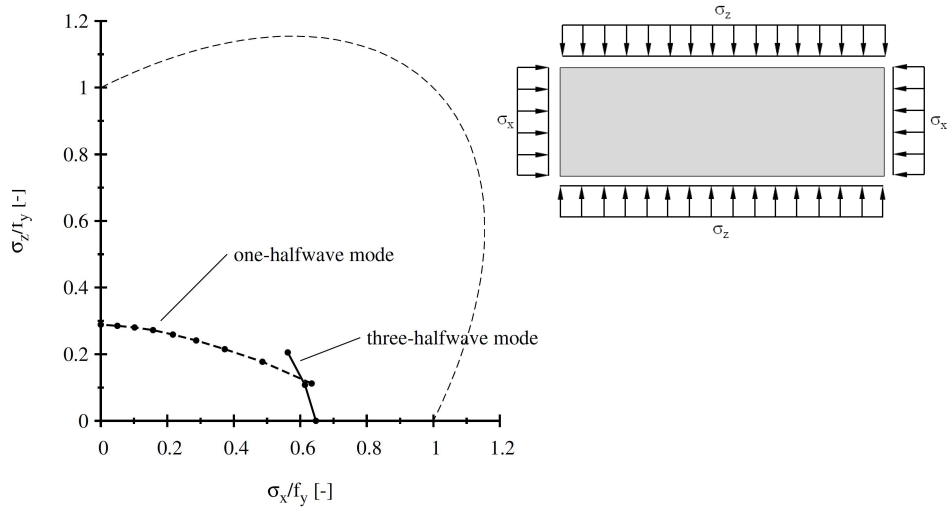

Figure 5.16: Effect of aspect ratio on the shape of interaction curves, exemplarily shown for an aspect ratio of $\alpha = 3$ [11].

5.5.3 Investigations on long plates

The investigations on long plates may be divided into two parts. The first one concerning long plates loaded with compression on the short side and the second one loaded with compression on the long edges. The plates loaded with compression on the short edge have a plate-like behaviour and are already covered by the investigations on square plates in Sec.5.5.2. Nevertheless, for the sake of completeness the results for long plates loaded with compression on the short edge are also shown briefly in the following. The plates loaded with compression on the long edges are conducted for investigating the influence of the tensile stresses on the column-like buckling behaviour, see Sec.2.4.2.3. Two or three half-wave shapes indirectly provide a stiffening of the plate in this case, resulting in increased resistances. Therefore the decisive imperfection is a one half-wave shape. Investigations from Braun [11] on the buckling behaviour of long plates under biaxial compression show this effect on the transition of the decisive imperfection from one half-wave to three half-waves mode, see Fig.5.16. The analyses in the present work investigate the "continuation" of the shown interaction curves in both directions.

Fig.5.17 shows exemplarily a comparison of the out-of-plane deformations of a long plate ($a = 3000\,\text{mm}$, $b = 1000\,\text{mm}$, $t = 10\,\text{mm}$) loaded with compression on the short edges and on the long edges. It is noted here, that for both illustrated cases a one half-wave imperfection shape has been applied to the model. While the model loaded on the long edges develops a one half-wave failure mode, for the plate loaded on the short edges a mode transition occurs and the plate buckles with three half-waves. Even if this looks very obvious, it highlights the fact that a three half-wave imperfection shape in case of the plate loaded on the short edge would lead to the minimum resistance, while this imperfection shape would lead to a stiffer behaviour when the plate is loaded on the long edge.

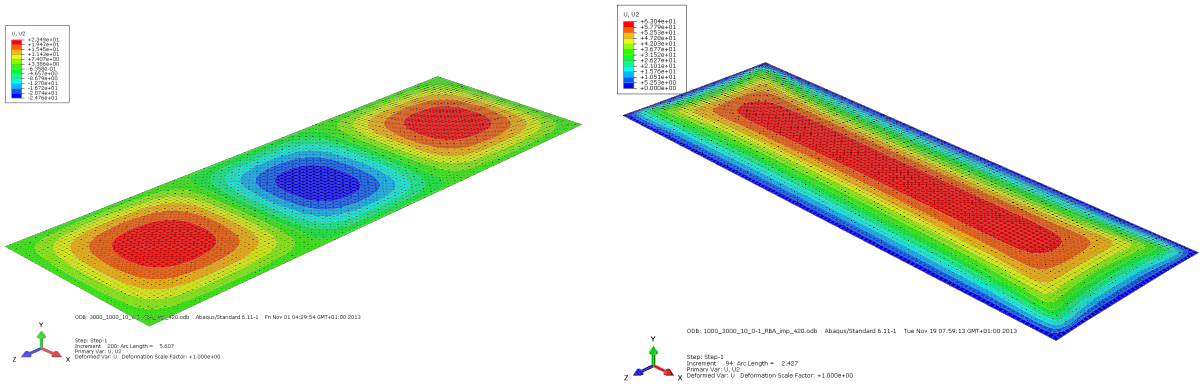

a) compression on short side

b) compression on long side

Figure 5.17: Numerical out-of-plane deformations of a long plate loaded with uniaxial compression on the short edges (a) and on the long edges (b).

Long plates loaded with compression on the short edges

The investigations on long plates loaded with compression on the short side are summarised in Fig.5.18 for BC-A. The results show a similar behaviour like the square plates, see Fig.5.6. Also here the presented results represent already the minimum resistance for different imperfection shapes. As also observed for square plates, mode transitions occur, which is clearly noticeable in the sudden drops of the curves. Even though the discontinuities are mainly evened out by the application of several imperfection shapes, still some slight dithering is visible pointing out the sensitivity of the numerical model.

However, since the results on square plates are found safe-sided and more stable, these results will be used as reference for the further evaluation of the buckling rules for plate-like behaviour.

Long plates loaded with compression on the long edges

The results for plates loaded with compression on the long side are illustrated in Fig.5.19 to Fig.5.21 for the investigated boundary conditions. While the results of BC-A and BC-B are quite similar, BC-C clearly shows higher reductions. As expected, the curves lie below the curves calculated for compression on the short side, because column–like behaviour has a decisive influence on buckling and therefore the resistance is reduced once more. The shapes of the curves show a favourable influence from tension stresses and reach the von Mises criterion with increasing interaction angle Θ. However, a strong impact from tensile stresses is not observed.

Nevertheless, the intersection points of the curves with the von Mises criterion do not approach the results for plates loaded with compression on the short side, showing that even with high tension stresses column–like behaviour still prevails.

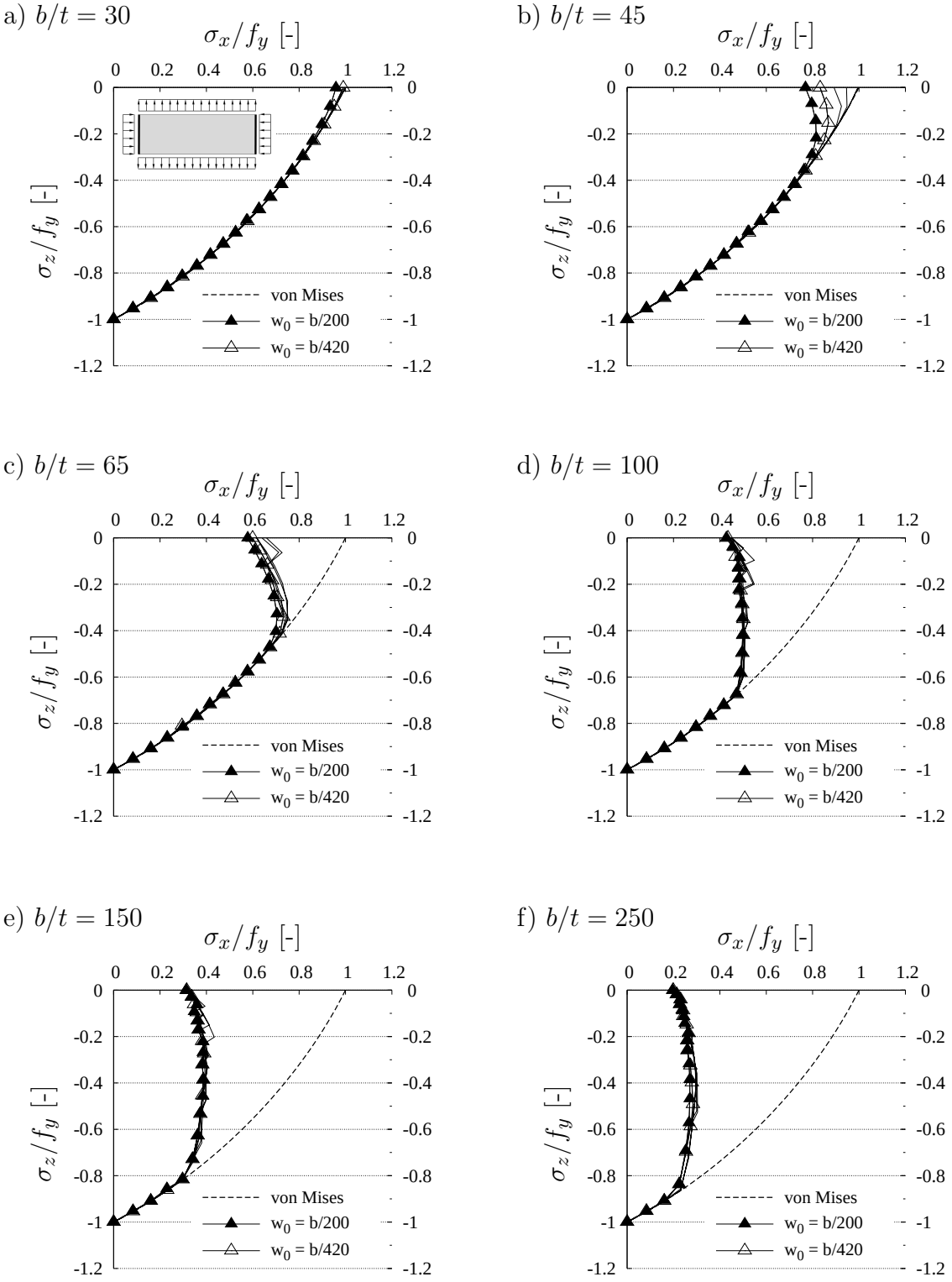

Figure 5.18: Numerical results for short edges loaded with compression being constrained (BC-A, $\alpha = 3$, all edges hinged, decisive imperfection).

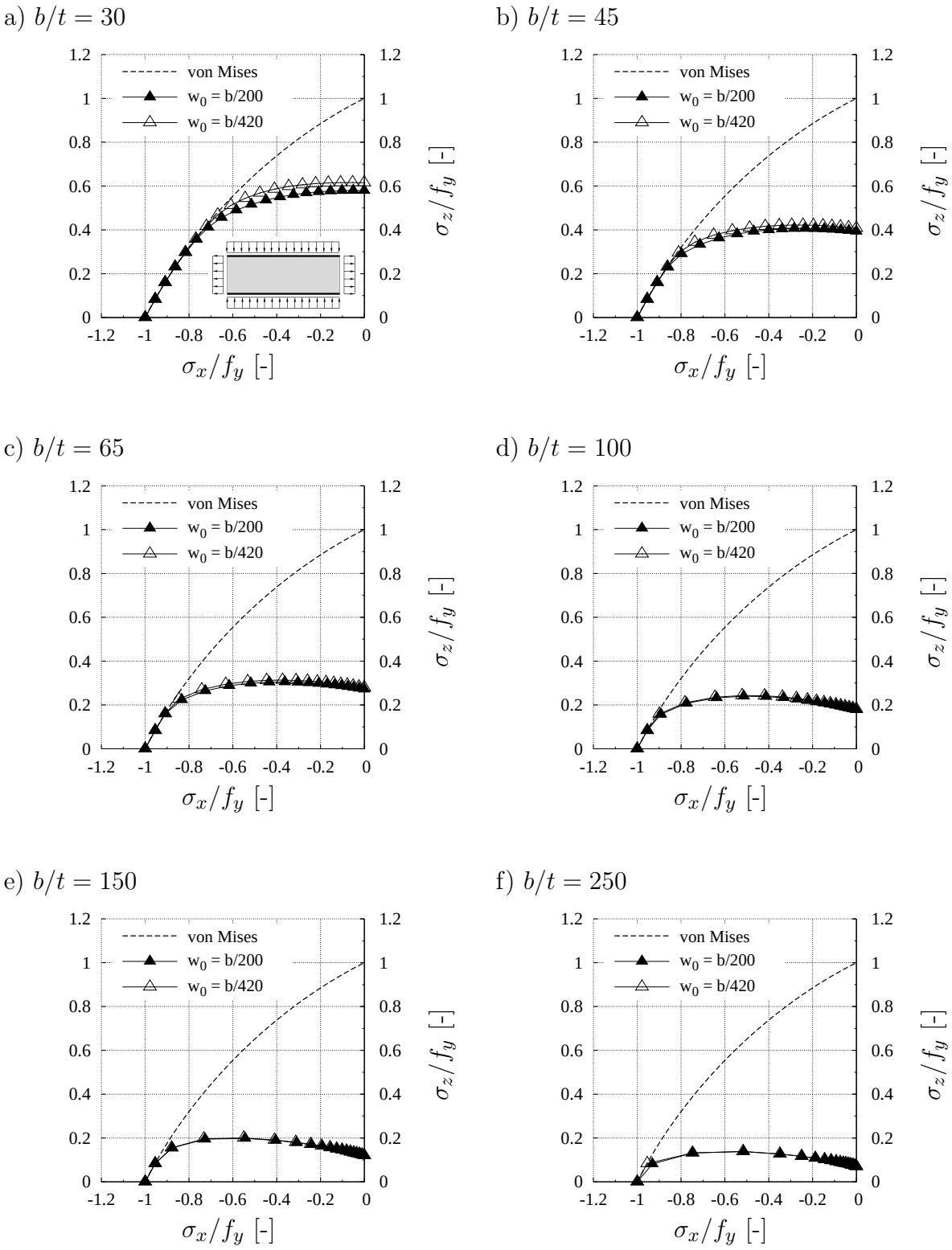

Figure 5.19: Numerical results for long edges loaded with compression being constrained, compression applied on long side (BC-A, $\alpha = 3$, all edges hinged).

a) $b/t = 30$

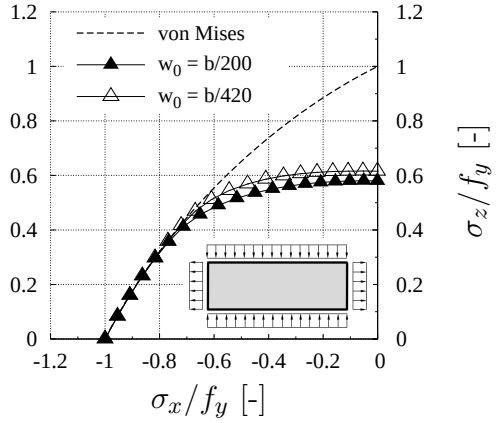

b) $b/t = 45$

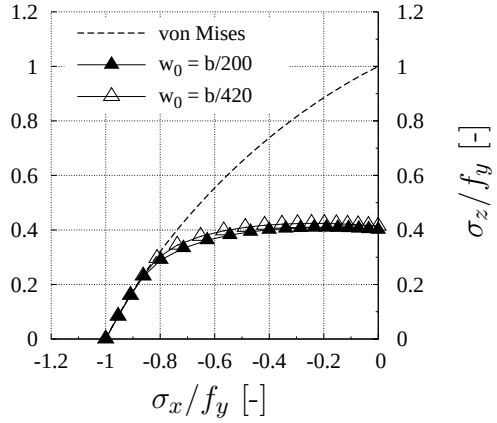

c) $b/t = 65$

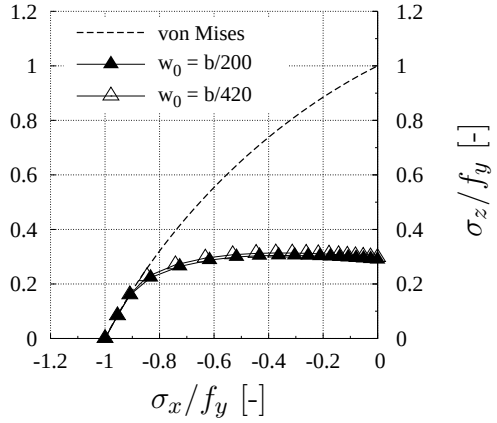

d) $b/t = 100$

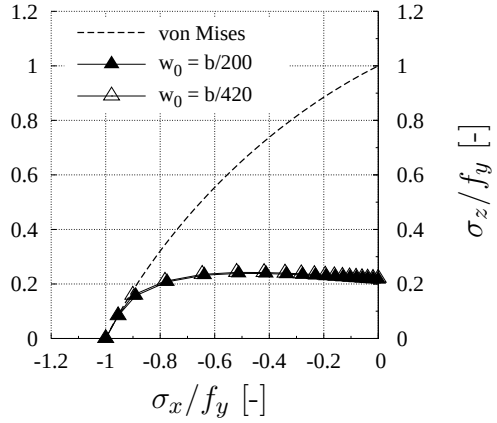

e) $b/t = 150$

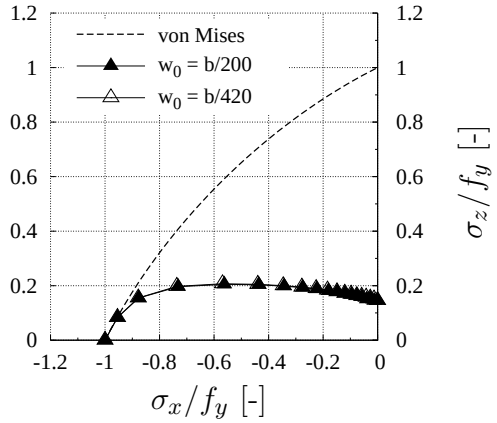

f) $b/t = 250$

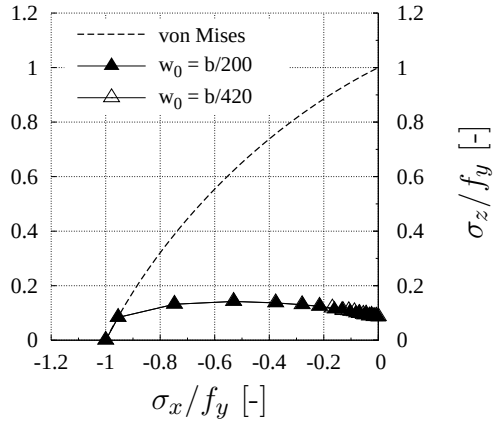

Figure 5.20: Numerical results for all edges constrained, compression applied on long side (BC-B, $\alpha = 3$, all edges hinged).

a) $b/t = 30$

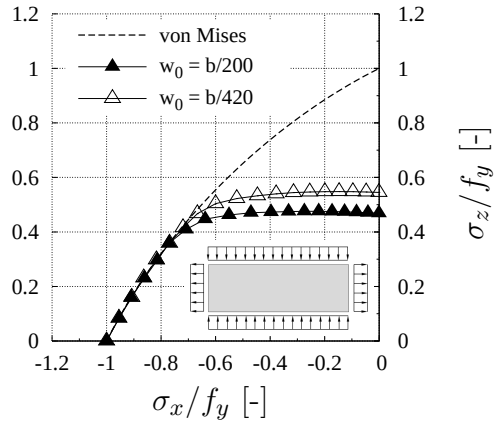

b) $b/t = 45$

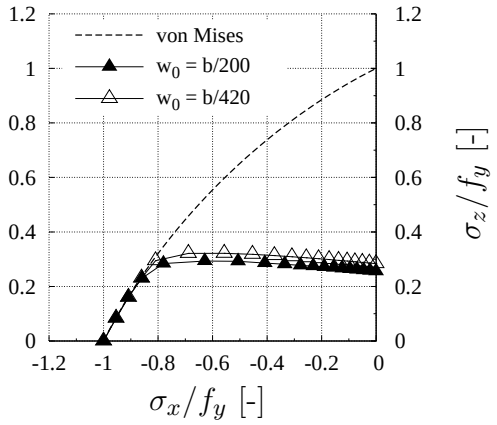

c) $b/t = 65$

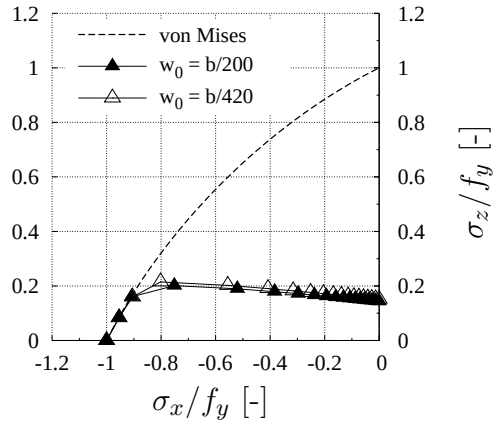

d) $b/t = 100$

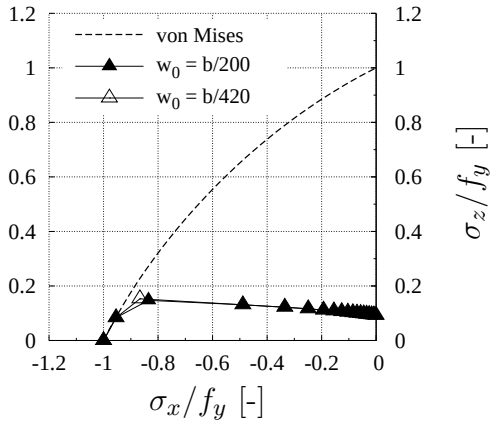

e) $b/t = 150$

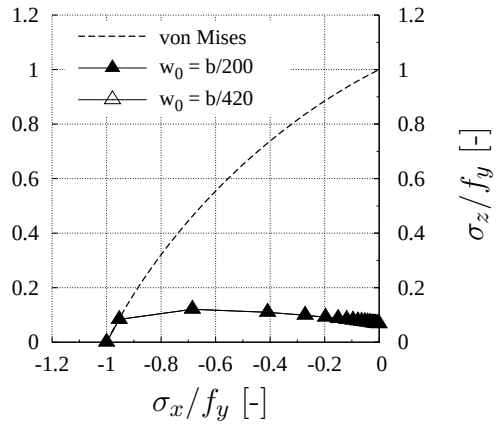

f) $b/t = 250$

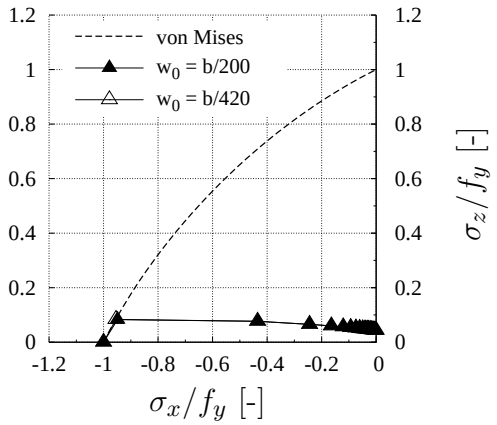

Figure 5.21: Numerical results for all edges unconstrained, compression applied on long side (BC-C, $\alpha = 3$, all edges hinged).

5.6 Tension-Shear

For evaluating the buckling behaviour of slender plates subjected to tension and shear stress, a variation of the ratio of direct and shear stress is conducted considering also the different stress gradients $\psi = 1$, 0.5, 0 and -0.5.

The b/t-ratios have been chosen slightly different from those for the tension–compression analyses, in order to better cover the interaction area also with regard to the subsequent compression–shear simulations conducted in Sec.5.7. According to EN 1993-1-5 [36] shear buckling has to be taken into account if the criterion given in Eq.(5.4) is fulfilled. For the investigated plates with S 355 the limiting slenderness is $b/t = 58.6$, so that $b/t = 60$ is used to represent the transition area between where yielding and where buckling becomes decisive for pure shear when the stress gradient is $\psi = 1$. However, this case is obviously not of interest if tensile stresses interact with shear, as then plate buckling is not relevant, but it is when compression stresses are involved, so that here the presented results are chosen for $b/t \geq 70$.

$$\frac{h_w}{t_w} \geq 72 \cdot \frac{\varepsilon}{\eta} \qquad \text{where:} \quad \varepsilon = \sqrt{235/f_y} \tag{5.4}$$

In Fig.5.22 the results for a tensile stress ratio of $\psi = 1$ are normalised and summarised showing the influence of the tension stresses referred to the pure shear buckling resistance τ_0. As also observed for the case of tension–compression, the positive influence of tensile stresses increase with the b/t-ratio. The results in the tension–shear interaction domain show a pronounced effect of tensile stresses on the shear-buckling resistance. In order to keep this section manageable, the results from the numerical simulations are shown in Sec.B.1 of the Annex. Fig.B.1 shows that the applicable shear stresses increase almost constantly until reaching the von Mises criterion. Generally it can also be seen that the imperfection amplitude does not have a noticeable influence on the resistance.

Effect of stress ratio ψ

Since in many practical cases, such as for webs, shear stresses occur together with bending moments leading to stress gradients for the direct stresses, the effect of these stress ratios is also investigated in order to verify a generally applicable design procedure. The results regarding the influence of the stress ratio ψ on the shear resistance are summarised in Fig.5.23. For a better overview only the results gained with an imperfection amplitude of $w_0 = b/200$ are shown and limited to $b/t = 70, 100, 150$ and 250.

As expected, the maximal increase of the shear resistance can be observed for the case of simultaneously acting pure tensile stress ($\psi = 1$). If a stress ratio of $\psi = 0.5$ is applied for the tensile stresses only a small influence can be noticed compared to the

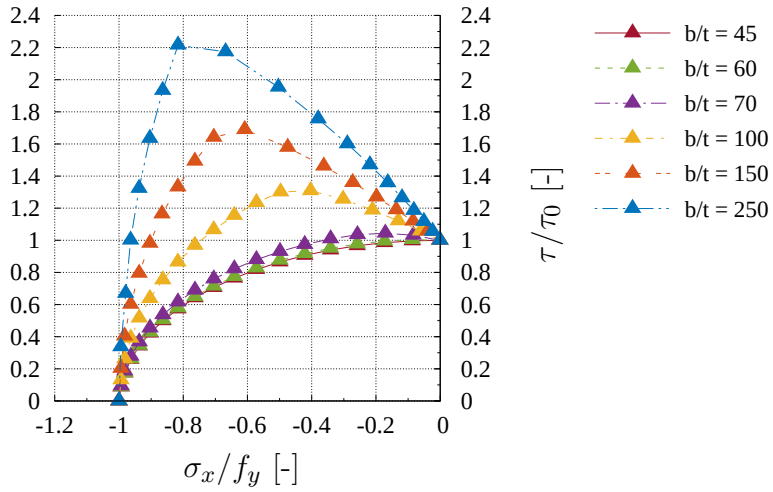

Figure 5.22: Numerical results for the short edges loaded with tension being constrained, referred to the pure shear buckling resistance τ_0 (BC-A, $\alpha = 2$, $w_0 = b/200$, all edges hinged).

pure tension case ($\psi = 1$), since the positive effect of the tensile stress is still dominant. In contrast to this, the plates subjected to a stress ratio of $\psi = 0$ show a clear drop in their shear resistance for $b/t \geq 100$, while the stockier plate with $b/t = 70$ remains almost untouched. If the stress ratio ψ is negative, thus applying also compression stresses of a small amount ($\psi = -0.5$), a pronounced drop of the curves for $b/t \geq 100$ occurs. Also here, for the stockier plate ($b/t = 70$) the stress ratio shows only marginal changes. While for the stress ratios $\psi \geq 0$ generally an increase of the shear resistance is observed, it is worth mentioning, that for negative stress ratios, even if the tensile stresses are higher than compression, a clear impact occurs to the shear resistance leading even to a declining interaction curve for very slender plates ($b/t = 250$).

5.7 Compression-Shear

In addition to the effect of the tension stresses on the shear buckling behaviour, a parametric study is conducted for investigating the influence of compression stresses. Therefore, the same parameters as described in Sec.5.6 are used, but with compression stress being larger than tension in case of $\psi \neq 1$.

In Fig.5.24 the results are normalised for a stress gradient $\psi = 1$ showing that the shape of the interaction curves is nearly independent from the plate slenderness. Furthermore, the curvature of the curves show that the shear resistance is more sensitive to compression stresses than vice versa. This effect is even better shown on the non-normalised results in Sec.B.2 of the Annex. Small shear stresses reduce the applicable compression stresses only by a small amount, while already comparable small compression stresses reduce the shear resistance noticeably. For $b/t \geq 100$ the imperfection

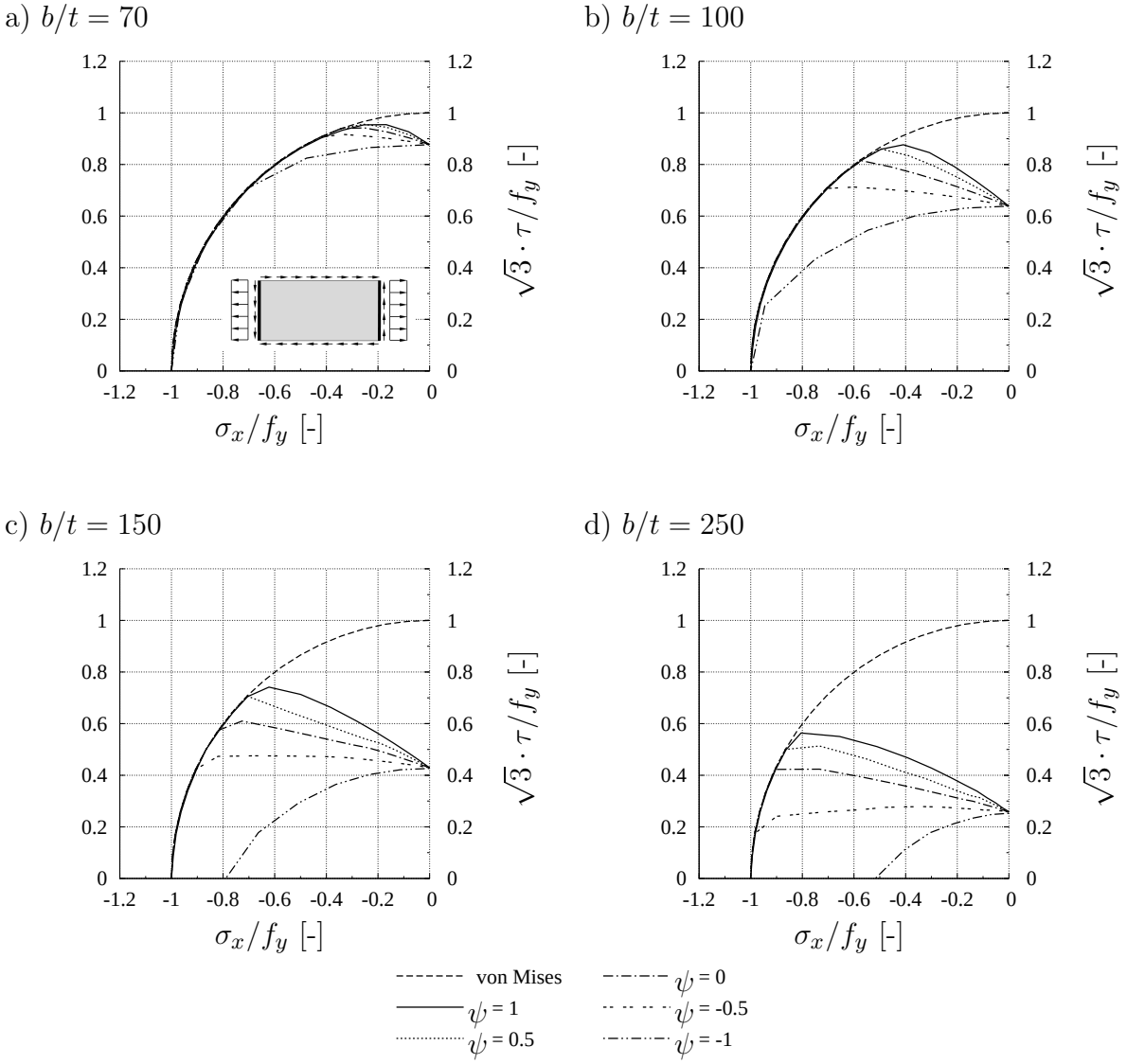

Figure 5.23: Effect of stress ratio ψ on numerical results (BC-A, $\alpha = 2$, $w_0 = b/200$, all edges hinged, $\sigma_t \geq \sigma_c$ applied on short edges).

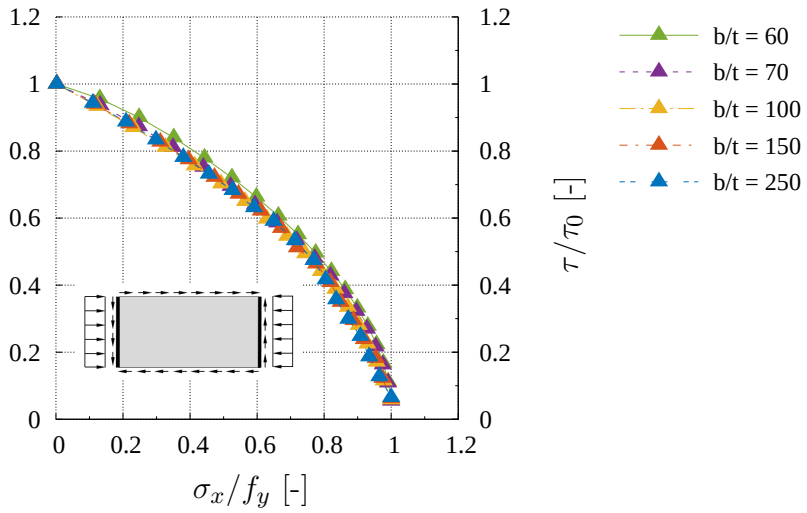

Figure 5.24: Numerical results for short edges loaded with compression being constrained, referred to the pure shear buckling resistance τ_0 (BC-A, $\alpha = 2$, $w_0 = b/200$, $\psi = 1$, all edges hinged).

amplitude does not have an influence on the resistance, while for smaller b/t-ratios the imperfection amplitude clearly influences the resistance, see Fig.B.5. Especially for $b/t = 45$ the impact of the imperfection amplitude is obviously pronounced and almost constant over the whole range.

Effect of stress ratio ψ

Since in many practical cases, such as for webs, shear stresses occur together with bending moments leading to stress gradients for normal stresses, the effect of these stress ratios is also investigated in order verify regarding a generally applicable design procedure. The results of the influence of the stress ratio ψ on the shear resistance is summarised in Fig.5.26. For a better overview only the results gained with an imperfection amplitude of $w_0 = b/200$ are shown.

In contrast to the results gained by applying pure compression and shear, in case of bending and shear the shapes of the reduction curves are dependent on the plate slenderness. Therefore, the normalised results for a stress gradient $\psi = -1$ are gathered in Fig.5.25 showing how the curves become flatter with increased b/t–ratio. Since the current design formula shown in Eq.(2.19) does not consider the shape of the interaction curves being dependent from the slenderness, as the exponents are constant and the slenderness is gained by critical buckling analyses, see Sec.2.2.3, this case seems of practical relevance for checking the design approach in a later step in Sec.6.

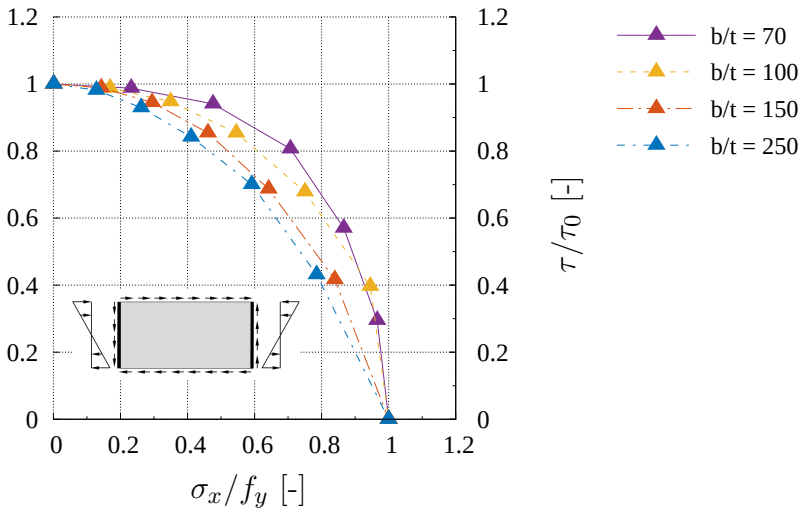

Figure 5.25: Numerical results for edges loaded with compression being constrained, referred to the pure shear buckling resistance τ_0 (BC-A, $\alpha = 2$, $w_0 = b/200$, $\psi = -1$, all edges hinged).

5.8 Numerical investigations on stiffened plates under biaxial compression

5.8.1 General

Investigations conducted by Braun in [11] focused on the buckling behaviour of unstiffened slender plates subjected to biaxial compression proposing a "V-factor" to overcome discrepancies found between numerical results and the current design rules, see Sec.2.5.8. However, recently questions arose from practitioners, if the proposed factor should be applied also for stiffened plates, since the behaviour might be more favourable due to e.g. clamping effects between the stiffeners. To the author's knowledge, until now systematic research relating to the buckling behaviour of biaxially loaded stiffened plates under compression such as e.g. [83], [84], [114] is settled in ship building or in aircraft constructions such as [120]. The issue is also addressed in [80] pointing out that investigations are still missing and desirable. In order to check the design rules with the behaviour of stiffened plates under biaxial compression, numerical parametric studies are presented in this section on the basis of the verified model according to Sec.4.7.

5.8.2 Imperfections

The imperfections for all numerical models are applied according to Annex C, EN 1993-1-5 [36] using sine functions for describing local and global imperfection shapes. This

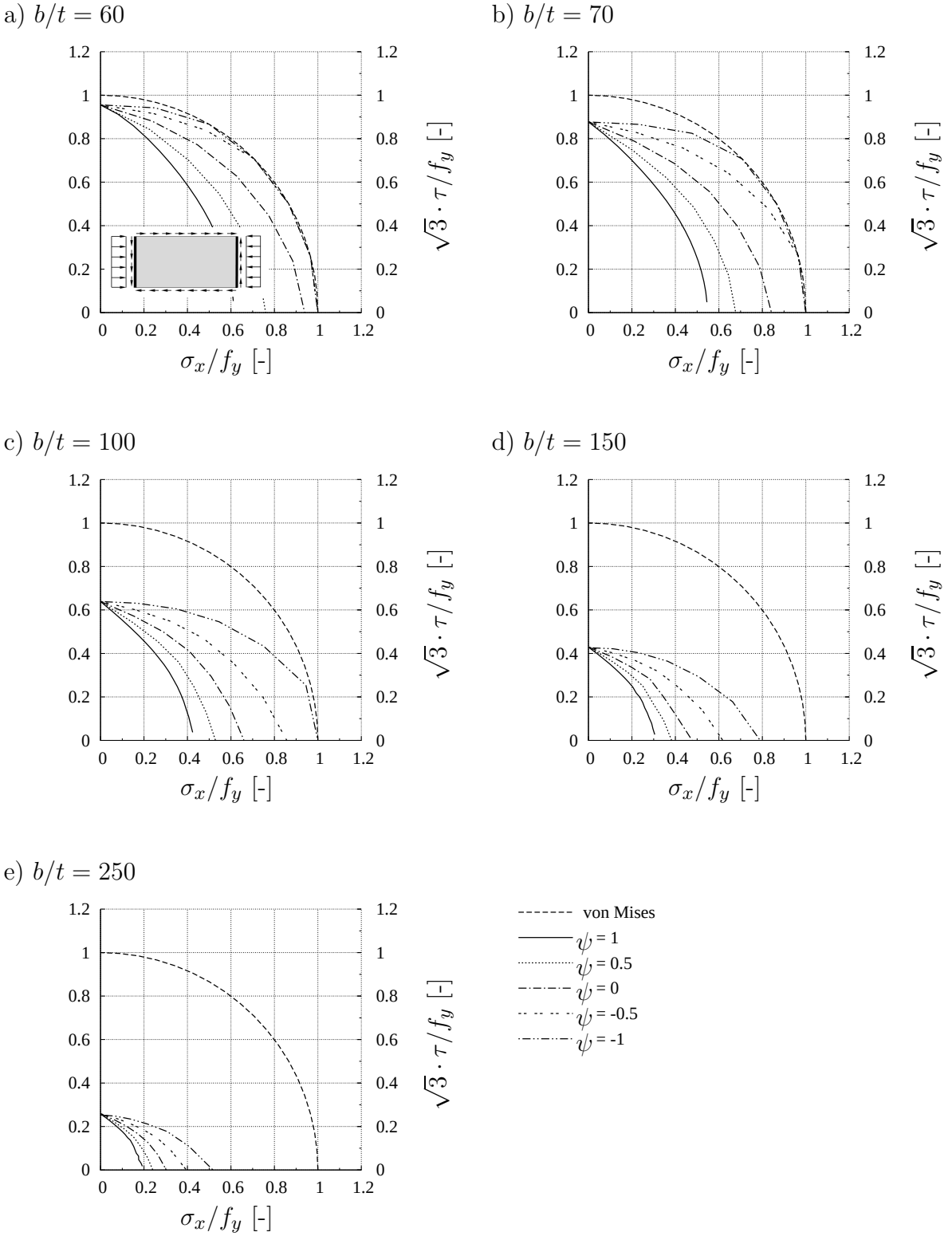

Figure 5.26: Effect of stress ratio ψ on numerical results (BC-A, $\alpha = 2$, $w_0 = b/200$, all edges hinged, $\sigma_c \geq \sigma_t$ applied on short edges).

Table 5.1: General layout for the combination of imperfections.

Combination	Description
1	global
2	local (one half-wave)
3	local (multi half-wave)
4	global + 0.7 local (one half-wave)
5	global + 0.7 local (multi half-wave)
6	local (one half-wave) + 0.7 global
7	local (multi half-wave) + 0.7 global

approach has also been adopted successfully in Sec.4.7.3 for the verification of the numerical model and allows for a systematic procedure in the superposition of several imperfection shapes. An approach where the buckling shapes are used from a foregoing elastic buckling analysis may contain "mixed" modes, where it becomes difficult to split them into the individual parts to apply comparable imperfections for all cases. Furthermore, the adoption of sine functions allows for a widely automatised and objective generation of sets of imperfection shapes.

For the global imperfection shape the "interpretation 3" according to Fig.4.37 is adopted, as it is representing the imperfections mostly found in reality. The verification of the model has been conducted successfully using this approach, see Sec.4.7. The local imperfections need several considerations. As found in Sec.5.5.3 for the long plates the decisive local imperfection shape strongly depends on the type of loading. Since the local subpanels of the investigated stiffened plates fall into this category, a special treatment is required, so that several local imperfection shapes are considered and combined according to the rules given in Annex C, EN 1993-1-5 [36]. Therefore, locally one and multi half-wave imperfection shapes are applied to the model and the minimum resistance of the gained results is taken and directly illustrated for the results in Sec.5.8.4. The general layout for the combination of the imperfections is shown in Tab.5.1

5.8.3 Parameters

The investigated parameters are summarised in Tab.5.2. In general, for consistence the parameters of the geometry correspond to the ones used for the validation of the numerical model in Sec.4.7. However, the investigated b/t-ratios have been limited to four representative values to keep the data manageable. The stress ratio, expressed as interaction angle Θ according to Fig.2.1, is varied from 270° to 360° by increments of $\Delta\Theta = 5°$ in order to cover the whole biaxial compression interaction range. Thus, the stress ratio results in 2 052 possible parameter combinations. When considering all imperfection shapes a total number of over 14 000 numerical simulations are conducted. As also done for the validation of the numerical model, the geometries of the stiffeners are chosen such as to guarantee that no torsional buckling of the stiffeners occurs, see Sec.4.7.2.

Table 5.2: Parameters for study on stiffened plates under biaxial compression.

Panel aspect ratio α	Stiffness of the stiffener γ	Slenderness b/t	Number of stiffeners N	Interaction angle Θ
1, 1.5, 2	7, 25, 65	65, 100 150, 250	1, 2, 4	$-90° \cdots 0°$ $(\Delta\Theta = 5°)$

5.8.4 Numerical results

The results of the numerical simulations are divided into several sets for the sake of a better overview and comparability. Therefore, the results for plates stiffened with one stiffener are presented split into different panel aspect ratios α in Fig.5.27 – Fig.5.29. Since the results with one stiffener have been shown for the validation in Sec.4.7.4 to be the closest to the design rules and conservative compared to plates with more than one stiffener, which give slightly higher resistances, the results from the parametric study are discussed for the case of one stiffener in the followings. For the sake of completeness, the results with two and four stiffeners are placed in the Annex, see Sec.B.3.

In Fig.5.27 the results for a global panel aspect ratio of $\alpha = 1$ are presented for the three types of stiffeners $\gamma = 7$, 25 and 65. The ratio σ_x/f_y denotes the resistance in longitudinal direction, while σ_z/f_y is the resistance in transverse direction, say in perpendicular direction to the stiffener. The graph shows that the resistance in transverse direction for pure compression is for all b/t–ratios almost independent from the stiffness of the stiffener γ, as a weak stiffener is already sufficient to prevent global buckling, so that local buckling becomes decisive. In longitudinal direction an increase of the resistance can clearly be observed from $\gamma = 7$ to $\gamma = 25$. The increase from $\gamma = 25$ to $\gamma = 65$ is less, since with $\gamma = 25$ local buckling already prevails, except for $b/t = 250$. The sharp bends in the curves show where the failure mode changes to a one-wave mode if transverse stresses become decisive.

A very interesting observation can be made for the interaction domain, where in case of weak stiffeners a very unfavourable interaction is found. In particular for $b/t = 250$, 150 and 100 a rather flat interaction is visible, where small transverse stresses lead to a significant drop of the resistance in longitudinal direction since the deviating forces is decisive. Stronger stiffeners lead to a rather round bodied and favourable interaction behaviour, which is dominated by local buckling. The results of the panel aspect ratio $\alpha = 1.5$ are shown in Fig.5.28. For weak stiffeners an almost linear interaction is found, which is also the case for $b/t = 150$ and 250 with stiffeners $\gamma = 25$. For the stronger stiffeners a similar behaviour is found as for square plates. However, for $\alpha = 1.5$ column–like behaviour in transverse direction leads to smaller resistances compared to $\alpha = 1$. For plates with a panel aspect ratio $\alpha = 2$ the resistance in transverse direction is reduced once more for the weak stiffeners, as global buckling occurs. The interaction in this case is almost linear. For the strong stiffeners the interaction again is found rather favourable, as local buckling of the subpanels becomes decisive.

In summary, it can be concluded that the buckling behaviour is strongly dependent from the panel aspect ratio, the slenderness and the stiffness of the stiffener, resulting in completely different types of characteristics for the interaction curves in the biaxial compression domain. Similar conclusions can be drawn also for plates stiffened with two and four stiffeners, see Sec.B.3 in the Annex. Furthermore, it can be seen that an increase of the amount of the stiffeners in case of weak stiffeners has only marginal influence on the resistance. From the findings of the numerical study it can be recommended not to use weak stiffeners, as especially with biaxial compression the buckling behaviour is very unfavourable.

If it is intended to prevent global failure, Chapter 9, EN 1993-1-5 [36] gives information on stiffeners and detailing. In case of transverse stiffeners the code defines minimum requirements on the stiffeners to provide a rigid support by a verification using a second order elastic method analysis, which satisfies that the maximum stress in the stiffener should not exceed f_y/γ_{M1} and that the additional deflection should not exceed $b/300$. However, regarding the minimum requirements for longitudinal stiffeners EN 1993-1-5 [36] gives just references to the buckling rules, see Sec.2.4.2. Recent publications such as [8] and [80] adopted the minimum requirements for transverse stiffeners also on longitudinal stiffeners in order to verify against global buckling. Anyway, in the frame of this work the weak stiffeners are used intentionally to investigate whether the design rules in general also cover correctly the global buckling behaviour so that the procedure given in EN 1993-1-5 [36] is followed, where the longitudinal stiffeners are checked within the buckling verification.

Effect of combined loads on the local and global buckling behaviour

The ratio of transverse and longitudinal stress may have a decisive impact on the failure shape of the stiffened plates. Due to the large amount of data, a detailed illustration of all failure modes would unnecessarily distend this work, so that a representative case is chosen to display the effects. Therefore, the case of a panel aspect ratio $\alpha = 2$ is chosen with $b/t = 65$ and $\gamma = 25$. Fig.5.30 shows the different out-of-plane deformations when reaching the ultimate load for (a) $\Theta = -90°$, (b) $\Theta = -70°$, (c) $\Theta = -45°$ and (d) $\Theta = 0°$, where – just as remembrance – an interaction angle of $\Theta = -90°$ means pure compression in longitudinal direction (σ_x) and $\Theta = 0°$ means pure compression in transverse direction (σ_z), see Eq.(2.5).

The deformed shapes show clearly the different failure modes that occurred in the numerical simulations. While for uniaxial compression, both in longitudinal and in transverse direction, pure local buckling of the subpanels is observed, for the combined actions global buckling is observed. This highlights the fact that transverse stresses lead to deviating forces for the stiffener, causing in combination with longitudinal stresses global buckling of the whole panel. The same effect of course happens also vice-versa, where longitudinal stresses lead to deviating forces and to global buckling even if transverse stresses are dominant.

a) $\gamma = 7$

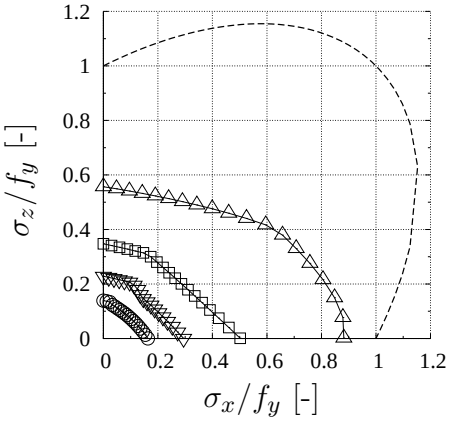

b) $\gamma = 25$

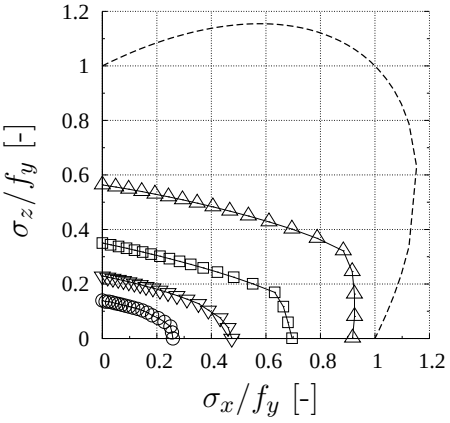

c) $\gamma = 65$

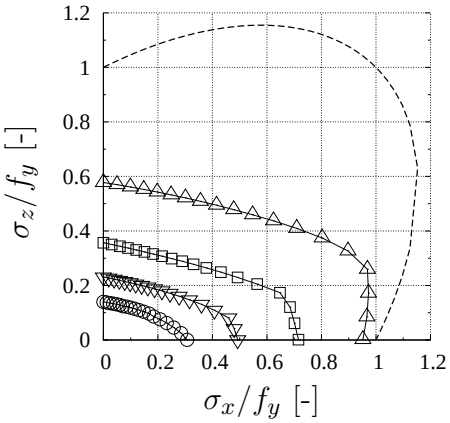

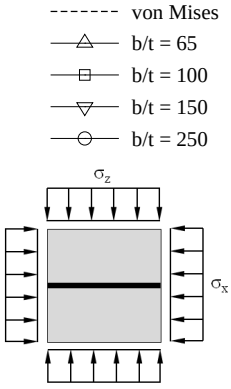

Figure 5.27: Numerical results for stiffened plates loaded with biaxial compression, ($\alpha = 1$, $n = 1$, $b/t = 30$, 45, 65 and 100).

a) $\gamma = 7$

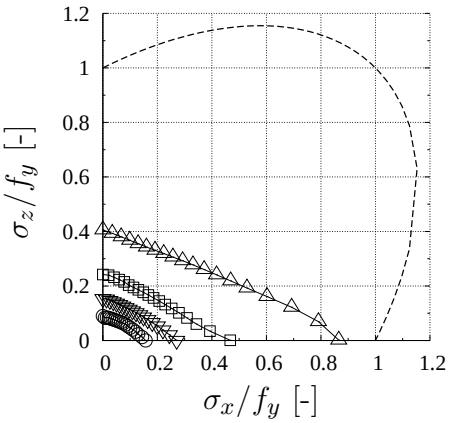

b) $\gamma = 25$

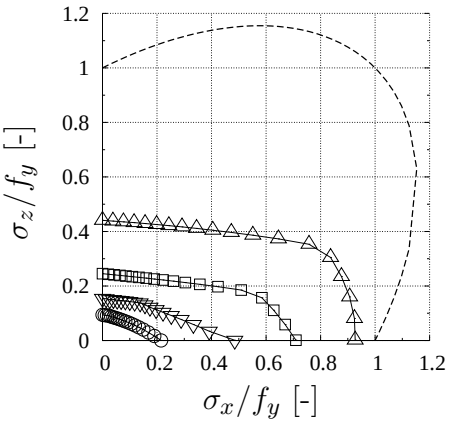

c) $\gamma = 65$

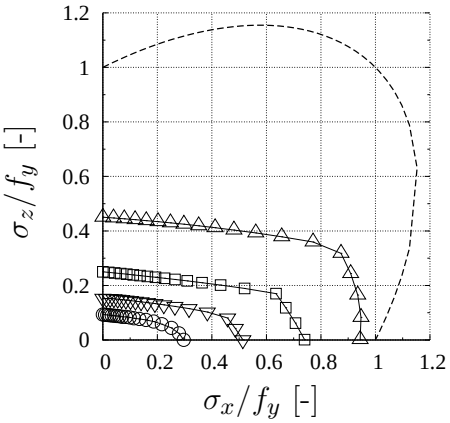

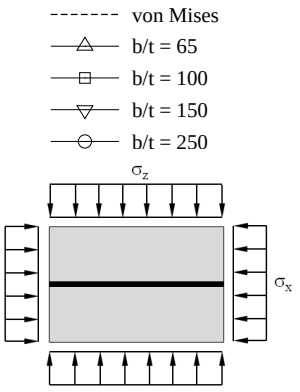

Figure 5.28: Numerical results for stiffened plates loaded with biaxial compression, ($\alpha = 1.5$, $n = 1$, $b/t = 30$, 45, 65 and 100).

a) $\gamma = 7$

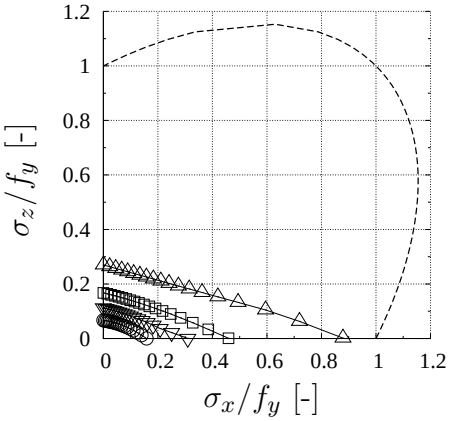

b) $\gamma = 25$

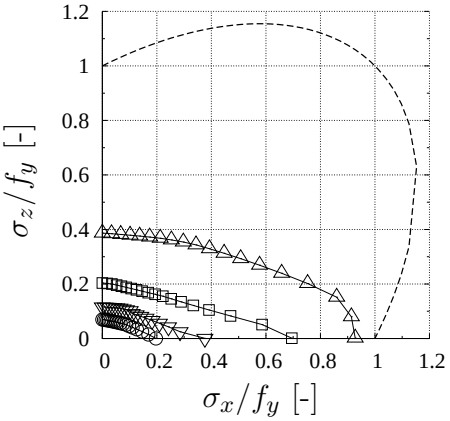

c) $\gamma = 65$

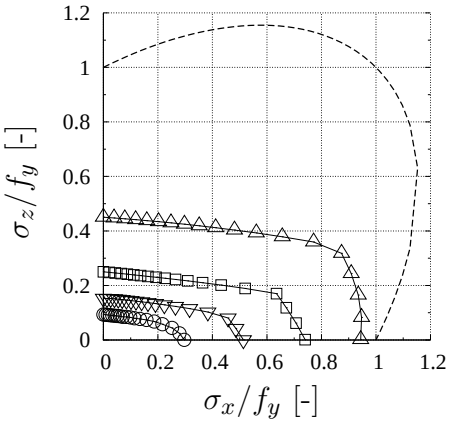

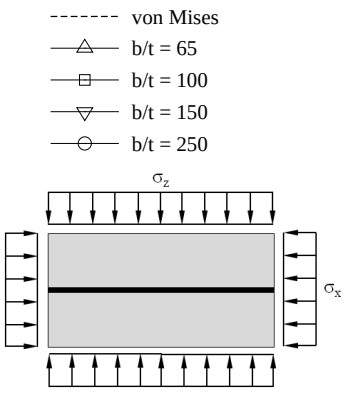

Figure 5.29: Numerical results for stiffened plates loaded with biaxial compression, ($\alpha = 2$, $n = 1$, $b/t = 30$, 45, 65 and 100).

a) $\Theta = -90°$ (dec. combination: no. 7)

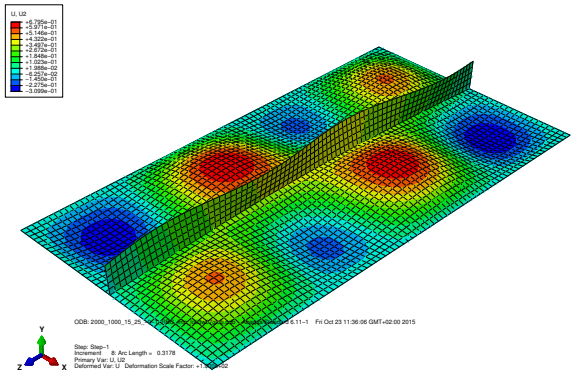

b) $\Theta = -70°$ (dec. combination: no. 5)

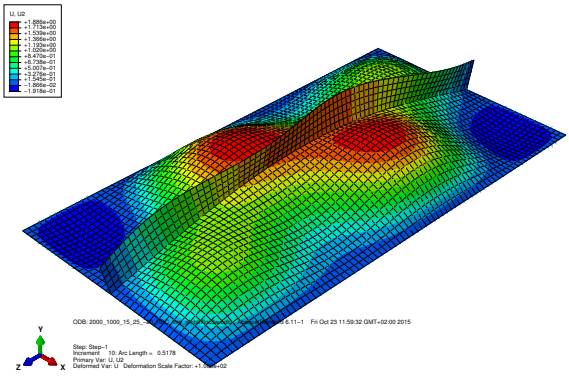

c) $\Theta = -45°$ (dec. combination: no. 4)

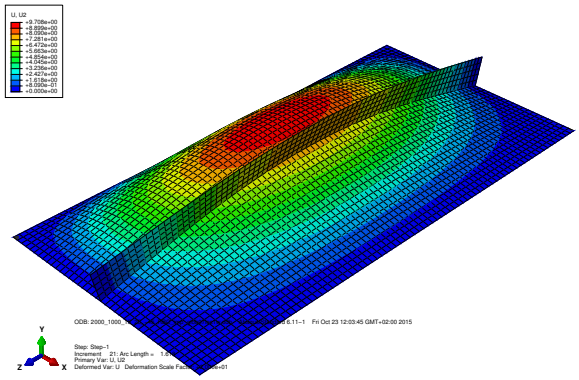

d) $\Theta = 0°$ (dec. combination: no. 6)

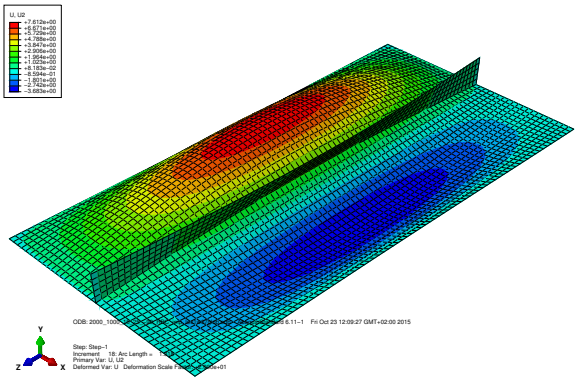

Figure 5.30: Out-of-plane deformations in dependence on loading situation and the decisive combination of imperfections, ($\alpha = 2$, $n = 1$, $b/t = 65$, $\gamma = 25$).

Furthermore, in Fig.5.30 the decisive combination of imperfection for the minimum resistance is given. By comparing the decisive combination with Tab.5.1 it becomes evident that for uniaxial compression the combination no. 7 with prevalent multi half-wave imperfection leads to the minimum resistance, while for uniaxial transverse stresses the decisive combination no. 6 with prevalent one half-wave imperfection is relevant. For combined loading the combinations no. 5 and no. 6 with prevalent global imperfection are decisive, where for predominant compression in longitudinal direction the global imperfection is combined with the multi half-wave local imperfection and for predominant transverse stresses the global imperfection shape is combined with the one half-wave local imperfection.

It is noted here that this effect, where local buckling occurs for the pure uniaxial compression cases and global buckling occurs for the combined cases, is more pronounced for long plates, where deviating forces can deflect the longitudinal stiffeners especially when they are not sufficiently stiff.

5.9 Summary

The analysis of the buckling behaviour under multiaxial stress states is conducted by means of numerical parametric studies on the validated numerical models. Since the stress ratio has a decisive impact on the failure mode, as also observed during the experimental investigations, several initial imperfection shapes are applied in order to aim at a lower safe-sided bound for the results and to avoid suppressed failure mode transitions. The parametric study itself is conducted using the ABAQUS-intern Python interpreter [105] and a parametrised model where the respective parameters and imperfections are applied using Matlab subroutines.

The results for plates subjected to tension–compression are presented and compared for several boundary conditions and panel aspect ratios. Suppressed mode transitions can be observed and are presented exemplarily on a square plate. If a one half-wave imperfection is applied an increased resistance is gained, which drops suddenly if the tension-compression ratio becomes higher so that finally for further investigations the lower envelope of the results using several imperfection shapes is considered. Boundary conditions show to have mainly an influence on the resistance for predominant uniaxial compression. With increasing tension the differences vanish, so that a simplified expression is presented to estimate if a multiaxially loaded panel is subjected to plate buckling independently from the boundary conditions. The investigations on long plates are subdivided into plates loaded with compression on the short edges and plates loaded with compression on the long edges. The plates loaded with compression on the short edges show to be already covered by the investigations on square plates, while plates loaded with compression on the long edges show higher reductions as column-like behaviour play a role. The decisive imperfection shape in this case is a one half-wave mode.

In order to analyse the effect of tensile as well as compressive stresses on shear buckling, further parametric studies are conducted. Since in practical cases shear loads usually act together with bending, the effect of stress gradients is taken into account in the investigations. For plates subjected to shear and predominantly tension a pronounced beneficial effect from tensile stresses is observed, especially for $\psi \geq 0$. In case of plates subjected to shear and predominantly compression the shape of the interaction curves from the numerical results show a stronger influence of direct stresses on the shear resistance than vice versa. While for uniaxial compression the shape of the interaction curves shows to be independent from the plate slenderness, in case of stress gradients the slenderness has an influence.

Further numerical investigations focus on the buckling behaviour of stiffened plates subjected to biaxial compression. Several combinations of imperfections are therefore applied to the numerical model according to Annex C, EN 1993-1-5 [36]. The investigations take into account several values for slenderness, panel aspect ratio, stiffness of the stiffener as well as number of the stiffeners. The results highlight the sensitivity of stiffened plates subjected to biaxial compression in case of weak stiffeners, where pro-

nounced reductions occur. Similar findings are also found for long plates, where global buckling might become decisive for transverse stress, while for smaller aspect ratios usually local buckling occurs even for weak stiffeners. For certain cases local buckling is found for uniaxial compression in both directions, while global buckling occurs in the interaction domain concluding that a "general separation of the load cases" for stiffened plates does not seem to be reasonable, as deviating forces may lead to a global failure, see Fig.5.30.

6 Improved design rules

6.1 General

The results from the numerical simulations presented in the foregoing Sec.5 are compared to the current design rules according to EN 1993-1-5 [36] in Sec.6.2. The comparisons of the numerical results to the current design rules show some shortcomings, which are therefore improved by a modified design proposal in Sec.6.3. In Sec.6.4 a statistical evaluation according to EN 1990 [34] is conducted for determining a partial factor.

6.2 Comparison of the numerical results with the current design rules

6.2.1 Overview

The comparisons are subdivided in unstiffened plates subjected to direct stresses in-Sec.6.2.2, where the effect of tension stresses on the buckling behaviour for the multiaxial stress state tension–compression is investigated. The numerical results for the influence of compression, tension as well as bending on shear buckling are compared to the current design rules in Sec.6.2.3. Finally the results for biaxially compressed stiffened plates are treated in Sec.6.2.4.

In order to keep the volume of this section manageable, only selected cases are shown and reference is made to Sec.C in the Annex for the remaining cases.

6.2.2 Plates subjected to direct stresses

The numerical results are compared to the current design rules described in detail in Sec.2.4.2 using the buckling coefficient as shown in Eq.(2.6) and Fig.2.2 for considering tension stresses for the determination of the slenderness, see Fig.2.16. The interaction curves for BC-A therefore correspond to Fig.2.19. The numerical results with BC-B and BC-C are compared using a buckling curve generated from Fig.4.22 and the buckling curve from Annex B, EN 1993-1-5 [36] respectively as identified in Sec.4.6.4.2. For the definition of the boundary conditions see Fig.4.19.

Generally, the results on plates subjected to direct stresses are subdivided into square and long plates, since the buckling behaviour is a different one due to column–like

behaviour. To keep this section readable, it is decided to include only the investigations on BC-C here and to move the results for the other boundary conditions to Sec.C.1 in the Annex.

Square plates

The comparison on square plates is presented in Fig.6.1 for BC-C and in Fig.C.1 and Fig.C.2 for BC-A and BC-B. It is noticeable that in general the influence of tensile stresses on the buckling behaviour matches quite well. The intersection with the von Mises criterion takes place at the same interaction angle Θ for the design as well as for the numerical simulations. However, for the area in between some lower results are found, whereby the current design rules would lead to an overestimation of the buckling resistance, if tensile stresses would be applied in the design procedure. Generally, similar results are found in principle for all regarded boundary conditions, so that it can be concluded that a common approach may be deduced independently from the boundary condition, which is advantageous for the practical design.

Another observation from the direct comparison is the absence of any sharp bends for the results from the numerical simulations, while the interaction according to EN 1993-1-5 [36] shows pronounced bends in the curve progression. These typical bends result, as already mentioned in Sec.2.4.2, from the peaks between the "garland"–curves for determining the buckling factor, which are very pronounced for the case of tension–compression, see Fig.2.2. As these peaks lead to higher buckling factors and in turn to lower slenderness, in that areas the mentioned sharp bends can be observed. The comparison shows clearly the necessity of improving the design procedure in order to take into account the positive effect of tensile stresses, while still assuring safe-sided results.

Long plates

Fig.6.2 shows the comparison of the current design rules according to EN 1993-1-5 [36], assuming the positive effect of tensile stresses, to the numerical results on BC-C. The results for boundary conditions BC-A and BC-B are shown in Fig.C.6 and Fig.C.7. Although the current design rules are found to be lower for BC-A and BC-B, the graphs clearly show that the "offset" is variable over the interaction range, leading to a safety variation. However, the interaction curves should generally follow the shape of the numerical results, so that the procedure works independently from the boundary conditions. Furthermore, e.g. a later change of the buckling curves for the reference strengths could lead to a shift of the curves, where possible unsafe results may be gained. In the opinion of the author, therefore it is important that the design procedure should not only lead to safe-sided results, but also follow qualitatively the numerical results in order to guarantee a general applicability and future-oriented procedure.

In contrast to the results for BC-A and BC-B the comparison for BC-C in Fig.6.2 shows lower results almost continuously over the whole range, even for pure compression. This was also observed by Braun [11] when investigating the case of biaxial compression

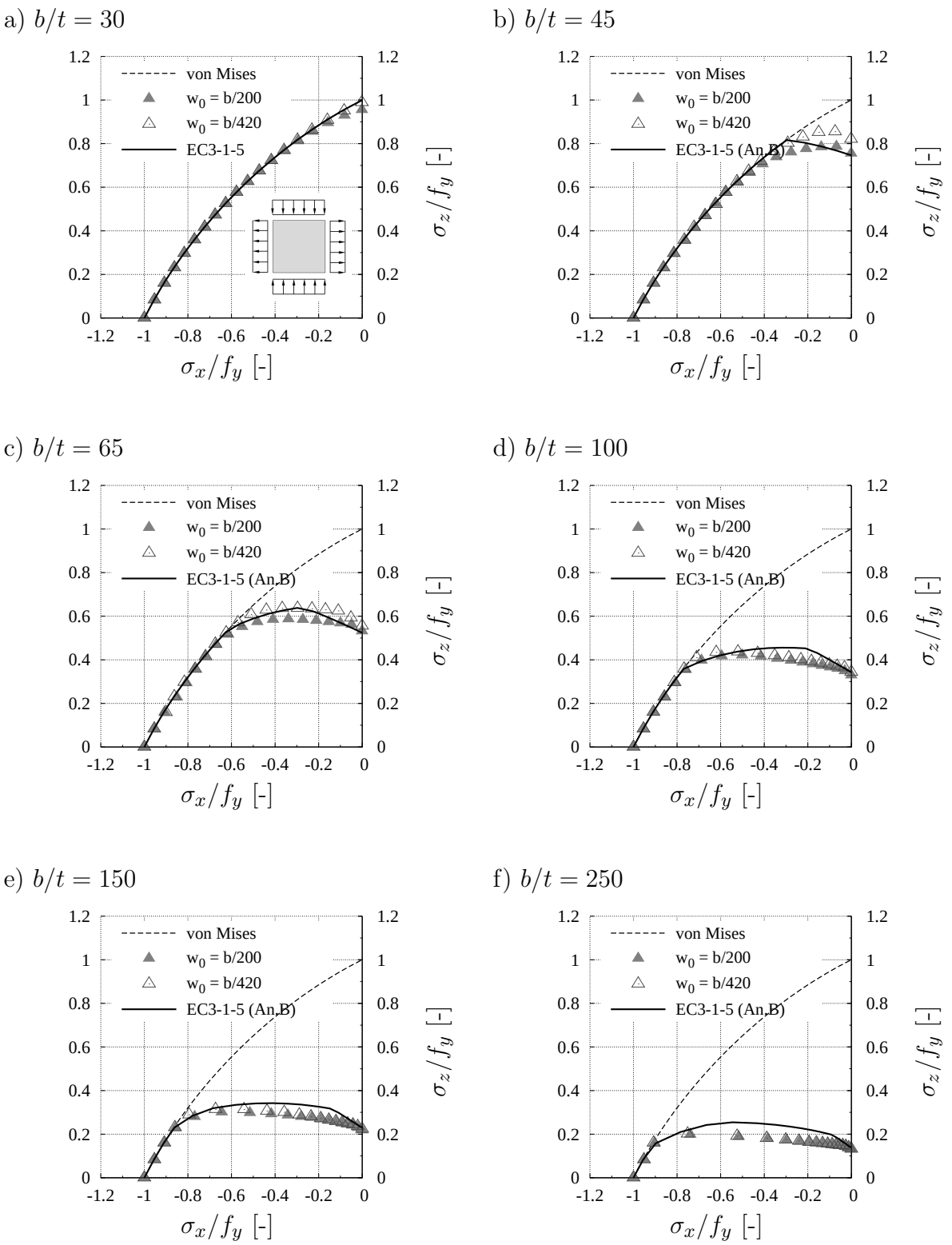

Figure 6.1: Comparison of the numerical results with the current design rules in EN 1993-1-5 [37] based on Annex B, (BC-C, $\alpha = 1$, all edges hinged and free to move in plane, decisive imperfection).

on long plates but the issue was not further addressed. Investigations conducted by Seitz [101] also led to similar conclusions and proposed a modified interpolation formula (see Eq.(2.34)) for column–like behaviour in order to take into account this effect, see Sec.2.5.7.

Additionally to the "wrong starting point" of the curves for BC-C, the shape of the curves according to EN 1993-1-5 [36] seem to be even more differing from the numerical results than it was the case for BC-A and BC-B, leading to the conclusion that a distinction of cases is needed to come to appropriate and also economic results.

6.2.3 Plates subjected to direct and shear stress

The comparisons on plates subjected to direct and shear stress for predominant tension are presented in Fig.6.3 for $\psi = 1$ (pure tension) and in Fig.6.4 for $\psi = -0.5$. For predominant compression the results are compared in Fig.6.5 for $\psi = 1$ (pure compression) and in Fig.6.6 for $\psi = -1$ (pure bending). The remaining comparisons are arranged in Sec.C.2 in the Annex for the sake of completeness.

The comparison of the numerical results for tension–shear ($\psi = 1$) with the current design rules show a good agreement. Therefore, currently there seems to be no need for a modification of the design rules for this case, as the effect of tensile stresses is represented correctly. In Fig.6.4 the comparison is made with a stress gradient for the direct stresses exemplarily for $\psi = -0.5$. Therefore the two possible interpretations A and B are adopted as discussed in Sec.2.4.2 and Fig.2.26. The results using interpretation A, where the buckling check is conducted on the point with the maximum stresses, lead to more conservative results compared to interpretation B, where a distinction of cases is done between buckling and yielding, see Fig.2.26. The comparison of the numerical results to both interpretations lead to the conclusion that interpretation B, which is only slightly more time-consuming than interpretation A, gives more economic results following the numerical results very closely. The check for interpretation B consists per se of a buckling check and an additional yielding check. Anyway, this theoretically allows for considering webs to partly plastify, which is formally not possible using interpretation A.

For the case of interaction between compression and shear, the results for pure compression ($\psi = 1$) show a good agreement between numerical simulations and the design rules according to EN 1993-1-5 [36], see Fig.6.5. The interaction curve follows the numerical results very closely, only for the stocky plate ($b/t = 45$) some overestimation is found, which was also observed in case of biaxial compression by Braun [11], as here the plate is more sensitive to the applied amplitude of imperfection. Especially for stocky plates the question arises what is a reasonable imperfection amplitude for numerical simulations. Nevertheless, the comparison shows that the code generally gives appropriate results and can be regarded as suited for plates under compression–shear. The numerical simulations in case of bending and shear with predominant compression

a) $b/t = 30$

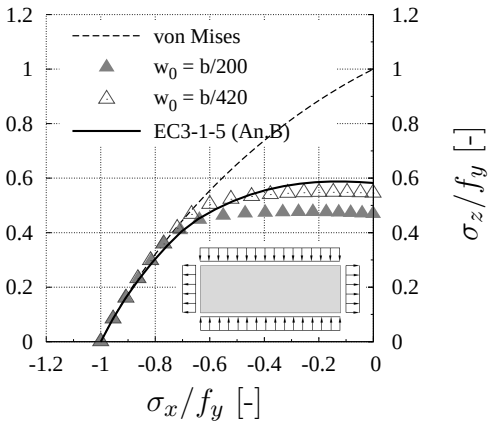

b) $b/t = 45$

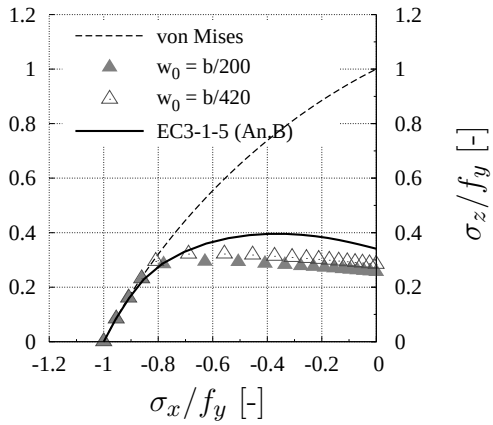

c) $b/t = 65$

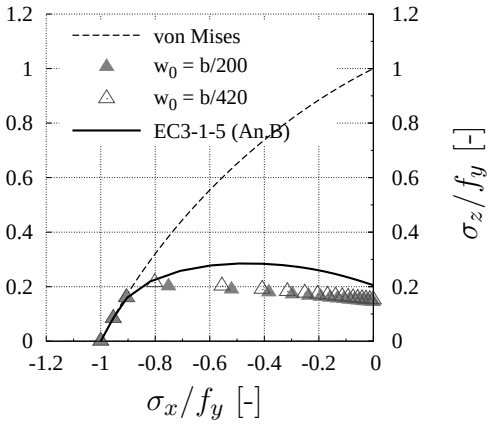

d) $b/t = 100$

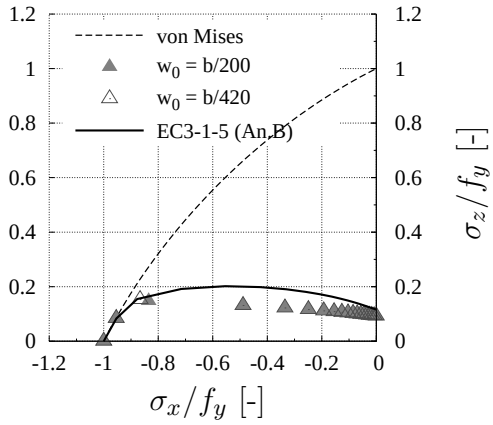

e) $b/t = 150$

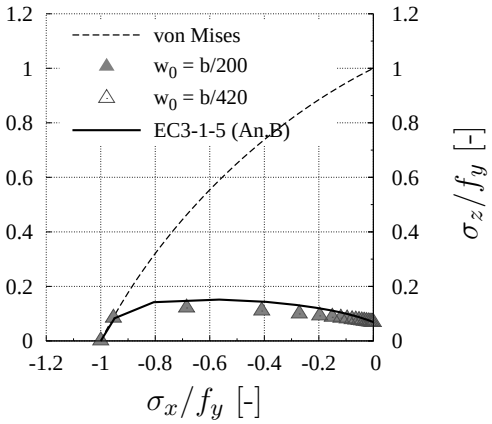

f) $b/t = 250$

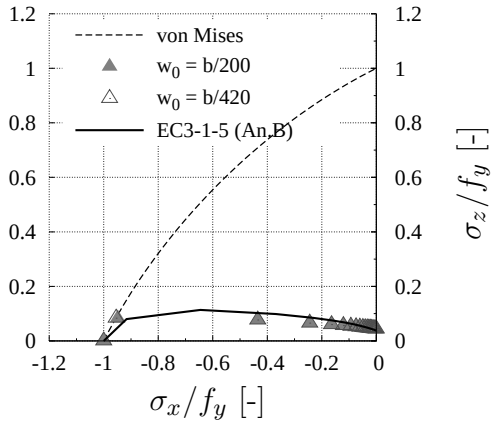

Figure 6.2: Comparison of the numerical results with the current design rules in EN 1993-1-5 [37] based on Annex B, (BC-C, $\alpha = 3$, all edges hinged and free to move in plane, compression applied on long edge).

c) $b/t = 70$ d) $b/t = 100$

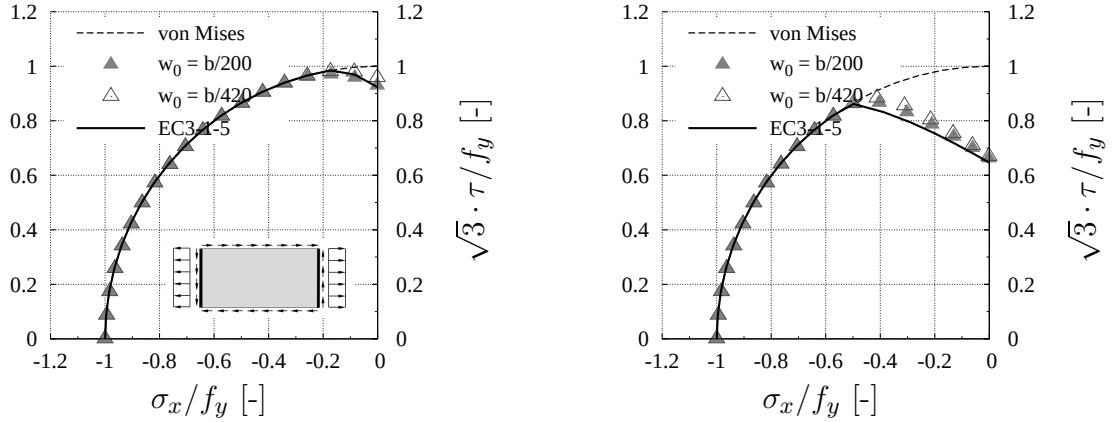

e) $b/t = 150$ f) $b/t = 250$

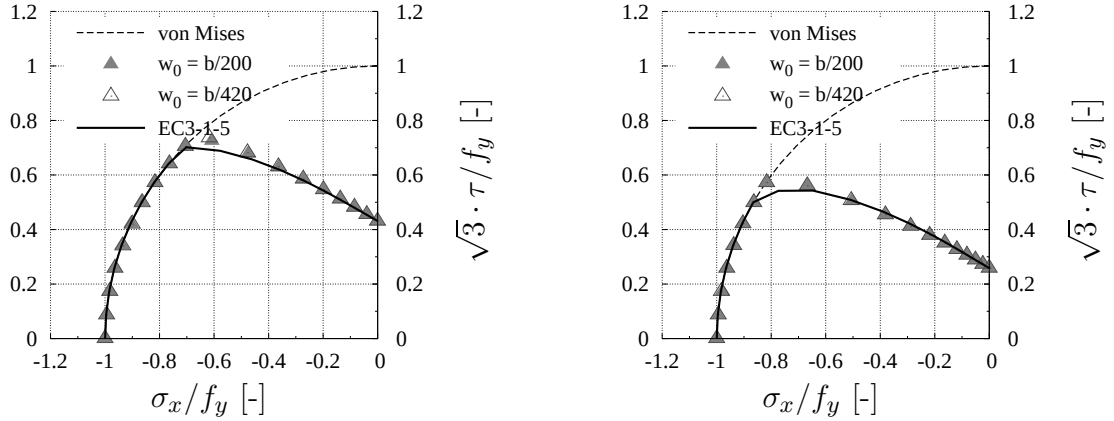

Figure 6.3: Comparison of the numerical results with the current design rules in EN 1993-1-5 [37], (BC-A, $\psi = 1$, $\alpha = 2$, all edges hinged).

($\sigma_c \geq \sigma_t$) are shown exemplarily for $\psi = -1$ in Fig.6.6. The other comparisons are shown in Sec.C.2 in the Annex. As the recalculation of the buckling curves in Sec.4.6.4.2 has shown a very good agreement of numerical simulations and the buckling curves from DIN 18800-3 [22] in case of bending, the comparisons in case of bending interaction with shear are presented using both the buckling curves from EN 1993-1-5 [36] and from DIN 18800-3 [22] (denoted as "DC" in the diagrams). The buckling curves from DIN 18800-3 [22] have been presented in Tab.2.4. The interaction curves according to EN 1993-1-5 [36] show good results in case of interaction. However, when approaching pure direct stresses, the curves show to be conservative and point out a potential for improvement. If the curves from DIN 18800-3 [22] are adopted, the results for pure bending match with the numerical simulations, but the interaction is overestimated. This leads to the general conclusion that the code as it is leads to appropriate results. Using the curves from DIN 18800-3 [22] could exploit the shown potential, but needs a modification of the current design formulation.

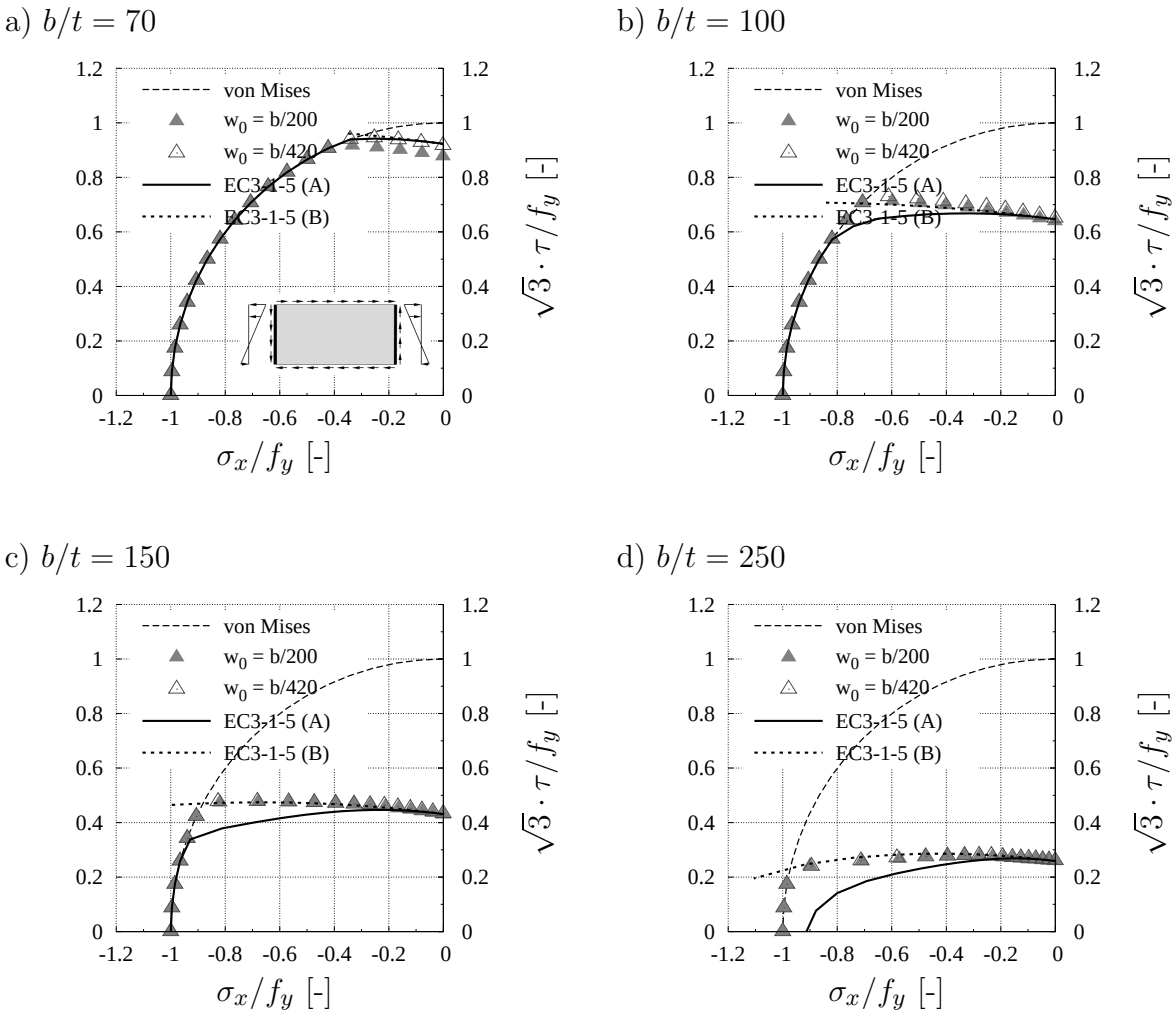

Figure 6.4: Comparison of the numerical results with the current design rules in EN 1993-1-5 [37], (BC-A, $\psi = -0.5$, $\sigma_t > \sigma_c$, $\alpha = 2$, all edges hinged).

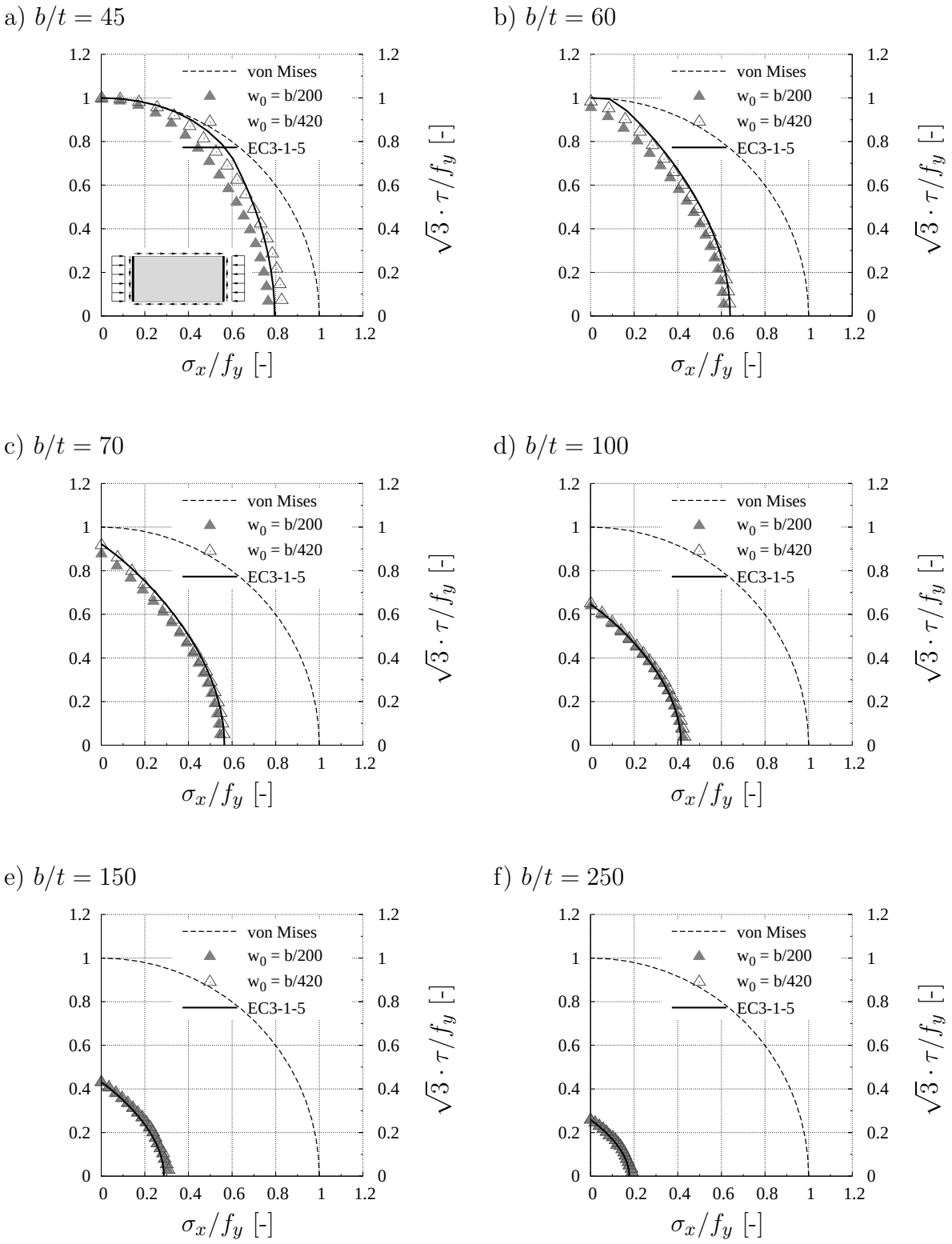

Figure 6.5: Comparison of the numerical results with the current design rules in EN 1993-1-5 [37], (BC-A, $\psi = 1$, $\alpha = 2$, all edges hinged).

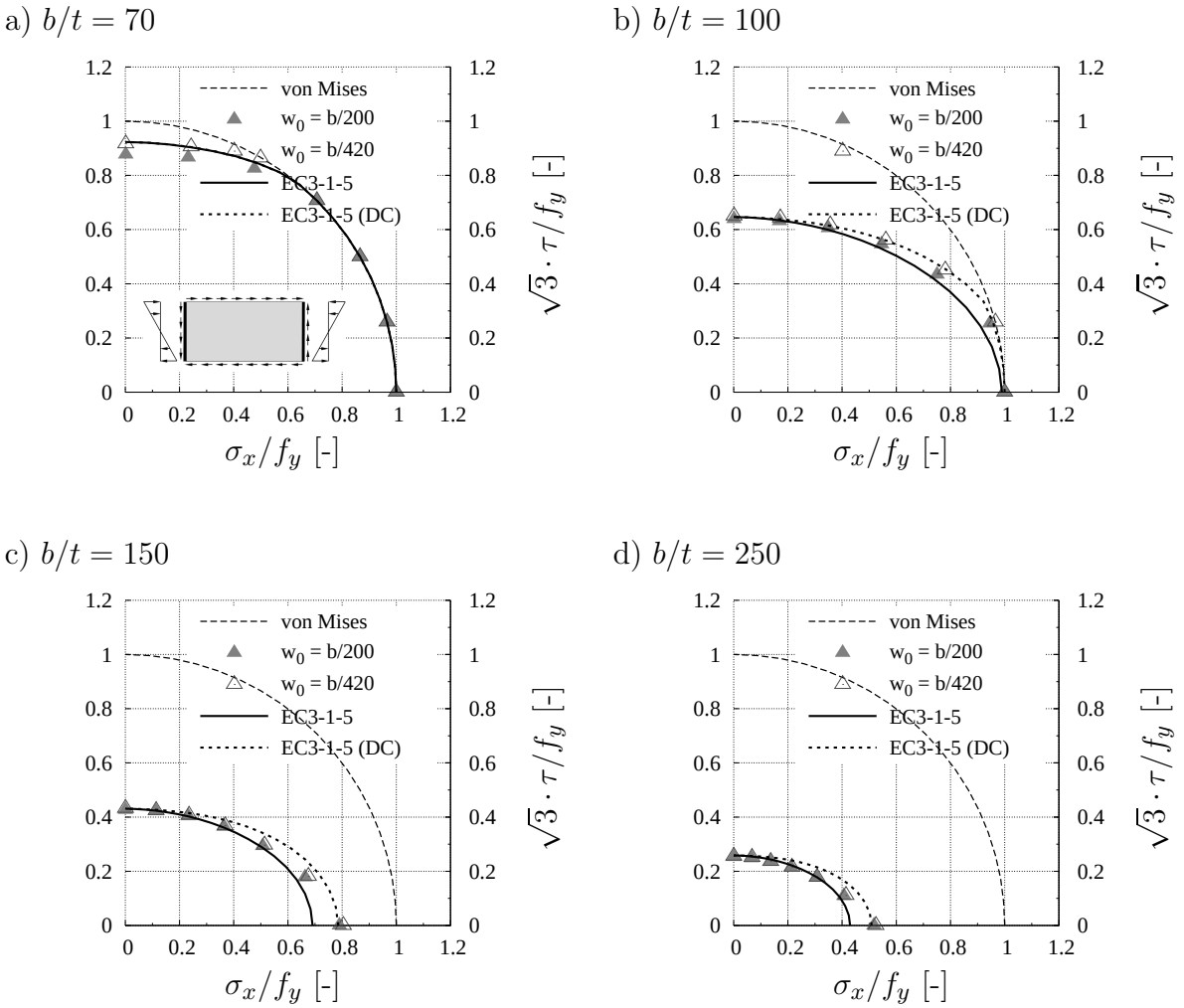

Figure 6.6: Comparison of the numerical results with the current design rules in EN 1993-1-5 [37], (BC-A, $\psi = -1$, $\alpha = 2$, all edges hinged).

6.2.4 Stiffened plates under biaxial compression

The numerical results on stiffened plates under biaxial compression are compared to the interaction curves according to EN 1993-1-5 [36] exemplarily for the case of one stiffener and $\alpha = 1$ in Fig.6.7. The other comparisons are arranged in Sec.C.3, see Annex. The numerical results are compared with EN 1993-1-5 [36] with and without the application of the V-factor according to Braun [11]. Generally, it can be noticed that the interaction curves using the V-factor also for stiffened plates lead to a more appropriate behaviour. Not applying the factor leads to large overestimations of the resistances in almost all cases, while the curve with V-factor follows the numerical results quite well. Even for the weak stiffeners, where global buckling becomes decisive, the rather linear characteristics of the numerical results are followed by the interaction curves. However, it should be noted that the use of weak stiffeners leads to a very strong interaction, which should be avoided in practice. Nevertheless, weak stiffeners may especially occur for the recalculation of existing bridges. For the medium and stronger stiffeners a good match between numerical simulations and the interaction curve is found, confirming that the application of the mentioned V-factor is appropriate for stiffened plates.

Furthermore, an overestimation of the resistance in transverse direction is observed in almost all cases. The overestimation takes place where column–like buckling behaviour plays a role and was already observed for unstiffened plates in Sec.6.2.2 and by Seitz [101] and Braun [11].

The resistances according to Chapter 10, EN 1993-1-5 [36] with and without the V–factor are put against the numerical simulations in Fig.6.8, which show that not applying the V–factor leads to unsafe results with resistances up to 50 % above the numerical simulations. Furthermore, a large variation of the ratio is observed. By use of the V–factor the ratio is smoother but still containing visible scattering. The peaks with higher results are, as mentioned above, the results for predominant transverse stresses where column–like behaviour occurs.

Influence of the interpolation between column and plate buckling

Since the comparison of the numerical simulations to the design rules reveals that for transverse stresses the resistance is systematically overestimated, it seems likely that a modification of the formulation for the interpolation could overcome this issue. Another possibility to adjust the reference strengths would be to change the buckling curves, which is not further investigated in the frame of this work.

Regarding the interpolation of plate–like and column–like buckling behaviour Seitz [101] proposed a modified formulation, see Sec.2.5.7. It should be noted that the reformulation was derived on the basis of unstiffened plates. However, for the sake of comparison the proposal is applied exemplarily in transverse direction for stiffened plates in Fig.6.9. The results show that the interpolation by Seitz [101] lead to lower resistances, which is a logical consequence from Fig.2.34.

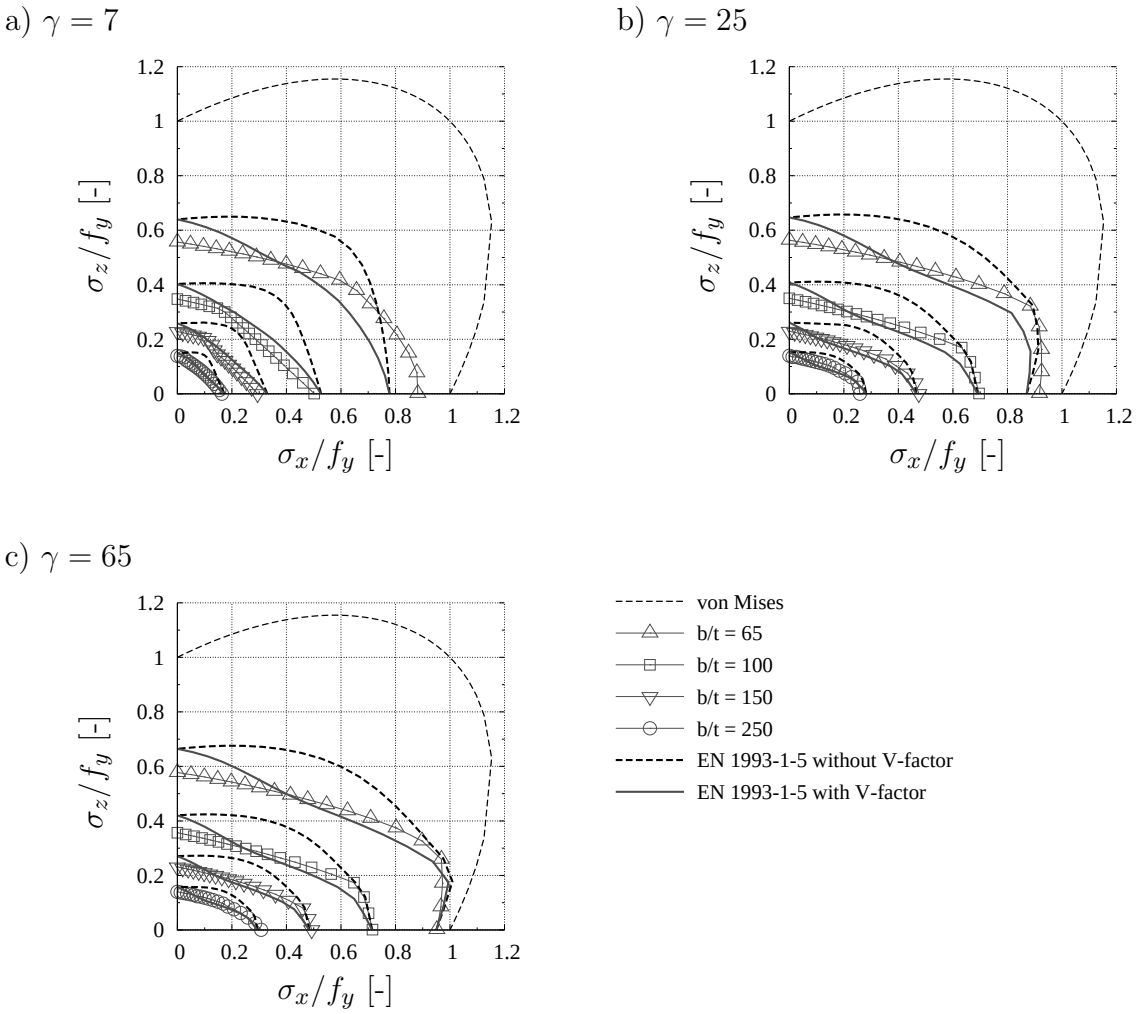

Figure 6.7: Comparison of numerical results with current design rules for stiffened plates loaded with biaxial compression, ($\alpha = 1$, $n = 1$, $b/t = 65$, 100, 150 and 250).

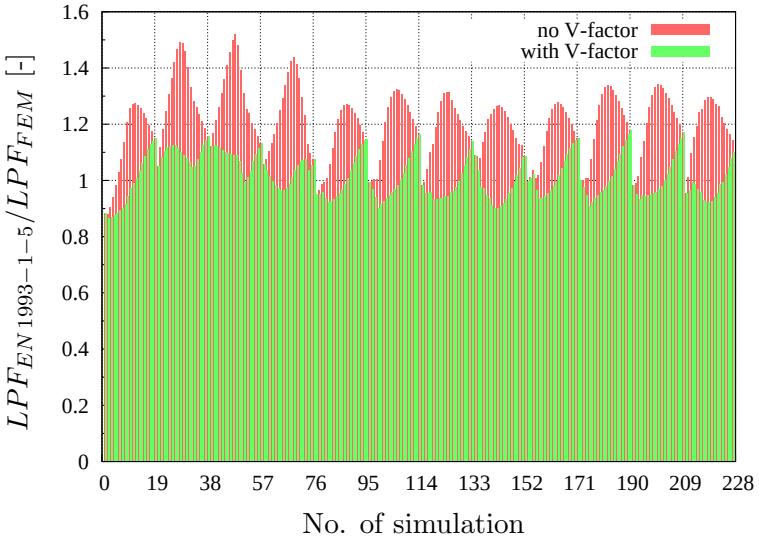

Figure 6.8: Influence of V–factor on the resistance according to EN 1993-1-5, Ch. 10 in comparison to the numerical simulations ($\alpha = 1$, $n = 1$).

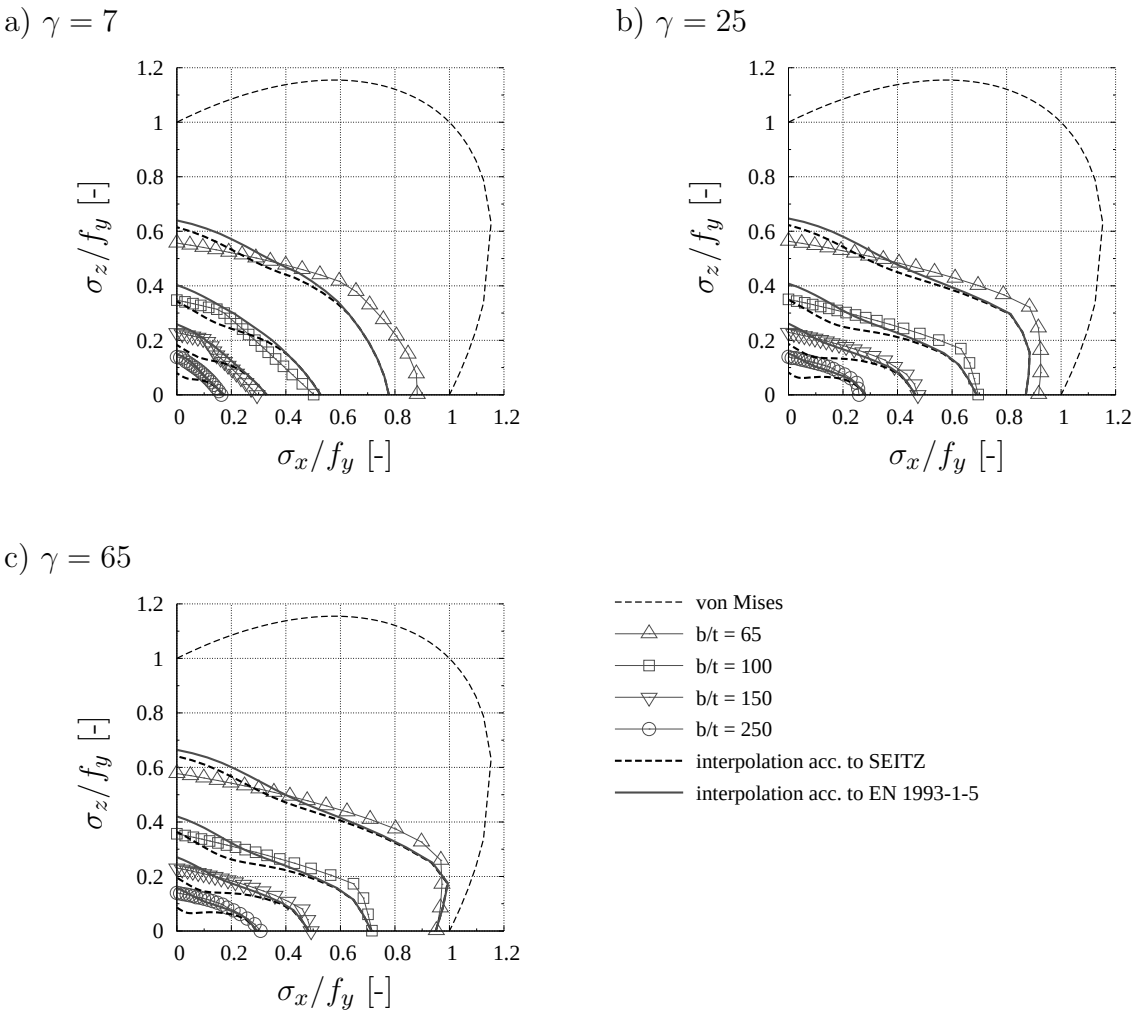

Figure 6.9: Comparison of numerical results with design rules using the V-factor and the SEITZ–approach [101] for stiffened plates loaded with biaxial compression, ($\alpha = 1$, $n = 1$, $b/t = 65$, 100, 150 and 250).

The results show that the modification of the interpolation is the right step in solving the mentioned issue for transverse stresses. The formulation derived by SEITZ [101] for unstiffened plates is also applied in the frame of this work for unstiffened plates, leading to appropriate results compared to the current formulation, see Sec.6.3.2. However, the proposed interpolation applied on stiffened plates shows still unsafe results leading to the conclusion that the formulation needs some recalibration for the case of stiffened plates, which is supported by the author but not within the scope of this work.

6.3 Improved design rules

6.3.1 Proposal

As shown in the foregoing sections the current design procedure may lead to resistances above the results from numerical simulations for multiaxially loaded plates. The numerical investigations have shown inconsistencies for the case of unstiffened plates subjected to tension–compression, where an enhancement of the V–factor is proposed in order to solve this issue. Furthermore, the investigations on plates subjected to tension and shear have shown that the current design procedure follows the numerical simulations properly, so that a modification in this case is not necessary. For the case of compression or bending and shear the current design procedure gives also safe results. However, recalculations of the buckling curves for bending show that the current buckling curves give quite conservative results, whereas the buckling curves according to DIN 18800-3 [22] match well with the numerical simulations, see Sec.4.6.4.2. Comparisons in Sec.6.2.3 show that, if the buckling curves according to DIN 18800-3 [22] are adopted, the numerical results approaching the case of pure bending match better to the design procedure, but in the interaction domain resistances may occur, which are above the results from numerical simulations. As the shape of the interaction curves show a dependency from the slenderness, for the case of bending–shear a modification of the exponent e_3 is proposed, which has a direct influence on it.

The general formulation for the interaction formula is shown in Eq.(6.1). According to EN 1993-1-5 [36] the exponents e_1, e_2 and e_3 are all set to 2 and $V = 1$. The proposed exponents and the V–factor are shown below the equation. The exponents e_1 and e_2 remain the same as before, while for e_3 a modification is proposed to account for the interaction case of bending–shear in order to obtain appropriate results when adopting the more favourable buckling curves from DIN 18800-3 [22]. Aiming at a harmonised format the proposed formulation of the exponent e_3 is oriented to EN 1993-1-6 [38]. However, it is noted here that according to EN 1993-1-6 [38] the determination of the slenderness values is conducted for each direction separately. The V-factor proposed by Braun [11] is modified for the case tensile stresses are acting. As the numerical simulations for long plates show that in transverse direction, where in practical cases usually deformable boundary conditions are present, the beneficial effect of tensile stresses is overestimated more than for the other boundary conditions, the formulation of the V-factor contains a dependence on the weighting factor ξ_z for column–like behaviour taking also into account the interpolation according to Seitz [101].

$$\left(\frac{\sigma_x}{\rho_{c,x}\cdot f_y}\right)^{e_1}+\left(\frac{\sigma_z}{\rho_{c,z}\cdot f_y}\right)^{e_2}-V\cdot\left(\frac{\sigma_x}{\rho_{c,x}\cdot f_y}\right)\cdot\left(\frac{\sigma_z}{\rho_{c,z}\cdot f_y}\right)+\left(\frac{\sqrt{3}\cdot\tau}{\chi_w\cdot f_y}\right)^{e_3}\leq 1 \quad (6.1)$$

where:	$e_1 = e_2 = 2$	
	$e_3 = 1.25 + 0.75 \cdot \chi_w^2$	for the general case, (if the reduction factor ρ_x is determined with the buckling curves from DIN 18800-3 [22], else $e_3 = 2$)
	$e_3 = 2$	if σ_x and/or σ_z are/is tension or pure compression
	$V = \rho_{c,x} \cdot \rho_{c,z}$,	if σ_x and σ_z are both compression [11]
	$V = 1/(\rho_{c,x} \cdot \rho_{c,z}^{2-\xi_z})$	if σ_x and/or σ_z are/is tension
	$\rho_{c,x}$	is the reduction factor for longitudinal stress from Table 1, DIN 18800-3 [22] or Sec. 4.5.4(1), EN 1993-1-5 [36] taking into account column–like behaviour where relevant
	$\rho_{c,z}$	is the reduction factor for transverse stress from Annex B, EN 1993-1-5 [36] taking into account column–like behaviour where relevant
	χ_w	is the reduction factor for shear stress from Sec. 5.3(1), EN 1993-1-5 [36]

Tab.6.1 shows a summary of different definitions for the exponent e_3. The new proposal is recommended for the case of bending–shear, if the buckling curves according to DIN 18800-3 [22] are adopted. Otherwise, if the buckling curves according to EN 1993-1-5 [36] are kept, the current exponent $e_3 = 2$ is regarded as sufficient, see Sec.6.2.3. An overview is given in Tab.6.2.

The peaks of the buckling coefficient, which have been discussed in Sec.2.2.2 are not taken into account as also proposed already by Lindner & Rusch in [74], since the increased resistances that would result are not observed neither in reality nor for numerical simulations. Furthermore, for the interpolation of plate–like and column–like behaviour for transverse stresses the proposal from Seitz [101] presented in Sec.2.5.7 is adopted, as the current formulation shows shortcomings in case of deformable edge boundary conditions, see Fig.6.2. For a better overview the interpolation for taking into account column–like behaviour in transverse direction according to Seitz is given once more in Eq.(6.2).

$$\rho_{c,z} = \chi_{c,z} + (\rho_z - \chi_{c,z}) \cdot f \tag{6.2}$$

where: $f = \bar{\lambda}_p^{-0.5} \cdot \ln(\xi_z + 1)^{0.9}$ and $\xi_z = \frac{\sigma_{cr,p,z}}{\sigma_{cr,c,z}} - 1$

The comparisons are conducted for different boundary conditions in order to separate their influence from the interaction criterion as the reference strengths are used. Furthermore, the proposal aims at fulfilling the criteria postulated by Scheer & Nölke [96] for a further development of a “generalised equivalent stress design”, see Sec.2.4.1.

Table 6.1: Different definitions for exponent e_3.

Factor e_3	according to	labeling
$e_3 = 2$	EN 1993-1-5 [36]	-
$e_3 = 1 + \kappa_x \cdot \kappa_z \cdot \chi_\tau^2$	DIN 18800-3 [22]	V1
$e_3 = 1.5 + 0.5 \cdot \chi_\tau^2$	EN 1993-1-6 [38] (general case)	V2
$e_3 = 1.75 + 0.25 \cdot \chi_\tau$	EN 1993-1-6 [38] (cylindrical shell)	V3
$e_3 = 1.25 + 0.75 \cdot \chi_w^2$	new proposal	NEW

Table 6.2: Overview for exponent e_3 in case of bending.

	Buckling curves according to DIN 18800-3 [22]	Buckling curves according to EN 1993-1-5 [36]
Formulation	$\rho = c \cdot \left(\frac{1}{\lambda_p} - \frac{0.22}{\lambda_p^2}\right) \leq 1$ where $c = 1.25 - 0.25 \cdot \psi \leq 1.25$	$\rho = \frac{\bar{\lambda}_p - 0.055 \cdot (3+\psi)}{\lambda_p^2} \leq 1.0$
$e_3 =$	$1.25 + 0.75 \cdot \chi_w^2$	2

6.3.2 Plates subjected to direct stresses

The comparison of the improved design rules is conducted in the following with the numerical simulations from Sec.5 and subdivided again for square and long plates to assess the influence of column–like behaviour. In order to keep this section readable, only the results for boundary condition BC-C are arranged here, while BC-A and BC-B can be found in Sec.D.1 in the Annex.

Square plates

Fig.6.10 shows the comparison of the new proposed design procedure and the numerical simulations for boundary condition BC-C. It can be noticed that the proposed interaction curves follow the numerical results so that the positive effect of tensile stresses can be taken into account for the design procedure. The comparisons for boundary conditions BC-A and BC-B are presented in Fig.D.1 and Fig.D.2. The figures also show a good match between the proposed interaction curve and the numerical results, so that the proposal seems to work independently from the boundary conditions.

From the comparisons of the numerical simulations to the improved design rules it can be concluded that the proposal performs well for all regarded boundary conditions allowing for a safe reliable design of slender plates for the whole parametric range.

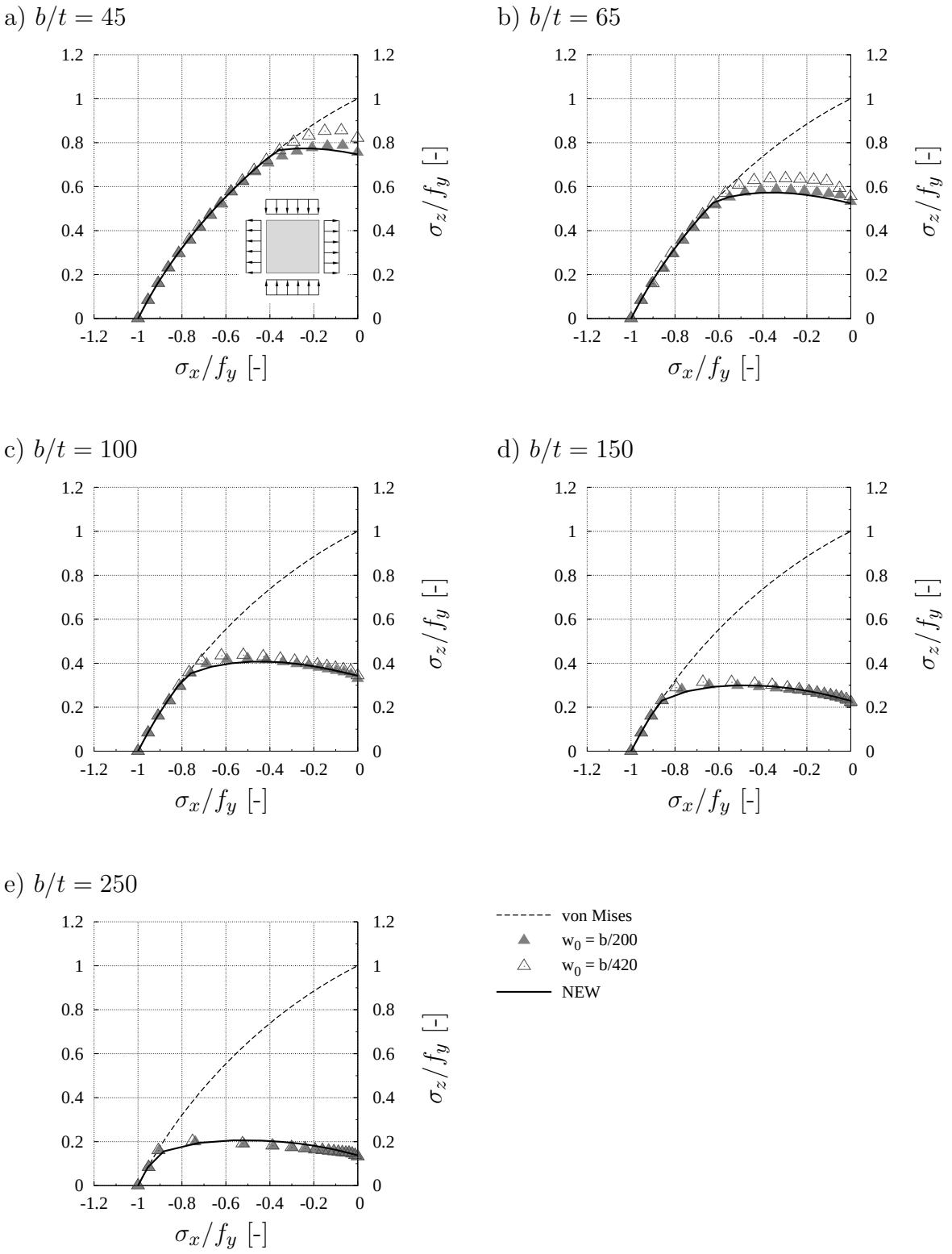

Figure 6.10: Comparison of the numerical results with the new proposal based on Annex B, (BC-C, $\alpha = 1$, all edges hinged, decisive imperfection).

Long plates

The comparison for long plates with BC-C is presented in Fig.6.11. As in case of column–like behaviour the comparison of the numerical results to the current rules shown in Sec.6.2.2 revealed a more sensitive behaviour of plates with the not restrained boundary condition BC-C, a distinction of cases is introduced by the exponent for ρ_z of $(2 - \xi_z)$ in the definition of the V-factor, see Eq.(6.1). Since in x–direction usually restrained boundary conditions are present, the exponent is applied only for the transverse direction, where the edge is idealised as free to move in–plane. The proposed interaction curves in Fig.6.11 show a good agreement with the numerical simulations. In addition to the new proposal, the curves without the application of the mentioned exponent are shown and denoted as "NEW*" in Fig.6.11 as comparison.

The results for boundary condition BC-A and BC-B are presented in Fig.D.6 and Fig.D.7 in the Annex. It can be seen that the new proposal performs well for all cases so that the effect of tensile stresses can be accounted for also for plates where column–like behaviour becomes decisive. It is noted here that the mentioned interaction curves already include the proposal from Seitz [101].

6.3.3 Plates subjected to direct and shear stress

As shown in Fig.6.5 the current design procedure gives appropriate results for the case of interaction of shear and pure compression ($\psi = 1$), so that in this case and also for the tension–shear interaction an exponent of $e_3 = 2$ is recommended. However, for the sake of completeness the interaction curves for the exponent e_3 according to Tab.6.1 are presented in Fig.6.12 showing in all cases safe results but a rather conservative characteristic for the new proposal, which is calibrated for the case of bending–shear, see Fig.6.13.

The comparison of the numerical results and the interaction curves for the case of bending–shear is presented in Fig.6.13. The interaction curves are calculated using the buckling curves according to DIN 18800-3 [22], which in case of $\psi \neq 1$ match better to the numerical simulations than the buckling curves according to EN 1993-1-5 [36], see Sec.4.6.4.2. The new proposal follows the numerical results properly in case of $\psi = -1$ as well as for the other regarded cases, see Sec.D.2 in the Annex. Therefore, also for plates subjected to direct and shear stress, the proposal leads to reliable results. A direct comparison of the current design rules according to EN 1993-1-5 [36] and the new proposal is given for $\psi = -1$ in Fig.6.14. It can be seen that in case of dominant shear stresses the new proposal gives marginally more conservative results due to the different exponent e_3. However, the differences can be regarded as insignificant in the opinion of the author. For the sake of completeness a comparison of the interaction curves using $e_3 = 2$ with the reduction curves for direct stresses from DIN 18800-3 [22] and EN 1993-1-5 [36] are given in Sec.6.2.3 and Sec.C.2 in the Annex.

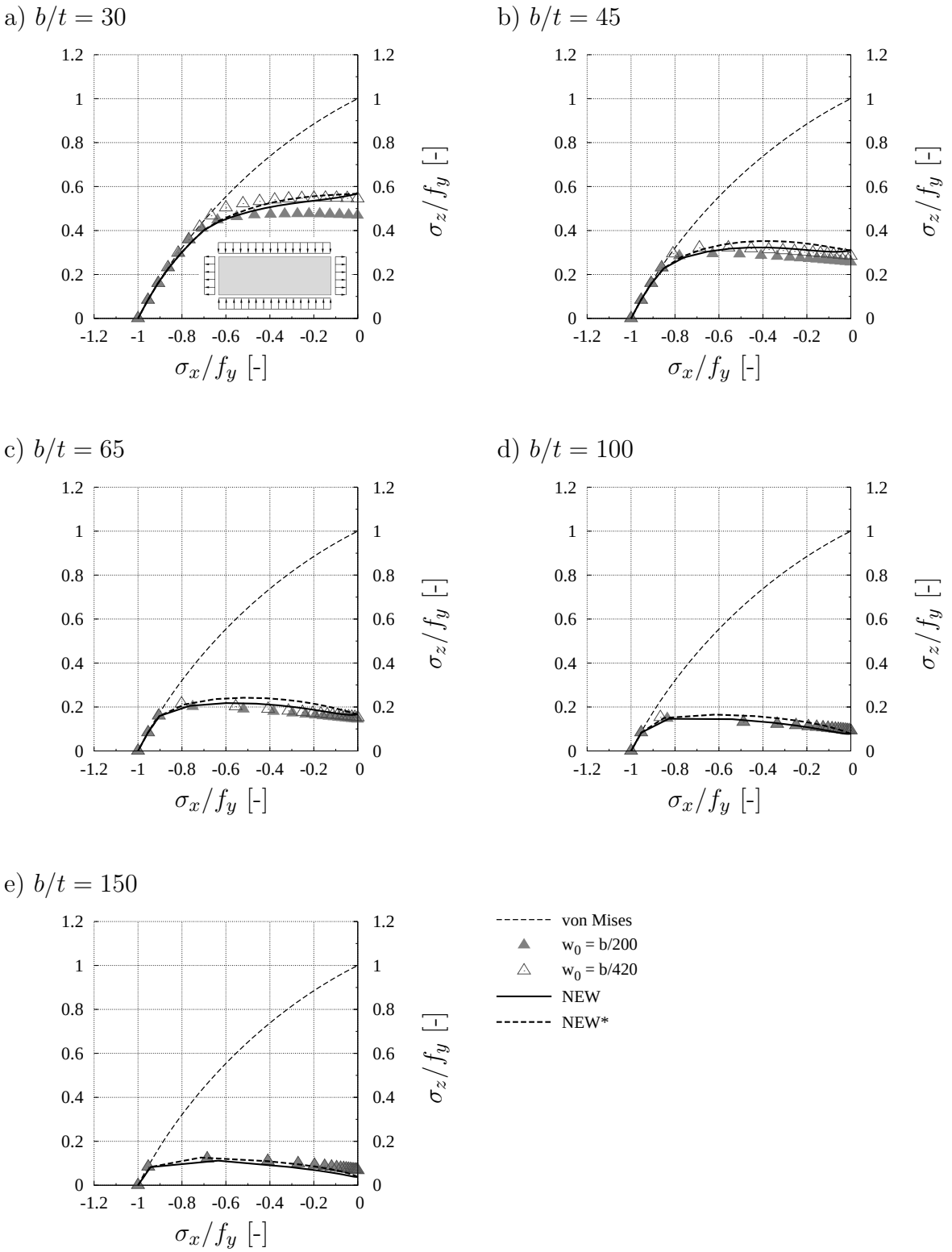

Figure 6.11: Comparison of the numerical results with the new proposal, (BC-C, $\alpha = 3$, all edges hinged, compression applied on long edge).

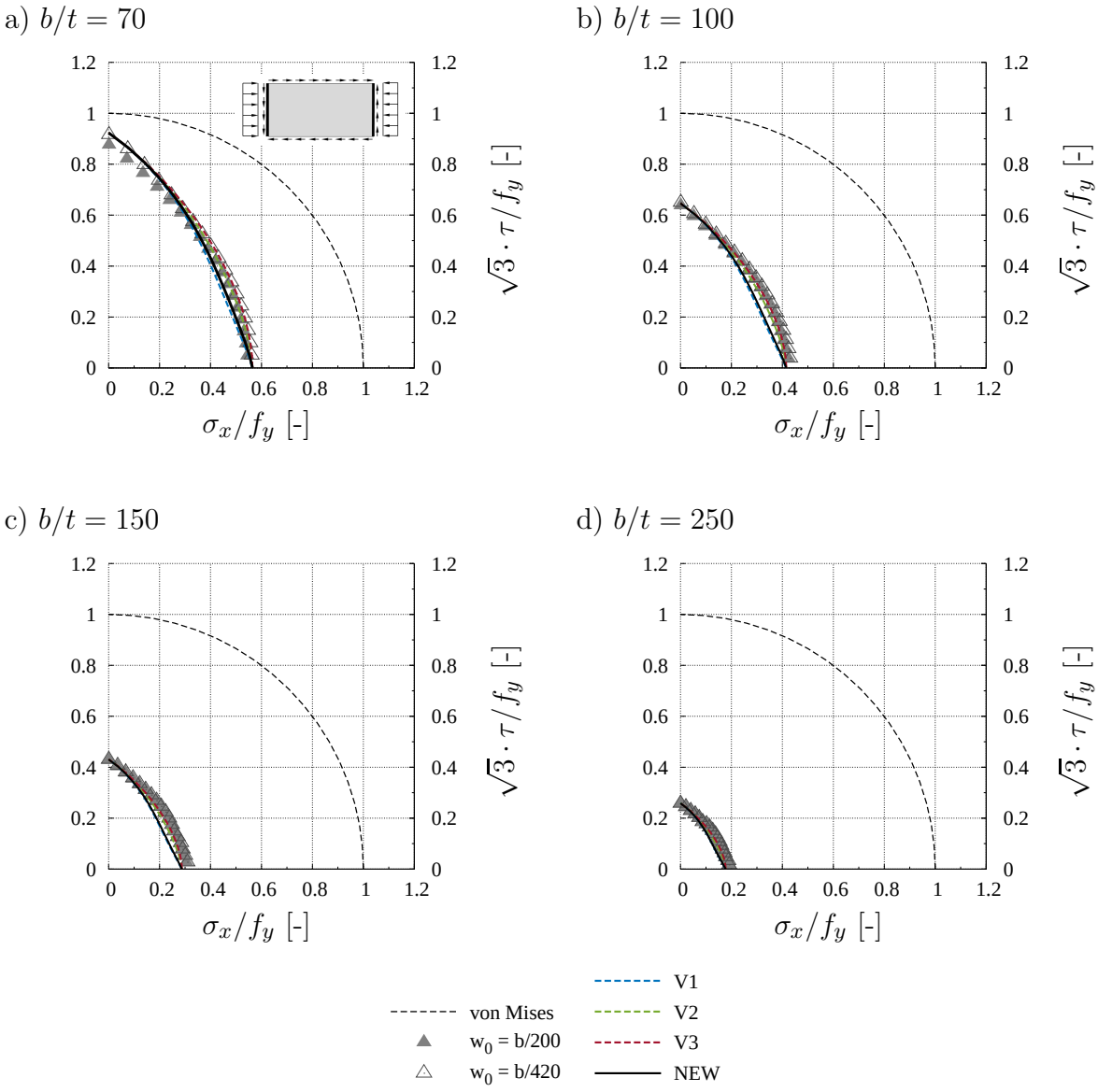

Figure 6.12: Comparison of the numerical results with the different approaches for factor e_3, (BC-A, $\psi = 1$, $\alpha = 2$, all edges hinged).

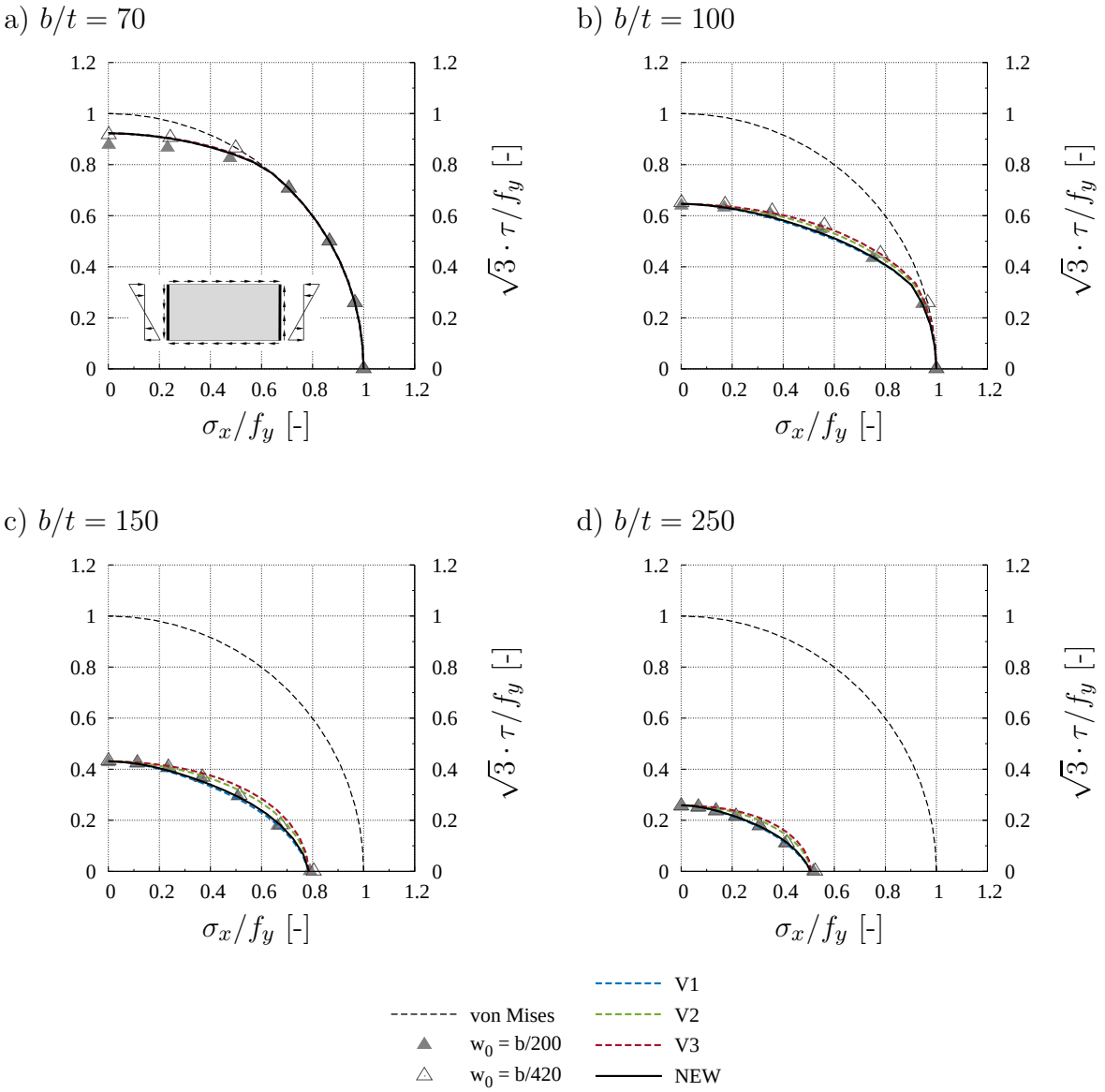

Figure 6.13: Comparison of the numerical results with the different approaches for factor e_3, (BC-A, $\psi = -1$, $\alpha = 2$, all edges hinged).

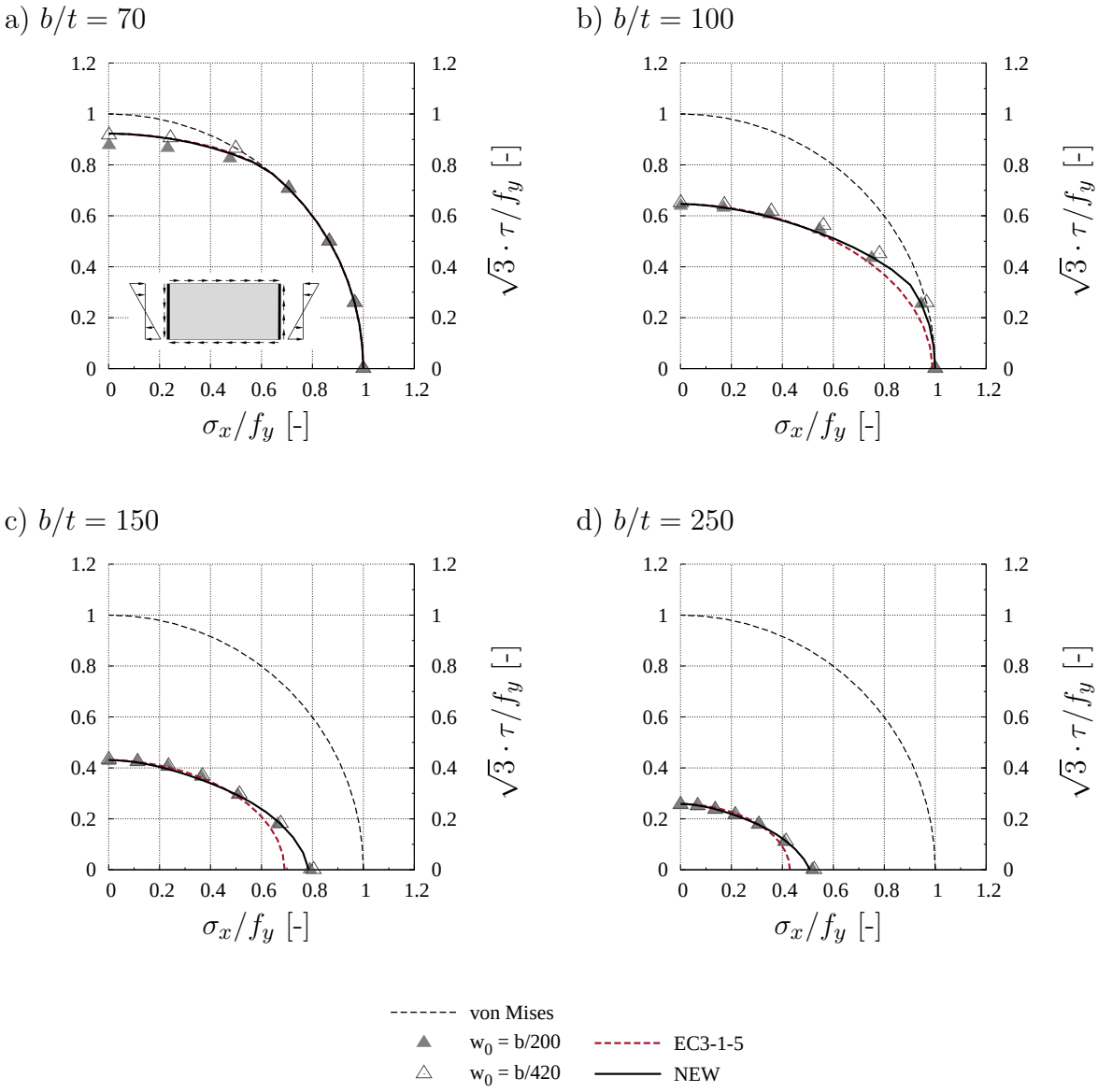

Figure 6.14: Comparison of the numerical results with the current formulation according to EN 1993-1-5 [36] and the new proposal, (BC-A, $\psi = -1$, $\alpha = 2$, all edges hinged).

6.4 Statistical evaluation of the improved design rules

6.4.1 General

As for the structural design the resistance is calculated as a design value considering several uncertainties, a statistical evaluation of the new proposal is conducted to verify the reliability. EN 1990 [34] contains the basis of structural design according to the Eurocodes and gives detailed information on how to conduct statistical analyses. The determination of the partial factor is described in EN 1990, Annex D [34] and gives generally two methods:

- Statistical determination of a single property (Annex D, Chapter 7),
- Statistical determination of resistance models (Annex D, Chapter 8).

The first method gives details on deriving design values for a single property such as the strength as the only statistical variable. EN 1990 [34] presumes for the application of this method specific tests to establish directly the ultimate resistance or serviceability properties for given loading conditions. Furthermore, the procedure is suitable for tests to obtain specific material properties using specified testing procedures. Since the requirements for the application of the first method are not fulfilled, in the frame of this work the more general procedure according to EN 1990, Annex D.8 [34] is adopted. This method considers the influence of the variation of parameters that are not covered by the numerical simulations. In the following the procedure is described as in EN 1990 [34] step by step.

6.4.2 Statistical determination using the resistance model method

In EN 1990, Annex D.8 [34] the procedure for the statistical evaluation is subdivided into seven steps. Kövesdi [58] as well as Sinur [106] added one more step for the determination of V_{FEM}. Kövesdi [58] additionally handled the material properties separately, which is also adopted within this work and in accordance to the principles of EN 1990 [34], see Fig.6.15. In the following, the single steps for the determination of the partial factor are shown including exemplarily the procedure for the case of tension–compression of square plates.

Step 1: Develop a design model

A theoretical resistance model has to be developed, which corresponds to the numerically obtained results and is a function of independent variables $\underline{X}$, see Eq.(6.3). The theoretical model has been presented in Sec.6.3 and is evaluated in the followings.

$$r_t = g_{rt}(\underline{X}) \tag{6.3}$$

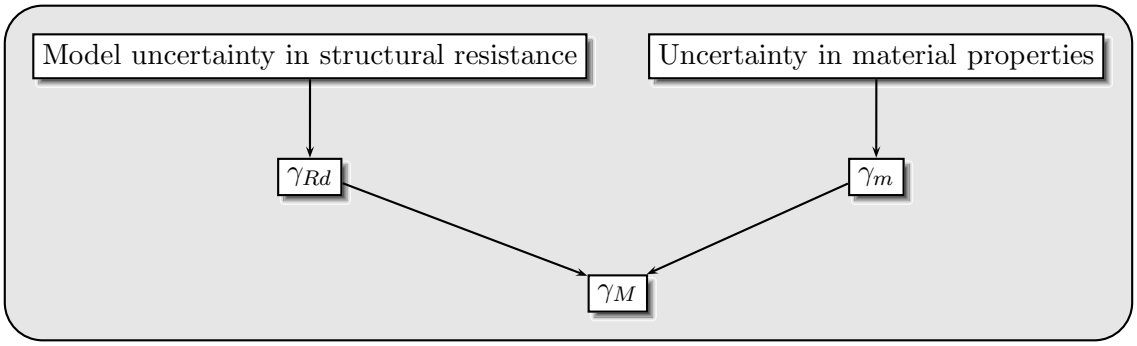

Figure 6.15: Relation between individual partial factors on the action side according to EN 1990 [34].

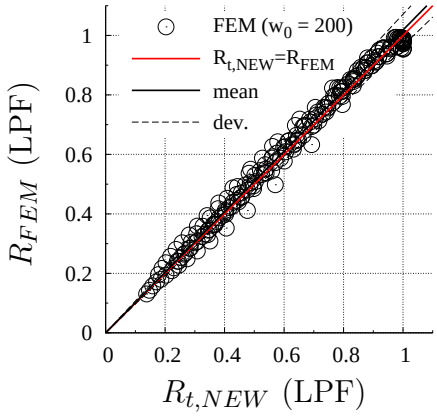

Figure 6.16: $r_e - r_t$ diagram (Tension/Compression).

Step 2: Compare experimental and theoretical values

The numerical results are used for representing the experimental values (r_e) and now compared against the theoretical values (r_t) in a diagram, to check if the resistance model performs well and to exclude any systematic errors in the resistance function. If the resistance function is exact and complete, all the points should lie on the bisecting line. However, in practice the points usually scatter somehow. Fig.6.16 shows exemplarily the $r_e - r_t$ diagram for the aforementioned case. The other relevant diagrams have also already been shown in the respective chapter along with the interaction curves.

Step 3: Estimate the mean value correction factor b

As mentioned in step 2, in practice the points are usually located at a gradient different than $\Theta = 45°$ which is taken into account with the parameter b calculated with the least square method:

$$b = \frac{\sum_i r_{ei} \cdot r_{ti}}{\sum_i r_{ti}^2} = 1.0104 \tag{6.4}$$

Step 4: Estimate the coefficient of variation of the errors

The error term for each value is determined using the mean value correction factor from step 3. Afterwards, the following procedure is followed to eventually determine the coefficient of variation of the model.

- Error term for each value:

$$\delta_i = \frac{r_{ei}}{b \cdot r_{ti}} \tag{6.5}$$

- Logarithm of the error terms:

$$\Delta_i = \ln(\delta_i) \tag{6.6}$$

- Mean value of logarithm of the error terms:

$$\overline{\Delta} = \frac{1}{n} \sum_{i=1}^{n} \Delta_i = 0.0064 \tag{6.7}$$

- Standard deviation of the error terms:

$$s_\Delta^2 = \frac{1}{n-1} \sum_{i=1}^{n} (\Delta_i - \overline{\Delta})^2 = 0.0027 \tag{6.8}$$

- Finally, the coefficient of variation of the error terms is defined as:

$$V_\delta = \sqrt{\exp(s_\Delta^2) - 1} = 0.0517 \tag{6.9}$$

Step 5: Analyse compatibility

The analysis of the compatibility has two main objectives. One is in case of the scatter being too high to give economical design resistance functions, where the design model needs to be corrected or b and V_δ to be modified by dividing the total test population into appropriate sub-sets. The second aim is to determine the influence of important parameters on the scatter by rearranging the results also into sub-sets and comparing the mean values and the coefficient of variation. Since in the foregoing chapters the results have been presented separately for each b/t ratio and several boundary conditions graphically, the compatibility of the resistance function was already successfully checked.

However, for the sake of completeness the variation of the error terms is calculated for the different boundary conditions and summarised in Tab.6.3, showing that in all cases the value is very small and similar. For BC-B even an extremely small variation coefficient is found, which is quite logical, since the reference strength for uniaxial loading is based on numerical calculations, showing that in this case the resistance model performs almost perfectly.

Table 6.3: Variation of the error terms for the different boundary conditions.

Boundary condition	V_δ
BC-A	0.0570
BC-B	0.0186
BC-C	0.0446

Table 6.4: Variation coefficients of the basic variables according to [51].

	Coeff. of variation
Thickness t	0.05
Plate width b	0.005

Step 6: Determine the coefficients of variation V_{Xi} of the basic variables

Since the scatter effects of basic parameters may not be represented by the test population, prior knowledge is needed for the determination of the variation. In the commentary on EN 1993-1-5 [51] the values for V_t and V_b are given, see Tab.6.4. This approach has already been adopted by Gabeler [44], Kövesdi [58], Sinur [106] and Timmers [110] and is applied also for the present work.

Kövesdi [58] additionally conducted the statistical evaluation using variation coefficients from JCSS [52], where the deviation characteristics are given as shown in Eq.(6.10) and Eq.(6.11). Timmers [110] pointed out that the given deviations there seem to be too high for slender plates, so that he proposed a smaller standard deviation in this case. However, for the statistical evaluation in the end the values from [51] were used. Furthermore, it should be noted here that the values given in JCSS [52] are based just on some preliminary results obtained for hot rolled I-profiles (IPE 80 to 200) in Czech Republic, see [40]. Therefore, it is questionable if these values can be directly transferred to other cases, so that this work sticks on the approach given in [51].

- Mean value:

$$-1.0\,\text{mm} \leq X_m \leq +1.0\,\text{mm} \tag{6.10}$$

- Standard deviation:

$$s_x \leq 1.0\,\text{mm} \tag{6.11}$$

Step 7: Determine the coefficient of variation V_{FEM} of the FE model

To cover numerical uncertainties, the coefficient of variation V_{FEM} of the FE model is determined based on the recalculation of the buckling curves from Sec.4.6.4.2 and the experimental investigations presented in Sec.4.4. Therefore steps 1 to 5 are repeated leading to the variation coefficients given in Tab.6.5 and to $V_{FEM} = 0.0449$.

Table 6.5: Variation coefficients of the FE model.

BC	ψ	V_{FEM}
A	+1.0	0.0449
A	+0.5	0.0287
A	0	0.0346
A	−0.5	0.0116
A	−1.0	0.0216
C	+1.0	0.0355
Tests	+1.0	0.0362

Step 8: Determine the partial factor

In a next step the coefficient of variation of the whole resistance model is then calculated with Eq.(6.12).

$$V_r^2 = (V_\delta^2 + 1) \cdot \left[\prod_{i=1}^{j} (V_{Xi}^2 + 1) \right] \cdot (V_{FEM}^2 + 1) - 1 = 0.0072 \tag{6.12}$$

Based on the coefficient of variation of the whole resistance model the auxiliary variable Q is calculated according to Eq.(6.13).

$$Q = \sqrt{\ln(V_r^2 + 1)} = 0.0847 \tag{6.13}$$

The partial factor γ_{Rd} is calculated according to Eq.(6.14) using the characteristic resistance r_k and the design resistance r_d, which can be calculated for a large number of tests ($n \geq 100$) according to Eq.(6.15). Finally, the corrected factor $\gamma_{Rd}^\star$ is determined using the mean value correction factor b.

$$\gamma_{Rd} = \frac{r_k}{r_d} = 1.125 \quad \rightarrow \quad \gamma_{Rd}^\star = \frac{\gamma_{Rd}}{b} = 1.113 \tag{6.14}$$

$$\begin{aligned} r_k &= b \cdot g_{rt}(X_m) \cdot \exp(-k_\infty Q - 0.5Q^2) \\ r_d &= b \cdot g_{rt}(X_m) \cdot \exp(-k_{d,\infty} Q - 0.5Q^2) \end{aligned} \tag{6.15}$$

where: $k_\infty = 1.64$

$k_{d,\infty} = \alpha_R \cdot \beta = 0.8 \cdot 3.8 = 3.04$

Step 9: Determine the partial factor γ_m for uncertainities in the material properties

As shown in Fig.6.15 the partial factor γ_M consists of a model uncertainity in structural resistance γ_{Rd} and an uncertainity in material properties γ_m. The latter is determined according to Eq.(6.16) from [103].

$$\gamma_m = \frac{f_{y,nom}}{f_{yd}} = \frac{f_{y,nom}}{f_{y,m} \cdot (1 - 1.64 \cdot V_{fy})} \tag{6.16}$$

where: $f_{y,nom}$: nominal value of the yield strength
$f_{y,m}$: mean value of the yield strength
V_{fy}: coefficient of variation of the yield strength

However, in literature several interpretations and approaches can be found. The most frequently encountered ones are listed and described shortly in the following.

- Johansson et al. [51]

In [51] the relationships expressed in Eq.(6.17) are assumed for the nominal and the mean value of the yield strength.

$$f_{y,m} = 1.14 \cdot f_{y,nom} \quad \text{and} \quad V_{fy} = 0.07 \tag{6.17}$$

By putting this relationship in Eq.(6.16) the partial factor for uncertainties in the material properties is determined according to Eq.(6.18).

$$\gamma_m = \frac{f_{y,nom}}{f_{yd}} = \frac{f_{y,nom}}{1.14 \cdot f_{y,nom} \cdot (1 - 1.64 \cdot 0.07)} = 0.9909 \tag{6.18}$$

- Joint Committee on Structural Safety (JCSS) [52]

In [52] the JCSS gives the formulation shown in Eq.(6.19) for determining the mean value of the yield strength. Kövesdi [58] summarised the results for several steel grades according to Tab.6.6. The recommendations are based primarily on European studies from 1970 onwards. However, in [52] it is remarked that the given recommendations may be used for steel grades up to $380\,\mathrm{N/mm^2}$ and should not be used for high strength steels (e.g. $f_y = 690\,\mathrm{N/mm^2}$). As Tab.6.6 shows, γ_m decreases with increasing f_y, which is in contradiction to statistical evaluations according to experiments conducted by Simões da Silva et al. [103].

$$f_{y,m} = \alpha \cdot f_{y,nom} \cdot \exp(-u \cdot V_{fy}) - C \tag{6.19}$$

Table 6.6: Determination of γ_m according to the recommendations of the JCSS [52].

Steel grade ($f_{y,nom}$)	$f_{y,m}$ N/mm^2	γ_m
S 235	250.32	1.061
S 275	296.33	1.048
S 355	388.35	1.033
S 460	(509.14)	(1.021)
S 690	(773.71)	(1.008)

Table 6.7: Determination of γ_m according to Simões da Silva et al. [103].

Steel grade ($f_{y,nom}$)	n [-]	$f_{y,m}$ N/mm^2	V_{fy}	γ_m
S 235	795	284.74	0.064	0.922
S 275	4333	316.23	0.055	0.956
S 355	1879	405.01	0.044	0.945
S 460	666	474.63	0.040	1.037
S 490	36	793.19	0.050	0.948

where:
$\alpha = 1.0$: a spatial position factor
$-1.5 \geq u \geq -2$: a factor related to the fractile of the distribution used in describing the distance between the code specified or nominal value and the mean value ($u = -2$ is used by [58] and in the following)
$C = 20\,\mathrm{N/mm^2}$: a constant reducing the yield strength as obtained from usual mill tests to the static yield strength

- Simões da Silva et al. [103]

Based on a large statistical evaluation of steel properties for S 235 up to S 690 conducted on over 6 000 experimental data from all over the world, the findings were merged in [103]. Since bi-normal distributions have been observed that cannot be described by a uni-modal function, a linear regression was performed on the lowest part of the distribution, leading to new values for the mean, standard deviation and coefficient of variation, see Fig.6.17. The main reason for this bi-normal distribution is the common practice of downgrading of material, i.e. re-classifying higher grade steel to a lower grade if it fails to meet the code specified values for the higher grade on the basis of quality control tests, see [52]. Kövesdi [58] summarised the outcomes according to Tab.6.7.

As the evaluation in [103] is based on real distributions from experiments and representing the most sophisticated collection of data available to the author at this time, the approach is also exemplarily adopted in the followings.

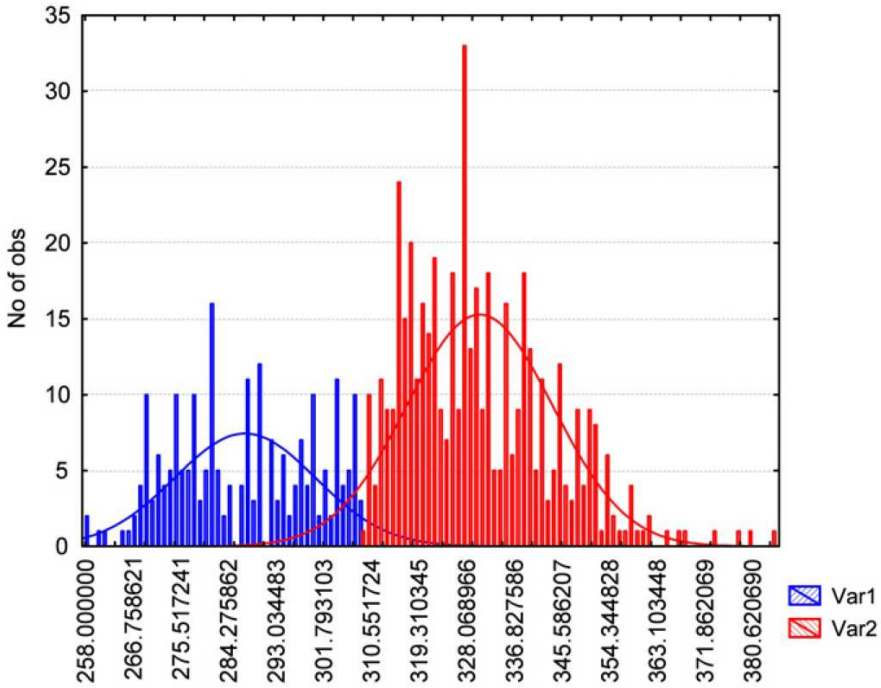

Figure 6.17: Histogram of all results for S235 [103].

Step 10: Determine the partial factor $\gamma^{\star}_{M1}$

Finally, the partial factor $\gamma^{\star}_{M1}$ is calculated by the product of the model uncertainity in structural resistance $\gamma^{\star}_{Rd}$ and the uncertainity in material properties γ_m according to Eq.(6.20).

$$\gamma^{\star}_{M1} = \gamma_m \cdot \gamma^{\star}_{Rd} \tag{6.20}$$

If the approach from Johansson et al. [51] for γ_m is adopted, then the final reduction factor is determined to $\gamma^{\star}_{M1} = 1.103$. The results using the approaches from JCSS [52] and Simões da Silva et al. [103] are summarised in Tab.6.8.

From the evaluation of the partial factor $\gamma^{\star}_{M1}$ for plates subjected to tension–compression it is noticeable that different approaches may lead to significantly different results. However, if the approach for γ_m according to Eq.(6.18) is adopted, the results justify the use of a value of $\gamma_{M1} = 1.1$.

The same procedure as described before is conducted also for the other investigated cases such as tension–compression where column-like behaviour occurs, tension–shear, compression–shear as well as biaxial compression for stiffened plates. The results are summarised in Tab.6.9. It can be seen that the required partial factors justify the use of $\gamma_{M1} = 1.1$ for the investigations on unstiffened plates. The determination of the partial factor for stiffened plates subjected to biaxial compression is conducted for the case of

Table 6.8: Comparison of $\gamma^{\star}_{M1}$ using the γ_m approaches from JCSS [52] and SIMÕES DA SILVA ET AL. [103].

Steel grade ($f_{y,nom}$)	$\gamma^{\star}_{M1}$ (γ_m acc. to [52])	$\gamma^{\star}_{M1}$ (γ_m acc. to [103])
S235	1.181	1.026
S275	1.166	1.064
S355	1.149	1.052
S460	(1.136)	1.154
S690	(1.122)	1.055

Table 6.9: Determination of $\gamma^{\star}_{M1}$ for regarded cases.

Description	$\gamma^{\star}_{M1}$ (γ_m acc. to Eq.(6.18))
tension–compression	1.103
tension–compression (column-like behaviour)	1.056
tension–shear	1.077
compression–shear	1.098
biaxial compression without V–factor (stiffened plates)	1.334
biaxial compression with V–factor (stiffened plates)	1.152

$\alpha = 1$ and $n = 1$, as shown in Fig.6.7. Even though the interaction curves in Fig.6.7 show already directly that not applying the V–factor may lead to unsafe results and that the curves do not qualitatively match to the simulations, a statistical evaluation is conducted nevertheless, resulting in a partial factor of $\gamma^{\star}_{M1} = 1.334$. The application of the V–factor as proposed by BRAUN [11] shows in Fig.6.7 that more proper results are gained and the partial factor is determined to $\gamma^{\star}_{M1} = 1.152$. The factor is still larger than 1.1, but a notable reduction is obtained.

Additionally, a determination of the partial factor without a separation of γ_{Rd} and γ_m but including the coefficient of variation $V_{fy} = 0.07$ according to Eq.(6.17) in step 6 of the procedure is conducted for plates subjected to tension–compression. This approach leads to a required partial factor of $\gamma^{\star}_{M1} = 1.154$, which is higher than 1.1. Anyway, this value seems too conservative, as the evaluation of the interaction curves in the foregoing sections has shown a very good matching of the numerical and the theoretical values, so that a logical consequence to "reduce" the partial factor would be to change the buckling curves, which is not intended here. Another possibility would be to split the data into sub-sets or to conduct more sophisticated statistical evaluations, where the values of the coefficients of variations are e.g. dependent on the slenderness. As this goes beyond the scope of this work, this possibility is not further pursued here.

6.5 Summary

The comparison of the numerical simulations to the current design rules shows the reasonability of taking into account the positive effect of tensile stresses. However, for the tension–compression domain cases are observed where the current formulation shows overestimations of the resistance and a large scatter for statistical comparisons. For the interaction curves sharp bends are found but not observed numerically. The sharp bends are caused by the peaks present in the calculation of the buckling coefficient. As also recommended by Lindner & Rusch [74], the peaks in the determination of the buckling coefficient should not be taken into account. In order to improve the current formulations due to the above mentioned shortcomings a modified V–factor is presented for the tension–compression domain. Furthermore, for the boundary condition BC-C (edges free to move in–plane) the resistance is found to be overestimated when column–like behaviour plays a role. This was already observed by Seitz [101], who proposed a modified formulation for the interpolation between plate–like and column–like behaviour in case of transverse stresses. The approach is adopted within this work for transverse stresses resulting in an appropriate agreement between the interaction curves and the numerical simulations.

For the case of plates subjected to direct and shear stress the comparison of the current design rules to the numerical simulations leads to the conclusion that the positive effect of tensile stresses is already reflected properly, so that a modification is not required. Additionally, the calculation of the resistance is done with and without a separation of the yielding and the stability phenomena according to Fig.2.26 showing that a separation of the phenomena leads to higher resistances and follows the numerical results properly, while a joint treatment leads to more conservative results but facilitates the design procedure by a small amount. For plates subjected to shear and compression the current rules reflect the numerical simulations adequately as well. In case of shear and bending with predominant compression the current rules are on the safe side, but show to be quite conservative if the pure direct stress domain is approached. As the recalculation of the buckling curves in Sec.4.6.4.2 shows that for the case of bending the buckling curves according to DIN 18800-3 [22] follow closely the numerical simulations, while the curves according to EN 1993-1-5 [36] are more conservative, the buckling curves from DIN 18800-3 [22] are used additionally within the procedure for assessing the interaction curves. The comparison of these interaction curves to the numerical simulations shows that in the interaction domain some unsafe results are gained, so that a modification of the exponent e_3 in the design formula is proposed. However, this approach can be regarded as an alternative to the current formulation. The use of the current buckling curves for bending together with the current exponent e_3 lead also to appropriate results, but as mentioned above shows to be conservative if the pure direct stress domain is approached.

The numerical simulations for stiffened plates subjected to biaxial compression are compared to the current design rules with and without the V–factor pointing out the

necessity for its application not only for unstiffened but also for stiffened plates. As also observed by Braun [11] the resistance in transverse direction is overestimated. However, while for unstiffened plates this issue is remediated using the proposed interpolation from Seitz [101], for stiffened plates this is not fully appropriate.

Furthermore, for the sake of completeness the improved design rules are evaluated statistically according to Annex D, EN 1990 [34] justifying the modifications in accordance to the safety requirements.

In order to give a useful ready to hand tool to the practical engineer for conducting buckling analyses according to the proposal within this work, interaction charts are given in Sec.F in the Annex for a simplified procedure. Additionally the formulation given in Eq.(5.3) may be used for a quick estimation of whether the plate is subjected to buckling or not.

7 Discussion

7.1 Summary

The design of slender steel plated structures in Europe is conducted according to EN 1993-1-5 [36] where generally, apart from the possibility of using the Finite Element Method, the design might be conducted according to the following two different methods: the "effective width method" and the "reduced stress method". The latter one is based on a single plate slenderness and theoretically allows for calculating the resistance of plated structures for almost any practical case, making it a general all-purpose procedure.

In the frame of this work the stability behaviour of slender steel plates subjected to several multiaxial stress states was investigated, compared to the current design rules using the reduced stress method and improved design rules were proposed. Therefore, in the beginning of this work the fundamentals by means of elastic buckling under multiaxial stress states were described as well as the postcritical behaviour, which are both the basics of the reduced stress method. The design rules according to EN 1993-1-5 [36] were explained in detail pointing out the advantage in the assessment of the resistance for multiaxially loaded plates using a single plate slenderness on the one hand and on the other hand the possible misinterpretations due to shortcomings in the phrasing of the current code rules. The design rules according to DIN 18800-3 [22] as well as existing studies dealing with the issue of plates subjected to multiaxial loading were presented and put into the context of this work.

Experimental investigations on stiffened and unstiffened steel panels were conducted and recalculated with the Finite Element Method showing a good agreement between the experiments and the numerical simulations. Based on a simplified numerical model, which was validated using the known buckling curves, systematic numerical parametric studies were conducted in order to analyse the buckling behaviour of plates subjected to several multiaxial stress states. The numerical studies comprised investigations on unstiffened plates subjected to tension–compression, tension–shear, compression–shear and bending–shear as well as the case of biaxial compression for stiffened plates. As observed during the experimental investigations on plates subjected to tension–compression, mode changes may occur, so that in the numerical investigations several imperfection shapes were applied to the model aiming at a lower bond for the resistance and to avoid increased values due to suppressed mode changes. The numerical investigations showed a clear positive effect of the buckling behaviour due to tensile stresses. Since the influence of the boundary conditions showed to vanish with increasing ratio of tensile and com-

pressive stresses a simplified approach was presented to quickly evaluate if a multiaxially loaded plate is subjected to plate-buckling. In practical cases shear loads usually act together with bending, so that the effect of stress gradients was taken into account in the investigations.

Furthermore, numerical investigations were conducted focusing on the buckling behaviour of stiffened plates subjected to biaxial compression. The investigations consisted in a large parametric study for, besides the load ratio, also evaluating the influence of several parameters such as e.g. the stiffness of the stiffeners. The numerical investigations showed that weak stiffeners lead to a very unfavourable buckling behaviour even if the number is increased. In addition, cases were found where local buckling was observed for uniaxial loading in both directions, while global buckling was observed for the combined loading, leading to the conclusion that a completely separated treatment of the load cases does not seem to be reasonable, as deviating forces may lead to a global failure.

Finally, the comparison of the numerical simulations to the current design rules led to a modification of the approach in order to have an improved procedure, which allows for taking into account the positive effect of tensile stresses on the buckling behaviour of slender plates. The modified approach is evaluated with the numerical simulations graphically by the interaction diagrams as well as statistically using the procedure according to Annex D, EN 1990 [33].

7.2 Outlook

The numerical investigations on longitudinally stiffened plates subjected to biaxial compression within this work focused on the usage of open stiffeners. However, since for plates stiffened with many stiffeners generally a stronger increase of the resistance was observed for the numerical simulations than for the design rules, it would be of practical relevance to investigate this effect on plates stiffened with closed stiffeners where clamping effects might even augment this effect. Furthermore, closed stiffeners usually possess a higher relative stiffness, so that it would be interesting to investigate in how far deviating forces play a role for the case of combined loading. For stiffened plates under biaxial compression subjected to predominant transverse stress in some cases an overestimation of the resistance was observed. While for unstiffened plates the approach from Seitz [101] showed to overcome this issue, this is not always the case for stiffened plates. Therefore, a recalibration of the interpolation between plate-like and column-like behaviour seems to be reasonable.

To finally confirm the procedure for all kind of situations, investigations could be conducted for unstiffened and stiffened plates subjected to the full interaction domain including σ_x, σ_z and τ. A clarification for the application of initial imperfection on stiffened plates would be interesting and could lead to clearer recommendations in Annex C, EN 1993-1-5 [36] for the adoption of the Finite Element Method for buckling analyses.

8 Bibliography

[1] Allgemeines Rundschreiben Straßenbau Nr.1/1972. Stabilität von Druckgurten im Stahlbrückenbau. Verkehrsblatt, H. 5. 1972.

[2] American Iron and Steel Institute. Specification for the Design of Cold-Formed Steel Structural Members, 2007.

[3] K. J. Bathe. *Finite-Elemente-Methoden*. Springer-Verlag, 2nd edition, 2002.

[4] D. Beg, U. Kuhlmann, L. Davaine, and B. Braun. *Design of Plated Structures.: Eurocode 3: Design of Steel Structures. Part 1-5 Design of Plated Structures. (ECCS Eurocode Design Manuals)*. Ernst & Sohn, 1 edition, 2010.

[5] D. Beg, K. Rejec, and F. Sinur. Evaluation of plate buckling design rules in EN 1993-1-5: Normal stresses (compression). In *Document TWG83-2013-013, ECCS TWG8.3 Meeting, 15th March 2013*, Barcelona, 2013.

[6] S. Bergmann and H. Reissner. Über die Knickung von rechteckigen Platten bei Schubbeanspruchung. *Z. Flugtech Motorluftschiffahrt*, 23:6, 1932.

[7] J. Betten and C. H. Shin. Elastic-plastic buckling analysis of rectangular plates subjected to biaxial loads. *Forschung im Ingenieurwesen*, 65(9):273–278, mar 2000.

[8] D. Bitar, T. Adamakos, and P. Mangin. Ponts haubanés à tablier métallique orthotrope - Vérification des plaques orthotropes sous compression bi-axiale. *Revue Construction Métallique*, 52(1), 2015.

[9] F. Bleich and L. B. Ramsey. *A Design Manual on the Buckling Strength of Metal Structures*. Society of Naval Architects and Marine Engineers, Washington DC, 1951.

[10] F. Bloom and D. Coffin. *Handbook of thin plate buckling and postbuckling*. Chapman & Hall/CRC, Boca Raton, Fla., 2001.

[11] B. Braun. *Stability of steel plates under combined loading*. Dissertation, No.2010-3, Institute of Structural Design, University of Stuttgart, 2010.

[12] B. Braun and U. Kuhlmann. Bemessung und Konstruktion von aus Blechen zusammengesetzten Bauteilen nach DIN EN 1993-1-5. In U. Kuhlmann, editor, *Stahlbau-Kalender 2009*, pages 381–453. Ernst & Sohn GmbH & Co. KG, 2009.

[13] B. Brune. *Ein Modell zur Ermittlung der Tragfähigkeit vierseitig und dreiseitig gelagerter Stahlbleche unter Druckbeanspruchung*. Dissertation, Universität Dortmund, 1994.

[14] E. Chwalla. Beitrag zur Stabilitätstheorie des Stegblechs vollwandiger Träger. *Stahlbau*, 9:81, 1936.

[15] M. Cramer and N. Haala. Documents from the lectures: Photogrammetrie & GIS and Computer Vision zur bildbasierten Geodatenerfassung. Institute for Photogrammetry, University of Stuttgart, 2015.

[16] CTICM. EBPlate, Piece of Software for the determination of elastic critical stresses in plates. EBPlate can be downloaded for free from www.cticm.com.

[17] DASt-Richtlinie 012. Beulsicherheitsnachweise für Platten, 1980.

[18] L. Davaine and P.-O. Martin. Alternative method for global buckling in stiffened plate elements. In *ECCS TWG8.3 Amendment AM-1-5-2012-12 and Background document*, 2016.

[19] B. de Saint-Venant. *p. 704 of his discussion of Clebsch's Theory of Elasticity of Solid Bodies.* 1883.

[20] A. Dier and P. Dowling. Plates under combined loading and lateral compression. Technical report, Department of Civil Engineering, Imperial College, London, 1980.

[21] A. Dier and P. Dowling. The strength of plates subjected to biaxial forces. In J. Rhodes and J. Spence, editors, *Behaviour of thin-walled structures*, pages 329–353. 1984.

[22] DIN 18800-3. Stahlbauten - Teil 3: Stabilitätsfälle - Plattenbeulen, 1990.

[23] DIN 4114. Stahlbau: Stabilitätsfälle (Knickung, Kippung, Beulung), 1952.

[24] DIN 4114. Ergänzende Bestimmungen zu DIN 4114, 1973.

[25] DIN EN 1993-1-5/NA:2010-12. Nationaler Anhang - National festgelegte Parameter - Eurocode 3: Bemessung und Konstruktion von Stahlbauten - Teil 1-5: Plattenförmige Bauteile, 2010.

[26] D. Dinkler and B. Kröplin. Zum Tragsicherheitsnachweis für quadratische, scheibenartig beanspruchte Einzelfelder aus Stahl. *Stahlbau*, 53(6):174–178, 1984.

[27] DNV-RP-C201. Det Norske Veritas: Buckling Strength of Plated Structures. Recommended practice, 2010.

[28] R. Dow and C. Smith. Effects of localized imperfections on compressive strength of long rectangular plates. *Journal of Constructional Steel Research*, 4(1):51–76, jan 1984.

[29] P. Dowling, J. Harding, and J. Slatford. Strength of Ships Plating - Plates in biaxial compression. Technical report, Department of Civil Engineering, Imperial College, London, 1979.

[30] P. Dubas and E. Gehri. *Behaviour and Design of Steel Plated Structures (ECCS Publication No. 44).* Publication (European Convention for Constructional Steelwork). Applied Statics and Steel Structures, Swiss Federal Institute of Technology,

Zürich, 1 edition, 1986.

[31] E DIN 18800-3. Stahlbauten - Teil 3: Stabilitätsfälle - Plattenbeulen (Entwurf), 1988.

[32] EN 10025-2. Hot rolled products of structural steels - Part 2: Technical delivery conditions for non-alloy streuctural steels, 2004.

[33] EN 1090-2. Execution of steel structures and aluminium structures - Part 2: technical requirements for steel structures, 2008.

[34] EN 1990. Eurocode 0: Eurocode - Basis of structural design, 2002.

[35] EN 1993-1-1. Eurocode 3: Design of steel structures - Part 1-1: General rules and rules for buildings, 2005.

[36] EN 1993-1-5. Eurocode 3 - Design of steel structures - Part 1-5: Plated structural elements, 2006.

[37] EN 1993-1-5/AC. Eurocode 3 - Design of steel structures - Part 1-5: Plated structural elements (corrigendum), 2009.

[38] EN 1993-1-6. Eurocode 3 - Design of steel structures - Part 1-6: Strength and Stability of Shell Structures, 2007.

[39] European Convention for Constructional Steelwork. Introductory Report - Second International Colloquium on Stability, 1976.

[40] M. Fajkus, M. Holicky, L. Rozlivka, and M. Vorlicek. Random Properties of Steel Elements Produced in Czech Republic. In *Eurosteel*, Prague, 1999.

[41] M. Fischer, R. Grube, H. Rieger, and P. Wenk. Messung der Vorverformungen von beulgefährdeten Stahlblechen mit und ohne Steifen. Technical report, Universität Dortmund, Mitteilung Nr.6, Bericht aus dem Fachgebiet Stahlbau, 1989.

[42] M. Fischer and W. Harre. Ermittlung der Traglastkurven von einachsig gedrückten Rechteckplatten aus Baustahl der Seitenverhältnisse a/b kleiner/gleich 1 mit Hilfe von Versuchen (Teil I). *Der Stahlbau*, 47(7):199–204, 1978.

[43] M. Fischer and W. Harre. Ermittlung der Traglastkurven von einachsig gedrückten Rechteckplatten aus Baustahl der Seitenverhältnisse a/b kleiner/gleich 1 mit Hilfe von Versuchen (Teil II). *Stahlbau*, 47(8):239–247, 1978.

[44] L. Gabeler. *Statistical Evaluation of Patch Loading Resistance Models for Welded Steel Girders*. Diploma thesis, Institute of Structural Design, University of Stuttgart, 2009.

[45] Y. Galéa and P.-O. Martin. Longitudinally stiffened plates in Eurocode 3: Calculation of the global critical buckling stress. *Journal of Constructional Steel Research*, 66(11):1345–1353, nov 2010.

[46] K. Geißler. *Handbuch Brückenbau*. Ernst & Sohn GmbH & Co. KG, Berlin, 1st edition, 2014.

[47] G. Gerard and H. Becker. Handbook of Structural Stability Part I: Buckling

of Flat Plates, National Advisory Committee for Aeronautics, Technical Note, Washington, DC, United States, 1957.

[48] D. Grotmann. *Verbesserung von Sicherheitsnachweisen für Stahlkonstruktionen mit rechteckigen Hohlprofilen*. Dissertation, RWTH Aachen, 1997.

[49] T. Höglund. *Design of thin plate I girders in shear and bending with special reference to web buckling*. PhD thesis, Tekniska Högskolan, Stockholm, 1973.

[50] S. Iguchi. Die Knickung der rechteckigen Platte durch Schubkräfte. *Ing. Arch.*, 9:1, 1938.

[51] B. Johansson, R. Maquoi, G. Sedlacek, C. Müller, and D. Beg. *Commentary and Worked Examples to EN 1993-1-5 "Plated Structural Elements"*. Joint Report Prepared under the JRC - ECCS cooperation agreement for the evolution of Eurocode 3 (programme of CEN / TC 250), 1 edition, 2007.

[52] Joint Committee on Structural Safety. Probabilistic Model Code, available on: http://www.jcss.byg.dtu.dk/Publications/Probabilistic_Model_Code, 2001.

[53] J. Jönsson and T. Bondum. Analysis of Biaxially Stressed Bridge Deck Plates. In *Nordic Steel Construcion Conference*, number September, pages 1–10, Oslo, 2012.

[54] K. Klöppel and K. H. Möller. *Beulwerte Ausgesteifter Rechteckplatten. II. Band*. Ernst & Sohn, Berlin, 1 edition, 1968.

[55] K. Klöppel and J. Scheer. *Beulwerte ausgesteifter Rechteckplatten: Kurventafeln zum direkten Nachweis der Beulsicherheit fuer verschiedene Steifenanordnungen und Belastungen*. Ernst & Sohn, Berlin, 1 edition, 1960.

[56] J. Korelc. AceGen - Multi-Language, Multi-Environment numerical code generation. *University of Ljubljana, Faculty of Civil and Geodetic Engineering, http://www.fgg.uni-lj.si/Symech*, 2007.

[57] J. Korelc. AceFEM - Mathematica finite element environment. *University of Ljubljana, Faculty of Civil and Geodetic Engineering, http://www.fgg.uni-lj.si/Symech*, 2010.

[58] B. Kövesdi. *Patch loading resistance of girders with corrugated webs*. Dissertation, Budapest University of Technology and Economics, 2010.

[59] B. Kövesdi and L. Dunai. Stiffness requirements for cross girders on orthotropic plates subjected by pure compression. In *Document TWG83-2016-012, ECCS TWG8.3 Meeting, 25th February 2016*, Stuttgart, 2016.

[60] K. Kraus. *Photogrammetrie Band 1: Geometrische Informationen aus Photographien und Laserscanneraufnahmen*. De Gruyter, 7th edition, 2004.

[61] N. Kristanič. *Limit State Design Using Exact Sensitivity Analysis and Shape Optimization*. Doctoral thesis, University of Ljubljana, Faculty of Civil and Geodetic Engineering, 2008.

[62] N. Kristanič and J. Korelc. Optimization method for the determination of the most

unfavorable imperfection of structures. *Computational Mechanics*, 42(6):859–872, apr 2008.

[63] U. Kuhlmann, D. Beg, A. Zizza, and F. Sinur. Beulverhalten längsausgesteifter Platten unter Interaktion von Biegung und Querkraft. *Stahlbau*, 81(11):820–827, nov 2012.

[64] U. Kuhlmann, D. Beg, A. Zizza, F. Sinur, and K. Rejec. Bending-shear interaction of longitudinally stiffened steel plates. Report on the DFG-Project KU 1130/14-1. Technical report, 2013.

[65] U. Kuhlmann and B. Braun. Untersuchung des Einflusses von Vorbeulen auf die Tragfähigkeit von stählernen Leichtbau-Hallenkonstruktionen - Längs- und Schubspannungen -. Technical report, Institut für Konstruktion und Entwurf, Stuttgart, 2008.

[66] U. Kuhlmann, B. Braun, M. Feldmann, J. Naumes, P.-O. Martin, Y. Galéa, B. Johansson, P. Collin, J. Eriksen, H. Degée, N. Hausoul, J. Chica, J. Raoul, L. Davaine, and A. Petel. Competitive steel and composite bridges by improved steel plated structures (COMBRI) / Report of the RFCS-Project RFS-CR-03018. Technical report, 2007.

[67] U. Kuhlmann and A. Zizza. Stahlbaunormen, DIN EN 1993-1-5: Bemessung und Konstruktion von Stahlbauten - Plattenförmige Bauteile. In U. Kuhlmann, editor, *Stahlbau-Kalender 2012*, pages 79–134. Ernst & Sohn GmbH & Co. KG, 2012.

[68] U. Kuhlmann, A. Zizza, and V. Pourostad. Beulen mehrachsig beanspruchter Platten. Technical report, DASt-AiF Project-No. 18 213, in progress.

[69] U. Kuhlmann, A. Zizza, and V. Pourostad. Optimal Use of High Strength Steel Grades Within Bridges (OPTIBRI). Technical report, Project-Partners: University of Liège (Coordinator), University of Stuttgart, University of Coimbra, Belgian Welding Institute, GRID Consulting Engineers and Industeel, Work Package 3 of the RFCS Project-No. RFSR-CT-2014-00026, in progress.

[70] J. Lindner. Kurventafeln für einen vereinfachten Beulsicherheitsnachweis. *Stahlbau*, 50(10):294–297, 1981.

[71] J. Lindner and W. Habermann. Zur mehrachsigen Beanspruchung beim Plattenbeulen. In *Festschrift Joachim Scheer*, pages 159–183. Braunschweig, 1987.

[72] J. Lindner and W. Habermann. Zur Weiterentwicklung des Beulnachweises für Platten bei mehrachsiger Beanspruchung. *Stahlbau*, 57(11):333–339, 1988.

[73] J. Lindner and W. Habermann. Berichtigung zu: Zur Weiterentwicklung des Beulnachweises für Platten bei mehrachsiger Beanspruchung. *Stahlbau*, 58(11):349–351, 1989.

[74] J. Lindner and A. Rusch. *Grenz (b/t)-Verhältnisse in Abhängigkeit der Belastung unter besonderer Berücksichtigung von Imperfektionen [Schlussbericht zum DIBt-Forschungsvorhaben P 32-5-16.91.32-965/00].* Fraunhofer IRB Verlag, Stuttgart,

2000.

[75] J. Lindner, J. Scheer, and H. Schmidt. *Stahlbauten - Erläuterungen zu DIN 18800 Teil 1 bis Teil 4*. Beuth Verlag, 3rd edition, 1998.

[76] T. Luhmann. *Nahbereichsphotogrammetrie: Grundlagen, Methoden und Anwendungen*. Wichmann, H., 3rd edition, 2010.

[77] R. Maquoi and J. Rondal. From thick to thin or from thin to thick? In *IABSE Colloquium: Thin Walled Metal Structures*, Stockholm, 1986.

[78] R. Maquoi and J. Rondal. Parametric study of imperfect compressed plates. In *Second Regional Colloquium on Stability of Steel Structures*, Budapest, 1986.

[79] Matlab R2010b. MathWorks, 2010.

[80] M. Mensinger and J. Ndogmo. Beulnachweise im Stahlbrückenbau. *Brückenbau - Construction Engineering*, (5):24–33, 2015.

[81] K. Meyberg and P. Vachenauer. *Höhere Mathematik 1*. Springer-Lehrbuch. Springer Berlin Heidelberg, Berlin, Heidelberg, 2001.

[82] C. Müller. *Zum Nachweis ebener Tragwerke aus Stahl gegen seitliches Ausweichen*. Dissertation, Dissertation, RWTH Aachen, 2003.

[83] J. K. Paik and J. K. Seo. Nonlinear finite element method models for ultimate strength analysis of steel stiffened-plate structures under combined biaxial compression and lateral pressure actions - Part II: Stiffened panels. *Thin-Walled Structures*, 47(8-9):998–1007, aug 2009.

[84] J. K. Paik, A. K. Thayamballi, and B. Ju Kim. Large deflection orthotropic plate approach to develop ultimate strength formulations for stiffened panels under combined biaxial compression/tension and lateral pressure. *Thin-Walled Structures*, 39(3):215–246, mar 2001.

[85] C. Petersen. *Statik und Stabilität der Baukonstruktionen*. Vieweg-Verlag, 2 edition, 1992.

[86] V. Pourostad. *Numerische Untersuchungen an ausgesteiften Blechfeldern und analytische Parameterstudie bei mehrachsiger Beanspruchung*. Master thesis, 2015-14X, Institute of Structural Design, University of Stuttgart, 2015.

[87] prEN 1993-1-5. Eurocode 3 - Design of steel structures - Part 1-5: Plated structural elements. - stage 49 draft, 2004.

[88] Python Software Foundation. URL: www.python.org, date accessed: 2016-04-17.

[89] E. Riks. An incremental approach to the solution of snapping and buckling problems. *International Journal of Solids Structures*, 15(7):529–551, 1979.

[90] D. C. Ruff and U. Schulz. Der Einfluß von Imperfektionen auf das Tragverhalten von Platten. *Stahlbau*, 68(10):829–834, 1999.

[91] D. C. Ruff and U. Schulz. Ergänzende Stellungnahme. *Stahlbau*, 69(6):503, 2000.

[92] A. Rusch and J. Lindner. Tragfähigkeit von beulgefährdeten Querschnittsele-

menten unter Berücksichtigung von Imperfektionen. *Stahlbau*, 70(10):765–774, oct 2001.

[93] B. W. Schafer and T. Peköz. Cold-Formed Steel Members with Multiple Longitudinal Intermediate Stiffeners. *Journal of Structural Engineering*, 124(10):1175–1181, 1998.

[94] J. Scheer. *Auswertung von internationalen Veroeffentlichungen, Versuchsberichten, Kommissionspapieren u.ä. auf dem Gebiet des Beulens von Platten aus Stahl*. Fraunhofer IRB Verlag, 1987.

[95] J. Scheer and H. Nölke. Neuer Vorschlag zum Nachweis der Beulsicherheit von Platten unter mehreren Randspannungen. *Festschrift G. Valtinat*, pages 261–274, 2001.

[96] J. Scheer and H. Nölke. Zum Nachweis der Beulsicherheit von Platten bei gleichzeitiger Wirkung mehrerer Randspannungen. *Stahlbau*, 70(9):718–729, sep 2001.

[97] J. Scheer and J. Vayas. Traglastversuche an längsgestauchten, versteiften Rechteckplatten mit allseitiger Lagerung. *Stahlbau*, 52(3):78–84, 1983.

[98] H. Schmidt. Stability of steel shell structures: General Report. *Journal of Constructional Steel Research*, 55:159–181, 2000.

[99] G. Sedlacek, M. Feldmann, U. Kuhlmann, M. Mensinger, J. Naumes, C. Müller, B. Braun, and J. Ndogmo. Entwicklung und Aufbereitung wirtschaftlicher Bemessungsregeln für Stahl- und Verbundträger mit schlanken Stegblechen im Hoch- und Brückenbau. Technical report, DASt-Forschungsbericht, AiF-Projekt-Nr. 14 771, 2008.

[100] P. Seide and M. Stein. Compressive Buckling of Simply Supported Plates with Longitudinal Stiffeners. *NACA Tech. Note No. 1825*, 1949.

[101] M. Seitz. *Tragverhalten längsversteifter Blechträger unter quergerichteter Krafteinleitung*. Dissertation, No.2005-2, Institute of Structural Design, University of Stuttgart, 2005.

[102] E. Seydel. Über das Ausbeulen von rechteckigen isotropen oder orthogonalisotropen Platten bei Schubbeanspruchung. *Ing. Arch.*, 4:169, 1933.

[103] L. Simões da Silva, C. Rebelo, D. Nethercot, L. Marques, R. Simões, and P. Vila Real. Statistical evaluation of the lateral -torsional buckling resistance of steel I-beams, Part 2: Variability of steel properties. *Journal of Constructional Steel Research*, 65(4):832–849, apr 2009.

[104] Simulia. *Abaqus 6.11 Documentation*. Dassault Systèmes, 2011.

[105] Simulia. *Abaqus Scripting User's Manual*. Dassault Systèmes, 2011.

[106] F. Sinur. *Behaviour of Longitudinally Stiffened Plate Girders Subjected to Bending-Shear Interaction*. Dissertation, PhD Thesis, University of Ljubljana, 2011.

[107] F. Sinur and D. Beg. Imperfection Sensitivity Analysis of Longitudinally Stiffened Plated Girders Subjected to Bending - Shear Interaction. In *Stability and Ductility of Steel Structures*, pages 787–794, Rio, Brazil, 2010.

[108] F. Sinur, A. Zizza, U. Kuhlmann, and D. Beg. Buckling interaction of slender plates - Experimental and numerical investigations. *Thin-Walled Structures*, 61:121–131, dec 2012.

[109] P. Steinke. *Finite-Elemente-Methode : rechnergestützte Einführung*. Springer-Verlag, Berlin, 2004.

[110] R. Timmers. *Zur direkten Bestimmung der Traglastkurve nicht ausgesteifter und ausgesteifter Beulfelder durch Anwendung der Fließlinientheorie*. Dissertation, Leopold-Franzens-Universität Innsbruck, 2015.

[111] S. P. Timoshenko. Einige Stabilitätsprobleme der Elastizitätstheorie. *Z. Math. Phys.*, 58:337, 1910.

[112] S. P. Timoshenko. Stability of the Webs of Plate Girders. *Engineering*, 138:207, 1934.

[113] S. P. Timoshenko and J. M. Gere. *Theory of Elastic Stability*. McGraw-Hill, New York, 2nd edition, 1961.

[114] Y. Ueda, S. Rashed, and J. K. Paik. Buckling and ultimate strength interaction in plates and stiffened panels under combined inplane biaxial and shearing forces. *Marine Structures*, 8(1):1–36, jan 1995.

[115] Y. Ueda and T. Yao. The influence of complex initial deflection modes on the behaviour and ultimate strength of rectangular plates in compression. *Journal of Constructional Steel Research*, 5(4):265–302, jan 1985.

[116] H. Unterweger and M. Kettler. Einzelfeldbeulen - Wirklich große Unterschiede zwischen Eurocode EN 1993-1-5 und DIN 18800-3? *Stahlbau*, 82(8):597–608, aug 2013.

[117] H. Unterweger and M. Kettler. Plattenbeulen nach Eurocode EN 1993-1-5 und Vergleich mit den (alten) nationalen Normen DIN bzw. ÖNORM. In *35. Stahlbauseminar 2013*, Neu-Ulm, 2013. Akademie der Hochschule Biberach.

[118] T. Usami. Effective width of locally buckled plates in compression and bending. *Journal of Structural Engineering*, 119(5):1358–1373, 1993.

[119] S. Valsgard. Numerical design prediction of the capacity of plates in biaxial inplane compression. *Computers & Structures*, 12(5):729–739, 1980.

[120] S. L. Veldman. Approximate buckling interaction curves for long anisotropic flat plates in biaxial compression and shear. *Composite Structures*, 103:161–167, sep 2013.

[121] E. Watanabe, T. Usami, and A. Hasegawa. Strength and design of steel stiffened plates - A literature review of japanese contributions. In *Inelastic Instability of Steel Structures and Structural Elements; U.S.-Japan Joint Seminar*, pages 396–

417, Tokio, 1981.

[122] G. Winter. Strength of Thin Steel Compression Flanges. *Transactions of the American Society of Civil Engineers*, 112:527–554, 1947.

[123] T. A. Winterstetter. *Stabilität von Kreiszylinderschalen aus Stahl unter kombinierter Beanspruchung*. Dissertation, Universität GH Essen, 2000.

[124] T. A. Winterstetter. Zum Nachweis der Beulsicherheit von Platten- und Schalentragwerken aus Stahl bei mehrachsiger Beanspruchung. *Stahlbau*, 71(11):816–822, nov 2002.

[125] R. D. Ziemian, editor. *Guide to Stability Design Criteria for Metal Structures*. John Wiley & Sons, 6 edition, 2010.

[126] O. C. Zienkiewicz and R. L. Taylor. *Finite Element Method, volume 1: The Basis*. Butterworth-Heinemann, 5th edition, 2000.

[127] O. C. Zienkiewicz and R. L. Taylor. *Finite Element Method, volume 2: Solid Mechanics*. Butterworth-Heinemann, 5th edition, 2000.

[128] A. Zizza and U. Kuhlmann. Tensile Stresses on the Buckling Behaviour of Slender Plates. In *IABSE Young Engineers Colloquium*, pages 10–11, Dresden, 2014.

List of Annexes

A Design drawings of the tested longitudinally stiffened girders

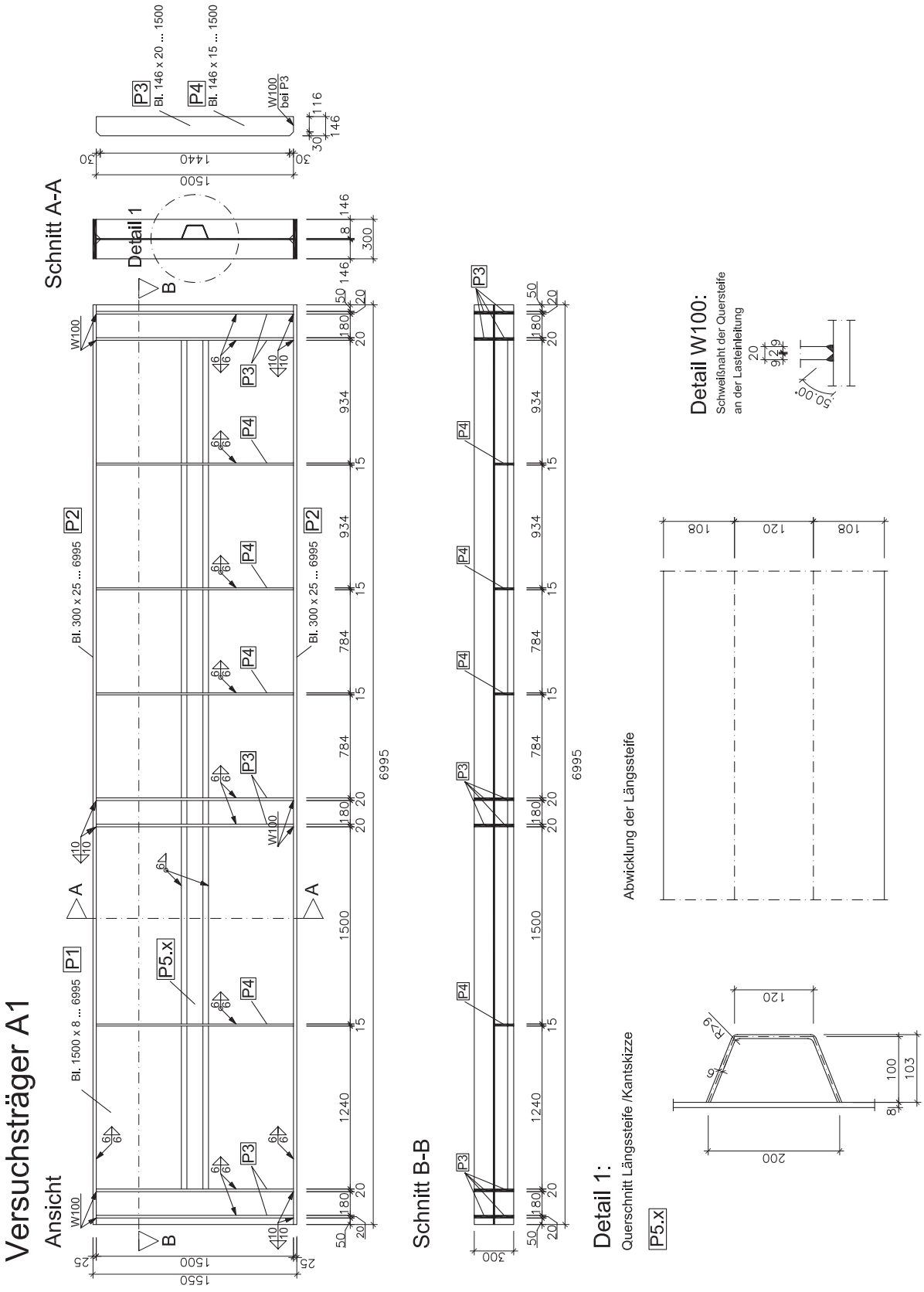

Figure A.1: Girder A1: Design drawings.

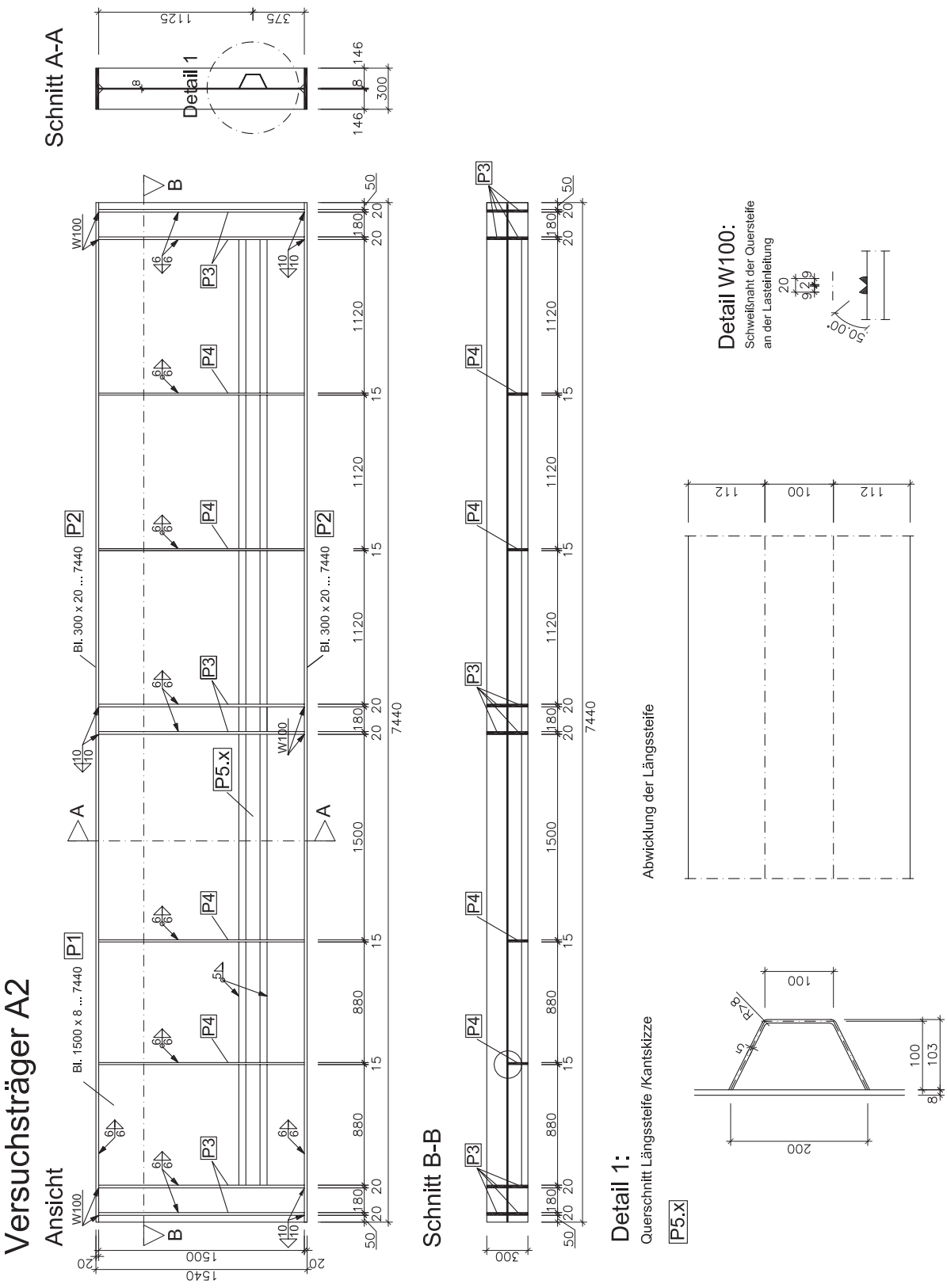

Figure A.2: Girder A2: Design drawings.

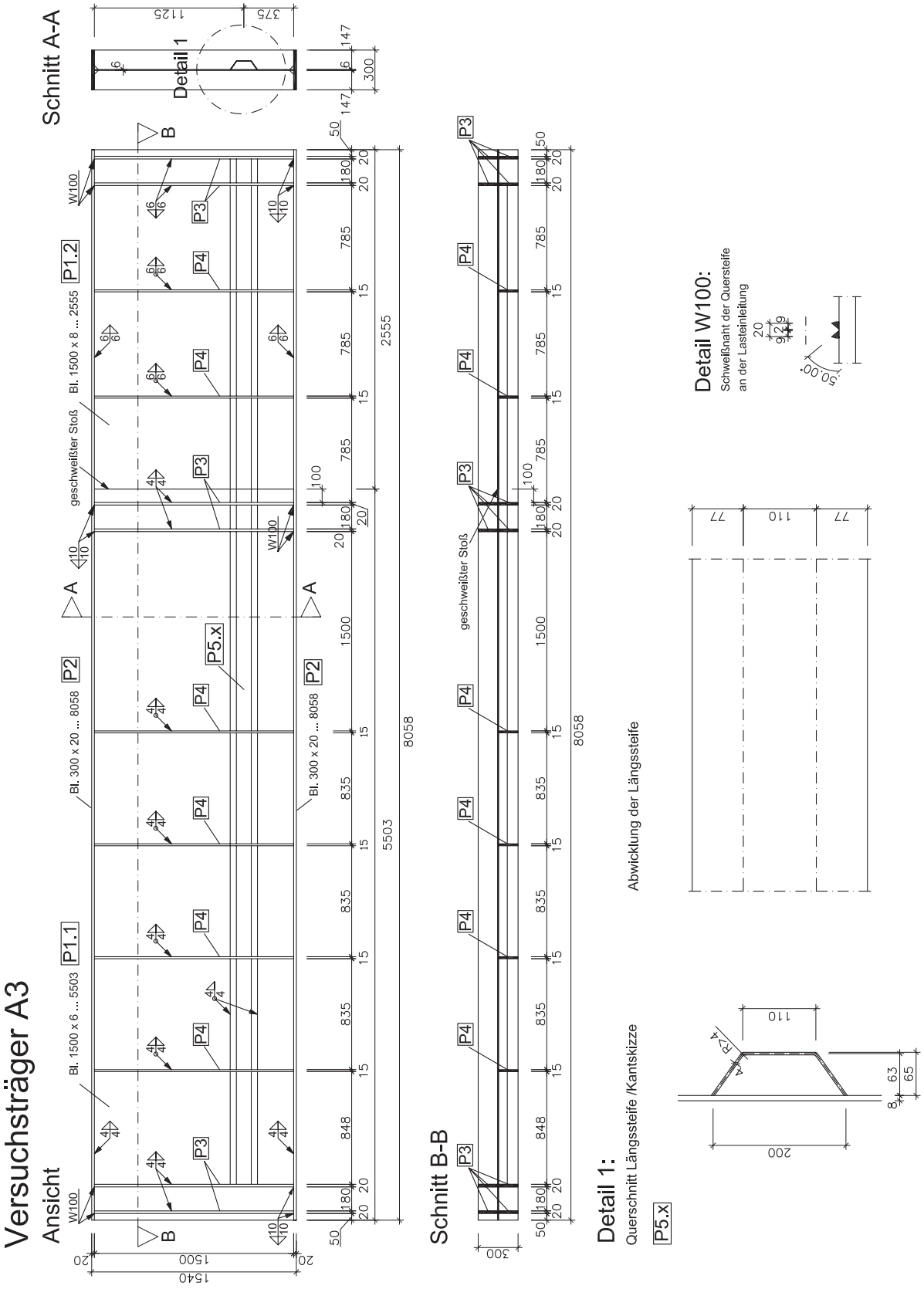

Figure A.3: Girder A3: Design drawings.

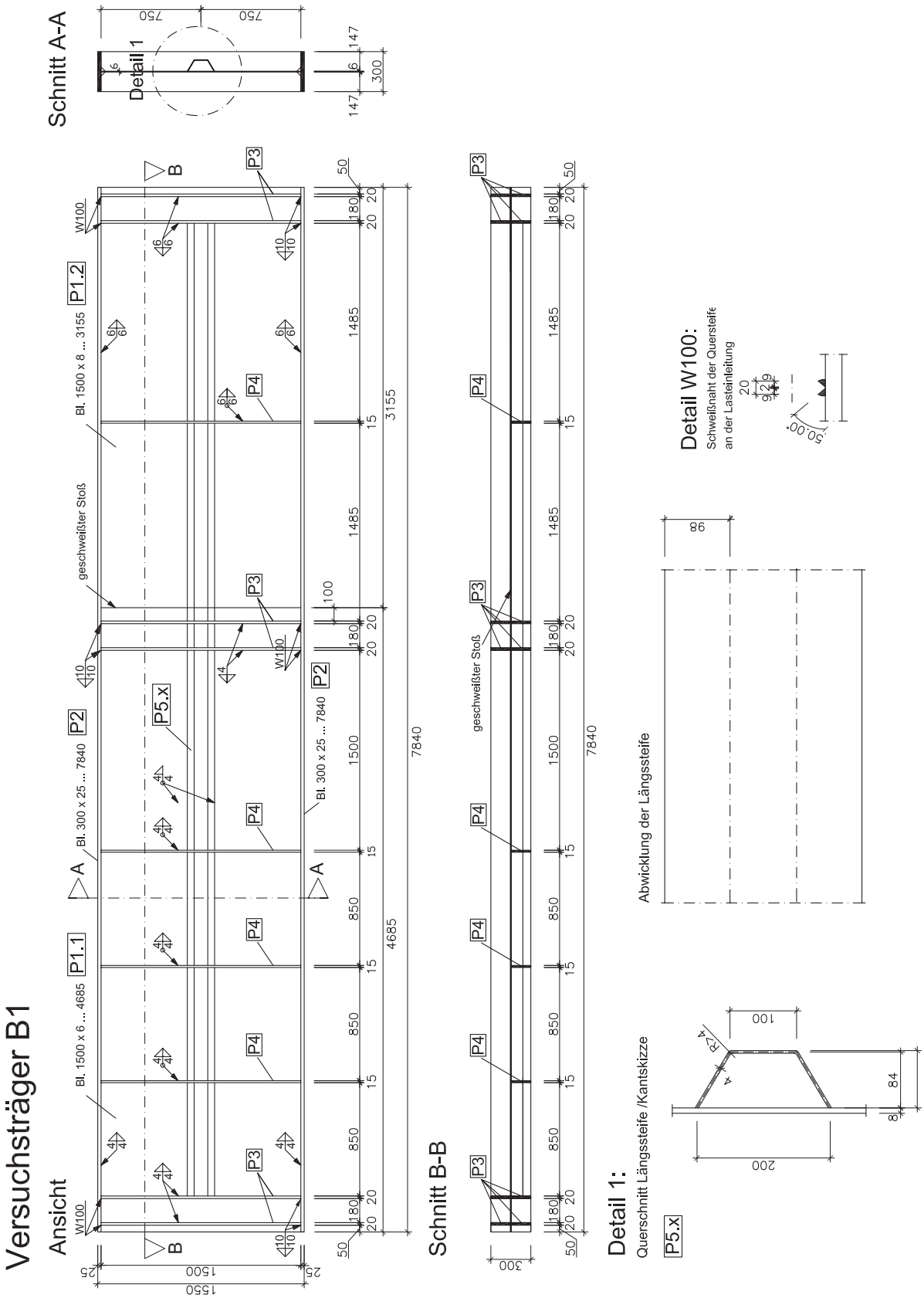

Figure A.4: Girder B1: Design drawings.

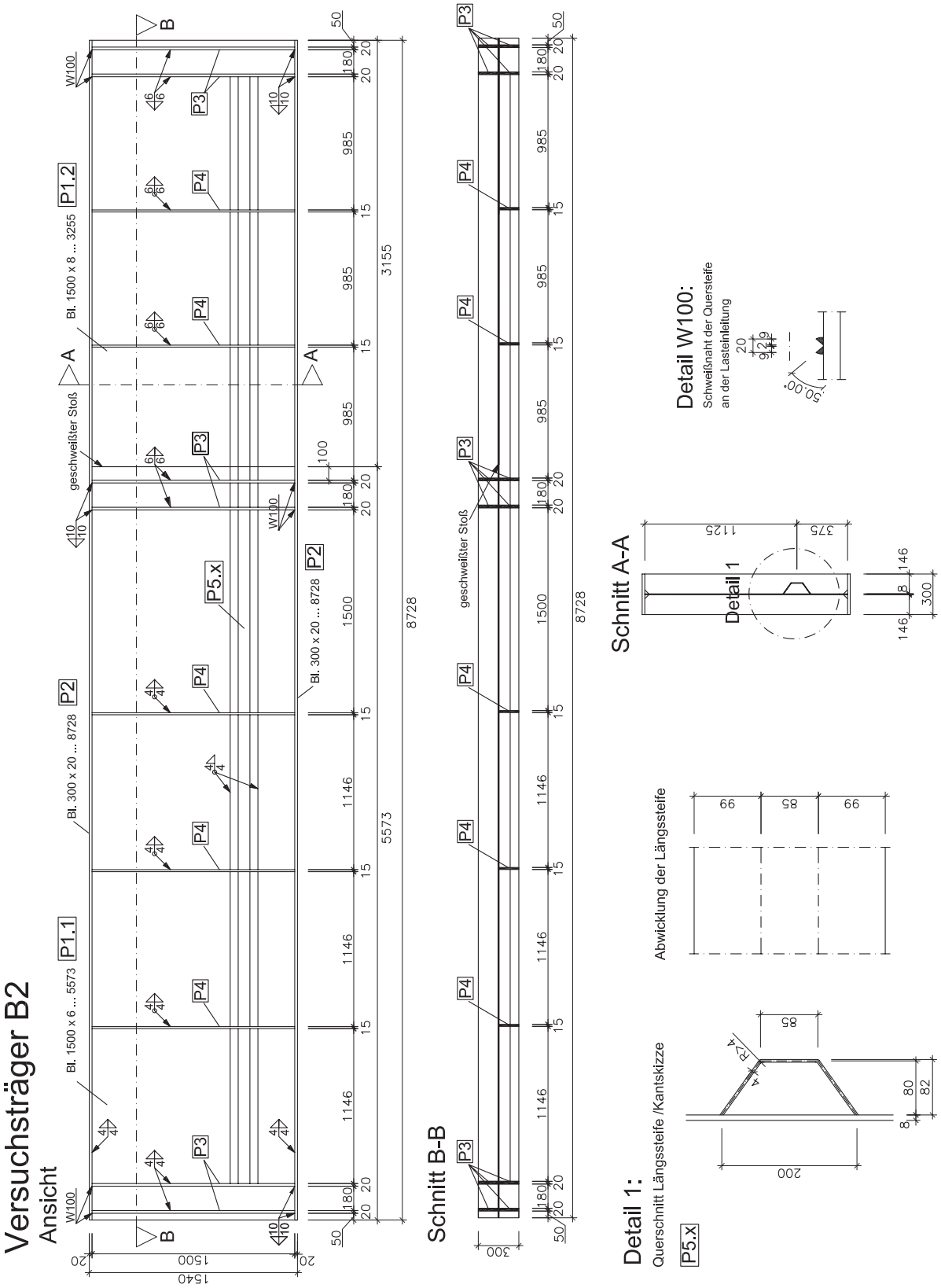

Figure A.5: Girder B2: Design drawings.

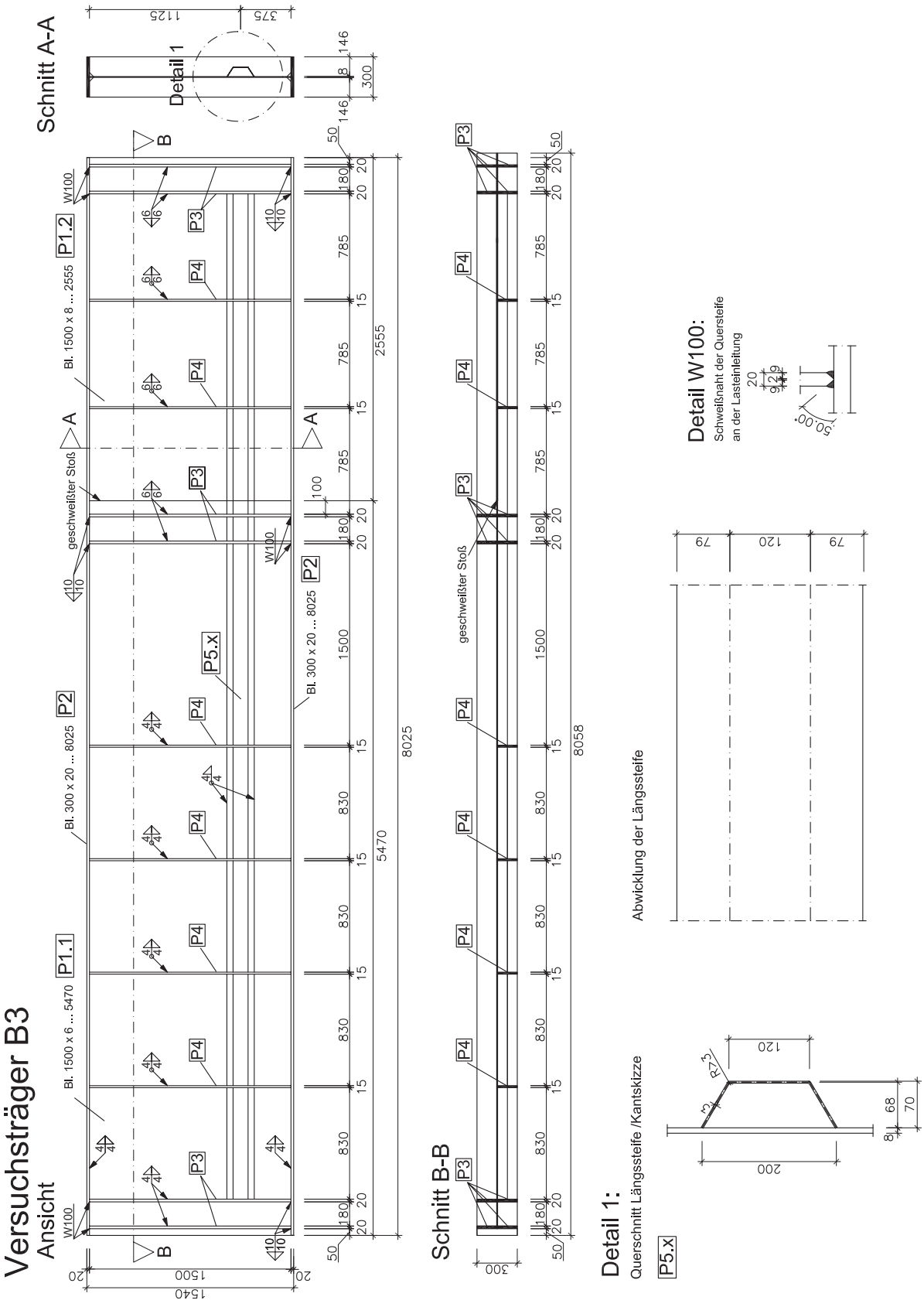

Figure A.6: Girder B3: Design drawings.

B Numerical interaction curves

B.1 Tension-Shear

a) $b/t = 70$

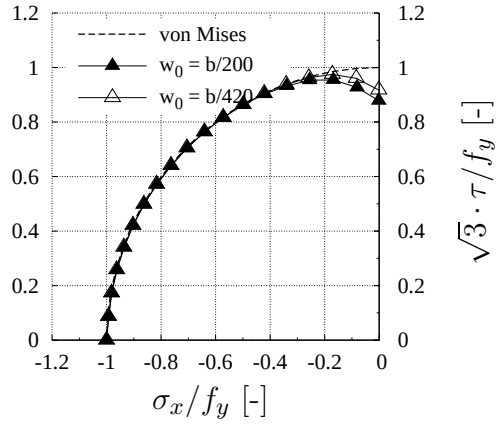

b) $b/t = 100$

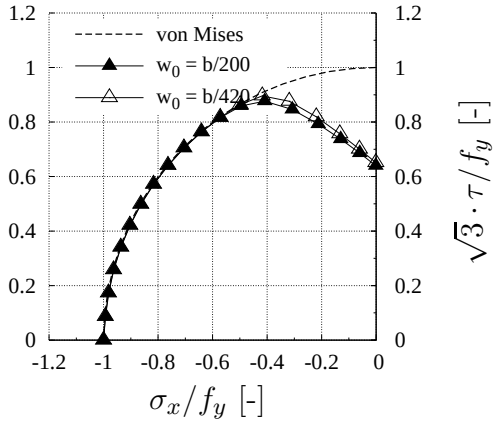

c) $b/t = 150$

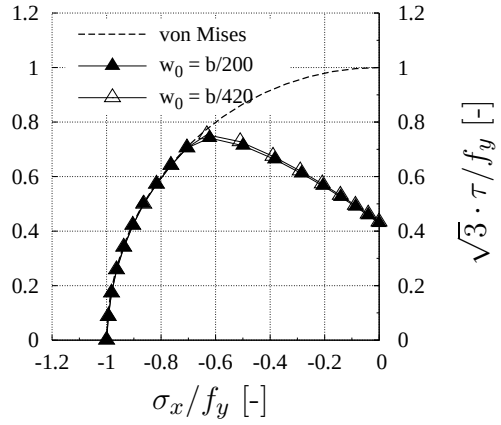

d) $b/t = 250$

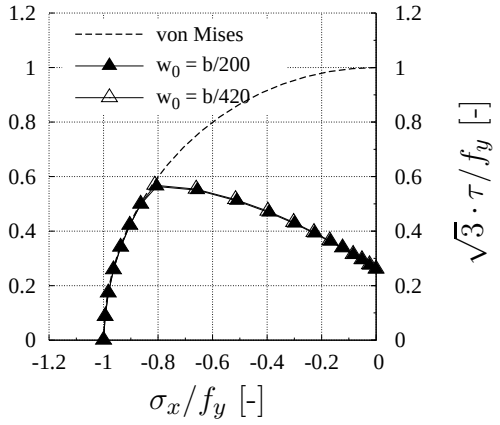

Figure B.1: Numerical results edges loaded with tension being constrained (BC-A, $\alpha = 2$, all edges hinged).

a) $b/t = 70$

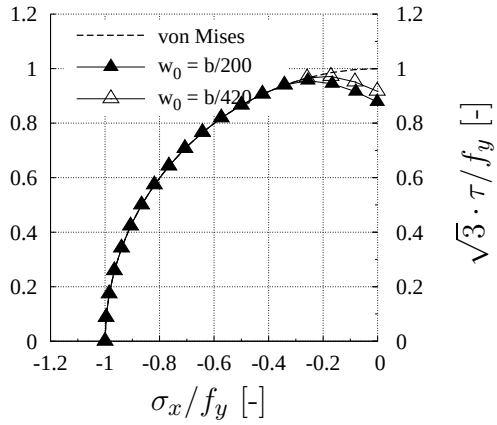

b) $b/t = 100$

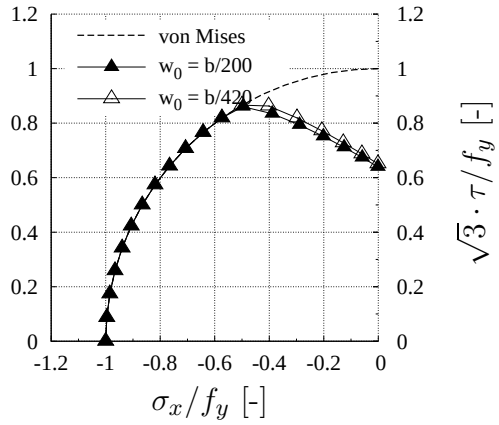

c) $b/t = 150$

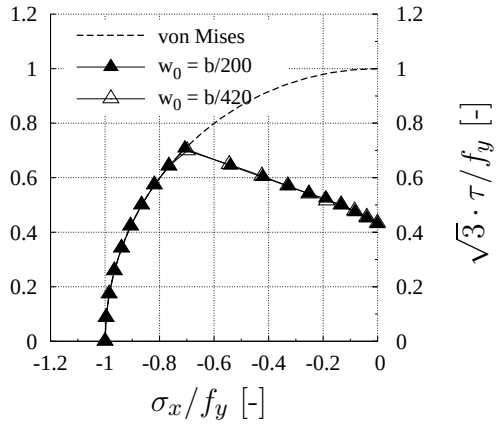

d) $b/t = 250$

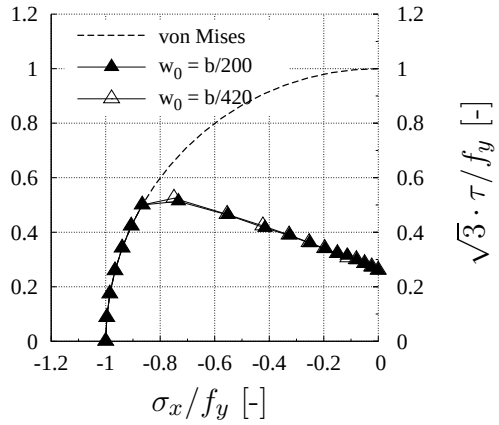

Figure B.2: Numerical results for edges loaded with tension $\psi = 0.5$ being constrained (BC-A, $\alpha = 2$, all edges hinged).

a) $b/t = 70$

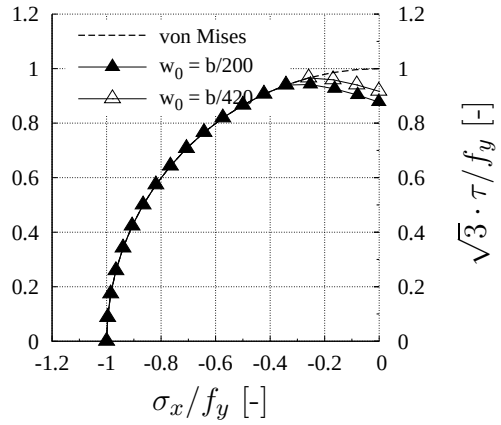

b) $b/t = 100$

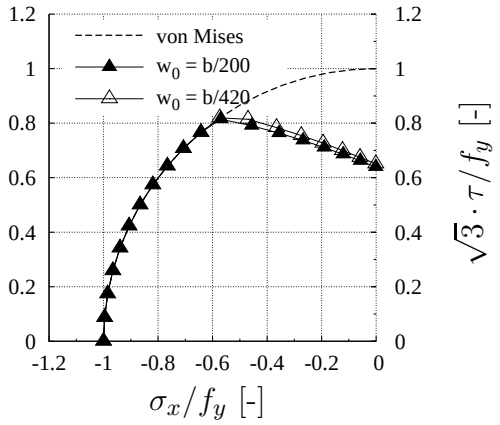

c) $b/t = 150$

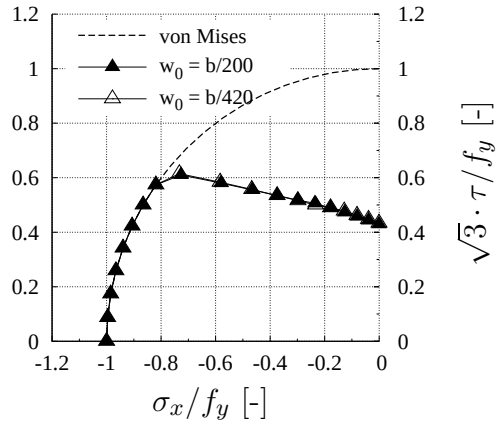

d) $b/t = 250$

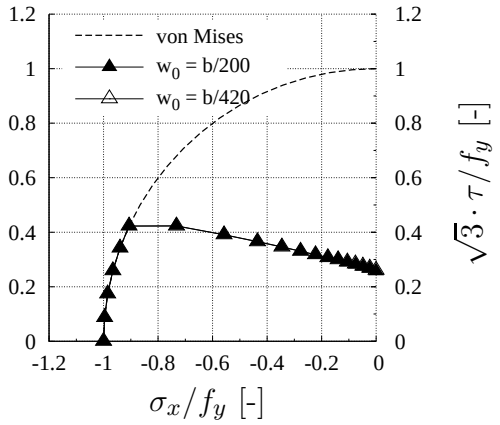

Figure B.3: Numerical results for edges loaded with tension $\psi = 0$ being constrained (BC-A, $\alpha = 2$, all edges hinged).

a) $b/t = 70$

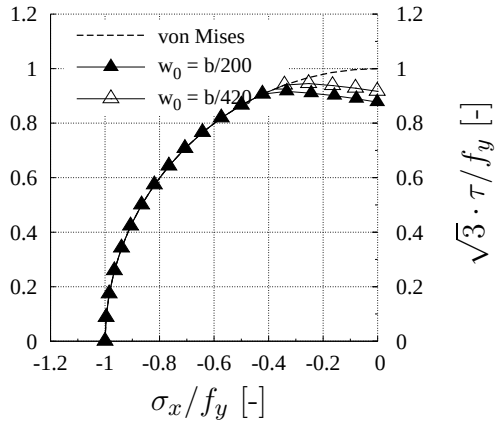

b) $b/t = 100$

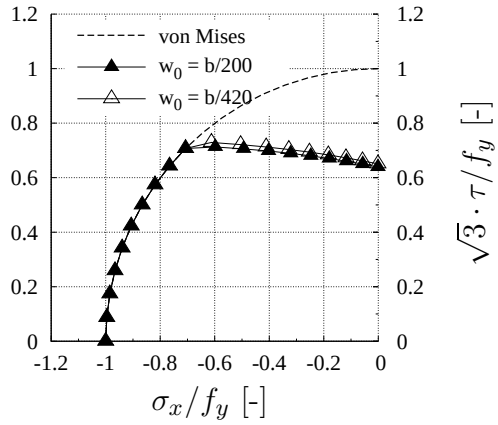

c) $b/t = 150$

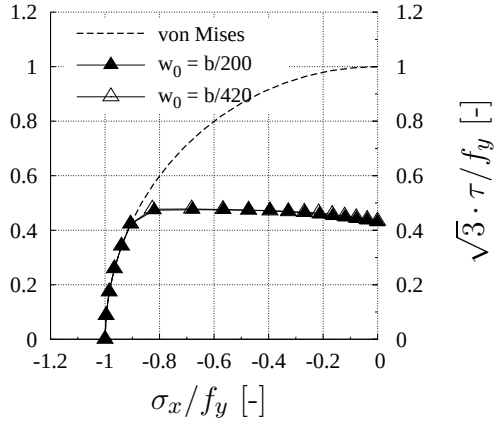

d) $b/t = 250$

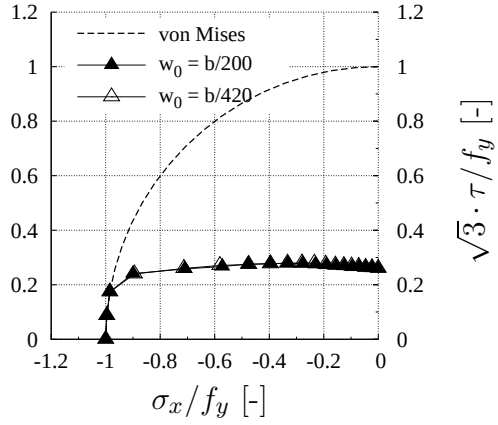

Figure B.4: Numerical results for edges loaded with tension $\psi = -0.5$ being constrained (BC-A, $\alpha = 2$, all edges hinged).

B.2 Compression-Shear

a) $b/t = 45$

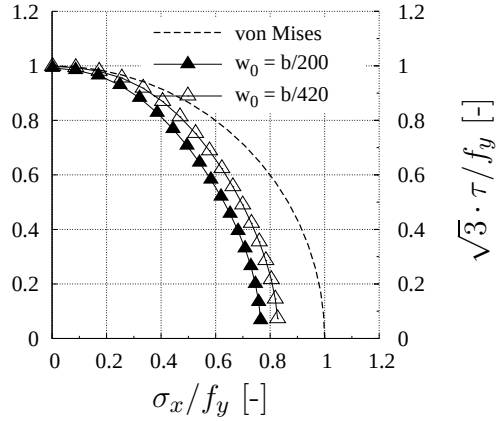

b) $b/t = 60$

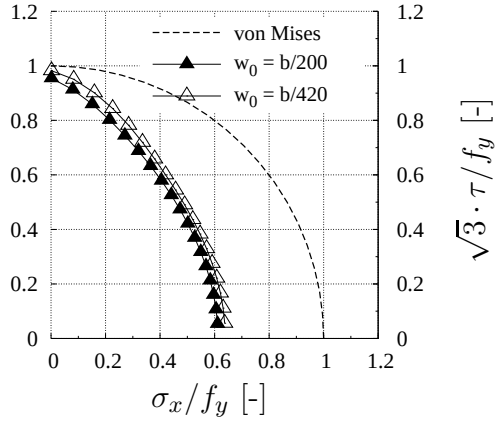

c) $b/t = 70$

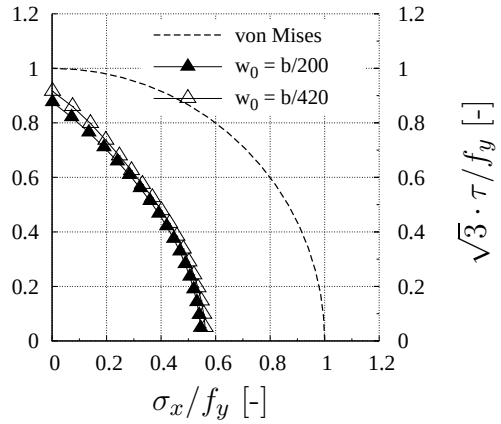

d) $b/t = 100$

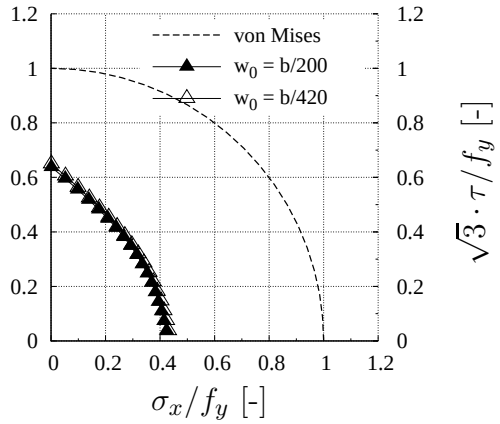

e) $b/t = 150$

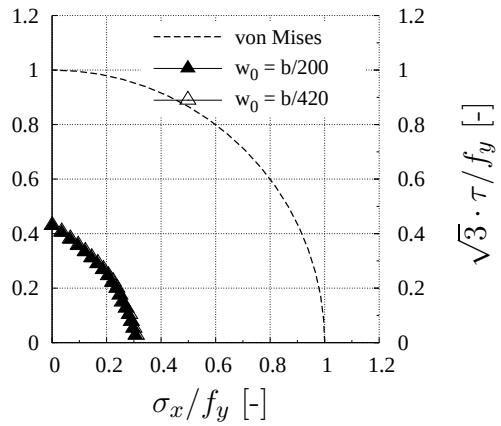

f) $b/t = 250$

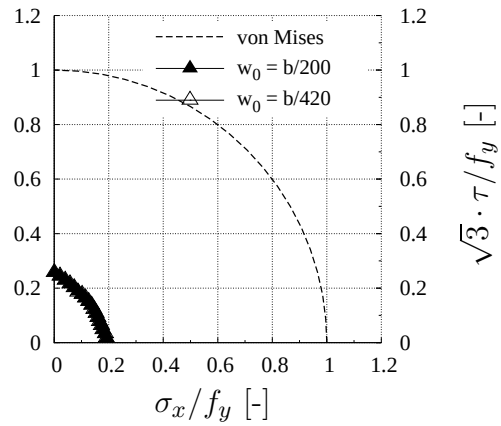

Figure B.5: Numerical results for short edges loaded with compression $\psi = 1.0$ being constrained (BC-A, $\alpha = 2$, all edges hinged).

a) $b/t = 60$

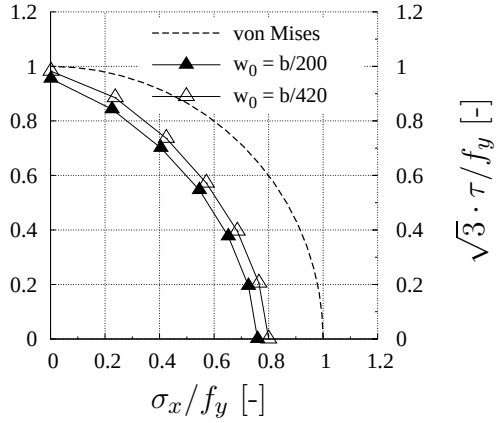

b) $b/t = 70$

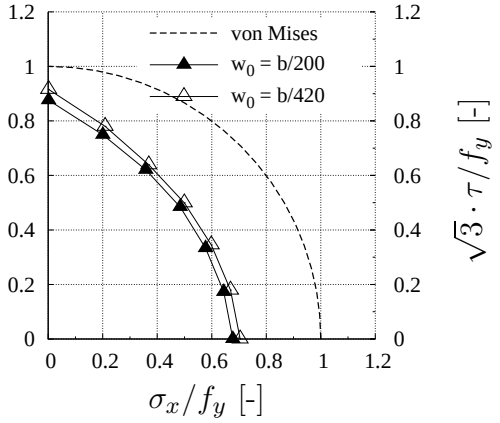

c) $b/t = 80$

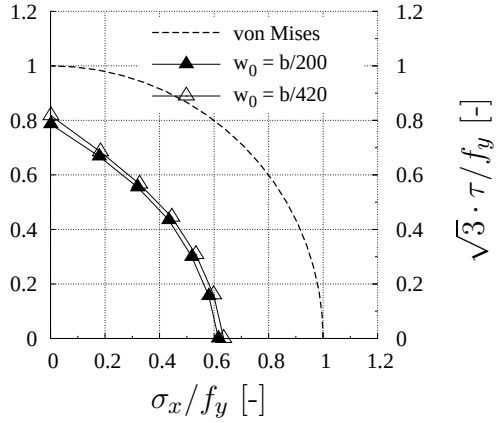

d) $b/t = 100$

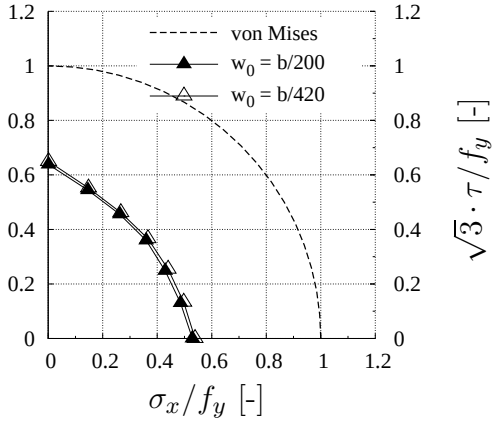

e) $b/t = 150$

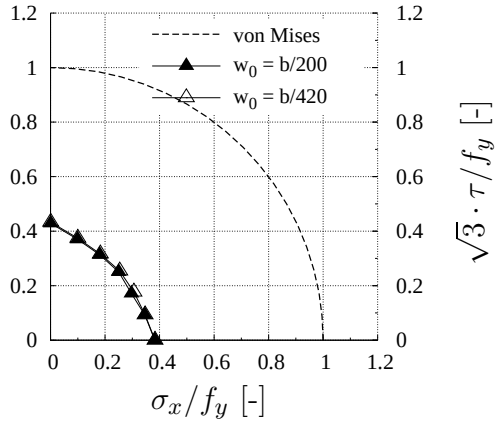

f) $b/t = 250$

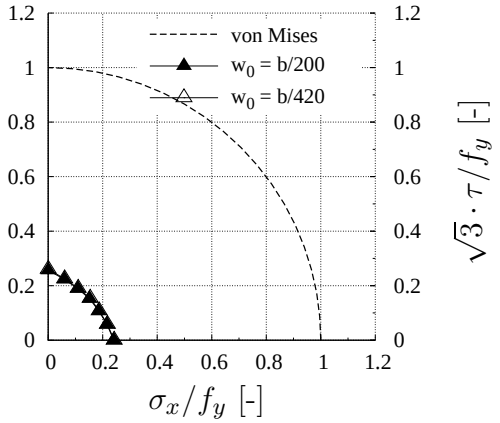

Figure B.6: Numerical results for edges loaded with compression $\psi = 0.5$ being constrained (BC-A, $\alpha = 2$, all edges hinged).

a) $b/t = 60$

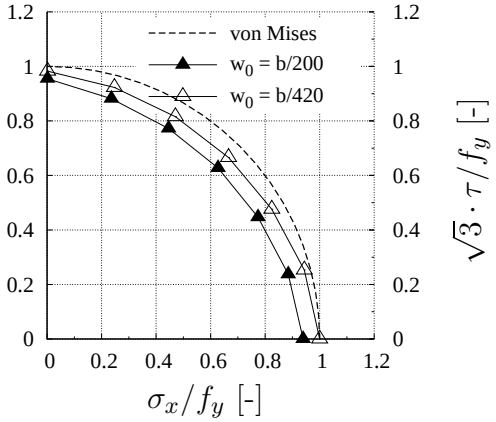

b) $b/t = 70$

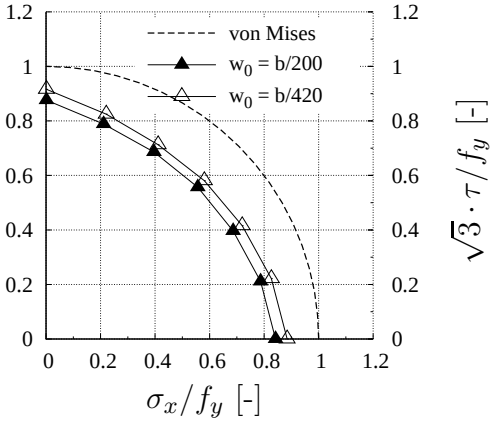

c) $b/t = 80$

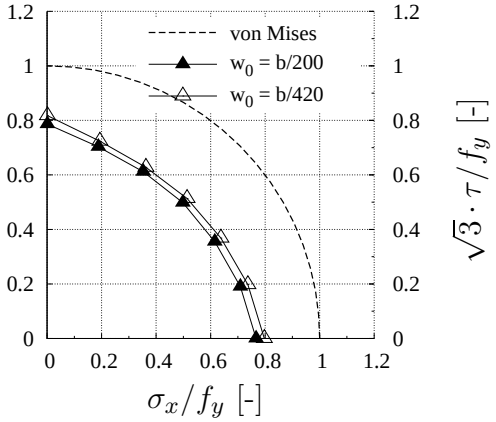

d) $b/t = 100$

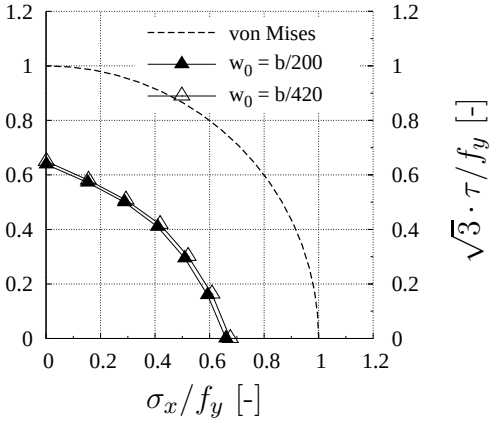

e) $b/t = 150$

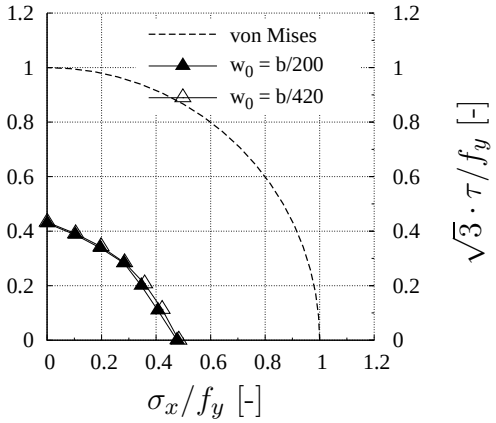

f) $b/t = 250$

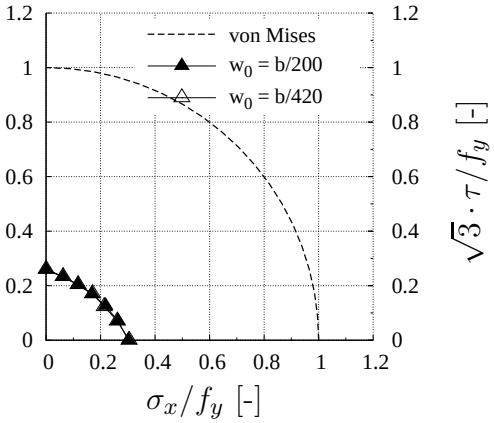

Figure B.7: Numerical results for edges loaded with compression $\psi = 0$ being constrained (BC-A, $\alpha = 2$, all edges hinged).

a) $b/t = 60$

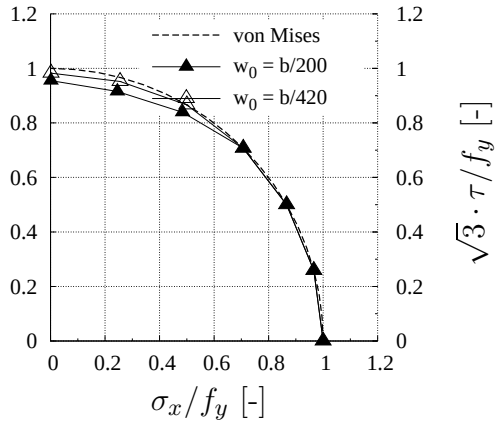

b) $b/t = 70$

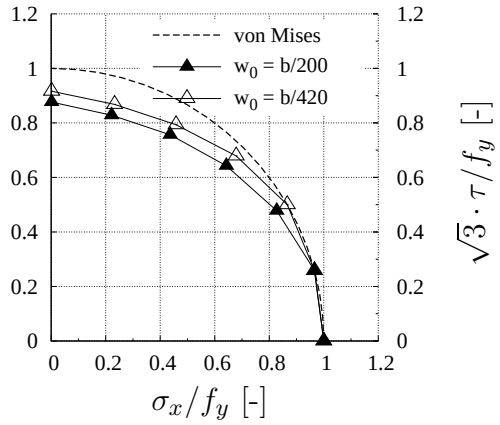

c) $b/t = 80$

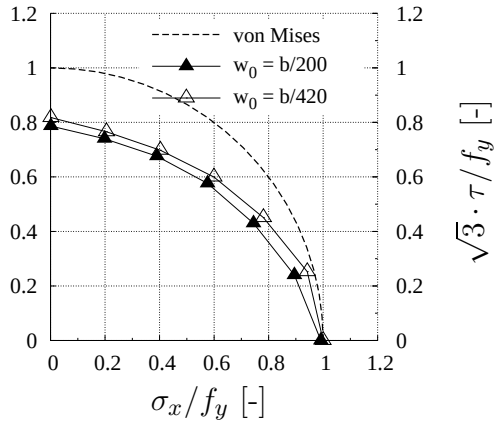

d) $b/t = 100$

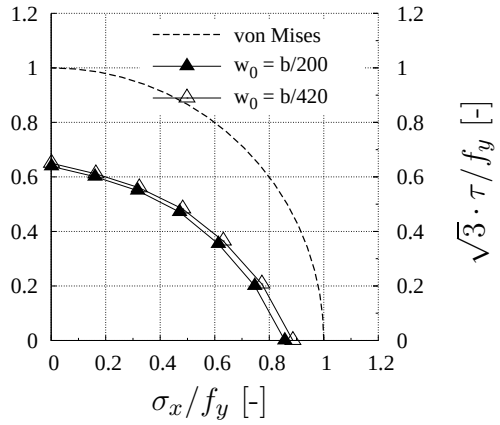

e) $b/t = 150$

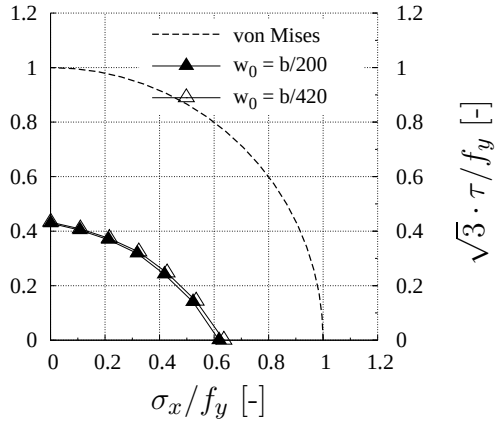

f) $b/t = 250$

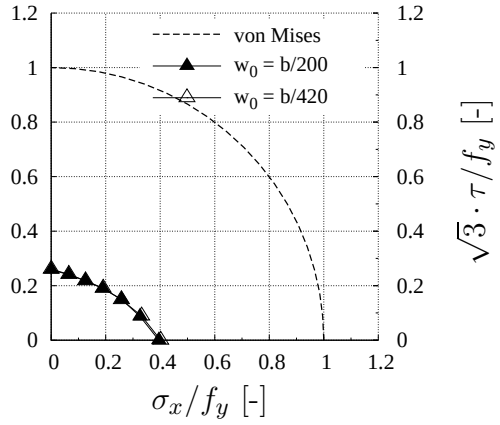

Figure B.8: Numerical results for edges loaded with compression $\psi = -0.5$ being constrained (BC-A, $\alpha = 2$, all edges hinged).

a) $b/t = 60$

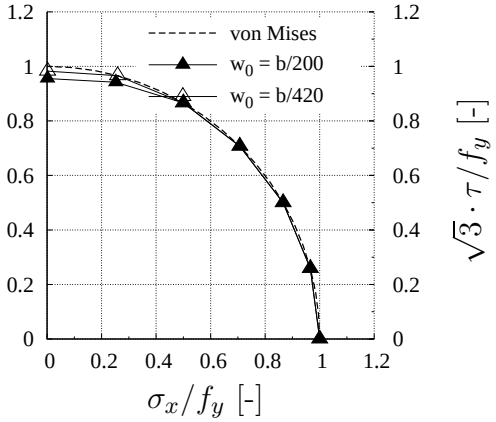

b) $b/t = 70$

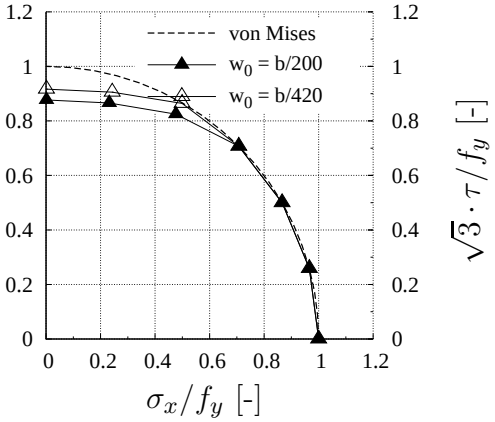

c) $b/t = 80$

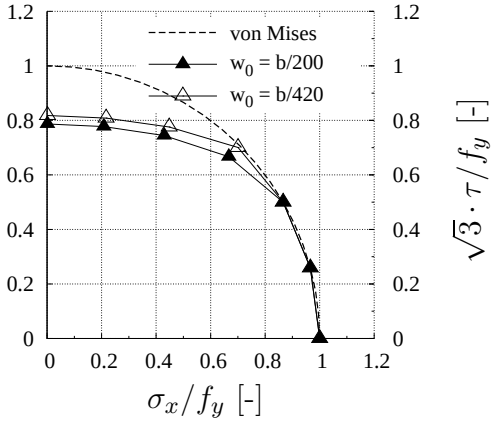

d) $b/t = 100$

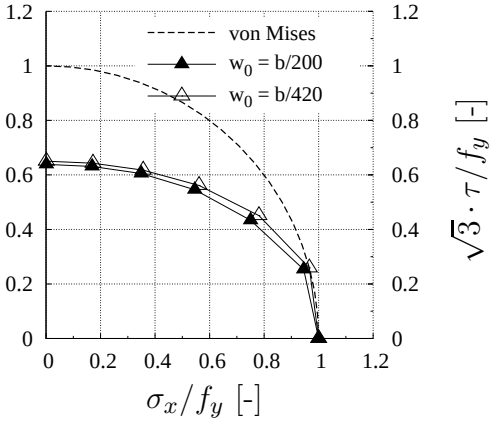

e) $b/t = 150$

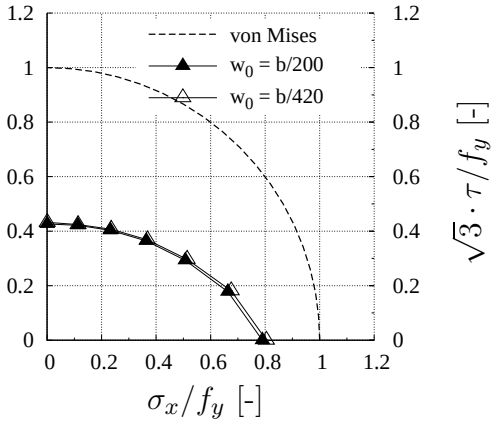

f) $b/t = 250$

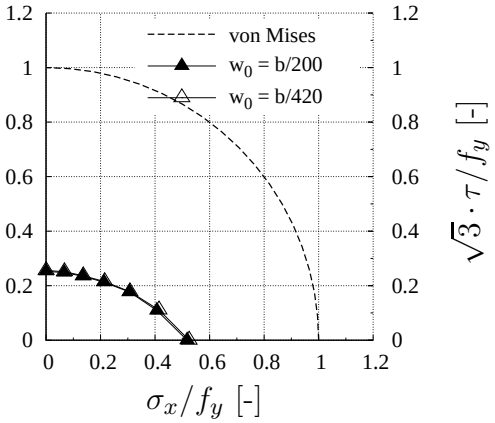

Figure B.9: Numerical results for edges loaded with compression $\psi = -1$ being constrained (BC-A, $\alpha = 2$, all edges hinged).

B.3 Biaxial compression (stiffened plates)

a) $\gamma = 7$

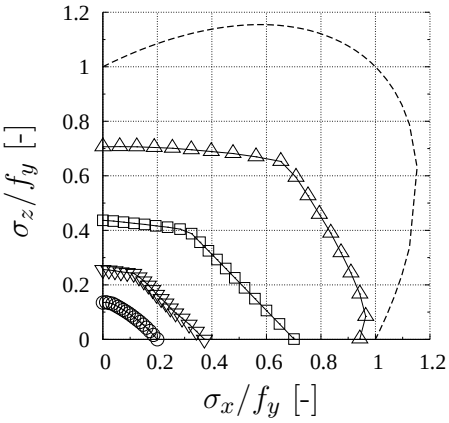

b) $\gamma = 25$

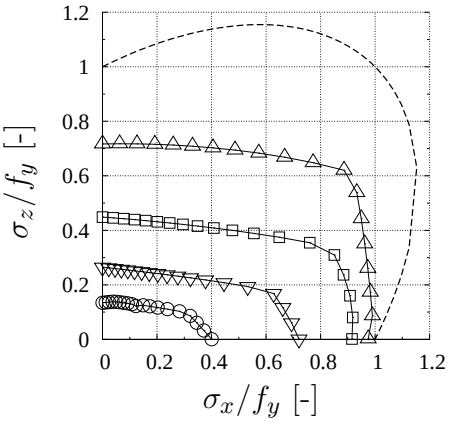

c) $\gamma = 65$

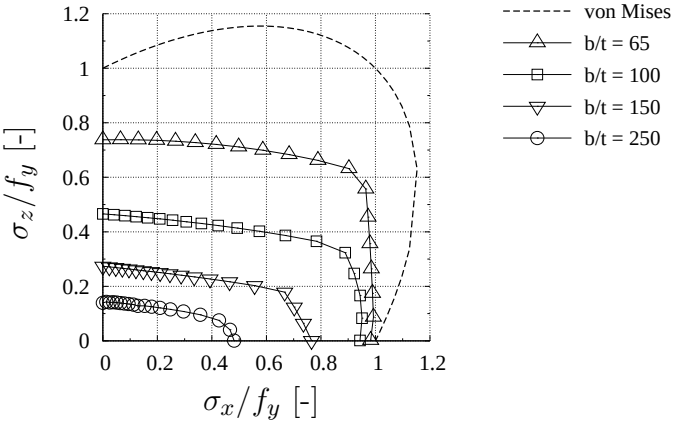

Figure B.10: Numerical results for stiffened plates loaded with biaxial compression, ($\alpha = 1$, $n = 2$, $b/t = 30$, 45, 65 and 100).

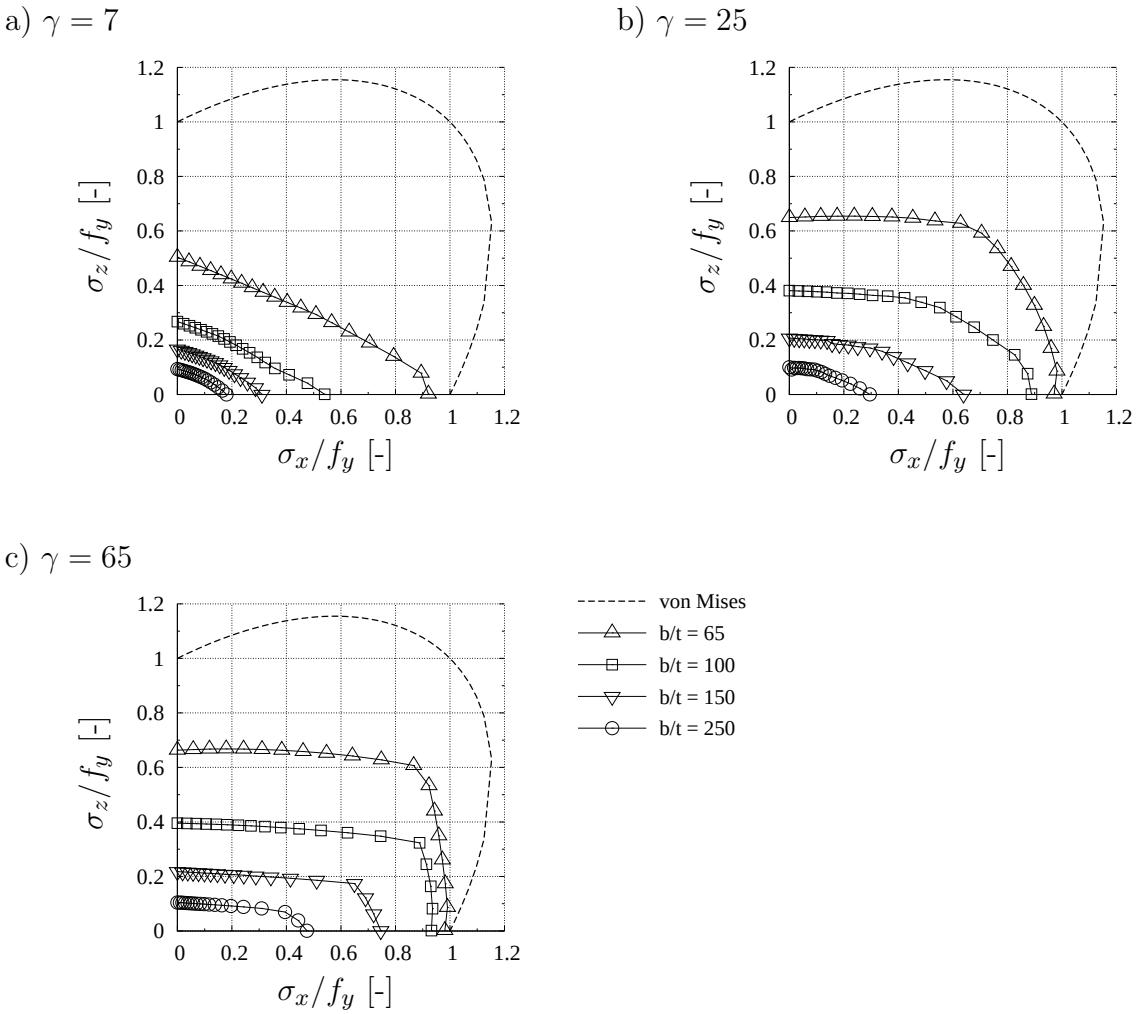

Figure B.11: Numerical results for stiffened plates loaded with biaxial compression, ($\alpha = 1.5$, $n = 2$, $b/t = 30$, 45, 65 and 100).

a) $\gamma = 7$

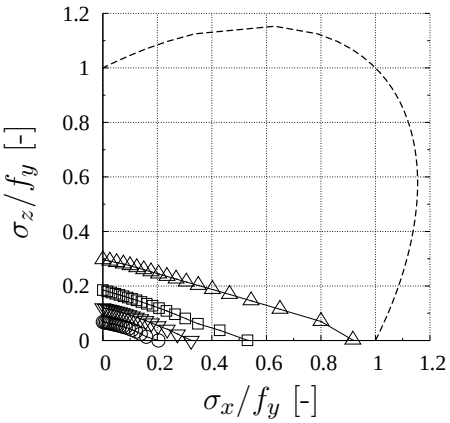

b) $\gamma = 25$

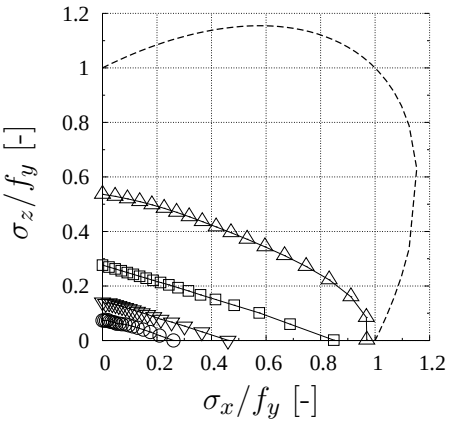

c) $\gamma = 65$

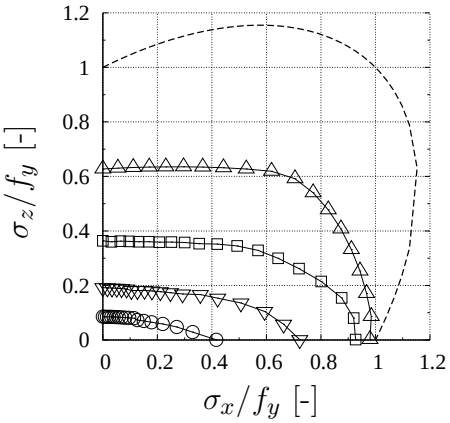

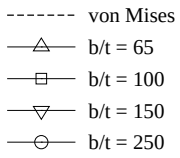

Figure B.12: Numerical results for stiffened plates loaded with biaxial compression, ($\alpha = 2$, $n = 2$, $b/t = 30$, 45, 65 and 100).

a) $\gamma = 7$

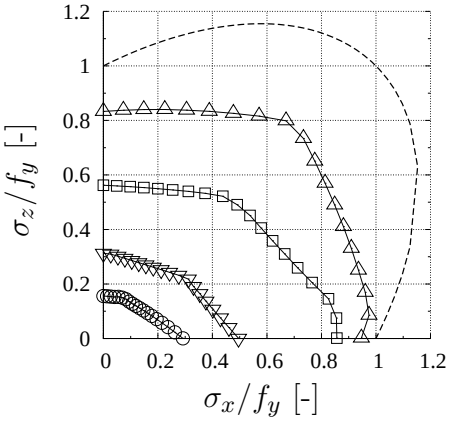

b) $\gamma = 25$

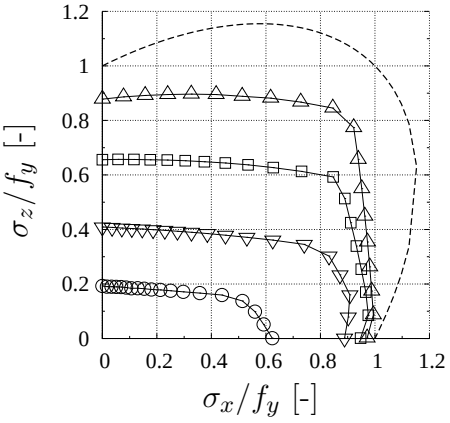

c) $\gamma = 65$

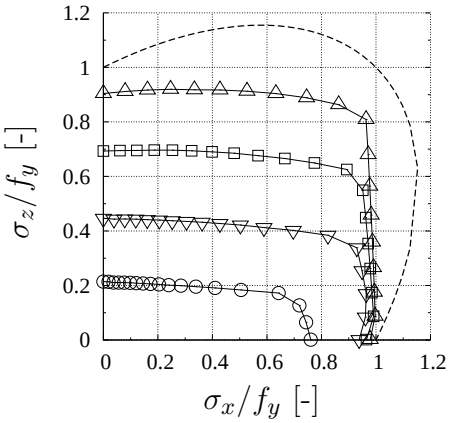

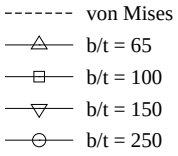

Figure B.13: Numerical results for stiffened plates loaded with biaxial compression, ($\alpha = 1$, $n = 4$, $b/t = 30$, 45, 65 and 100).

a) $\gamma = 7$

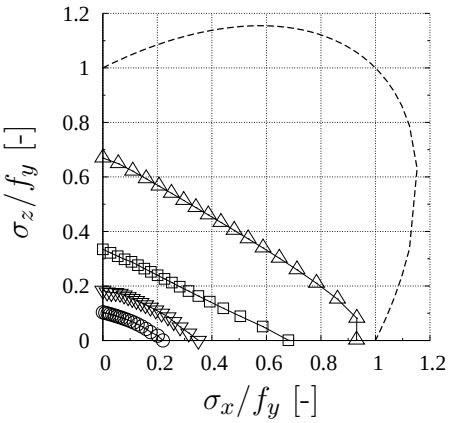

b) $\gamma = 25$

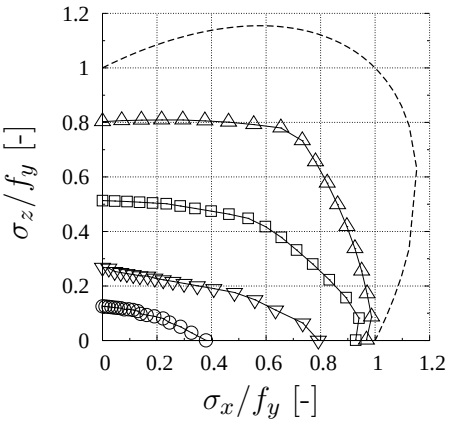

c) $\gamma = 65$

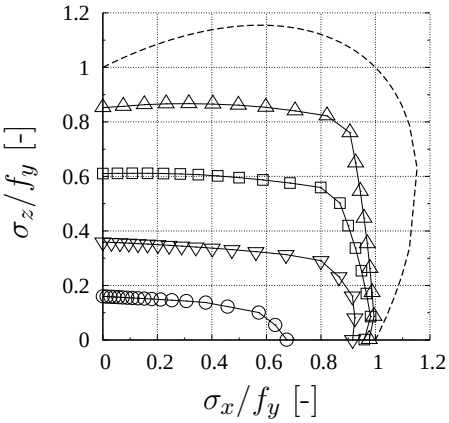

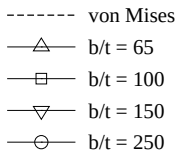

Figure B.14: Numerical results for stiffened plates loaded with biaxial compression, ($\alpha = 1.5$, $n = 4$, $b/t = 30$, 45, 65 and 100).

a) $\gamma = 7$

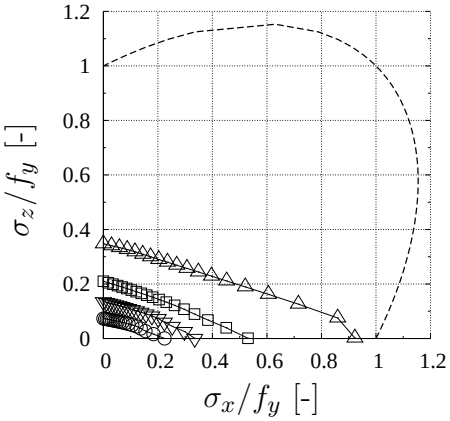

b) $\gamma = 25$

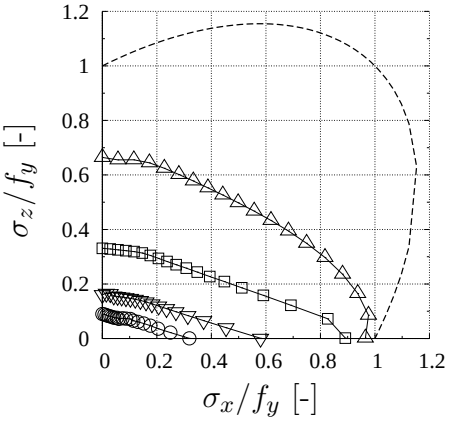

c) $\gamma = 65$

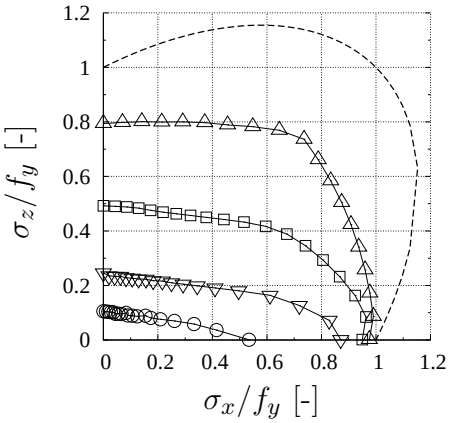

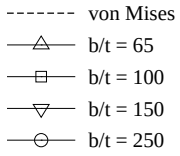

Figure B.15: Numerical results for stiffened plates loaded with biaxial compression, ($\alpha = 2$, $n = 4$, $b/t = 30$, 45, 65 and 100).

C Comparison of numerical results to current design rules

C.1 Plates subjected to direct stresses

a) $b/t = 30$

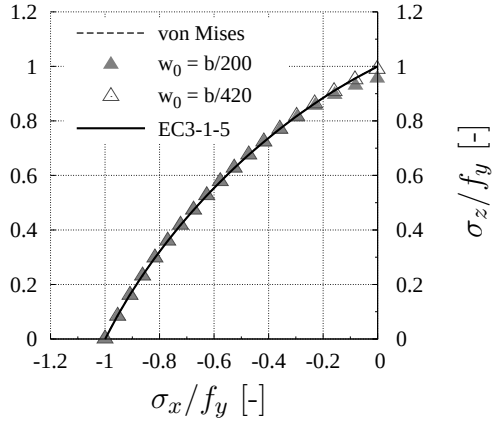

b) $b/t = 45$

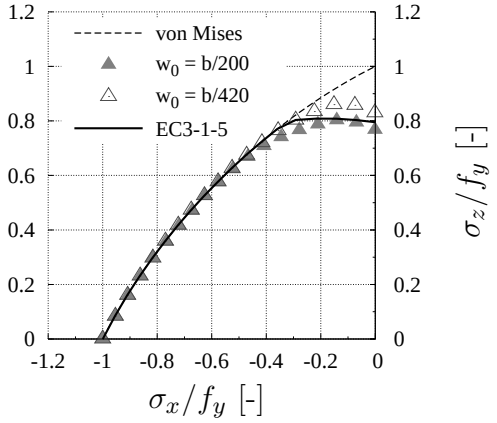

c) $b/t = 65$

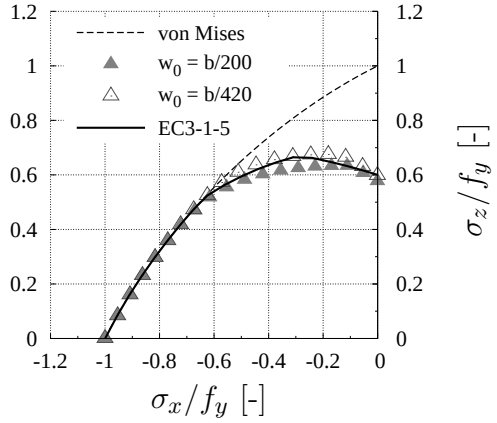

d) $b/t = 100$

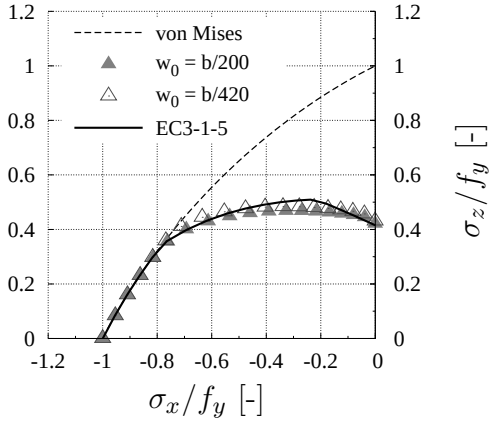

e) $b/t = 150$

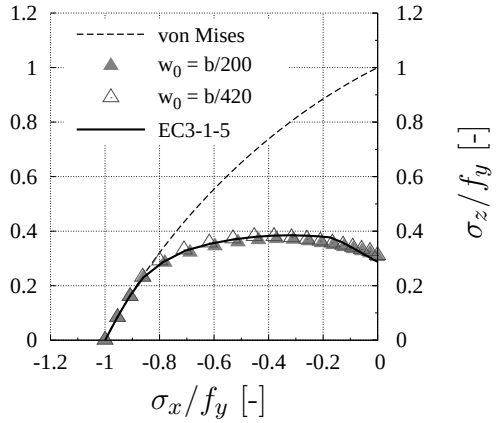

f) $b/t = 250$

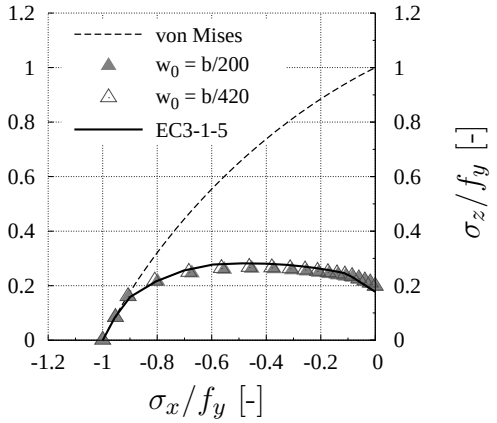

Figure C.1: Comparison of the numerical results with the current design rules in EN 1993-1-5 [37], (BC-A, $\alpha = 1$, all edges hinged, decisive imperfection).

a) $b/t = 30$

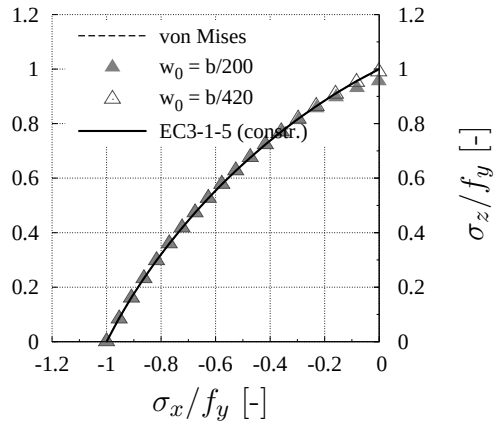

b) $b/t = 45$

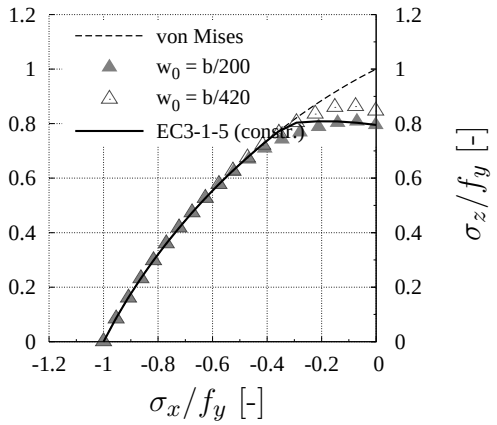

c) $b/t = 65$

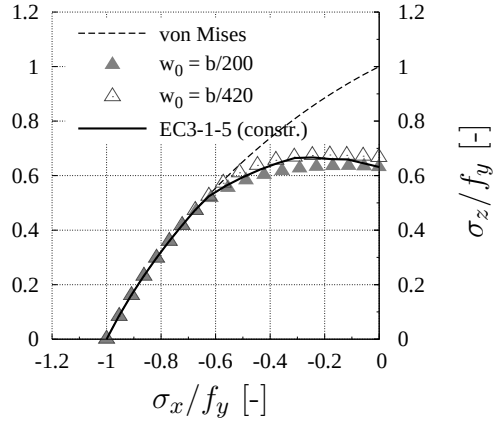

d) $b/t = 100$

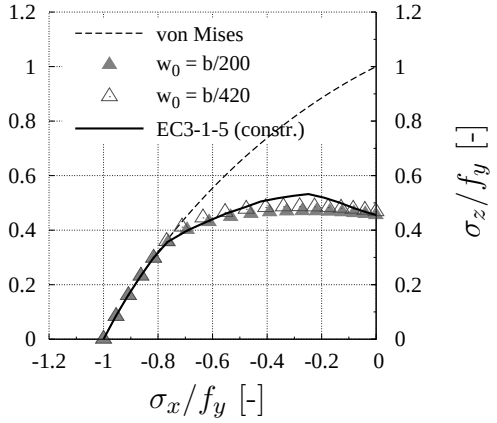

e) $b/t = 150$

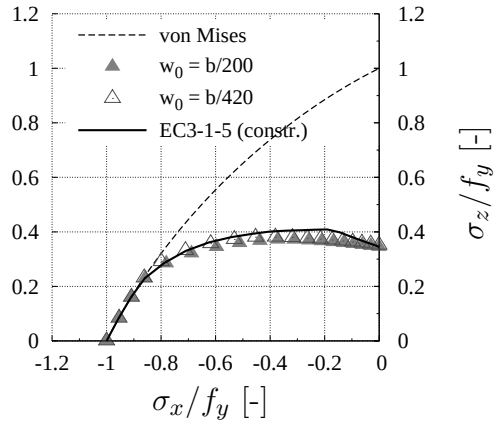

f) $b/t = 250$

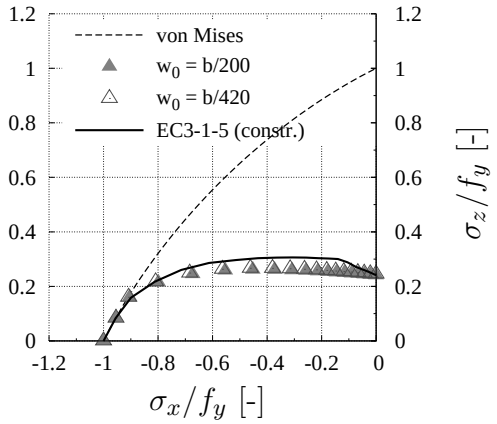

Figure C.2: Comparison of the numerical results with the current design rules in EN 1993-1-5 [37] based on Fig.4.22, (BC-B, $\alpha = 1$, all edges hinged and constrained, decisive imperfection).

a) $w_0 = b/200$ b) $w_0 = b/420$

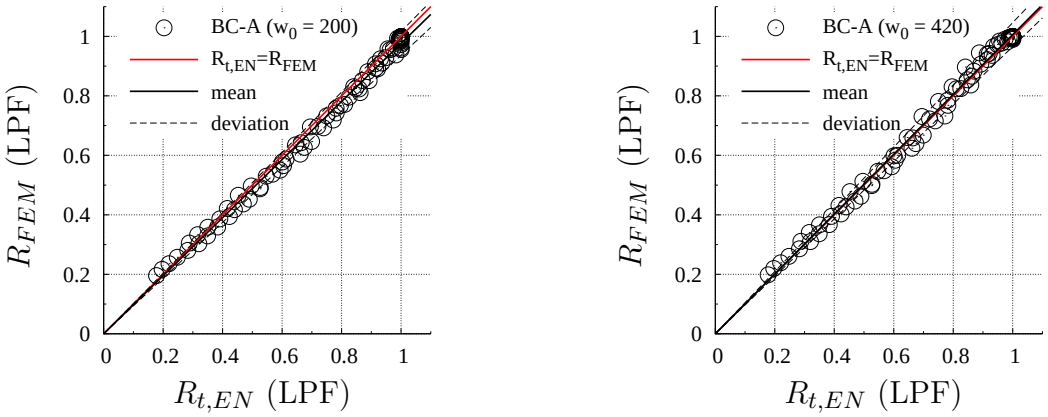

Figure C.3: Statistical comparison of the numerical results with the current design rules in EN 1993-1-5 [37], (BC-A, $\alpha = 1$, all edges hinged, decisive imperfection).

a) $w_0 = b/200$ b) $w_0 = b/420$

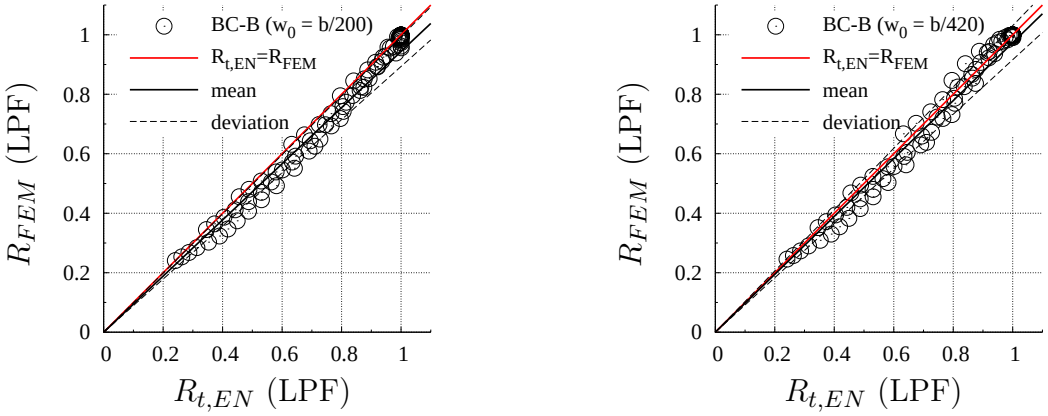

Figure C.4: Statistical comparison of the numerical results with the current design rules in EN 1993-1-5 [37] based on Fig.4.22, (BC-B, $\alpha = 1$, all edges hinged and constrained, decisive imperfection).

a) $w_0 = b/200$ b) $w_0 = b/420$

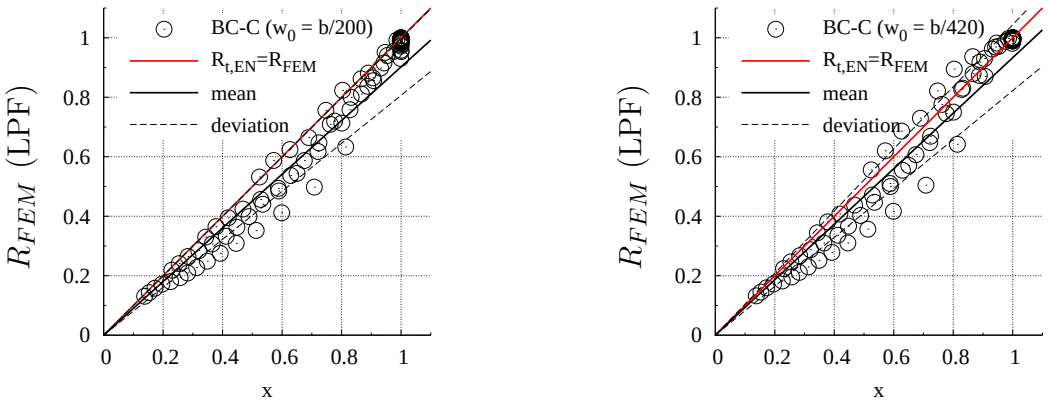

Figure C.5: Statistical comparison of the numerical results with the current design rules in EN 1993-1-5 [37] based on Annex B, (BC-C, $\alpha = 1$, all edges hinged, decisive imperfection).

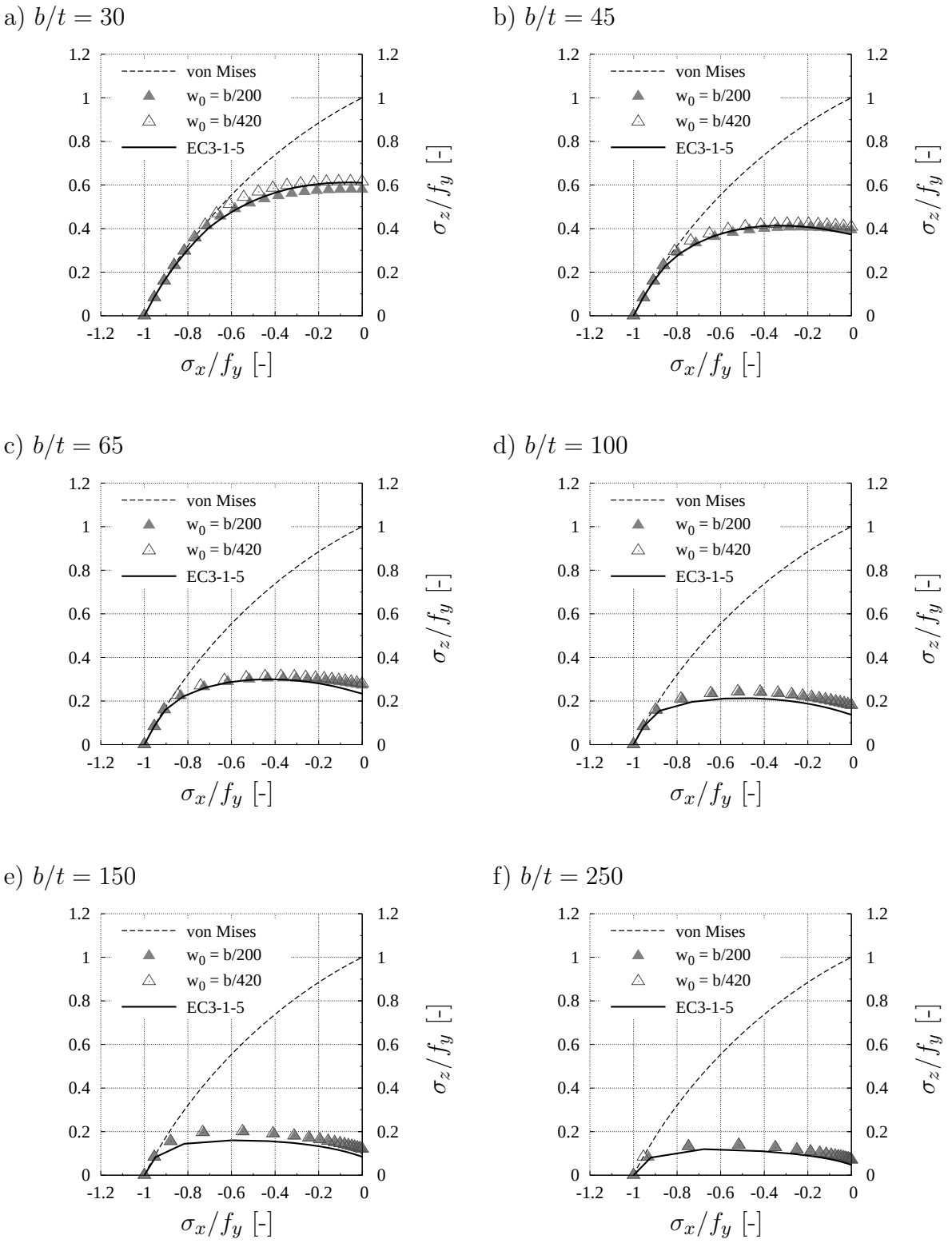

Figure C.6: Comparison of the numerical results with the current design rules in EN 1993-1-5 [37], (BC-A, $\alpha = 3$, all edges hinged, compression applied on long edge).

a) $b/t = 30$

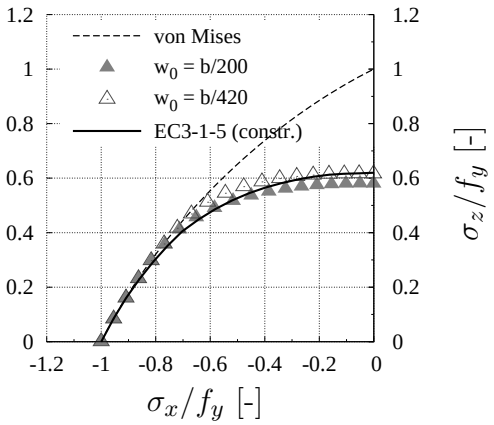

b) $b/t = 45$

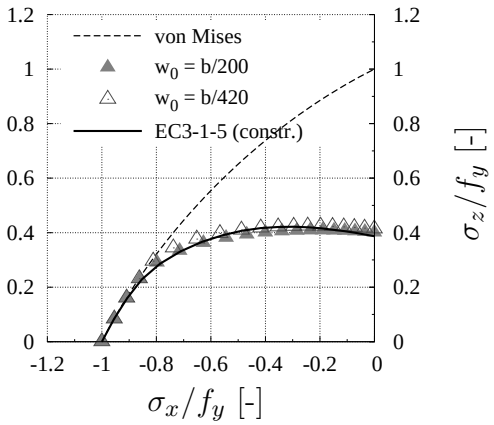

c) $b/t = 65$

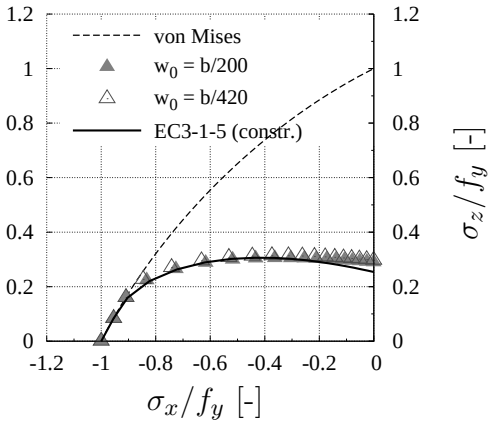

d) $b/t = 100$

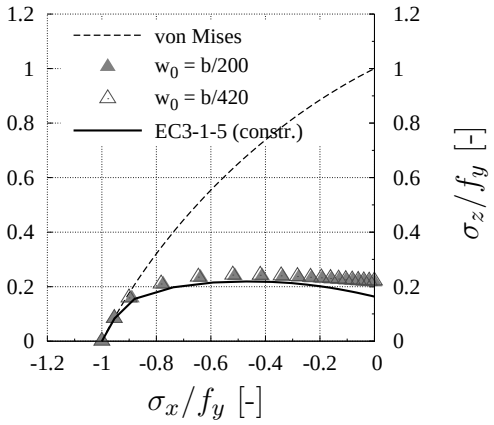

e) $b/t = 150$

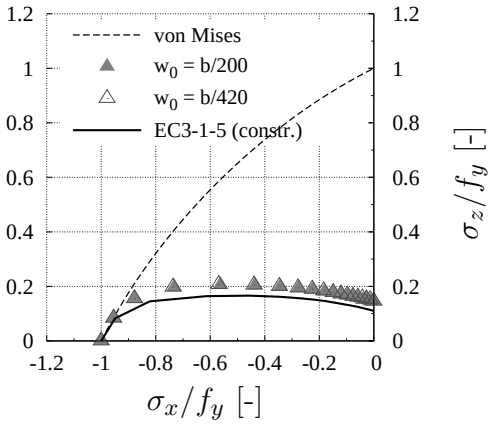

f) $b/t = 250$

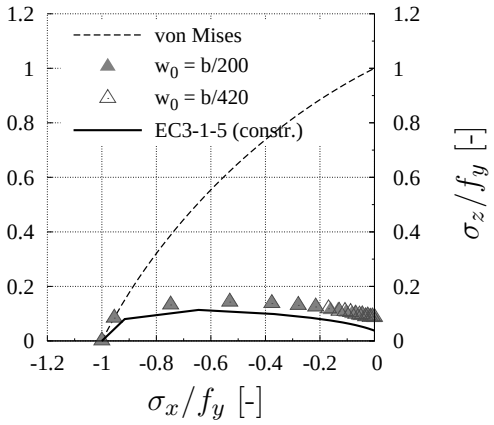

Figure C.7: Comparison of the numerical results with the current design rules in EN 1993-1-5 [37] based on Fig.4.22, (BC-B, $\alpha = 3$, all edges hinged and constrained, compression applied on long edge).

C.2 Plates subjected to direct and shear stress

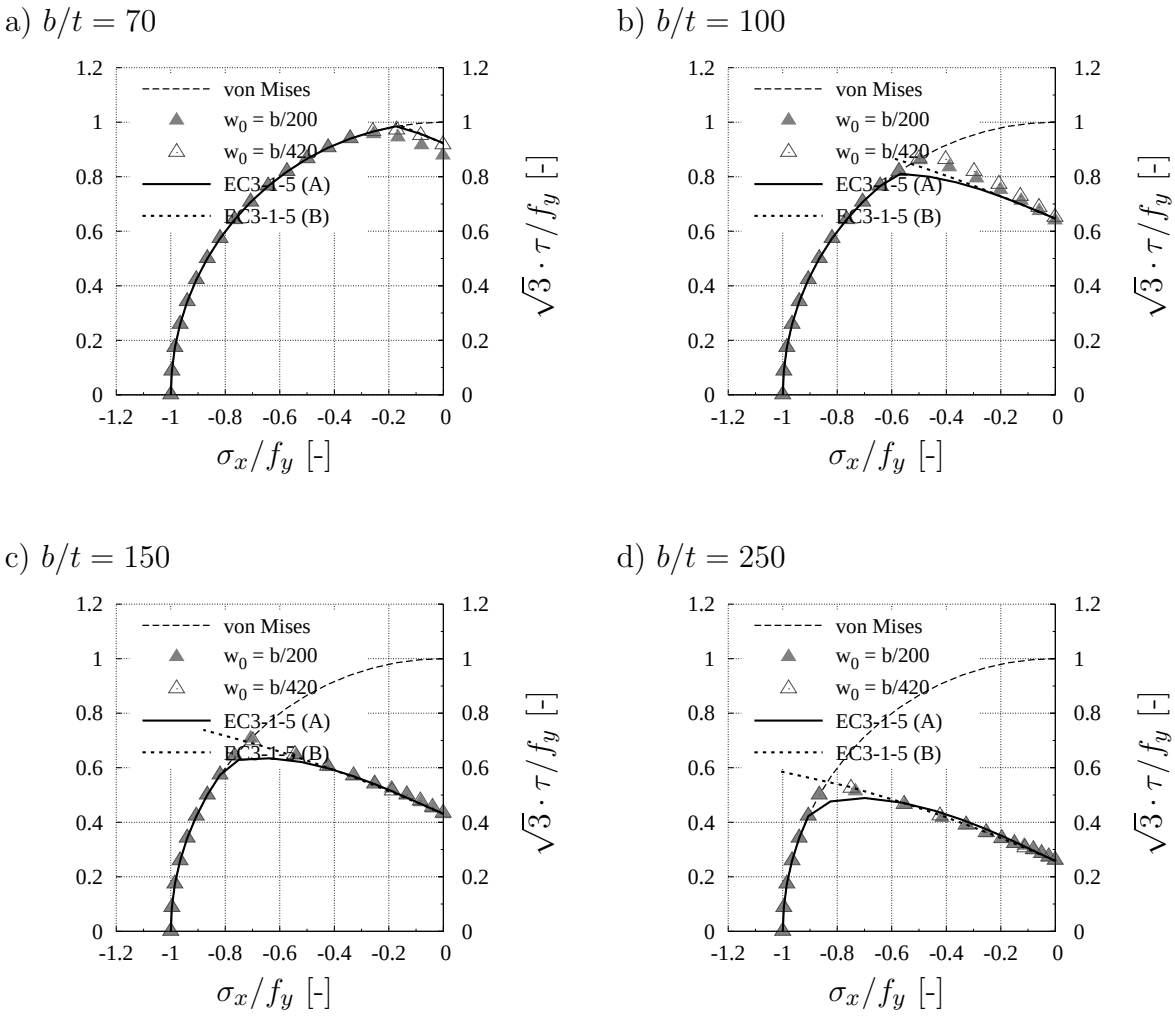

Figure C.8: Comparison of the numerical results with the current design rules in EN 1993-1-5 [37], (BC-A, $\psi = 0.5$, $\alpha = 2$, all edges hinged, interpretation A and B according to Fig.2.26).

a) $b/t = 70$

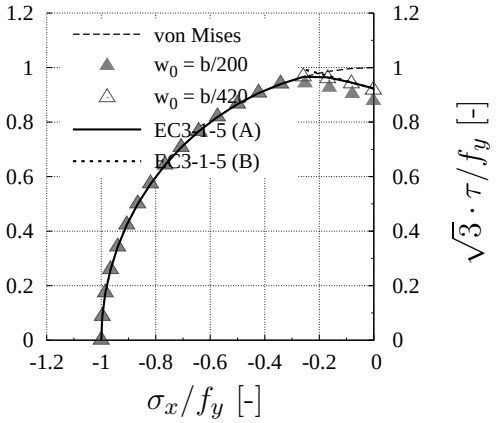

b) $b/t = 100$

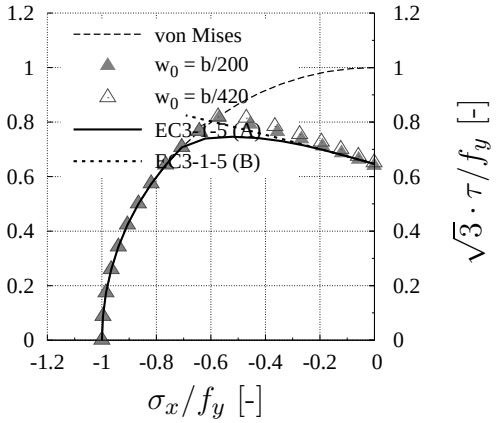

c) $b/t = 150$

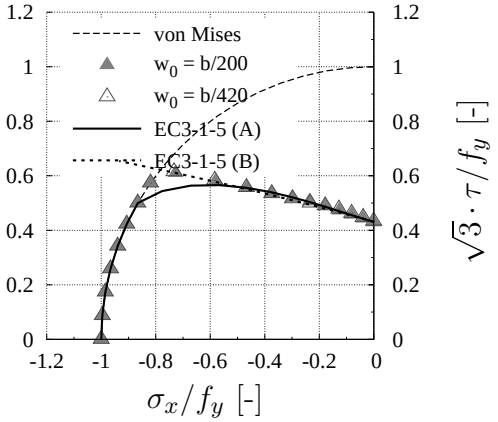

d) $b/t = 250$

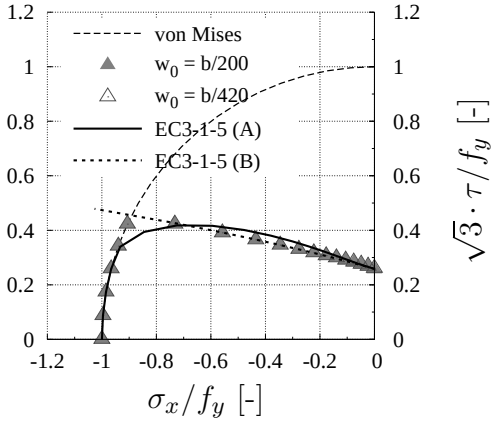

Figure C.9: Comparison of the numerical results with the current design rules in EN 1993-1-5 [37], (BC-A, $\psi = 0$, $\alpha = 2$, all edges hinged, interpretation A and B according to Fig.2.26).

a) $b/t = 60$

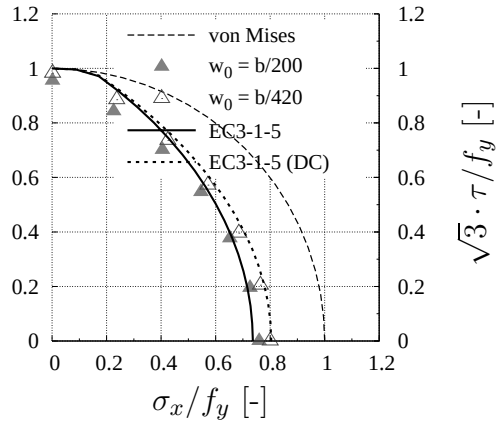

b) $b/t = 70$

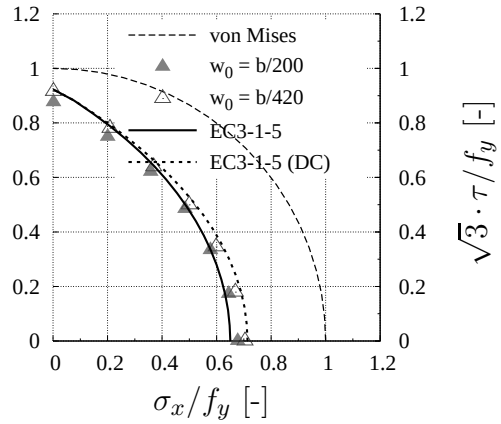

c) $b/t = 100$

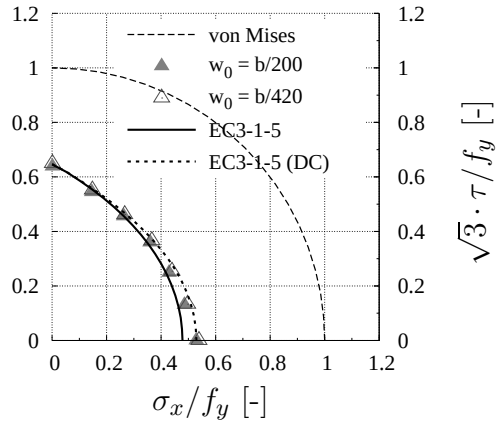

d) $b/t = 150$

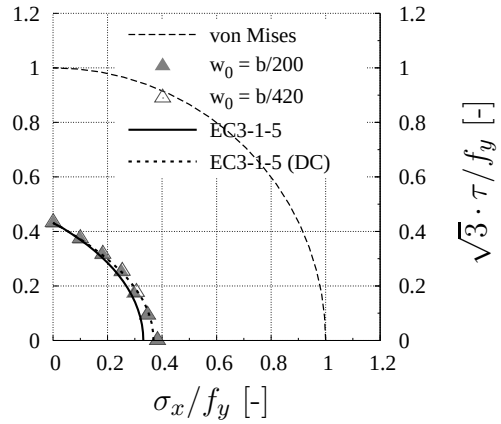

e) $b/t = 250$

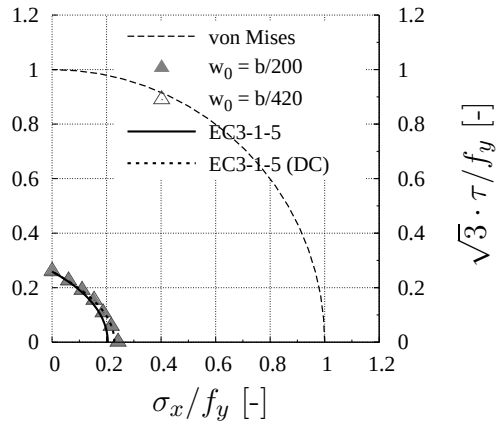

Figure C.10: Comparison of the numerical results with the current design rules in EN 1993-1-5 [37], (BC-A, $\psi = 0.5$, $\alpha = 2$, all edges hinged).

a) $b/t = 60$

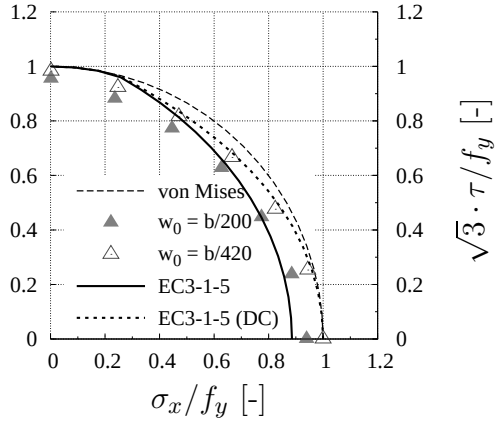

b) $b/t = 70$

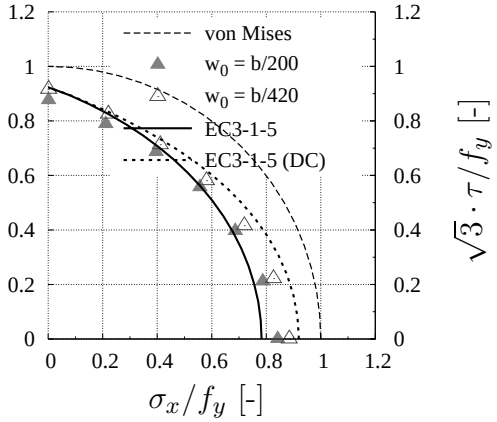

c) $b/t = 100$

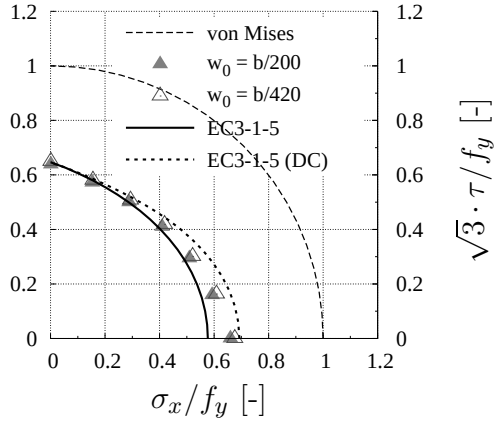

d) $b/t = 150$

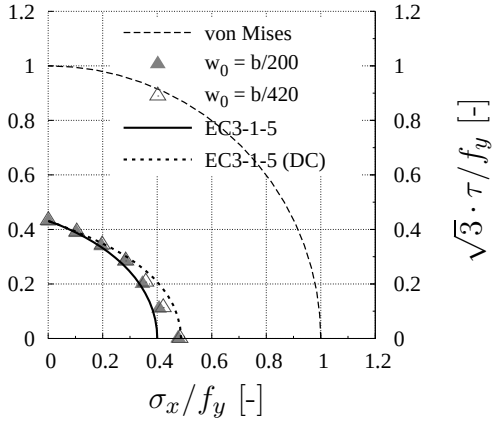

e) $b/t = 250$

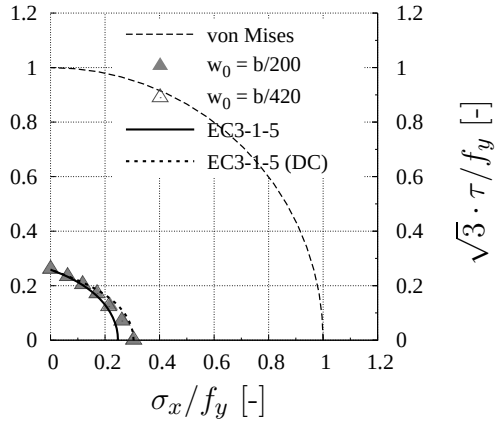

Figure C.11: Comparison of the numerical results with the current design rules in EN 1993-1-5 [37], (BC-A, $\psi = 0$, $\alpha = 2$, all edges hinged).

a) $b/t = 70$

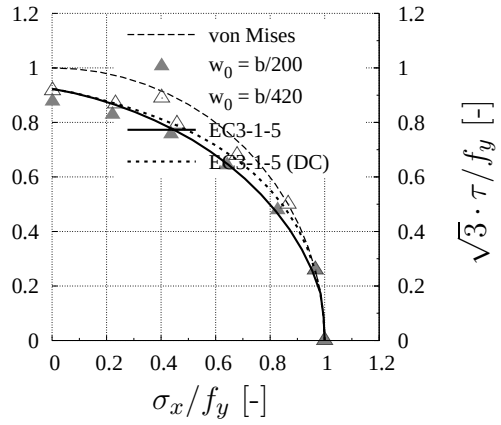

b) $b/t = 100$

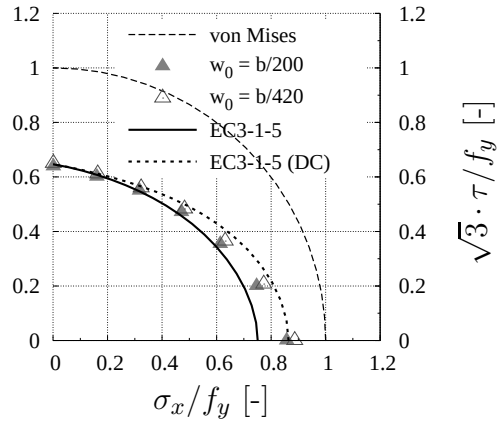

c) $b/t = 150$

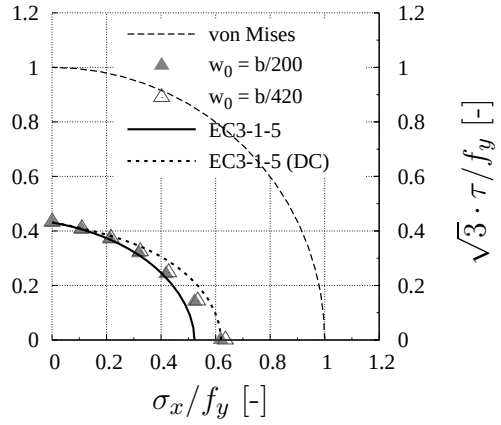

d) $b/t = 250$

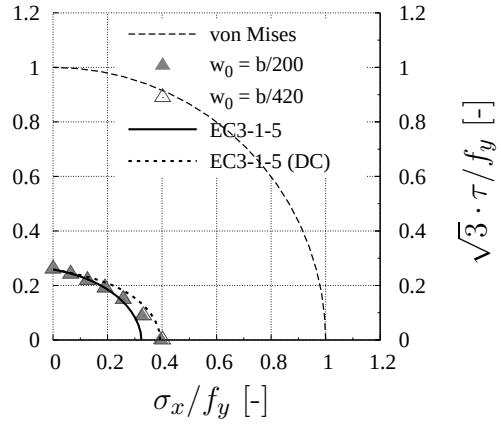

Figure C.12: Comparison of the numerical results with the current design rules in EN 1993-1-5 [37], (BC-A, $\psi = -0.5$, $\alpha = 2$, all edges hinged).

C.3 Stiffened plates under biaxial compression

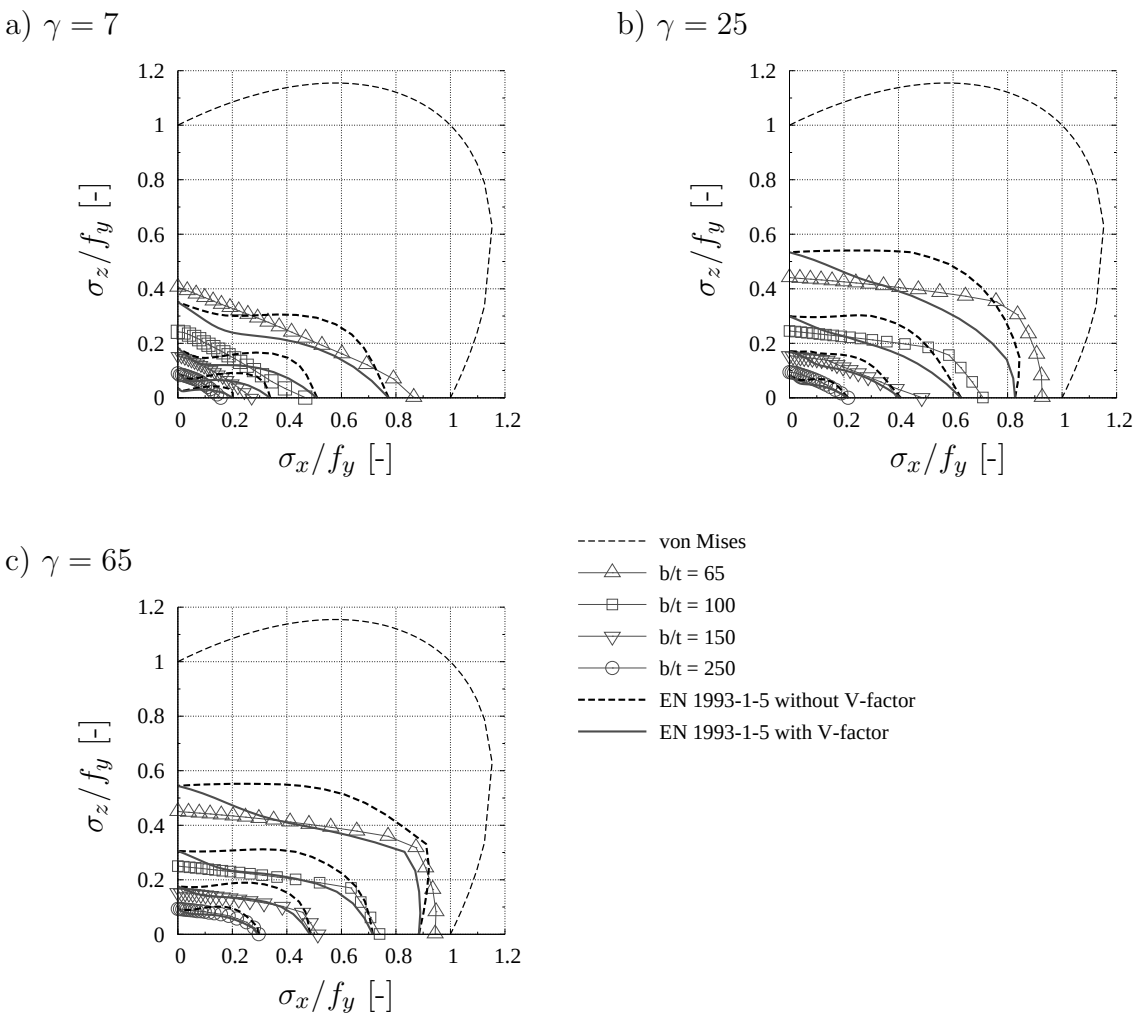

Figure C.13: Comparison of numerical results with current design rules for stiffened plates loaded with biaxial compression, ($\alpha = 1.5$, $n = 1$, $b/t = 65$, 100, 150 and 250).

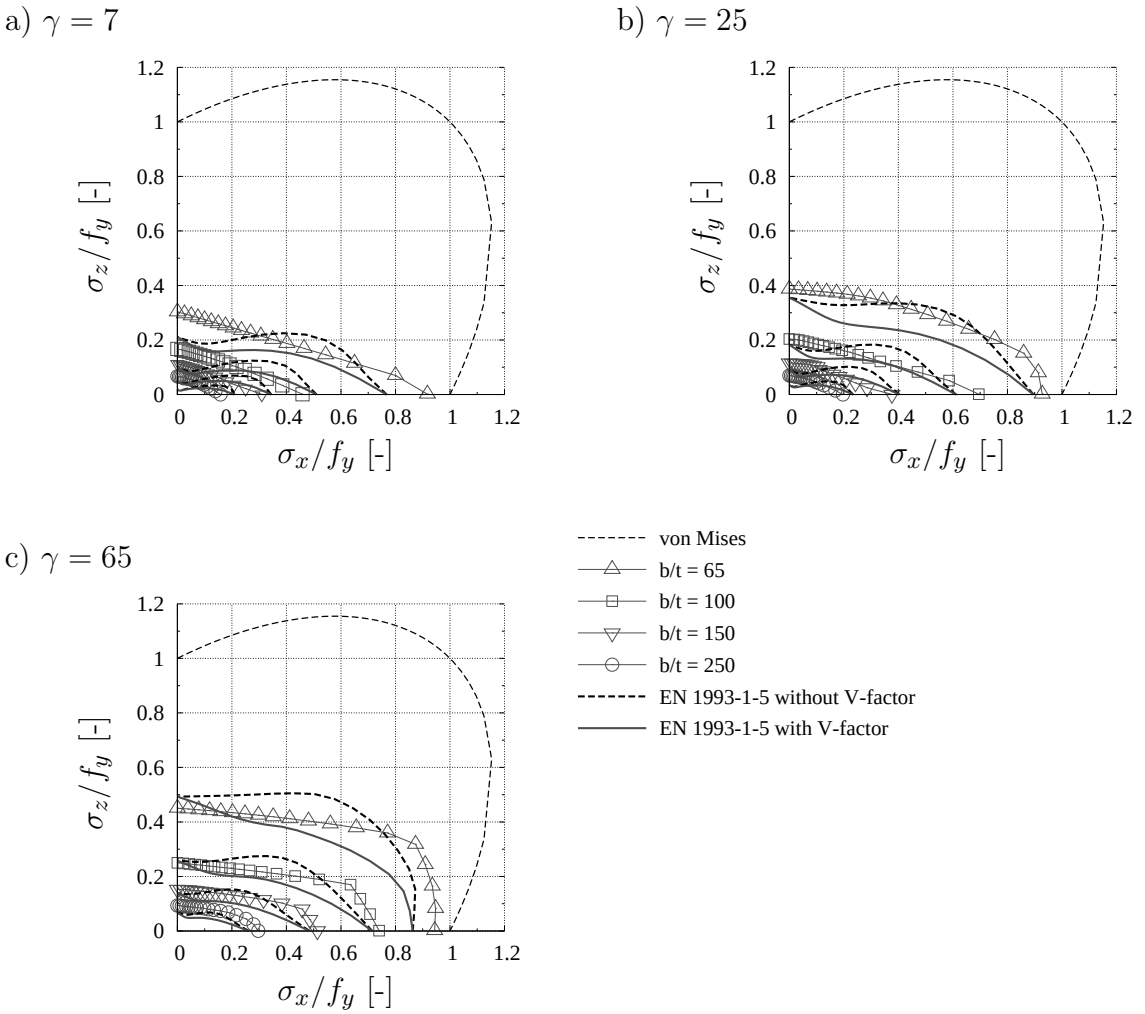

Figure C.14: Comparison of numerical results with current design rules for stiffened plates loaded with biaxial compression, ($\alpha = 2$, $n = 1$, $b/t = 65$, 100, 150 and 250).

a) $\gamma = 7$

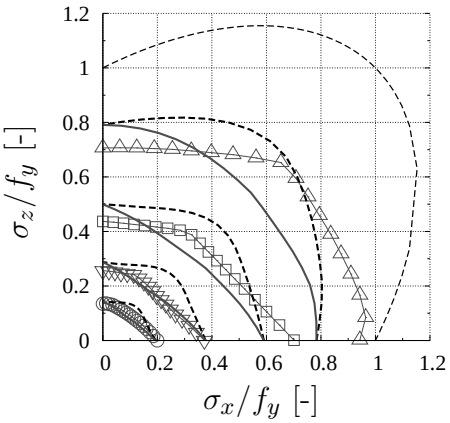

b) $\gamma = 25$

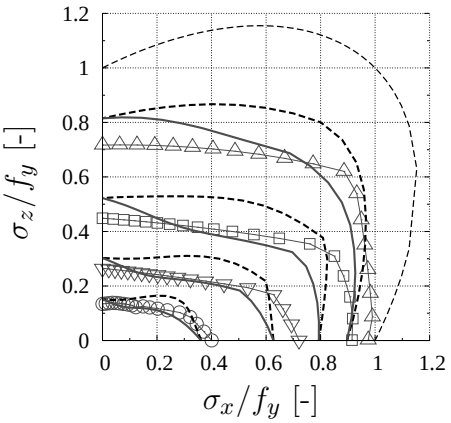

c) $\gamma = 65$

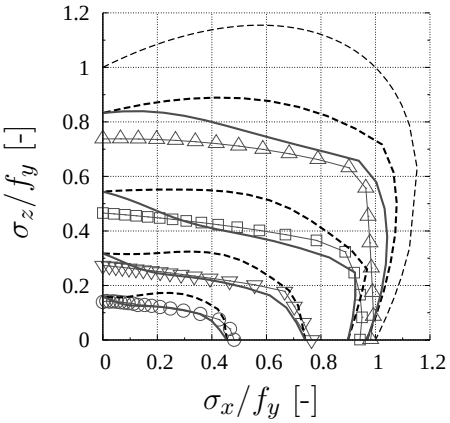

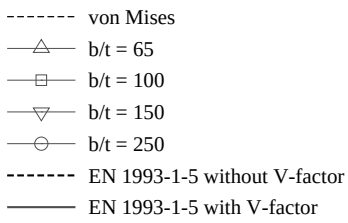

Figure C.15: Comparison of numerical results with current design rules for stiffened plates loaded with biaxial compression, ($\alpha = 1$, $n = 2$, $b/t = 65$, 100, 150 and 250).

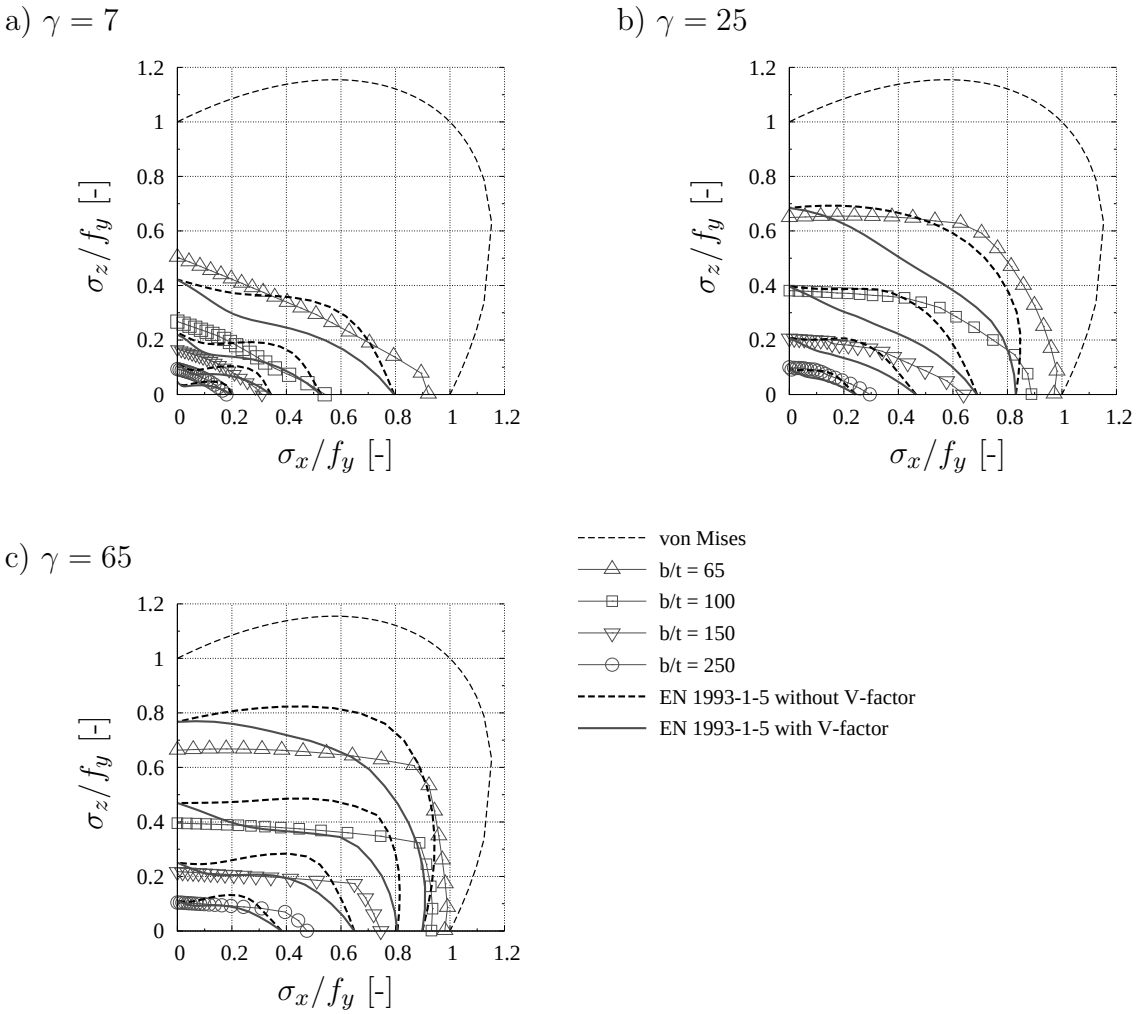

Figure C.16: Comparison of numerical results with current design rules for stiffened plates loaded with biaxial compression, ($\alpha = 1.5$, $n = 2$, $b/t = 65$, 100, 150 and 250).

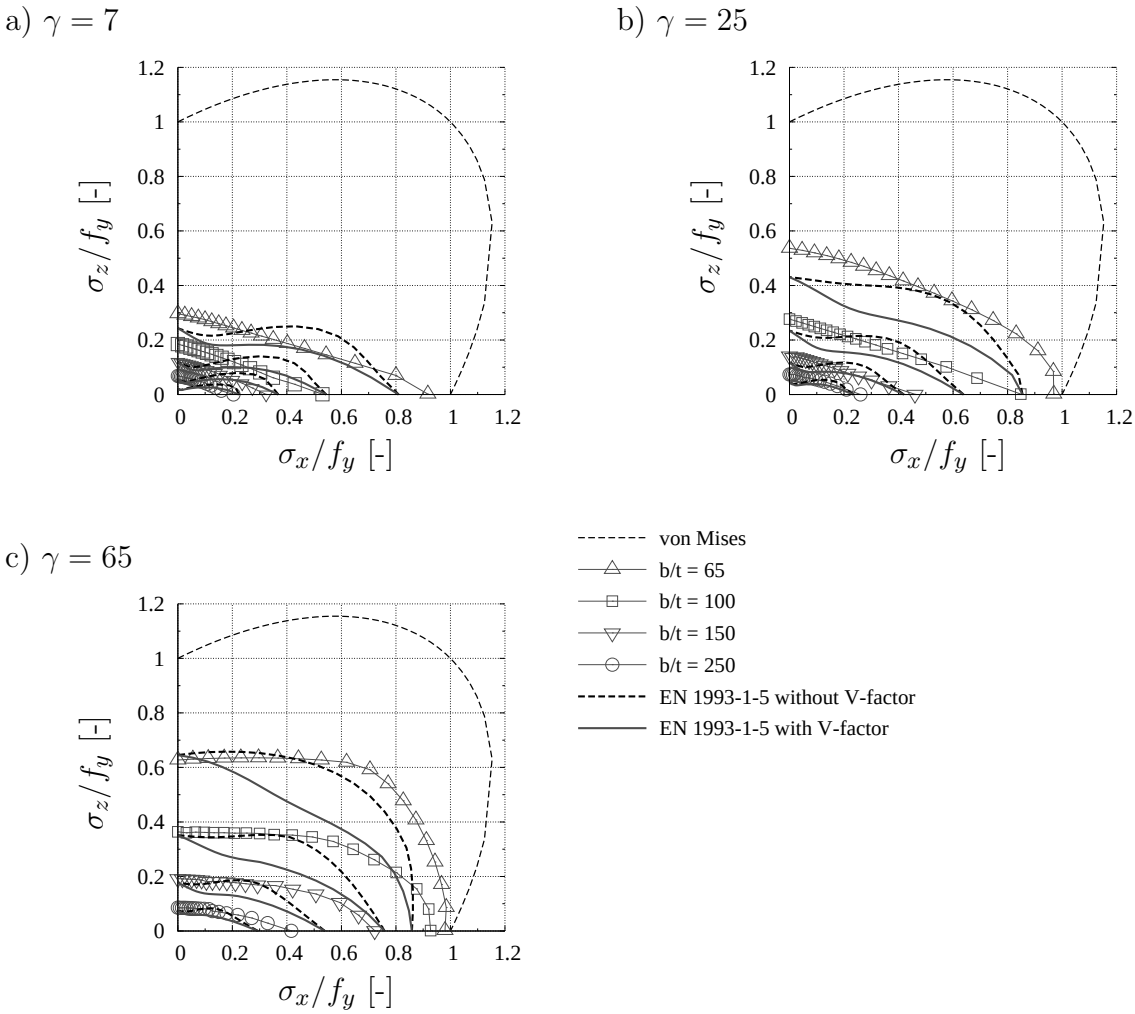

Figure C.17: Comparison of numerical results with current design rules for stiffened plates loaded with biaxial compression, ($\alpha = 2$, $n = 2$, $b/t = 65$, 100, 150 and 250).

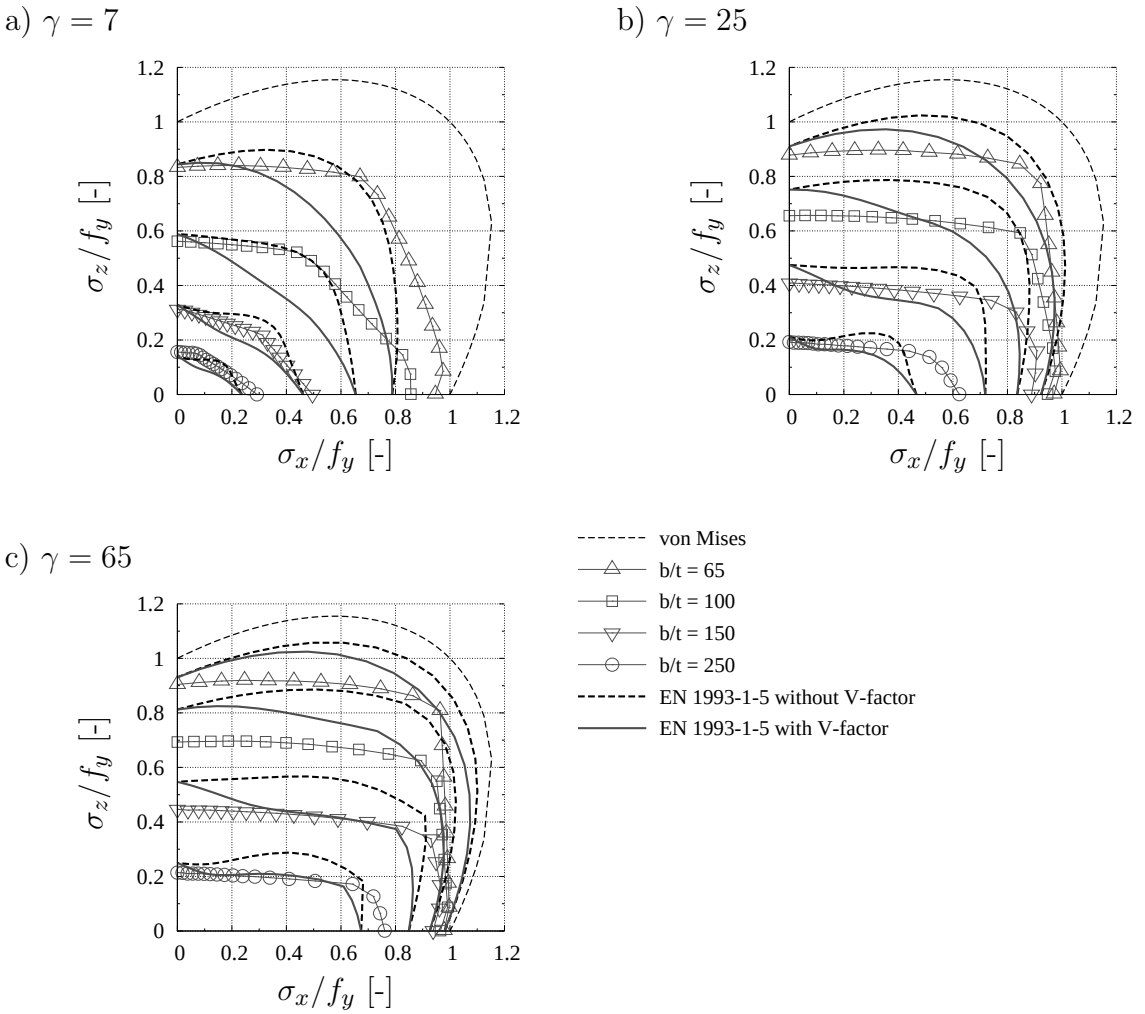

Figure C.18: Comparison of numerical results with current design rules for stiffened plates loaded with biaxial compression, ($\alpha = 1$, $n = 4$, $b/t = 65$, 100, 150 and 250).

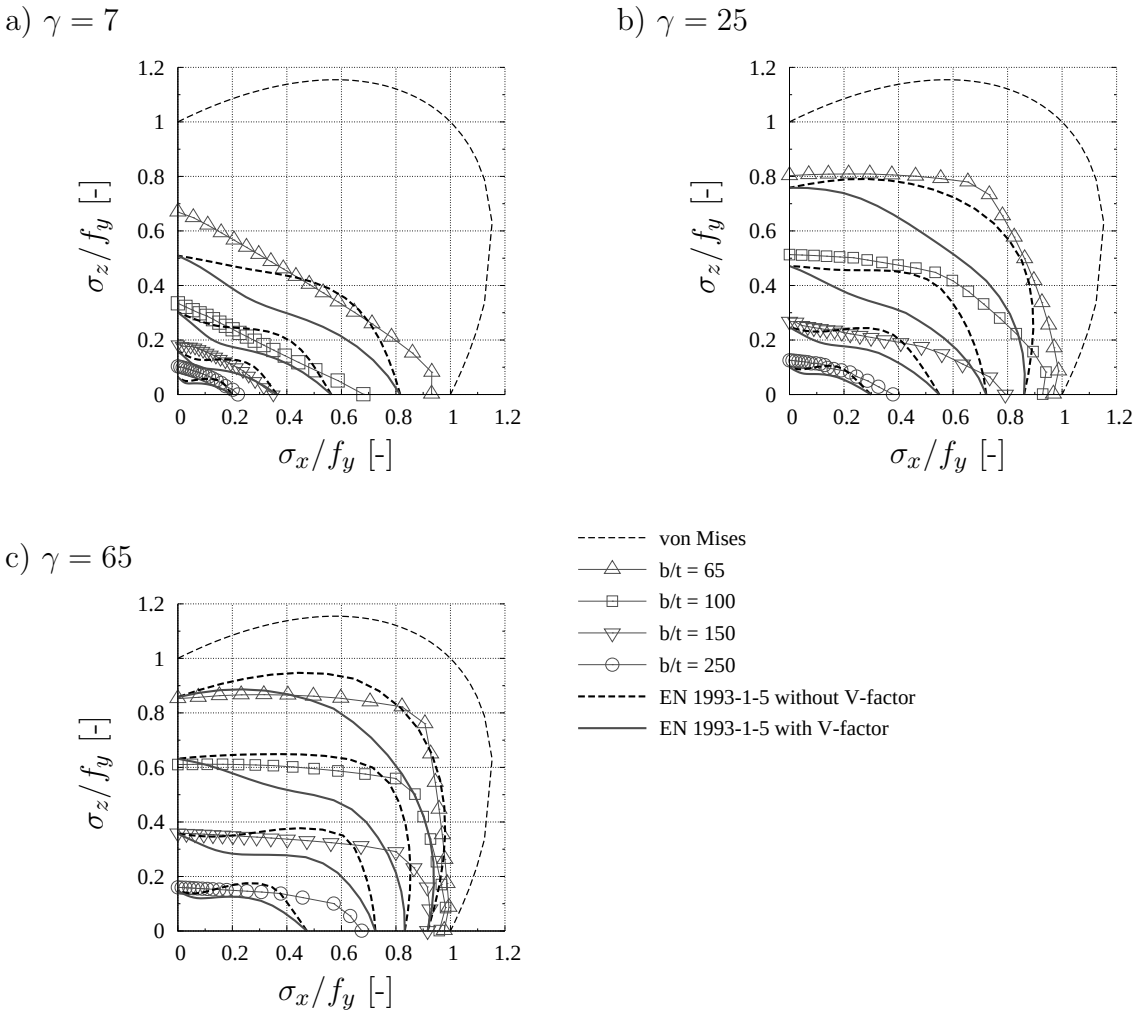

Figure C.19: Comparison of numerical results with current design rules for stiffened plates loaded with biaxial compression, ($\alpha = 1.5$, $n = 4$, $b/t = 65$, 100, 150 and 250).

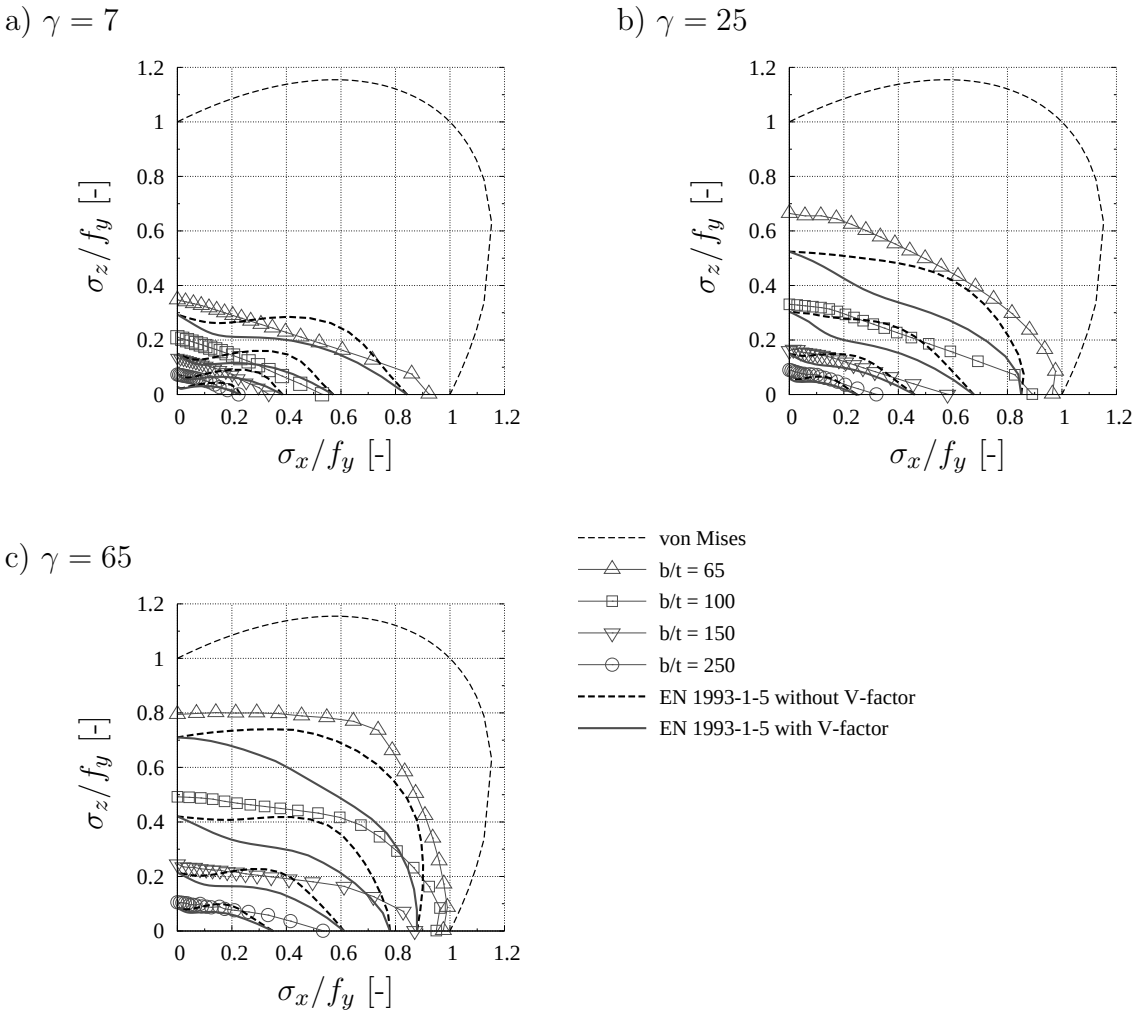

Figure C.20: Comparison of numerical results with current design rules for stiffened plates loaded with biaxial compression, ($\alpha = 2$, $n = 4$, $b/t = 65$, 100, 150 and 250).

D Comparison of numerical results to new proposal

D.1 Plates subjected to direct stresses

a) $b/t = 45$

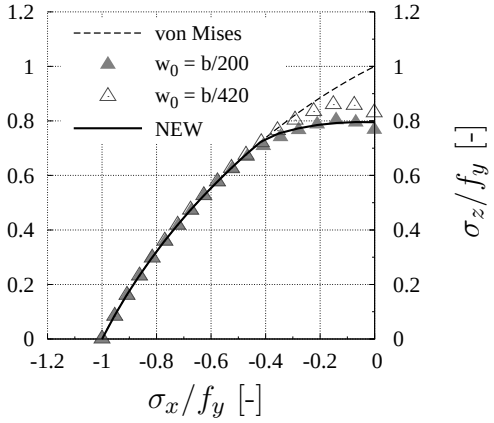

b) $b/t = 65$

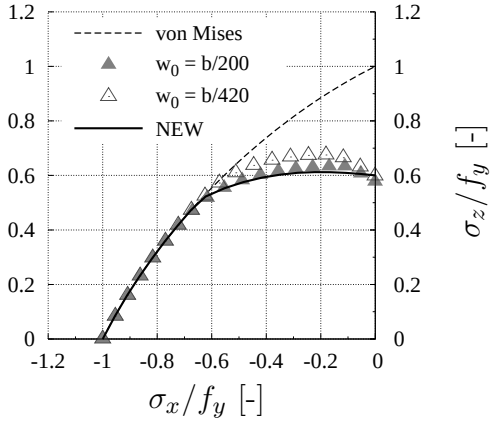

c) $b/t = 100$

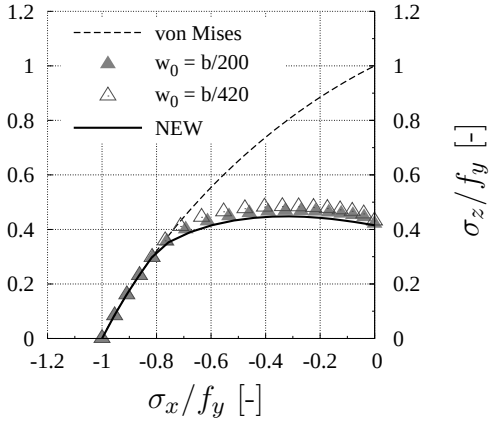

d) $b/t = 150$

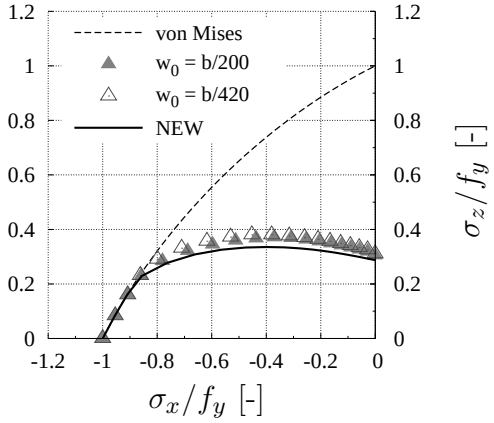

e) $b/t = 250$

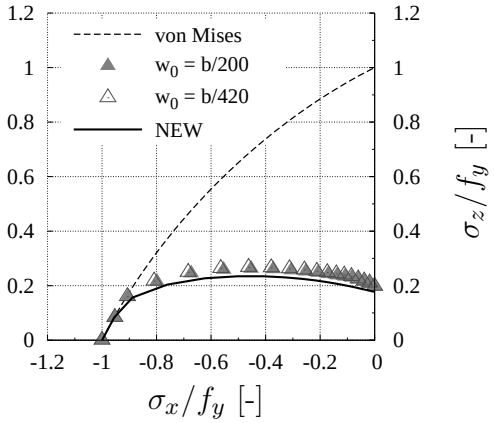

Figure D.1: Comparison of the numerical results with the new proposal, (BC-A, $\alpha = 1$, all edges hinged, decisive imperfection).

a) $b/t = 45$

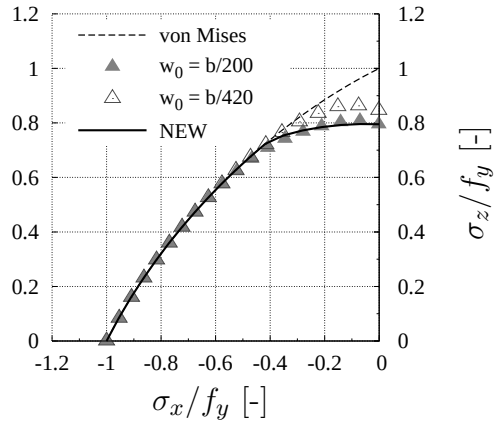

b) $b/t = 65$

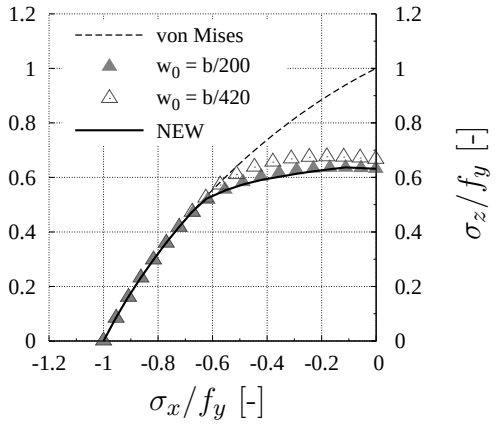

c) $b/t = 100$

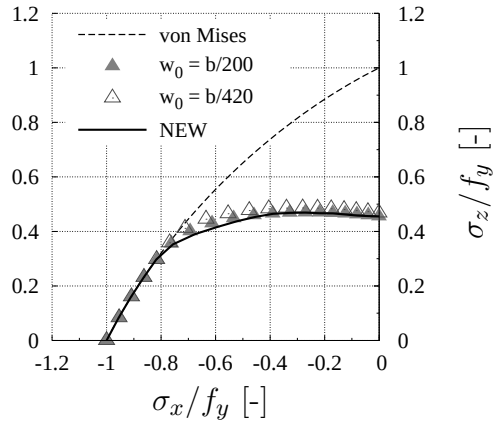

d) $b/t = 150$

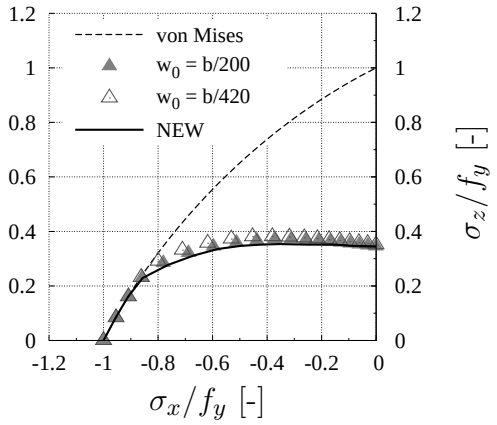

e) $b/t = 250$

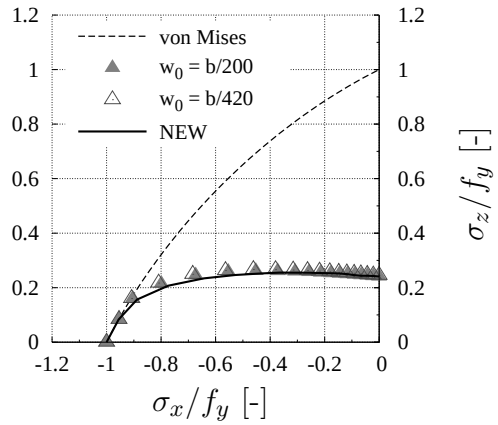

Figure D.2: Comparison of the numerical results with the new proposal, (BC-B, $\alpha = 1$, all edges hinged and constrained, decisive imperfection).

a) $w_0 = b/200$ b) $w_0 = b/420$

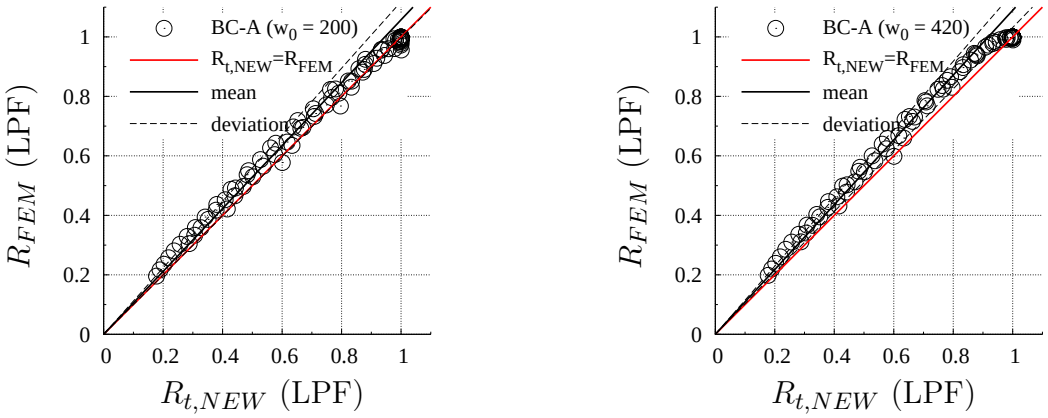

Figure D.3: Statistical comparison of the numerical results with the new proposal, (BC-A, $\alpha = 1$, all edges hinged, decisive imperfection).

a) $w_0 = b/200$ b) $w_0 = b/420$

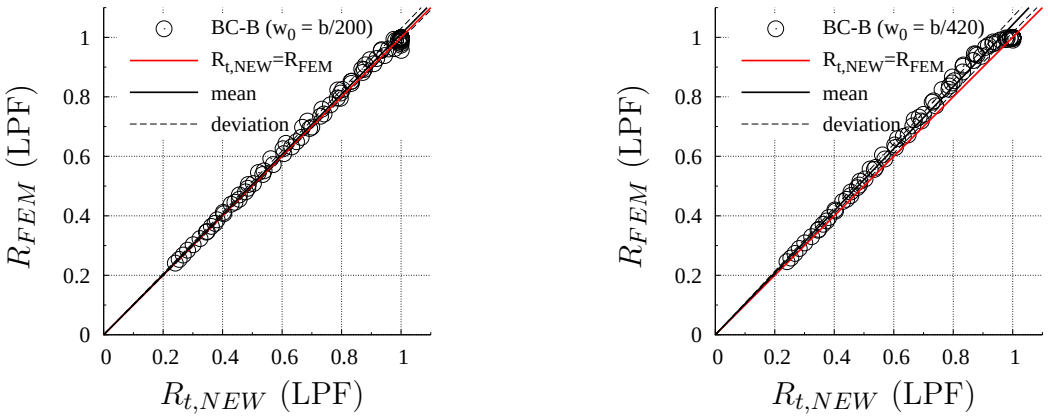

Figure D.4: Statistical comparison of the numerical results with the new proposal, (BC-B, $\alpha = 1$, all edges hinged and constrained, decisive imperfection).

a) $w_0 = b/200$ b) $w_0 = b/420$

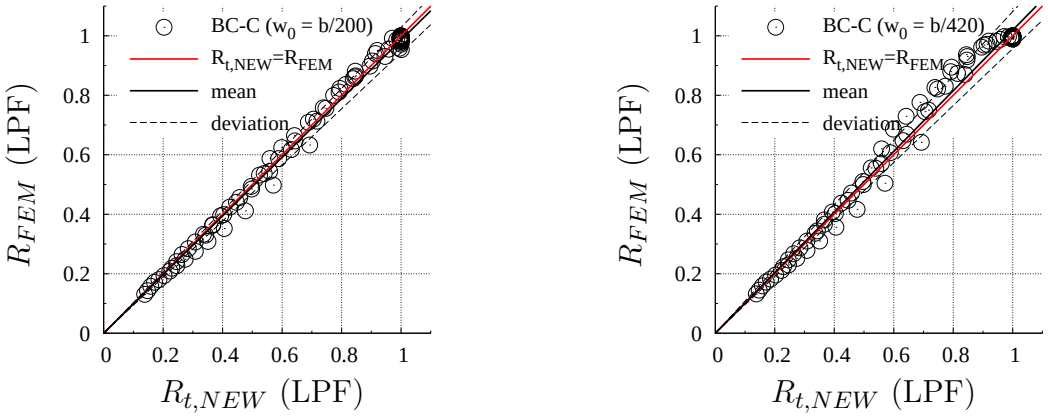

Figure D.5: Statistical comparison of the numerical results with the new proposal based on Annex B, (BC-C, $\alpha = 1$, all edges hinged, decisive imperfection).

a) $b/t = 30$

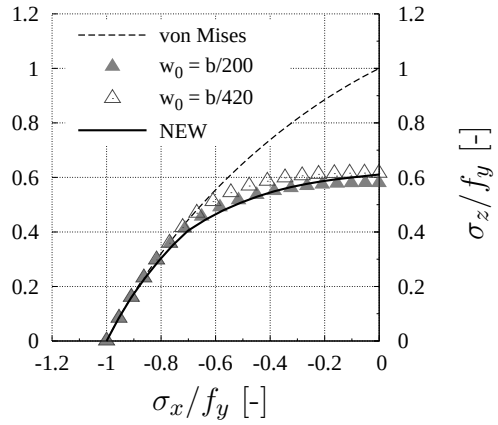

b) $b/t = 45$

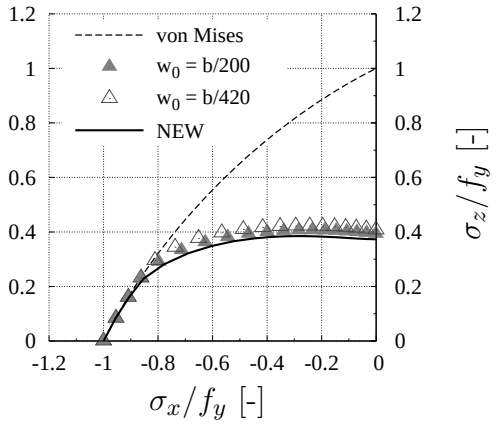

c) $b/t = 65$

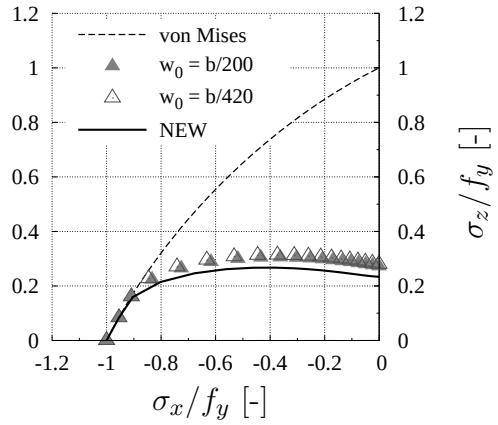

d) $b/t = 100$

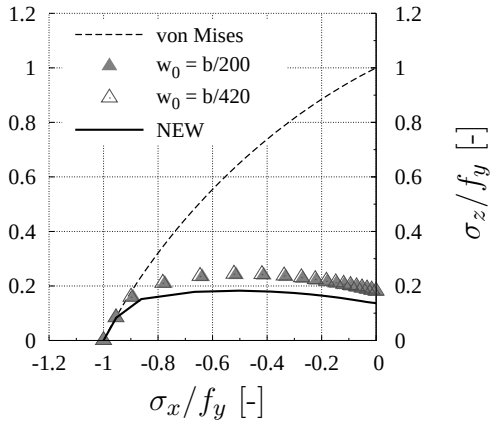

e) $b/t = 150$

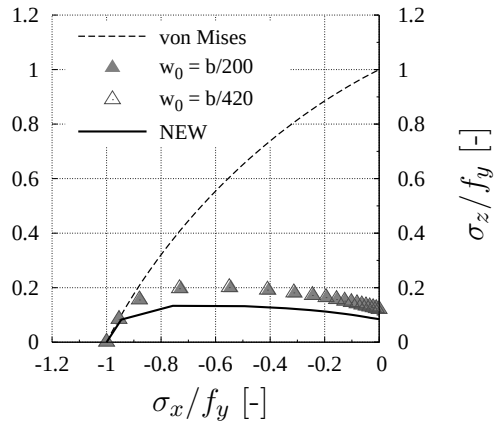

f) $b/t = 250$

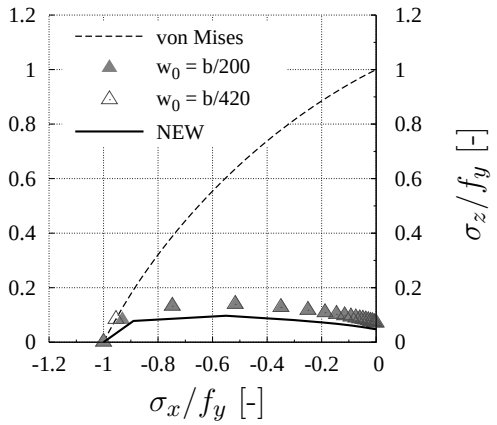

Figure D.6: Comparison of the numerical results with the new proposal, (BC-A, $\alpha = 3$, all edges hinged, compression applied on long edge).

a) $b/t = 30$

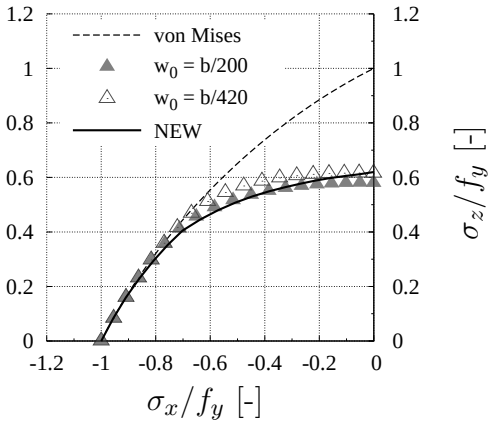

b) $b/t = 45$

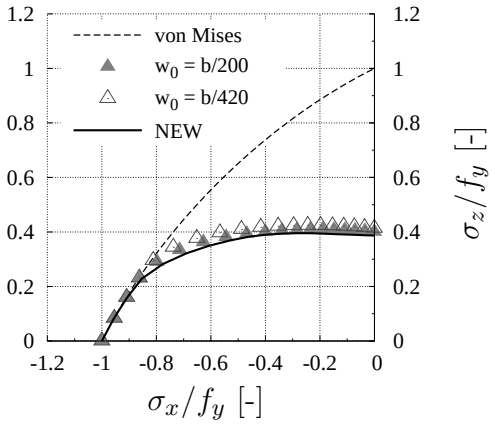

c) $b/t = 65$

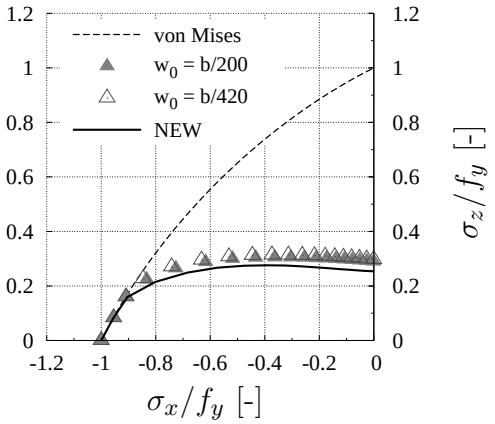

d) $b/t = 100$

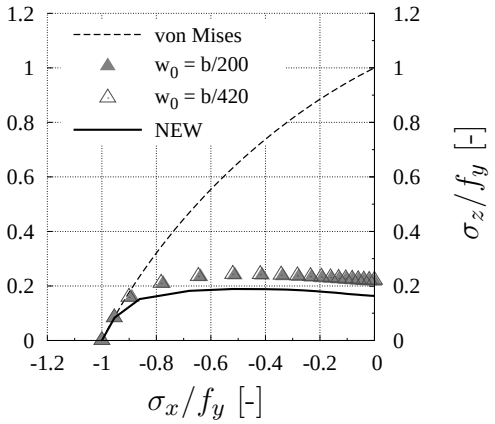

e) $b/t = 150$

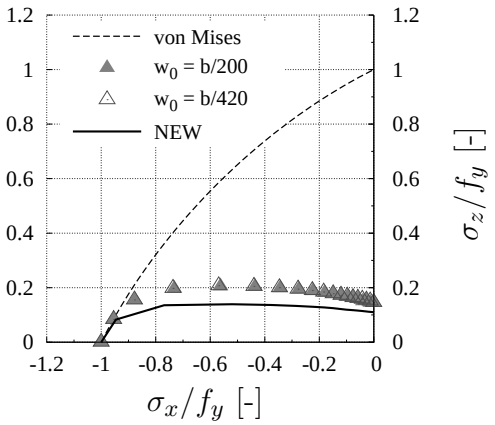

f) $b/t = 250$

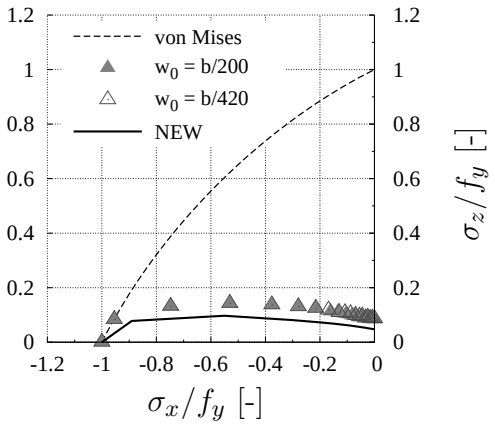

Figure D.7: Comparison of the numerical results with the new proposal, (BC-B, $\alpha = 3$, all edges hinged and restrained, compression applied on long edge).

D.2 Plates subjected to direct and shear stress

a) $b/t = 60$

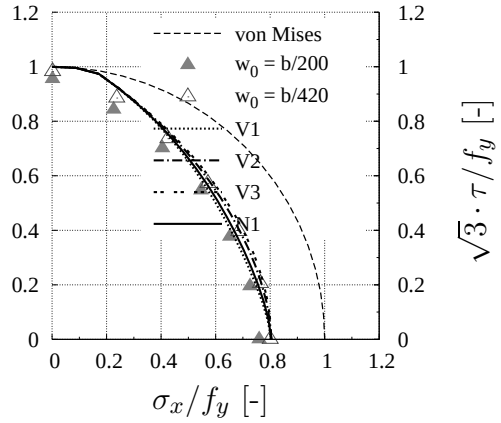

b) $b/t = 70$

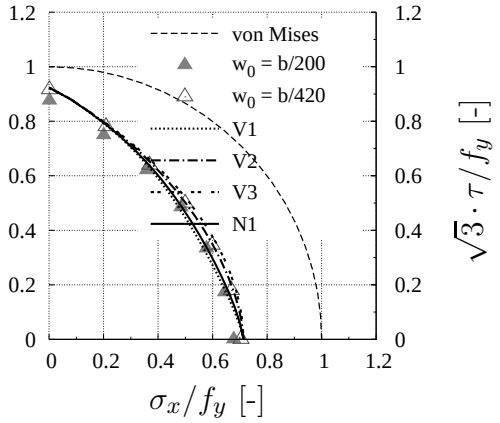

c) $b/t = 100$

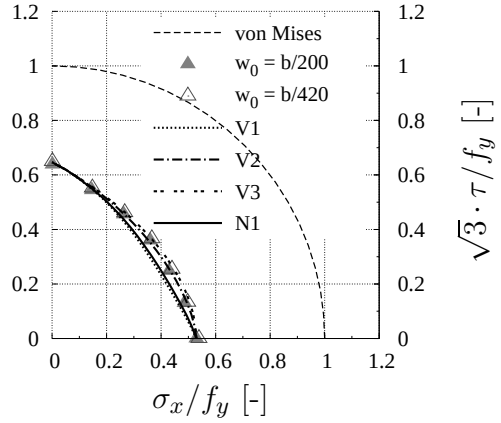

d) $b/t = 150$

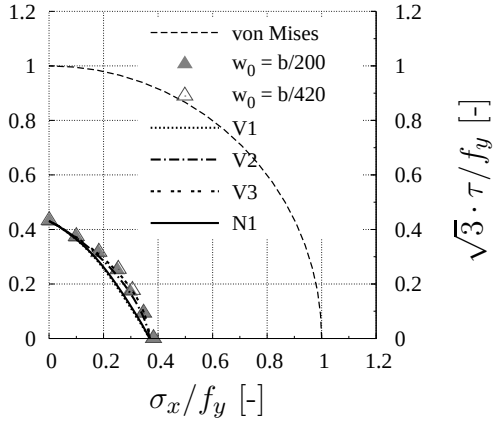

d) $b/t = 250$

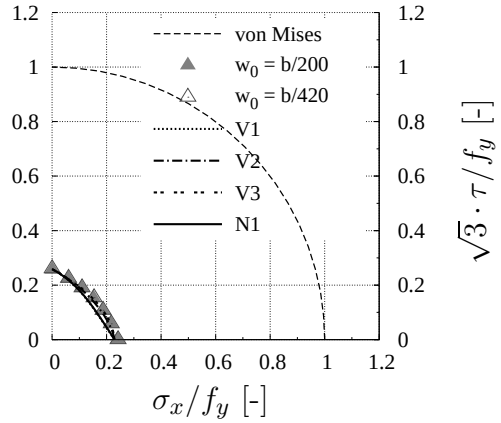

Figure D.8: Comparison of the numerical results with the different approaches for factor e_3, (BC-A, $\psi = 0.5$, $\alpha = 2$, all edges hinged).

a) $b/t = 60$

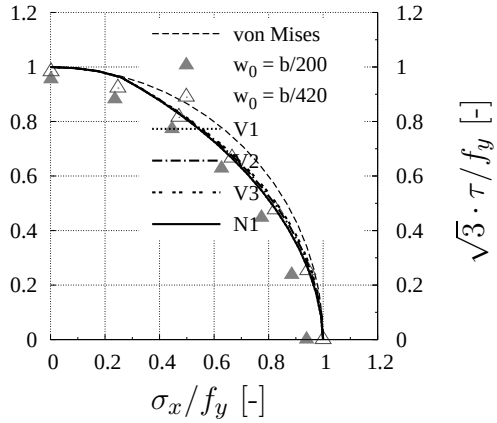

b) $b/t = 70$

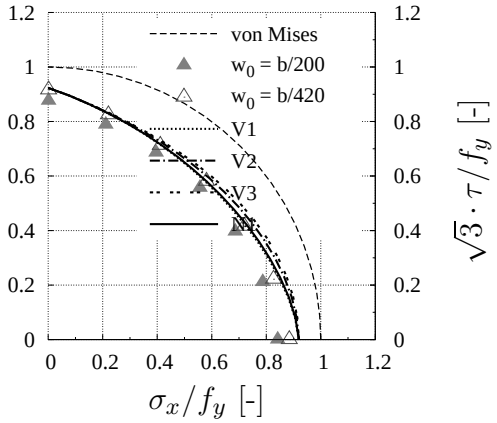

c) $b/t = 100$

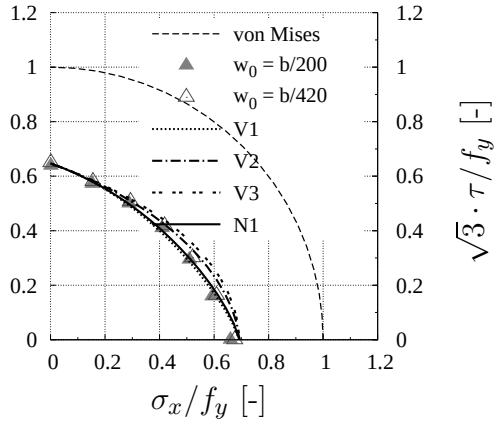

d) $b/t = 150$

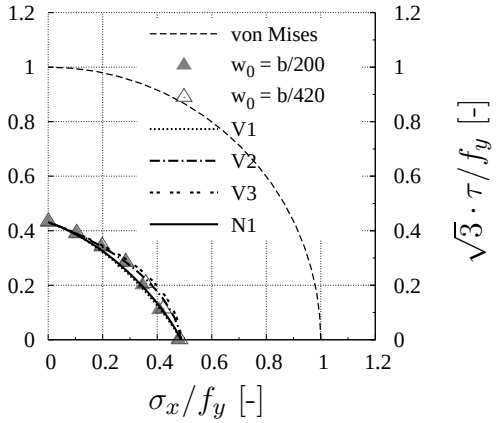

d) $b/t = 250$

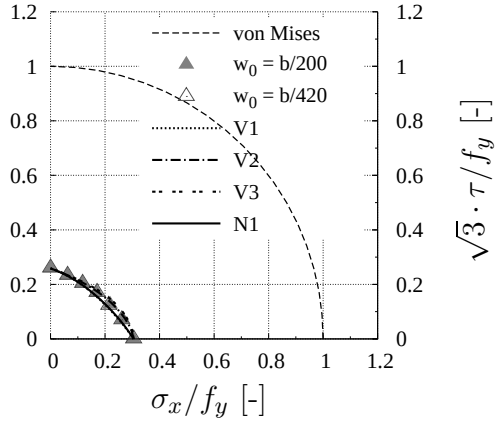

Figure D.9: Comparison of the numerical results with the different approaches for factor e_3, (BC-A, $\psi = 0$, $\alpha = 2$, all edges hinged).

a) $b/t = 70$

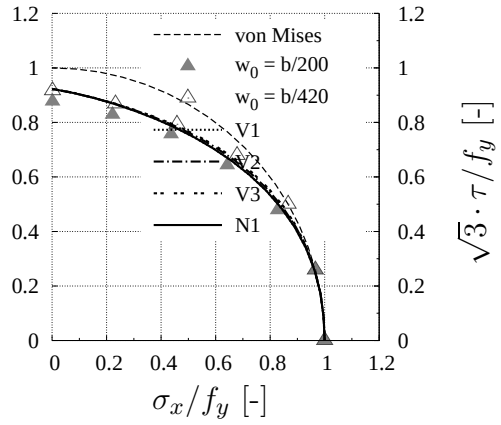

b) $b/t = 100$

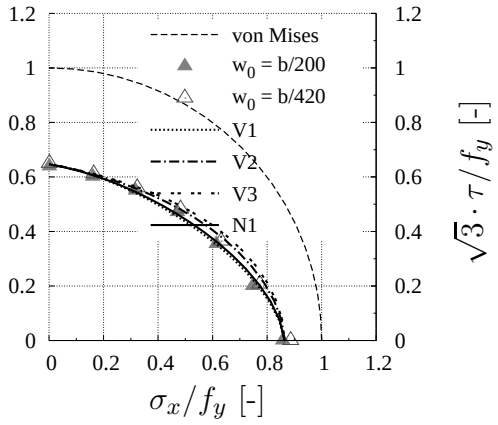

c) $b/t = 150$

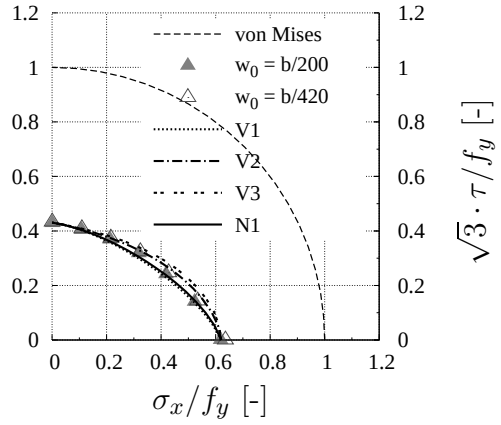

d) $b/t = 250$

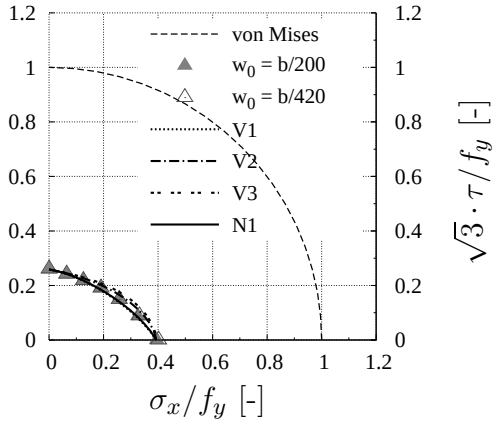

Figure D.10: Comparison of the numerical results with the different approaches for factor e_3, (BC-A, $\psi = -0.5$, $\alpha = 2$, all edges hinged).

E Improvement of EN 1993-1-5

In addition to the proposed changes from Braun [11] the following improvement is proposed to take into account the positive effect of tensile stresses on the buckling behaviour of slender plates as well as the more beneficent buckling curves according to DIN 18800-3 [22] in case of bending action. Furthermore, to highlight the relationship with the von Mises criterion the square root is taken for the whole term and the reduction factors contain the index "c" to avoid misinterpretations.

10 Reduced stress method

(2) For unstiffened or stiffened panels subjected to combined stresses $\sigma_{x,Ed}$, $\sigma_{z,Ed}$ and τ_{Ed} the resistance should satisfy:

$$\sqrt{\left(\frac{\sigma_x}{\rho_{c,x}\cdot f_y}\right)^{e_1}+\left(\frac{\sigma_z}{\rho_{c,z}\cdot f_y}\right)^{e_2}-V\cdot\left(\frac{\sigma_x}{\rho_{c,x}\cdot f_y}\right)\cdot\left(\frac{\sigma_z}{\rho_{c,z}\cdot f_y}\right)+\left(\frac{\sqrt{3}\cdot\tau}{\chi_w\cdot f_y}\right)^{e_3}}\leq 1 \tag{E.1}$$

where: $e_1 = e_2 = 2$

$e_3 = 1.25 + 0.75\cdot\chi_w^2$ for the general case, (if the reduction factor ρ_x is determined according to Eq.(E.2), else $e_3 = 2$)

$e_3 = 2$ if σ_x and/or σ_z are/is tension or pure compression

$V = \rho_{c,x}\cdot\rho_{c,z}$, if σ_x and σ_z are both compression

$V = 1/(\rho_{c,x}\cdot\rho_{c,z}^{2-\xi_z})$ if σ_x and/or σ_z are/is tension

$\rho_{c,x}$ is the reduction factor for longitudinal stress from 4.5.4(1) taking into account column–like behaviour where relevant

$\rho_{c,z}$ is the reduction factor for transverse stress from Annex B taking into account column–like behaviour where relevant

χ_w is the reduction factor for shear stress from 5.3(1)

As a more favourable alternative to Eq.(4.2) the reduction factor ρ_x may be determined according to Eq.(E.2).

$$\rho_x = c\cdot\left(\frac{1}{\bar{\lambda}_p}-\frac{0.22}{\bar{\lambda}_p^2}\right)\leq 1 \tag{E.2}$$

where: $c = 1.25 - 0.25\cdot\psi \leq 1.25$

The interpolation for taking into account column–like behaviour in transverse direction is conducted according to:

$$\rho_{c,z} = \chi_{c,z} + (\rho_z - \chi_{c,z})\cdot f \tag{E.3}$$

where: $f = \bar{\lambda}_p^{-0.5}\cdot\ln(\xi_z+1)^{0.9}$ and $\xi_z = \frac{\sigma_{cr,p,z}}{\sigma_{cr,c,z}} - 1$

F Interaction diagrams

In order to give a useful ready to hand tool to the practical engineer for conducting buckling analyses according to the proposal within this work, interaction charts are given in the following for a simplified procedure. The charts are prepared in the German tradition mainly influenced by LINDNER in [70], [72] and [73]. Therein, the regarded plate is simply verified against buckling, if the "existing" b/t–ratio is less or equal to the "limit" b/t–ratio from the respective chart.

The presented charts may be applied if the following requirements are met:

- unstiffened plate
- σ_x–τ diagrams: transverse stress $\sigma_z = 0$, direct stress σ_x and shear stress τ are constant in longitudinal direction and panel aspect ratio $\alpha = a/b \geq 1$
- σ_x–σ_z diagrams: shear stress $\tau = 0$, direct stresses σ_x and σ_z are constant in the respective direction and panel aspect ratio $\alpha = a/b = 1$
- column–like behaviour is not decisive
- the stresses σ_x, σ_z and τ are determined as design loads
- the partial factor $\gamma_{M1} = 1.1$ according to EN 1993-1-5 [36] is considered for the input parameters $\bar{\sigma}$ and $\bar{\tau}$

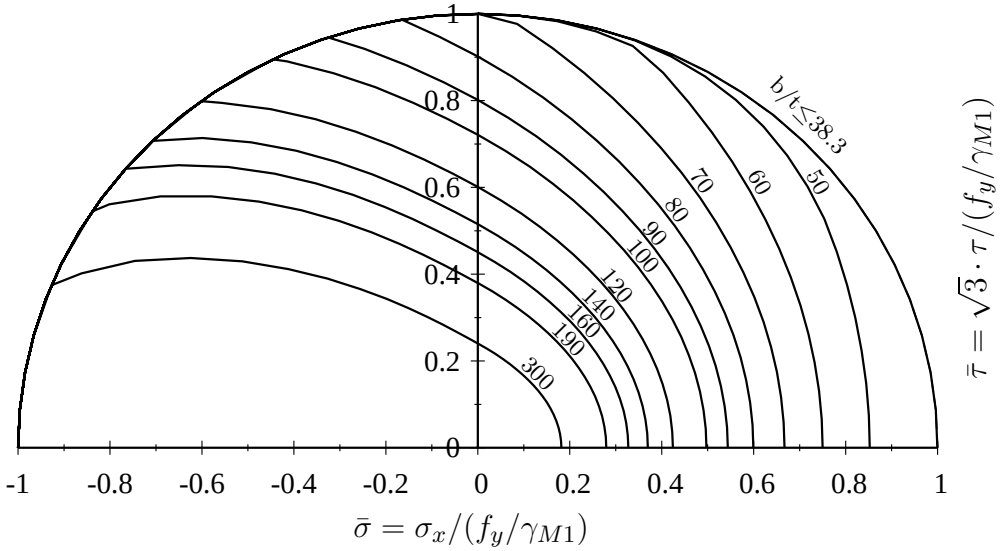

Figure F.1: Limits (b/t), σ_x–τ interaction curves for S 235, $\psi = 1$.

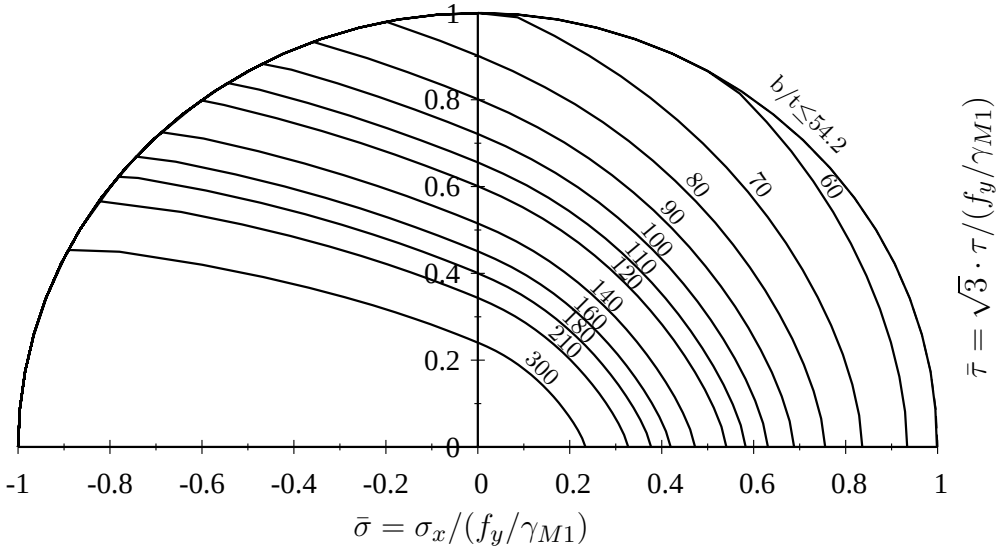

Figure F.2: Limits (b/t), σ_x–τ interaction curves for S 235, $\psi = 0.5$.

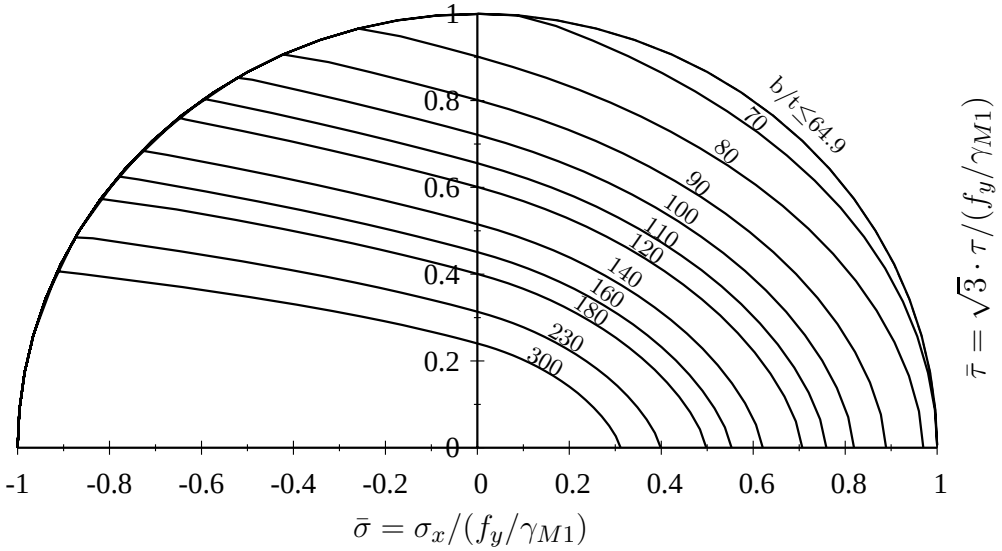

Figure F.3: Limits (b/t), σ_x–τ interaction curves for S 235, $\psi = 0$.

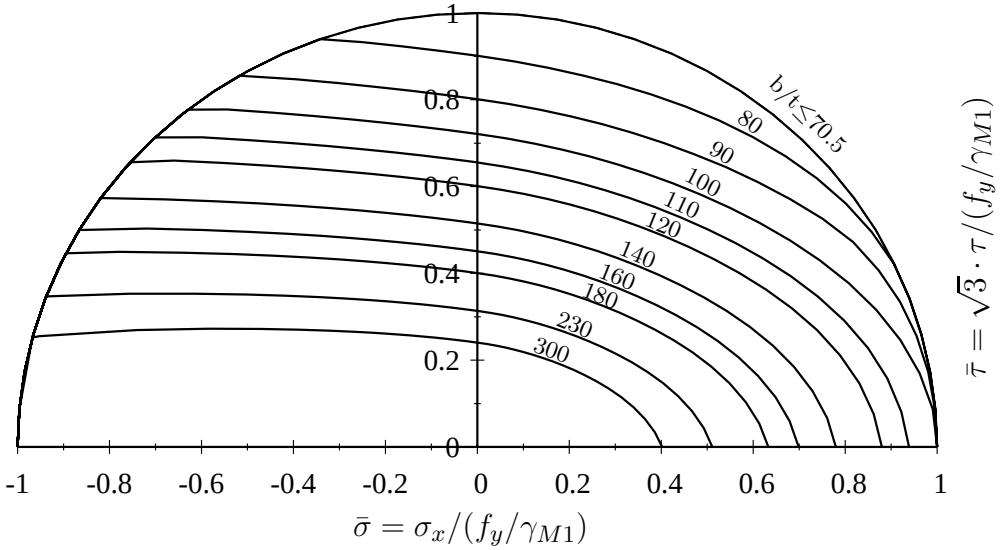

Figure F.4: Limits (b/t), σ_x–τ interaction curves for S 235, $\psi = -0.5$.

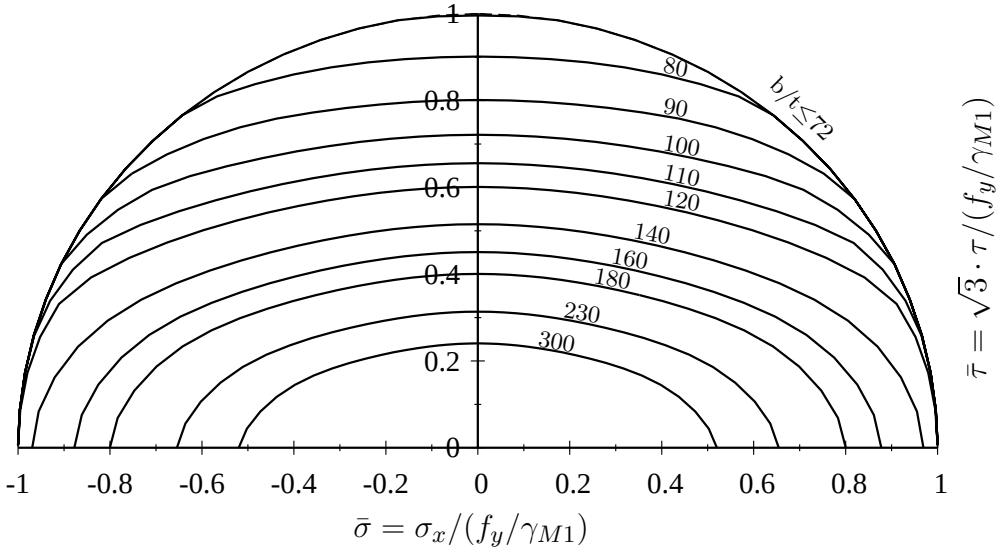

Figure F.5: Limits (b/t), σ_x–τ interaction curves for S 235, $\psi = -1$.

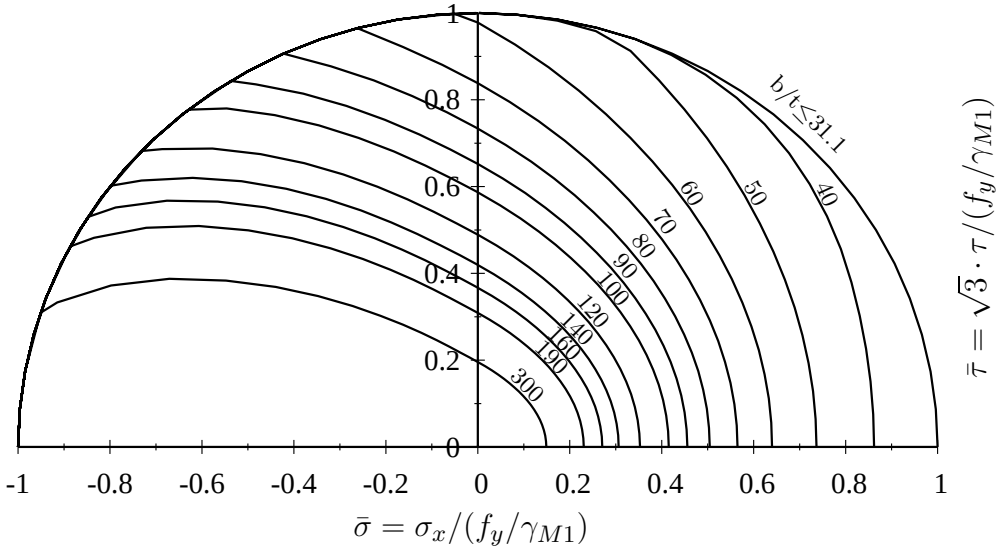

Figure F.6: Limits (b/t), σ_x–τ interaction curves for S 355, $\psi = 1$.

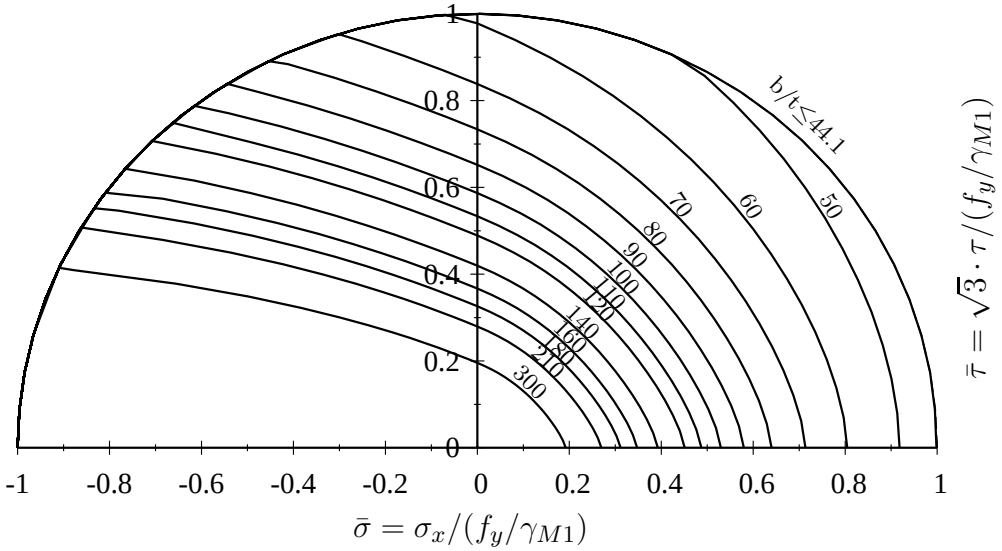

Figure F.7: Limits (b/t), σ_x–τ interaction curves for S 355, $\psi = 0.5$.

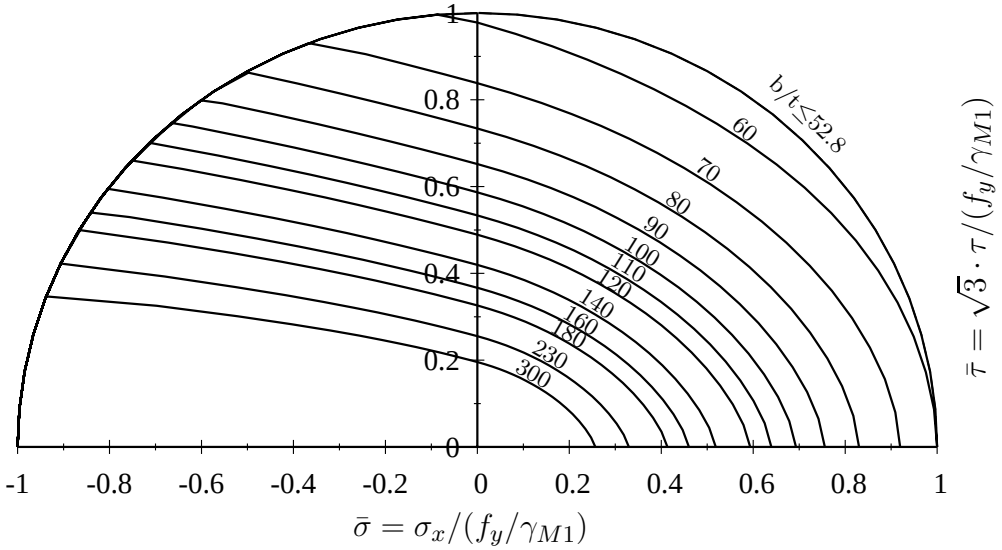

Figure F.8: Limits (b/t), σ_x–τ interaction curves for S 355, $\psi = 0$.

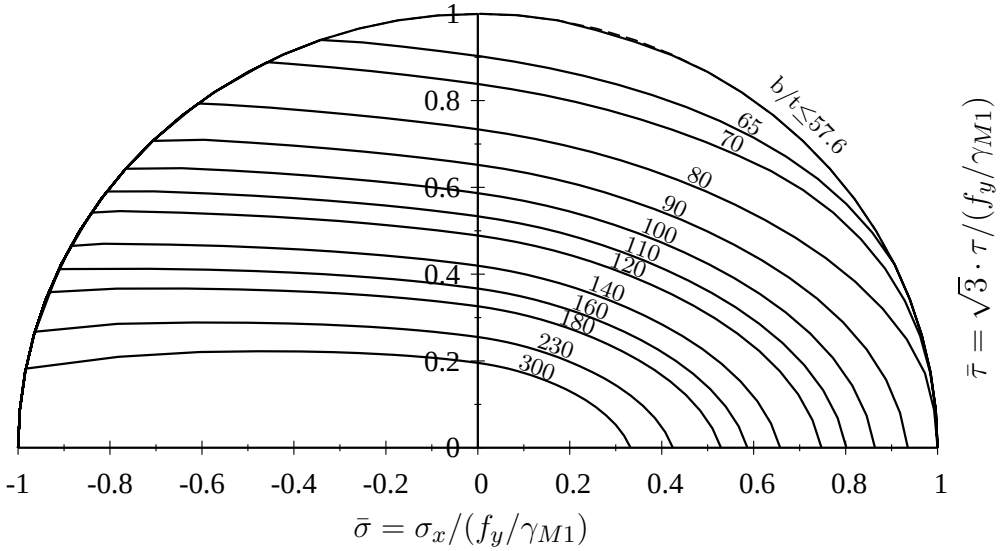

Figure F.9: Limits (b/t), σ_x–τ interaction curves for S 355, $\psi = -0.5$.

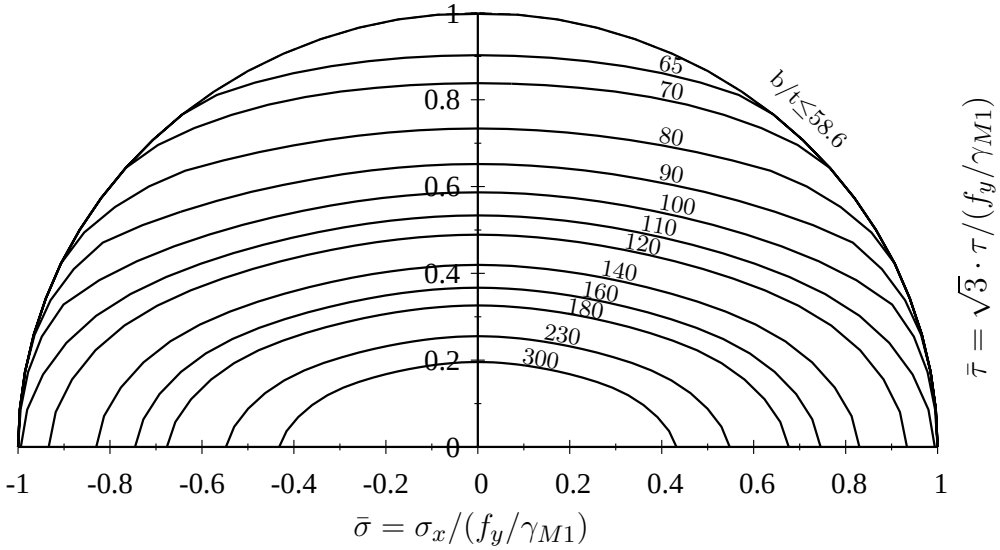

Figure F.10: Limits (b/t), σ_x–τ interaction curves for S 355, $\psi = -1$.

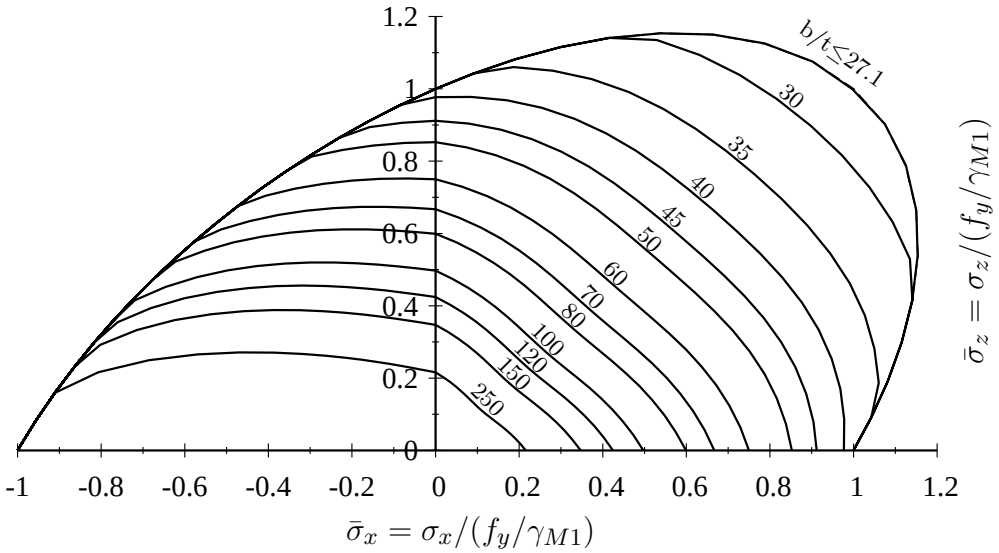

Figure F.11: Limits (b/t), σ_x–σ_z interaction curves for S 235 using the Winter curve as reference strength.

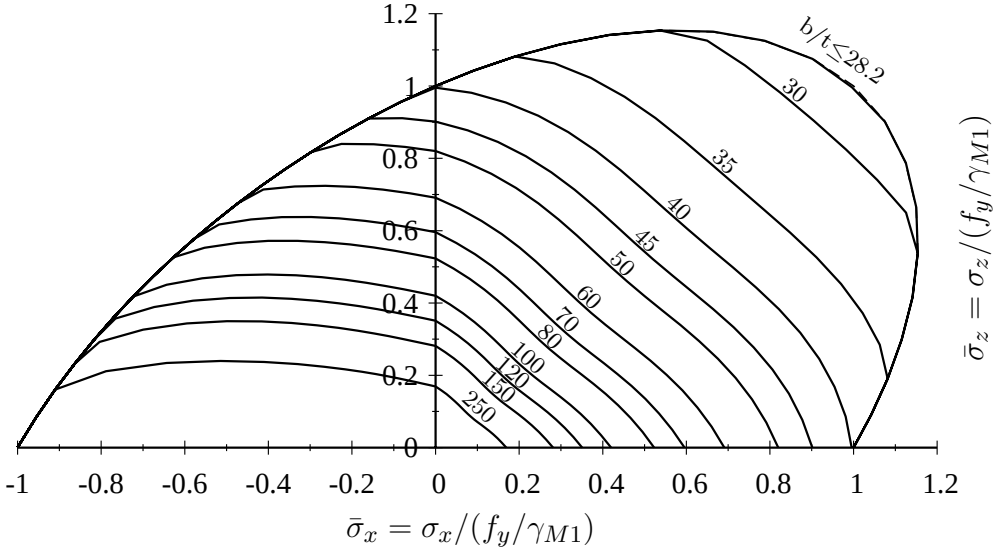

Figure F.12: Limits (b/t), σ_x–σ_z interaction curves for S 235 using the buckling curve from Annex B, EN 1993-1-5 [36] as reference strength.

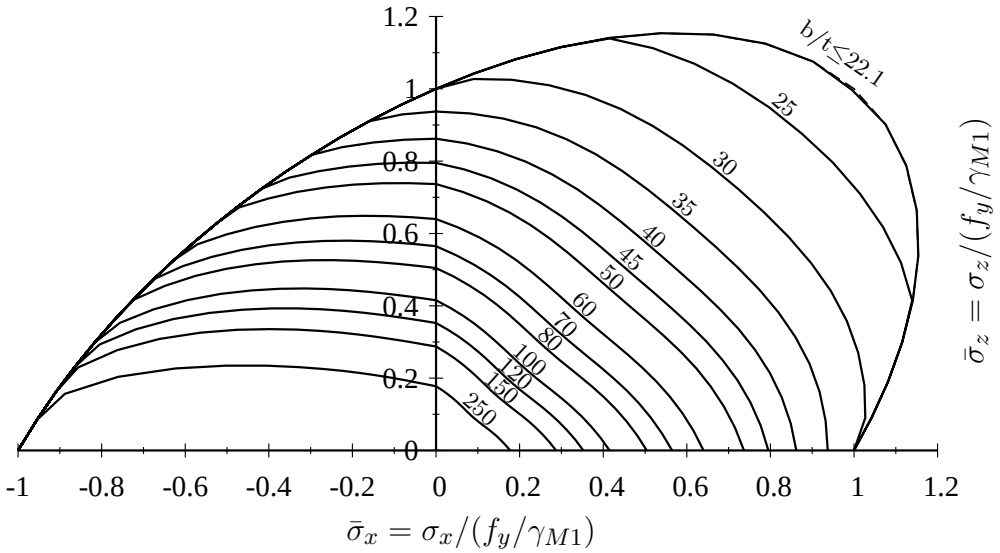

Figure F.13: Limits (b/t), σ_x–σ_z interaction curves for S 355 using the Winter curve as reference strength.

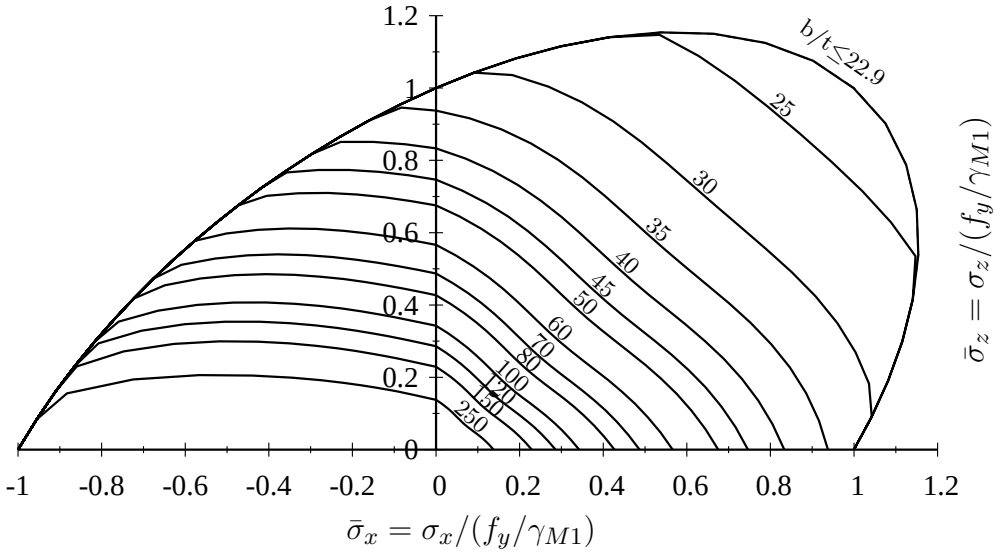

Figure F.14: Limits (b/t), σ_x–σ_z interaction curves for S 355 using the buckling curve from Annex B, EN 1993-1-5 [36] as reference strength.